



# PROBING QUASAR ENVIRONMENTS WITH TUNABLE FILTER IMAGING



JOHN D. SWINBANK  
HERTFORD COLLEGE  
UNIVERSITY OF OXFORD

*A thesis submitted in candidature for the degree of  
Doctor of Philosophy*

Michaelmas 2006

## **Declaration**

No part of this thesis has been accepted, or is in the process of being submitted, for any degree, diploma, certificate or other qualification in this university or elsewhere.

This thesis is the result of my own work unless otherwise stated. The research was carried out in collaboration with my supervisors, Drs Joanne Baker and Isobel Hook, and benefited greatly from the invaluable advice of Dr Jordi Barr.

The oral examination of this thesis was conducted on Monday 22 January 2007 by Steve Rawlings (University of Oxford) and Andrew Bunker (University of Exeter).

# Probing quasar environments with tunable filter imaging

John D. Swinbank  
Hertford College

*A thesis submitted in candidature for the degree of  
Doctor of Philosophy*

Michaelmas 2006

High redshift galaxy overdensities are amongst the earliest traces of today's massive galaxy clusters. There is convincing evidence active galaxies play a role in shaping the evolution of these clusters. Investigation of such systems offers insight into early structure formation in the universe and the impact of active galaxies on their environment.

The Taurus Tunable Filter (TTF) on the Anglo-Australian Telescope provides a powerful and flexible method of performing surveys for line-emitting objects, enabling near-monochromatic imaging over a narrow bandpass at wavelengths in the range 3700–9600 Å.

We have used the TTF to perform a search for Lyman  $\alpha$  emitting galaxies in the fields of three high-redshift quasars. Our targets are a pair radio-loud quasars at a redshift of  $z \sim 2.2$  (MRC B2158-206 and MRC B1256-243) and a radio-quiet quasar at  $z \sim 4.5$  (BR B0019-1522). We have identified candidate emission line galaxies in all three quasar fields: two in the case of MRC B2158-206, four in the field of MRC B1256-243 and seventeen in that of BR B0019-1522.

The analysis of tunable filter observations is complex. We have devoted considerable effort to understanding the properties of our data, including developing a comprehensive system for simulating observations of fields with a known emission-line population. This has enabled us to place tight constraints on the nature and robustness of our detections.

Our results differ strikingly from field to field. MRC B2158-206 displays no evidence of an overdensity of Lyman  $\alpha$  emitters in the quasar environment. Our observations of MRC B1256-243 lack the sensitivity to probe deep into the quasar environment, but detect a number of extremely luminous objects. In BR B0019-1522, we show convincing evidence of a protocluster, including both galaxy and star formation rate densities an order of magnitude higher than that observed in the field. This is one of the highest-redshift protoclusters detected around a radio-quiet AGN.

## Acknowledgements

During this project, I have benefited enormously from the input of not just one but two supervisors. First, many thanks are due to Joanne Baker for getting the whole thing started. Isobel Hook was generous (or foolish!) enough to take over part of the way through: her insights and advice were invaluable in reaching a conclusion. Thank you both.

After Joanne left, the remaining tasks seemed daunting indeed without the benefit of her experience in the area being studied. Fortunately, Jordi Barr was willing to lend his expertise. Thank to him, and also to Joss Bland-Hawthorn for his advice and enthusiasm.

I have benefited greatly from discussions with many members of the department over the years, and extend my thanks to them all. However, special mention must go to Katherine Blundell: I wouldn't be where I am today without her support, advice and encouragement (not to mention a few hot dinners).

Essential to the production of any thesis is a happy working environment. To that end, thanks to all my fellow denizens of the Tower over the years. Particular mention should go to Edd, Elizabeth, Emily, James and Thomas. Equally vital is copious 'liquid refreshment'—thanks to everybody who provided such convivial company in the Royal Oak on Tuesday (and other) nights: Dave, Dom, Philipp, Rachel, Sarah, Will, Tony and many more.

Outside the department, thanks are due to all the members of Hertford College, which has been a perfect base for my studies. In particular, thanks to its Physics fellows for providing me gainful employment (and to its undergraduates, for putting up with me) and to Steve Wilder, for both friendship and illuminating discussions on statistics.

Many occupants of *#keble* have provided welcome distractions over the years. In particular, thanks to Art and Saffie (and Ceefer!), who provided not just entertainment but also a roof over my head.

The final stages of this thesis were completed at the Astronomical Institute "Anton Pannekoek" in Amsterdam: thanks to all its members for making me feel so welcome.

Finally, thanks to my family, without whom neither I, nor this thesis, would be.

# The | *Contents*

<b>1</b>	<b>Introduction</b>	<b>1</b>
1.1	Quasars and active galactic nuclei . . . . .	1
1.1.1	Characteristics of AGN . . . . .	1
1.1.2	The unified scheme . . . . .	2
1.1.3	Quasars . . . . .	5
1.2	Clusters of galaxies . . . . .	6
1.2.1	The composition of a cluster . . . . .	6
1.2.2	Searching for clusters . . . . .	8
1.3	Star formation . . . . .	11
1.3.1	Disc-based star formation . . . . .	12
1.3.2	Circumnuclear star formation and starbursts . . . . .	13
1.3.3	The appearance of star forming galaxies . . . . .	14
1.3.4	Searching for high redshift star formation . . . . .	15
1.4	Tying together clusters, quasars and star formation . . . . .	17
1.4.1	The importance of clusters . . . . .	17
1.4.2	The cluster environment of quasars . . . . .	18
1.4.3	Star formation in relation to clusters and AGN . . . . .	19
1.5	Probing the cluster environments of high- $z$ AGN . . . . .	20
1.5.1	Traditional Lyman $\alpha$ searches . . . . .	21
1.5.2	Tunable filter imaging . . . . .	22
1.5.3	The very highest redshifts . . . . .	23
1.6	Aims and outline of this thesis . . . . .	24
<b>2</b>	<b>Tunable filter imaging: theory and practice</b>	<b>26</b>
2.1	The design and implementation of a tunable filter . . . . .	26
2.1.1	The Fabry-Pérot Interferometer . . . . .	27
2.1.2	Simplifying the Airy Function . . . . .	31

2.1.3	Design and implementation of the Taurus Tunable Filter . . . . .	32
2.1.4	Characteristics of tunable filter observations . . . . .	41
2.2	Target selection . . . . .	47
2.2.1	Redshift $\sim 2.2$ . . . . .	47
2.2.2	Redshift $\sim 4.5$ . . . . .	50
2.3	Observations . . . . .	52
2.3.1	Objects at $z \sim 2.2$ . . . . .	52
2.3.2	An object at $z \sim 4.5$ . . . . .	55
2.4	Summary . . . . .	57
<b>3</b>	<b>Data Reduction</b>	<b>59</b>
3.1	General data reduction techniques . . . . .	59
3.1.1	Bias correction . . . . .	60
3.1.2	Flat field correction . . . . .	60
3.1.3	Data cropping . . . . .	61
3.1.4	Aligning and combining frames . . . . .	62
3.1.5	Wavelength calibration: the ‘sausage cube’ . . . . .	63
3.1.6	An introduction to SExtractor . . . . .	65
3.1.7	Photometry . . . . .	67
3.1.8	Uncertainties and signal to noise ratio . . . . .	70
3.1.9	Object detection and catalogue creation . . . . .	74
3.2	Specifics of each field . . . . .	74
3.2.1	MRC B2158-206 . . . . .	74
3.2.2	MRC B1256-243 . . . . .	86
3.2.3	BR B0019-1522 . . . . .	92
3.3	Summary . . . . .	98
<b>4</b>	<b>Simulations</b>	<b>100</b>
4.1	Aims of the simulation process . . . . .	100
4.2	Building simulated images . . . . .	101
4.2.1	Background simulation . . . . .	101
4.2.2	Constructing objects . . . . .	104
4.2.3	Image production . . . . .	112
4.3	Individual image analysis . . . . .	112

4.3.1	Optimising detection parameters . . . . .	113
4.3.2	Aperture corrections redux . . . . .	114
4.3.3	Depth of individual images . . . . .	115
4.4	Overall field analysis . . . . .	119
4.4.1	Overall field completeness . . . . .	120
4.5	Summary . . . . .	124
<b>5</b>	<b>Identifying candidate galaxies</b>	<b>126</b>
5.1	Object detections . . . . .	126
5.1.1	MRC B2158-206 . . . . .	129
5.1.2	MRC B1256-243 . . . . .	133
5.1.3	BR B0019-1522 . . . . .	137
5.2	Contaminants . . . . .	144
5.2.1	Noise artifacts . . . . .	144
5.2.2	Continuum objects . . . . .	144
5.2.3	Lower redshift interlopers . . . . .	145
5.3	Summary . . . . .	153
<b>6</b>	<b>Distribution and properties of galaxy candidates</b>	<b>154</b>
6.1	Clustering of ELG candidates . . . . .	154
6.1.1	Distribution on the sky . . . . .	154
6.1.2	Distribution along the line of sight . . . . .	159
6.1.3	Space density of galaxies . . . . .	164
6.2	Star formation rates . . . . .	167
6.2.1	Lyman $\alpha$ calibration . . . . .	167
6.2.2	Weaknesses of Lyman $\alpha$ as a star formation diagnostic . . . . .	169
6.2.3	Calculated star formation rates . . . . .	170
6.3	Summary . . . . .	175
<b>7</b>	<b>Conclusions</b>	<b>177</b>
7.1	Our results . . . . .	177
7.2	Placing our results in context . . . . .	178
7.2.1	Emission line galaxies in the field . . . . .	178
7.2.2	The environments of AGN . . . . .	179

7.2.3	The star formation history of the universe . . . . .	182
7.3	Future work . . . . .	184
7.3.1	Spectroscopy of ELG candidates . . . . .	184
7.3.2	Further imaging of these fields . . . . .	185
7.3.3	Future surveys of AGN environments . . . . .	186
<b>A</b>	<b>Locating the centre of an object</b>	<b>190</b>
<b>B</b>	<b>Data reduction revisited</b>	<b>191</b>
B.1	The removal of charge trapping artifacts . . . . .	191
B.2	Distribution of frames contributing to the median . . . . .	192
B.3	A comparison of mean and median combining . . . . .	193
B.4	Conclusions . . . . .	195
<b>Bibliography</b>		<b>196</b>

# Chapter 1

## *Introduction*

This thesis describes an investigation into *star formation* in the *cluster environments of quasars*. This chapter sets each of those terms into context: first independently, and then by exploring the relationship between the three. We describe briefly the ways in which they have been investigated in the past, before moving on to discuss the contribution this thesis aims to make to the field.

### 1.1 *Quasars and active galactic nuclei*

Quasars are a particular class of active galactic nuclei (AGN). AGN themselves are extra-galactic sources associated with the nuclei of galaxies whose emission is dominated by non-stellar processes. Their emission covers the whole electromagnetic spectrum, from radio to  $\gamma$ -rays. This section briefly outlines their appearance and describes the current understanding of their composition.

#### 1.1.1 *Characteristics of AGN*

AGN may be categorised in a variety of ways; a simple taxonomy is shown in table 1.1, in which they are classified according to two parameters: radio-loudness and the width of their emission lines. Sometimes, more than one class of object shares a given radio categorisation and optical type: these are distinguished by other properties, such as total luminosity (which separates quasars from Seyfert galaxies, for example).

Although quasars were originally discovered due to their strong radio emission, most are in fact radio-quiet: only about 10–20% are classified as ‘radio-loud’ (that is, have a radio-to-optical flux ratio in excess of 10; Kellermann et al., 1989), although this fraction increases with the optical luminosity (Urry and Padovani, 1995). Radio-loud AGN produce

**Table 1.1:** A simplified outline of AGN taxonomy, based on that of Urry and Padovani (1995). The relevance of the orientation of the object with respect to the line of sight is discussed in section 1.1.2.

Radio	Optical characteristics		
	Narrow Line (type 2)	Broad Line (type 1)	Unusual (type 0)
Quiet	Seyfert 2	Seyfert 1 Radio-quiet quasars	
Loud	Narrow line radio galaxies	Broad line radio galaxies Radio-loud quasars	BL Lacertae objects Blazars
Decreasing angle to line of sight →			

large scale jets which give rise to radio emission through synchrotron radiation: in other respects, though, their properties are remarkably similar to their radio-quiet counterparts (Steidel and Sargent, 1991).

The other major parameter is the width (or, indeed, possible absence) of emission lines. These are recombination lines from various elements, and their width is due to Doppler motion of the emitting material. Objects are classified as displaying broad (type 1) or narrow (type 2) lines; the dividing point is taken as a full width at half maximum of  $1000 \text{ km s}^{-1}$ . Some unusual (type 0) objects display only very weak lines.

As table 1.1 shows, objects are seen with a variety of combinations of properties. For instance, type 1 objects are seen as both radio-quiet (radio-quiet quasars or type 1 Seyfert galaxies) and radio-loud (broad line radio galaxies or radio-loud quasars), and similarly for type 2 (type 2 Seyfert objects and narrow line radio galaxies). BL Lacertae objects are radio-loud objects with weak emission lines.

There is, then, a considerable range of properties among the objects we group together as AGN. However, efforts have been made to build a single model which can describe all these different characteristics: a unified scheme for AGN.

### 1.1.2 *The unified scheme*

The idea behind the development of unified schemes for AGN is that all the different types listed in table 1.1 may be regarded as different manifestations of a similar underlying

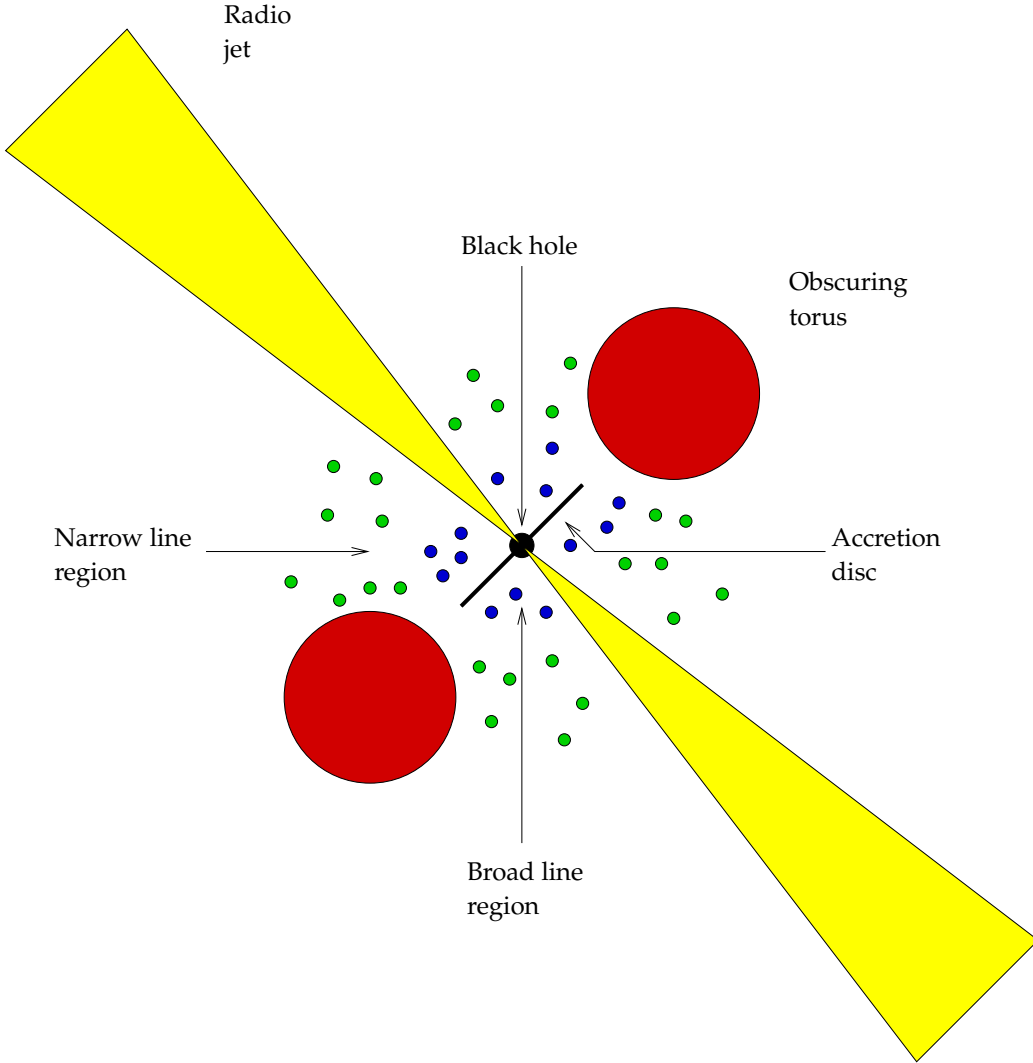


**Figure 1.1:** Schematic of the structure of a typical AGN, based on several such diagrams in the literature (e.g. Urry and Padovani, 1995) and, perhaps most directly, Barr (2003). A central accreting black hole is surrounded by an obscuring torus (shown in red), which limits the view of the rest of the system, and, perhaps, relativistic jets (yellow). The rest of the system includes fast-moving broad line emitting gas clouds (blue) near the black hole and the more distant narrow line clouds (green).

structure: the appearance to an external observer depends largely on the mass of the object and its relative orientation.

An outline of the commonly accepted scheme is given by Antonucci (1993) while figure 1.1 shows a cartoon representation of the structure. At its heart, the engine of the

AGN is an accreting black hole, surrounded by an accretion disc, which is very luminous in the UV and X-ray regimes. Broad emission lines are produced in fast moving clouds of gas orbiting close to the black hole: this is the “broad line region”. This central region is surrounded by a thick dusty torus, which obscures the view from transverse lines of sight. Further from the black hole, beyond the shadow of the torus, are slower moving gas clouds, emitting narrower lines: this is the “narrow line region”.

The above provides us with an explanation for the dichotomy between type 1 and type 2 AGN: it depends on the angle at which we are viewing them. “Side-on” observations, through the dusty torus, produce type 2 objects, as we see only the narrow line region together with some scattered light from the core; “face-on” observations, however, enable us to see to the depths of the object, observing directly the broad line region.

Radio synchrotron emission, in those cases where it is observed, is caused by the outflow of relativistic charged particles along magnetic field lines. These jets are perpendicular to the accretion disc surrounding the black hole. When we observe a radio-loud object face-on, Doppler beaming of the emission from the jets makes a large contribution to the flux: this is a blazar.

Such a description neatly explains the observed differences between the various types of AGN. However, it does not address the question of radio emission: why is this observed in some cases, but not others?

Beyond the obvious radio jets, the major differences observed between radio-loud and radio-quiet AGN is that radio-loud objects are associated with elliptical galaxies while radio-quiet objects can reside in spiral hosts (Smith et al., 1986; Hutchings et al., 1989). Perhaps the most likely explanation is that the normal process of accretion onto a black hole does not cause it to spin-up enough to cause radio jets: therefore, most AGN are radio-quiet. However, a merger between galaxies can both disrupt the spiral structure, forming an elliptical galaxy (Toomre and Toomre, 1972) and cause the black holes to form a binary system which eventually coalesces. Such an interaction can produce a very massive, very rapidly spinning black hole—and hence produce the ideal conditions for jet production (Wilson and Colbert, 1995; Cattaneo, 2002).

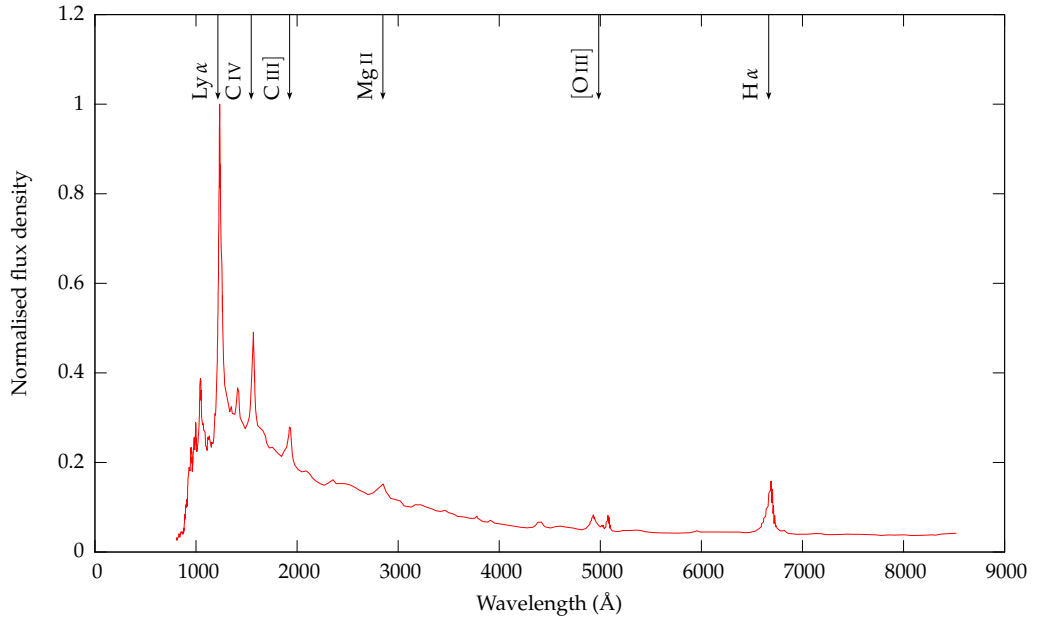


**Figure 1.2:** A composite quasar spectrum, based on that of Vanden Berk et al. (2001), produced by combining a homogeneous set of over 2200 quasar spectra from the Sloan Digital Sky Survey (York et al., 2000). The major emission lines are indicated.

### 1.1.3 Quasars

This thesis is specifically concerned with the environments of quasars, rather than AGN in general. As seen in table 1.1, these display broad line optical characteristics but may be observed either with or without powerful radio jets.

Quasars were first observed as star-like objects (“QUASi STELLAR”), but identification of characteristic emission lines in their spectra demonstrated they existed at high redshift—and hence had tremendous luminosities (Schmidt, 1963). A typical quasar spectrum is shown in figure 1.2, which shows the major emission lines. Note that the spectrum is peaked towards the blue: it does not follow a black-body shape, suggesting that most of the emission is non-thermal. The absorption features at wavelengths shorter than Lyman  $\alpha$  are caused by the neutral hydrogen clouds along our line of sight.

## 1.2 *Clusters of galaxies*

Having thus briefly outlined the structure of quasars, we now turn our attention to consider groups and clusters of galaxies and their cosmological importance.

It has long been apparent that galaxies do not exist in isolation: Hubble (1934) showed that the distribution of galaxies on the sky was non-random, while Zwicky (1938) recorded that “practically all nebulae are bunched in more or less regular clusters and clouds”. Clusters have continued to attract a great deal of observational attention over the subsequent 70 years, as it has become clear that not only are they interesting systems in their own right but also as tracers of structure formation in the universe.

Note that it is conventional to refer to structures with fewer than 50 members as “groups”; those with more, “clusters”. Groups are typically seen with sizes on the order of 1 Mpc, whereas clusters may be as large as 20 Mpc.

### 1.2.1 *The composition of a cluster*

Although we have referred to “clusters of galaxies”, there are actually three major components of a cluster: the galaxies themselves, the hot, gaseous intracluster medium (ICM) and a dark matter halo. Dark matter makes up around 80% of the total cluster mass, leaving around 14% as ICM and the rest in galaxies (Einasto and Einasto, 2000).

#### 1.2.1.1 *Galaxies in clusters*

The general population of galaxies in clusters is biased towards elliptical and S0 galaxies, whereas the field is dominated by spirals (and therefore typically higher star formation rates; Dressler, 1984). An analogous relationship is seen within clusters themselves—the morphological type of galaxies at a given point is a function of the cluster density: high density regions are dominated by elliptical galaxies, while lower density regions contain spirals (Dressler, 1980). Indeed, Oemler (1974) divided clusters into 3 groups: spiral rich, which have compositions similar to the field and irregular structures; cD clusters, which are rich in ellipticals and have a high density and central concentration, with few spirals

in the core; and spiral poor clusters, dominated by S0 galaxies, not as smooth, dense or centralised as cD clusters.

Early type (elliptical) galaxies in clusters have been shown to provide a very homogeneous population, occupying an extremely tight locus on the colour-magnitude diagram (see, for example, Bower et al., 1992a,b). The tightness of this relationship indicates that the galaxies formed the bulk of their stars over the same period. Furthermore, the red colour of the galaxies indicates that this star formation occurred at high redshift ( $2 < z < 4$ ), and that, since then, the galaxies have been evolving passively, with no significant bursts of new star formation (Aragón-Salamanca et al., 1993; Gladders et al., 1998; Kodama et al., 1998).

### **1.2.1.2** *The intracluster medium*

It has long been known that clusters emit strongly in the X-ray region of the electromagnetic spectrum. It was Felten et al. (1966) who first demonstrated that such emission was consistent with thermal bremsstrahlung from hot gas at temperature of around  $10^8$  K and a density of  $\sim 10^{-3}$  atoms cm $^{-3}$ . The initial suggestion for the origin of this gas was primordial intergalactic gas which had fallen into the cluster potential (Gunn and Gott, 1972); later observations demonstrated iron lines in the X-ray spectrum: since iron must have been produced in stars, at least some of the gas in the ICM must have been ejected from galaxies within the cluster (Bahcall and Sarazin, 1977).

The short dynamic timescale and diffuse nature of the gas means it is thermalised throughout the cluster. It is therefore a faithful tracer of the gravitation potential, and, indeed, can be used to estimate the mass of the cluster (e.g. Sarazin, 1986). Furthermore, searching for the X-ray emission from the ICM provides a useful mechanism for locating clusters, a technique explored further in section 1.2.2.2.

### **1.2.1.3** *Dark matter*

The first suggestion that dark matter played a role in clusters was made by Zwicky (1933), who showed that the mass derived from the rotation curves of galaxies in clusters is not

compatible with the virial theorem, arguing that this must be due to the presence of non-luminous mass. It was, however, only more recently that dark matter became a widely accepted concept, and it is now generally agreed that it forms the vast majority of the cluster mass (Einasto and Einasto, 2000).

Although it is not possible to observe the dark matter directly, weak lensing studies demonstrate that it is distributed with a strikingly similar morphology to the ICM (e.g. Smail et al., 1995). However, the precise nature of the dark matter itself is still, of course, an open question.

### **1.2.2** *Searching for clusters*

Broadly speaking, there are two traditional methods of locating clusters: X-ray and optical surveys, both of which we discuss here. An alternative technique, that of identifying clusters around specific high-redshift objects, is the subject of this thesis; as such, it is considered in detail in section 1.5.

Attention should also be drawn to the possibilities offered by the Sunyaev-Zel'dovich effect (Sunyaev and Zel'dovich, 1970). This enables the detection of massive clusters by measuring their effect on the cosmic microwave background (CMB): CMB photons undergo inverse Compton scattering from the hot electrons in the ICM, which increases their energy slightly. This redshift-independent brightening of the CMB can be used to estimate the mass of the cluster.

The Sunyaev-Zel'dovich effect offers great potential for detecting high redshift clusters. However, the first sensitive surveys are only now getting underway (Kneissl et al., 2001; Kosowsky, 2003; Ruhl et al., 2004; Loh et al., 2005): although the years to come offer great promise, the technique is not considered further here.

#### **1.2.2.1** *Optical searches for clusters*

Clusters were first identified by simply noting the non-uniform distribution of galaxies on the sky; the earliest efforts were made simply by counting the number of objects which fell within a given magnitude range in a particular region. The most famous of the early

optical catalogues is that of Abell (1958), who identified over 4000 clusters at redshifts of less than 0.2. Also notable are the efforts of Zwicky et al. (1968), who identified a total of almost 10000 clusters over the course of nearly a decade.

In more recent times, optical identifications of clusters have been made using much the same methods, but with ever increasing automation and more objective selection methods: for example, Lumsden et al. (1992) and Dalton et al. (1994) used computerised systems to automatically identify clusters in large catalogues of galaxies. However, this strategy is limited to lower redshifts, both by the relatively bright limiting magnitudes in such surveys and by the nature of hierarchical structure formation: high- $z$  clusters are smaller, and hence contrast less with the field.

Various techniques have been employed to overcome these limitations. The Palomar distant cluster survey (Postman et al., 1996), for example, pioneered the ‘matched-filter’ technique, identifying clusters by simultaneously considering the projected positions and apparent magnitudes of galaxies. They used this method to probe for clusters up to  $z \sim 1.2$ ; it has subsequently been refined (e.g. by Kawasaki et al., 1998) and used in other surveys such as that of Olsen et al. (1999). Another method was set forth by Gladders and Yee (2000), who specifically identify clusters based on the overdense population of passively evolving elliptical galaxies mentioned in section 1.2.1.1; they demonstrated that this method is effective to  $z \sim 1.5$ .

The massive volumes of space covered by the Sloan Digital Sky Survey (SDSS) (York et al., 2000) provide multicolour data on vast numbers of galaxies to be exploited by the next generation of cluster surveys. These search for clusters in a variety of ways, including variations on the matched-filter technique (Bahcall et al., 2003) and by exploiting the full range of colours available in SDSS to identify cluster galaxies based on the colour-magnitude relation (Goto et al., 2002).

However, there are weaknesses to the optical detection of clusters. Most notably, the selection procedure is highly vulnerable to projection effects: it is awkward to distinguish a truly dense cluster from two (or more) smaller systems falling along the same line of sight. The only sure way to confirm overdensities in this way is an extremely observationally expensive spectroscopic campaign.

There are other problems. At the highest redshifts, we expect to see only the progenitors of today's massive clusters. Distinguishing these disordered systems from the general population of field galaxies is awkward. Furthermore, the use of the colour-magnitude relation becomes less reliable at high- $z$ : Butcher and Oemler (1978) noted that the fraction of blue galaxies in a cluster increases with redshift, and, indeed, at the highest redshifts the massive red ellipticals the colour-magnitude relationship depends on will still be in the process of forming.

### **1.2.2.2 X-ray searches for clusters**

We have seen that a significant fraction of the mass in clusters is contained in the hot, gaseous intracluster medium. This gas emits X-rays through thermal bremsstrahlung; these can not only be used to locate the cluster, but also to estimate its total mass (Sarazin, 1986). X-ray emissions from clusters are centrally concentrated: they are easy to distinguish against the X-ray sky, and less prone to projection biases than their optical counterparts.

Of course, X-rays do not penetrate the Earth's atmosphere: all the observations must be carried out from space. The first X-ray survey carried out by Uhuru documented 52 clusters, but it was the launch of the Einstein X-ray imaging telescope in 1978 that really heralded the dawn of a new era of cluster discovery through its Medium Sensitivity Survey (Maccacaro et al., 1981), eventually discovering 104 clusters, 40% of them at redshifts greater than  $z = 0.15$ . ROSAT provided greater sensitivity and spatial resolution, prompting a variety of investigations which identified clusters at redshifts as high as  $z = 0.8$  (e.g Ebeling et al., 1996, 1998, 2001; Burke et al., 1997; Rosati, 1998; Perlman et al., 2002).

Spearheading the latest generation of orbital X-ray observatories, XMM-Newton offers 10 times the effective area and five times the spatial resolution of ROSAT. Its large public database provides ample opportunities for serendipitous cluster surveys (such as that of Romer et al., 2001, for instance), while particular attention should be drawn to the XMM Large Scale Structure survey (Pierre et al., 2004), a deep survey of 64 square degrees of the sky which has identified numerous clusters at a range of redshifts pushing towards  $z = 2$  (e.g. Valtchanov et al., 2004; Willis et al., 2005; Bremer et al., 2006).

However, X-ray searches for clusters are not without their weaknesses. Perhaps most importantly, they are biased to detecting only the most massive clusters at high redshift. This is simply because a luminous cluster at large  $z$  produces the same flux as a less luminous lower-redshift system. However, there other difficulties as well:

- High redshift protoclusters will not necessarily be virialised: the X-ray emission in such a case will not represent the true mass of the cluster;
- As we have seen, many AGN emit across all of the electromagnetic spectrum, including in the X-ray: there is a risk of confusing them with clusters in surveys where the sources are unresolved;
- Merging systems shock the ICM, enhancing its X-ray luminosity: a flux limited sample will, therefore, contain some proportion of sources which are intrinsically fainter than measured.

In short, using X-rays to detect protoclusters forming at high redshift is, even with the latest techniques, a challenge: even the latest generation of surveys with XMM-Newton detect only a few of the most massive clusters above  $z = 1.5$ .

### **1.3 Star formation**

An important step towards understanding the development of galaxies and hence large scale structure is a clear understanding of the evolution of the integrated star formation rate per unit volume. This is generally acknowledged as having been at a maximum around  $z \sim 1$ , declining at lower redshifts (Madau et al., 1998). At higher redshifts, a plateau to at least  $z \sim 3$  seems likely, but there is a clear decline by  $z \sim 6$  (Bunker et al., 2004). In this section, we describe the processes and properties within galaxies which control their star formation rate, before moving on to discuss strategies for locating and measuring high- $z$  star forming galaxies.

Galaxies may be observed with a wide range of star formation rates. At the highest end, galaxies displaying luminous infra-red starbursts—most usually associated with tidal interactions or mergers—may reach rates as high as  $1000 M_{\odot} \text{ year}^{-1}$ . Optical starbursts might reach  $100 M_{\odot} \text{ year}^{-1}$ , while gas-rich spiral galaxies are on the order of  $20 M_{\odot} \text{ year}^{-1}$ .

Meanwhile, gas-poor elliptical galaxies experience rates approaching zero. Of course, the star formation rate depends to a large extent upon the size of the galaxy itself; we naturally expect larger galaxies to have more material available for stars to form.

Although we analyse the star formation rate of the galaxy as a whole—at the redshifts encountered in this thesis, the galaxies are unresolved by the instrumentation we will use—there are actually two very different regions within a galaxy where star formation takes place (Kennicutt, 1998): in the compact, dense gas around the centre of the galaxy, and in the extended discs of spiral and irregular galaxies.

### **1.3.1 Disc-based star formation**

Disc-based star formation may account for rates up to  $20 \text{ M}_\odot \text{ year}^{-1}$  (Kennicutt, 1998). The rate is strongly correlated with the Hubble type: many elliptical and the earliest-type disc galaxies show no detectable star formation at all (Caldwell et al., 1994), while some seems to be present in all spirals (types Sa and later), according to the deep H $\alpha$  images of Caldwell et al. (1991). The rate then increases by a factor of around 20 from Sa to Sc (Kennicutt et al., 1994); this is due both to an increase in the total number of star forming regions per unit mass and by an increase in the mass of each region (Bresolin and Kennicutt, 1997).

What properties of the galaxy influence the star formation rate? We have seen that the rate depends on the Hubble type; Kennicutt (1998) suggested that this is due to an underlying relationship between gas density and star formation which is independent of galaxy type. The morphology of the galaxy—in terms of bars and spiral arm structure—has, however, been observed to have little effect: although bars perturb gas flows they do not seem to affect total disc SFRs (Ryder and Dopita, 1994). ‘Grand-design’ (that is, sharply defined two-arm) structure appears to concentrate star formation in the spiral arms (Cepa and Beckman, 1990) but without increasing the star formation in the galaxy as a whole (Elmegreen and Elmegreen, 1986; McCall and Schmidt, 1986).

External influences can have a much more significant effect on the disc SFR. For example, interacting and merging galaxies have often been observed to have excess star formation, as for example in Xu and Sulentic (1991) and Liu and Kennicutt (1995). The signif-

icance of this effect varies from case to case, and is particularly relevant to circumnuclear star formation (section 1.3.2). The cluster environment of galaxies plays a multi-faceted role, as star formation is on the one hand enhanced by tidal interactions, but simultaneously reduced by gas stripping (Moss and Whittle, 1993).

### **1.3.2 Circumnuclear star formation and starbursts**

It has long been known that the volume surrounding the nucleus in many spiral galaxies contains bright, star forming regions with properties which bear little relationship to the more extended galaxy discs (Morgan, 1958; Sérsic and Pastoriza, 1967). Ho et al. (1997a) reported on a sample of over 200 such emission-line nuclei: they occur in 42% of bright spirals, with the fraction increasing along the Hubble sequence from 8% in S0 galaxies to 80% in Sc types; the fraction in ellipticals is effectively zero. Most of these nuclei display modest star formation rates:  $\sim 0.1 M_{\odot} \text{ year}^{-1}$  in the Ho et al. sample, and the same order of magnitude in the samples of Scoville et al. (1983) and Devereux (1987), which were observed in the infra-red. However, the infra-red observations also reveal a number of more luminous regions, with star formation rates up to  $1000 M_{\odot} \text{ year}^{-1}$ ; these are less visible in the optical, as they are associated with dense molecular gas discs leading to high extinction (Young and Scoville, 1991). These dramatic star formation rates are referred to as ‘starbursts’, a term coined by Weedman et al. (1981).

High-resolution infra-red imaging of these luminous objects reveals that the star formation is taking place within a few kiloparsecs of the nucleus (Smith and Harvey, 1996), while molecular gas is concentrated over a similar area (Young and Scoville, 1991). Within this small region, the surface density of star formation is up to four orders of magnitude higher than in the disc overall; the limited volume of material limits the timescale of such activity to a fraction of a gigayear (Kennicutt, 1998). Within that timescale, though, the most powerful starbursts approach the limit for the maximum possible star formation rate in a galaxy (Lehnert and Heckman, 1996).

What triggers such dramatic activity? Perhaps most significantly, interactions and mergers with other galaxies. Keel et al. (1985) and Bushouse (1986) demonstrated that interacting galaxies display a significant excess of nuclear H $\alpha$  emission over their isolated

peers—and this is true even if the interaction is not strong enough to distort the galactic disc: it is relatively easy to plunge many nuclei into starbursts. Such interactions can also moderate the strength of starbursts: low luminosity starbursts need relatively modest supplies of matériel for star formation such that it can be provided by dynamical processes within the galaxy. However, the much larger bursts need huge quantities of fuel which can only be supplied under violent dynamical stress such as a merger.

Dynamical effects within the galaxy also play a role. Sérsic and Pastoriza (1967) first noticed the importance of a bar, demonstrating that a substantial fraction ( $\sim 25\%$ ) of barred S and SA galaxies displayed unusual nuclear activity which was not observed among their unbarred counterparts. Ho et al. (1997b) showed that, although a bar is neither a necessary nor a sufficient reason for elevated circumnuclear star formation to occur, barred spirals do show significantly higher star formation rates in this region than their unbarred counterparts.

Another property of galaxies which can have an impact on circumnuclear star formation is its Hubble type. The situation here is complex. Circumnuclear star formation is observed in spiral galaxies of all Hubble types, but is most significant in early-type galaxies, where disc based star formation is lowest. Indeed, nuclear star formation rates of some early-type galaxies are comparable to the total star formation of a late-type spiral (Devereux, 1987).

### **1.3.3 *The appearance of star forming galaxies***

Individual stars are unresolved in all but the very closest galaxies, and certainly in those covered by this work. It is therefore necessary to consider the properties of the galaxy as a whole when identifying star forming galaxies and calculating the star formation rate. Kennicutt (1992a,b) compiled an atlas of 55 galaxies in the local universe, using them to demonstrate how the spectrum varies with the star formation rate.

Bright, blue stars are shorter lived than their redder, less luminous counterparts. A simple method of quantifying the star formation in a galaxy is to consider the integrated luminosity in the blue or ultraviolet part of the spectrum: in the most naive approximation, this is directly proportional to the rate of formation of young stars. In fact, a more sophisti-

cated model is required to perform an accurate calibration as even old stars still emit some fraction of blue light; in general, however, star formation is reflected in the ‘blueness’ of a galaxy.

A more dramatic effect is seen in the emission lines of the galaxy. The nebular recombination lines effectively re-emit the integrated luminosity of the galaxy blueward of the Lyman limit; in this way, they directly probe the young, massive stellar population, and rapidly increase in strength with the star formation rate. In this thesis, Lyman  $\alpha$  is used as a marker of star forming galaxies and as a measure of their star formation rates, a calculation which is considered in some detail in section 6.2.

A similar effect is seen in forbidden lines. These lines are not direct indicators of the luminosity of the young stars in the galaxy, however, the properties of some—particularly [O II]—are sufficiently well understood that it is possible to derive the star formation rate from them, a calibration performed by Gallagher et al. (1989).

Star forming galaxies can also be identified by their far-infrared continuum emission. A significant fraction of the total galactic luminosity is absorbed by dust and re-radiated in the infrared. The dust absorption spectrum is peaked in the ultraviolet, so is particularly sensitive to bright, blue young stars. Kennicutt (1998) offers a calibration of the total far-IR luminosity to star formation rate; however, it is not one we exploit here.

#### **1.3.4** *Searching for high redshift star formation*

Until recently, identifying galaxies at high redshifts was an intractable problem. Systematic deep imaging and spectroscopic surveys were sensitive to objects only up to about  $z \sim 1$  (see Lilly et al., 1995, for example). However, over the last decade the latest generation of survey instruments, combined with a variety of new and more flexible set of search techniques, has extended this range to redshifts perhaps as high as  $z \sim 8$ . Here, we briefly outline these techniques and the successes they have brought.

As discussed in section 1.3.3, star forming galaxies exhibit strong nebular recombination lines. Perhaps the most prominent of these is Lyman  $\alpha$ : indeed, Partridge and Peebles (1967) suggested that it could form several percent of the total luminosity of young galax-

ies. At high redshifts, this Lyman  $\alpha$  emission (with a rest frame wavelength of 1216 Å) is shifted into the visible, making it an ideal target for optical surveys. Despite some unsuccessful early efforts (e.g. Thompson et al., 1995), Lyman  $\alpha$  emitters with redshifts up to  $z \sim 6$  were soon reported by Hu and McMahon (1996) and Hu et al. (1998) using narrow-band imaging and spectroscopy on the Keck II telescope. More recently, and on a rather larger scale, the Large Area Lyman  $\alpha$  (LALA) survey (Dawson et al., 2004) has identified nearly 400 Lyman  $\alpha$  emitters at redshifts up to  $z = 6.535$ .

Lyman  $\alpha$  is not, of course, the only emission line observed from primeval galaxies; indeed, others may be preferable due to a lower sensitivity to extinction by dust. Bunker et al. (1995) demonstrated the detection of (and estimation of the galactic star formation rate using) H  $\alpha$  in a  $z = 2.3$  galaxy, although further work did not reveal any previously undiscovered objects (Bunker, 1996). Some detections have, however, been made by other groups using similar methods (Thompson et al., 1996).

The previous section mentioned that star forming galaxies were luminous in the rest frame far-IR. The first detections exploiting this effect were made using the SCUBA camera on the James Clark Maxwell Telescope (Gear and Cunningham, 1995) in the mid-1990s. However, such early instruments were limited in terms of collecting area and resolution, and only a few such sources were detected. More recently, however, instrumentation just as the Spitzer Space Telescope (Werner et al., 2004) has reinvigorated the field, a process which looks set to continue with new instrumentation in the future (e.g. Nagamine et al., 2006).

Gravitational lensing provides a convenient way of magnifying the appearance of high redshift galaxies and hence bringing them within the detection limits of current surveys. The possibilities of such a method were graphically demonstrated by Yee et al. (1996a), who serendipitously stumbled upon a  $z = 2.7$  starburst ( $4000 M_{\odot} \text{ year}^{-1}$ ) in the CNOC cluster redshift survey (Yee et al., 1996b). Lensing studies continue to push to higher and higher redshifts; for example, the recent work of Richard et al. (2006) detects galaxies at  $z > 6$  and is able to put constraints on star formation rates out to  $z = 10$ .

Perhaps the most important method of detecting high-redshift galaxies has been the “Lyman-break technique”. This takes advantage of the Lyman discontinuity (‘break’) at

912 Å in the continuum of galaxy spectra due to the ionisation of hydrogen in the atmospheres of massive stars. This effect is enhanced by absorption in H<sub>I</sub> gas, which is abundant in young galaxies and intervenes in smaller clouds along our line of sight to the galaxy; the overall effect is a sudden drop in brightness of the galaxy by around an order of magnitude below the Lyman limit. At high redshifts, the break is shifted into the optical; the upshot is that a galaxy observed through one filter will suddenly ‘disappear’ when another at a somewhat shorter wavelength is used. The wavelength of this ‘drop-out’ identifies the redshift of the galaxy. For a comprehensive review of the properties of Lyman-break galaxies, see Giavalisco (2002).

The first to exploit the Lyman-break technique were Steidel and Hamilton (1992, 1993), who identified galaxies at  $z > 3$  in the fields of two quasars. Since then, the technique has been pushed to progressively higher and higher redshifts: the latest reports have Lyman drop-outs tentatively being identified at redshifts up to  $z \sim 8$  (e.g. Bouwens et al., 2004a).

A final method for identifying high- $z$  galaxies is to target the neighbourhood of luminous objects already known to be at high redshift. Such surveys have experienced a high degree of success, identifying galaxies out to redshifts around  $z \sim 6$  (e.g. Zheng et al., 2006). Such surveys are typically aimed at identifying galaxy overdensities around high- $z$  AGN: it is a survey such as this around which this thesis is based. As such, this technique is discussed in more detail in section 1.5.

## **1.4** *Tying together clusters, quasars and star formation*

We have, so far, considered clusters, quasars and star forming galaxies as independent entities. However, this thesis studies the interaction between the three. In this section, the connections between them are explored.

### **1.4.1** *The importance of clusters*

How did the Universe come to appear as we see it today? It is believed that structure forms from the initial density perturbations in the distribution of mass after the big bang

(Peacock et al., 2001): these collapse under gravitational instability, eventually causing gas to accumulate and cool, and star formation begins (White and Rees, 1978). The star forming regions grow hierarchically; eventually, the initial density perturbations become the massive clusters we see today (Kaiser, 1984).

Clusters, then, have a telling cosmological importance: their dark matter halos are the root of much of the structure that formed in the universe. The number and distribution of clusters can therefore be used to put constraints on cosmological parameters and thereby better understand the formation of the Universe (e.g. Peebles et al., 1989; Holder et al., 2001; Refregier et al., 2002).

#### **1.4.2** *The cluster environment of quasars*

The environments of quasars provide an important source of information for improving our understanding of the processes within AGN and, as such, they have long been the subject of scrutiny.

The earliest studies of the environments of quasars soon found evidence that they were often associated with groups and clusters of galaxies (?Oemler et al., 1972), while statistical analysis demonstrated that low redshift (i.e.  $z < 0.1$ ) radio sources are, in general, likely to be associated with richer groupings than other galaxies (Seldner and Peebles, 1978; Longair and Seldner, 1979).

Over the subsequent decades, several more studies have been made into the environments of quasars. Much of this work has been carried out by Green and Yee (1984) and collaborators (Yee and Green, 1984; Yee et al., 1986; Yee and Green, 1987; Ellingson et al., 1991a,b; Yee and Ellingson, 1993), who analysed an optically-selected sample of around 140 radio-loud and radio-quiet quasars at a variety of redshifts up to  $z \sim 0.6$ . They confirmed the hypothesis that quasars tend to lie in clusters, but found a dichotomy between the radio-loud and the radio-quiet type: radio-quiet objects were found in significantly less rich environments. The conclusion drawn was that radio-loud and radio-quiet quasars are quite different types of object—the one could not involve into the other.

Hall et al. (1998) and Hall and Green (1998) pursued a similar programme of obser-

vations at higher redshifts—up to  $z = 2$ . Although not specifically selected based on radio power, all their objects were radio-loud; their results extended the association of radio-loud quasars with rich clusters to much higher redshift, but did not shed any light on the radio-loud/radio-quiet dichotomy. Work investigating the cluster environments of AGN has subsequently continued to higher redshift still; we review some of the most recent work in the area in section 1.5.

The picture painted by McLure and Dunlop (2001) sharply contrasted with that of Green and Yee. They considered a sample of 44 AGN at  $z \simeq 0.2$  with Hubble Space Telescope imaging, finding no evidence that radio-quiet quasars inhabited poorer environments than their radio-loud counterparts. Instead, they concluded that quasars of both radio types were, in general, found in Abell (1958) class 0 clusters. Further, they argued that close match between the space density of clusters and the peak space density of quasars (at  $z \sim 2.5$ ; Warren et al., 1994) indicates that practically all clusters contained an AGN at high redshift.

#### **1.4.3 Star formation in relation to clusters and AGN**

We have seen that clusters and quasars are intimately linked. What, though, is the effect of the powerful quasar upon its surrounding environment? We have already seen that the core galaxies in clusters tend to be passively evolving massive ellipticals, which formed at high redshift. What processes moderated their formation?

Rawlings and Jarvis (2004) proposed that the influence of radio jets from an AGN is a major influence on star formation in clusters. Their suggestion is that early structure in the universe formed in dense protoclusters, each containing on the order of 100 galaxies massive galaxies. Eventually, hierarchical structure formation will cause two of the galaxies to merge; their central black holes will coalesce, triggering a radio-jet episode, as described in section 1.1.2. The powerful radio jets deliver energy to the intracluster medium (Nath and Roychowdhury, 2002), heating the ionised gas and preventing it falling into the protogalaxies.

The galaxies are now starved of any more fuel; Rawlings and Jarvis estimate that fresh supplies to galaxies 1 Mpc from the radio source will be cut off around  $3 \times 10^7$  years

after the jets trigger. Star formation and black hole activity throughout the protocluster is then shut down as the galaxies exhaust their internal reserves of gas. However, the time lag between the jet triggering and the exhaustion of fuel provides opportunity for many of the galaxies to shine as radio-quiet quasars—thereby explaining the excess of radio-quiet over radio-loud objects described in section 1.1.1.

Rawlings and Jarvis suggest that every protocluster would undergo such an episode: it is particularly interesting to compare this to the prediction of McLure and Dunlop (2001) that every cluster must contain a powerful AGN.

## **1.5 Probing the cluster environments of high- $z$ AGN**

Over the course of this chapter, we have briefly considered the cosmological significance of star formation and clusters of galaxies. Further, a short introduction was given to some of the major techniques used for probing both star forming galaxies and cluster environments out to high redshift.

In the last section, however, a link was drawn between cluster environments and star formation, by way of active galactic nuclei. Studying them in conjunction provides a method of enhancing our knowledge of both. The use of an AGN at a known high redshift provides a convenient method of ‘anchoring’ observations: a system that can be shown to be associated with the AGN is demonstrated to be at a given redshift, minimising the possibility of contamination from objects at other redshifts.

Most galaxy clusters detected around AGN (for example, those identified by Green and Yee, 1984, and collaborators) have been identified based on statistical overdensities of objects found close to it. However, a better strategy for overcoming foreground contamination of the sample is to identify individual star forming galaxies in the AGN field by their characteristic redshift-dependent features. Broadly speaking, many of the same techniques discussed in section 1.3.4 may be employed; for example, among the early work in this area was that of Lacy and Rawlings (1996), who used a Lyman-break technique to identify potential companion galaxies to the  $z = 3.8$  radio galaxy 4C 41.17.

### 1.5.1 Traditional Lyman $\alpha$ searches

Perhaps the most profitable way of identifying galaxies in the neighbourhood of AGN has been through their characteristic emission lines (section 1.3.3). Indeed, among the first high-redshift objects identified by emission lines were the  $z = 4.55$  Lyman  $\alpha$  emitters observed in the field of the quasar BR B2237-0607 by Hu and McMahon (1996).

Since then, many of the most important detections of clusters and AGN fields have been centred on work carried out at Leiden Observatory. Kurk et al. (2000) searched for Lyman  $\alpha$  emitters in the vicinity of the  $z = 2.156$  radio galaxy PKS B1138-262. They used the FORS1 spectrograph on the ESO VLT (Appenzeller et al., 1998) to carry out narrow- (FWHM 65 Å) and broad- (FWHM 880 Å) band imaging around the expected wavelength of Lyman  $\alpha$  emission from galaxies at the AGN redshift. They classified objects which have twice the flux density in the narrow-band images as in the broad-band as potential emission line galaxies (ELGs), identifying 60 sources in this way. Followup spectroscopy reported by Pentericci et al. (2000), also using FORS1, produced a clear confirmation of Lyman  $\alpha$  in 15 of these cases, which they classify as 14 star forming galaxies and one AGN. They conclude that there is a substantial overdensity of galaxies within 1.5 Mpc of the AGN.

Motivated by the success of that result, the Leiden group embarked on a campaign of similar observations to probe the fields of radio galaxies. The next target was TN J1338-1942 ( $z = 4.1$ ; Venemans et al., 2002): 28 potential ELGs were identified, of which 20 of the 23 spectroscopically followed-up were confirmed as Lyman  $\alpha$  emitters. The density of sources was estimated as an order of magnitude larger than might be expected from the blank field. Venemans et al. (2004) produced similar results for the  $z = 5.2$  radio galaxy TN J0924-2201, detecting fourteen candidates (of which six were spectroscopically confirmed) and estimating a density up to six times greater than the field. Most recently, the group has investigated the  $z = 3.13$  radio galaxy MRC B0316-257, identifying 31 Lyman  $\alpha$  emitters at a similar redshift. They reported an overdensity of Lyman  $\alpha$  emitters by a factor of 3.3 compared to the field, but were not able to constrain the size of the structure: it is larger than their  $3.3 \times 3.3$  Mpc field of view (Venemans et al., 2005).

Two of the above fields have been the subject of follow up observations used the Ad-

vanced Camera for Surveys (ACS) on the Hubble Space Telescope. Overzier et al. (2006a) examined the field of TN J0924-2201, verifying the earlier identification of Lyman  $\alpha$  emitters and using a Lyman-break technique to identify further galaxies, confirming the presence of a protocluster around the radio galaxy. A similar analysis of the TN J1338-1942 field (Overzier et al., 2006b) also confirmed the presence of clustering, identifying a pronounced filamentary structure. They also noted that the Lyman  $\alpha$  emitters tend to exist in regions which are lacking in Lyman-break galaxies.

### **1.5.2 Tunable filter imaging**

The mixed broad- and narrow-band technique described above has produced demonstrably successful results. However, the most direct antecedents of this thesis have adopted an alternative *tunable filter* approach to identifying star forming galaxies about AGN, making use of the Taurus-2 system instrument on the Anglo-Australian Telescope. In chapter 2 the design and implementation of the Taurus Tunable Filter (TTF) are discussed in some detail: for now, suffice it to say that it enables near-monochromatic imaging with a narrow (of order 10 Å) bandpass at effectively arbitrary wavelengths within the visible range.

Bremer and Baker (1999) introduced the strategy behind such a survey. The fundamental idea is to target [O II] 3727 Å emission from star forming galaxies; as discussed in section 1.3.3, this is a good indicator of star formation and can be calibrated to measure the star formation rate. Broadly, the strategy adopted is to step the tunable filter across a range of wavelengths spaced around the expected redshifted position of the [O II] emission. Emission line galaxies should then appear brighter in those frames centred on the spectral line, falling away to their continuum magnitudes at different wavelengths.

Considerable success has been achieved with this technique. Baker et al. (2001) reported the detection of a cluster around the  $z = 0.9$  radio-loud quasar MRC B0450-221 using a combination of this technique and broadband multi-colour imaging designed to identify the red population of the cluster. They identified nine candidate emission line galaxies, some of which were spectroscopically confirmed to lie in a group 200–700 kpc away from the quasar; the broadband imaging detected a significant overdensity of red galaxies more directly around the quasar itself.

This work was continued by Barr et al. (2004), who examined the [O II] in the fields of six radio-loud quasars at redshifts  $0.8 < z < 1.3$ . Forty-seven candidate emission line galaxies were identified, at an average space density 100 times that found locally. They also saw significant structure in the clustering of the ELGs around the quasars. There was a significant variation in the density of the fields, though: they ranged from similar to the field to very rich clusters.

Further work with TTF was performed by Francis and Bland-Hawthorn (2004). Rather than search for [O II], they used much the same technique in an attempt to detect Lyman  $\alpha$  emitters using much within 1 Mpc of the extremely luminous radio-loud  $z = 2.159$  quasar PKS B0424-131. However, the reported no detections, speculating that this was due to the effects of the enormous UV luminosity of the quasar clearing its neighbourhood of neutral hydrogen.

### **1.5.3    *The very highest redshifts***

At time of writing, clusters have been identified around some of the highest-redshift AGN known. Section 1.5.1 above recorded the study of a  $z = 5.2$  radio galaxy by Venemans et al. (2004); there are two further extremely high- $z$  studies that should be recorded.

Stiavelli et al. (2005) identified evidence of primordial clustering around the  $z = 6.28$  radio quiet quasar SDSS J1030+0524. Working with the Advanced Camera for Surveys on the Hubble Space Telescope, they used two filters—centred on 7750 Å and 8500 Å—to identify objects where appeared significantly brighter in the red due to Lyman absorption in neutral hydrogen. They identified a seven candidate objects in the field, estimating a greater than 99% chance that this constitutes a significant overdensity.

A similar study was carried out by Zheng et al. (2006), focusing on the region around SDSS J0836+0054, at  $z = 5.82$  the most distant radio-loud quasar identified to date. They used the same technique as Stiavelli et al., identifying objects by their red colour in images using the Hubble Space Telescope’s ACS. They observed a  $5 \times 5$  arcminute field, identifying five galaxies: a surface density of potential cluster members 6 times higher than the field.

## 1.6 Aims and outline of this thesis

Over the course of this chapter, we have emphasised the cosmological importance of, and the relationship between, active galactic nuclei, star formation and clusters of galaxies. We have discussed numerous techniques to identify clusters and the galaxies within them, and have seen that structures of luminous, star forming galaxies have been observed out to very high redshifts.

One of the most promising techniques for probing the cluster environments of AGN is that of tunable filter imaging. We have seen that considerable success has been achieved through this method at redshifts up to  $z \sim 1.3$ . The aim of this thesis is to apply the tunable filter techniques pioneered at lower redshifts to explore the environments of higher-redshift quasars. Our quasar sample is drawn from two redshift ranges— $z \sim 2.2$  and  $z \sim 4.5$ —and consists of both radio-loud and radio-quiet objects. We will attempt to identify clusters of star forming galaxies around the quasars and study their properties, looking for trends in their richness with redshift or with the radio power of the quasar.

We approach this investigation quasar environments by attempting to identify star forming galaxies within quasar fields. Broadly, our approach is similar to that taken by earlier tunable filter studies, as described in section 1.5.2. That is, we configure a tunable filter to take a series of (near-)monochromatic images at a range of wavelengths, closely spaced around those at which we might expect to identify emission lines characteristic of star forming galaxies at a given redshift. If and when our observations coincide with an object emitting the line, it appears brighter than in our other images at slightly divergent wavelengths. Most of the previous work in this vein has focused on observing [O II] emission, with a rest frame wavelength of 3727 Å. However, at the high redshifts we aim to investigate, this is shifted into the infra-red. Instead, we focus on Lyman  $\alpha$ —as discussed in section 1.3.3, we expect this to be emitted by star forming galaxies.

In chapter 2, we outline the design and implementation of the Taurus Tunable Filter, an instrument which is key to this work. We consider its capabilities and the issues that must be considered when using it to make observations. We go on to describe the observations we have made with it, and hence the data available for the rest of this study.

Chapter 3 describes in detail the complex data reduction techniques necessary for analysing tunable filter observations.

In order to reach a thorough understanding of the statistical properties of our observations, we have performed a thorough set of simulations of the results it is possible to obtain using the TTF. Chapter 4 discusses these simulations and demonstrates how we apply them to our data.

The work of actually identifying potential emission line galaxies is recorded in chapter 5. Full details of all the objects identified are presented, together with an analysis of any possible contamination of the sample from other sources.

The physical properties of the candidate ELGs are considered in chapter 6. We estimate their star formation rates and consider evidence for structure in the field.

The conclusion of the thesis is reached in chapter 7. We set our results in the context of the cluster environments of AGN at a range of redshifts, and consider what we have learnt from this study. We outline possibilities for future work which would build upon the basis set down here.

Throughout this thesis, we adopt a  $\Lambda$ CDM cosmology, with  $H_0 = 70 \text{ km s}^{-1} \text{ Mpc}^{-1}$ ,  $\Omega_\Lambda = 0.7$  and  $\Omega_M = 0.3$ .

# Chapter 2

## *Tunable filter imaging: theory and practice*

The key to this thesis is the ability to make near-monochromatic images of high-redshift fields. For this purpose, we use the Taurus Tunable Filter (TTF): at heart, a Fabry-Pérot interferometer. In this chapter, we discuss the design and implementation of the TTF, and, armed with this background, describe the observations we have made of high redshift quasar fields.

### **2.1** *The design and implementation of a tunable filter*

This section is devoted to a detailed description of the TTF, the instrument used for collecting all the data used in this thesis. Starting with the basic principles of tunable filter imaging, it goes on to describe the design of the TTF itself and the specific issues that must be taken into account when making observations with it.

Note that the design and construction of the TTF was not carried out as part of this thesis; it is, however, essential to the understanding of the material which follows. The properties of a general Fabry-Pérot interferometer are based on a standard textbook treatment, such as that found in Born and Wolf (1999); details specific to the Taurus-2 system including TTF are from Bland-Hawthorn and Jones (1998), Jones (1999), Jones et al. (2002), Hawthorn and Kedziora-Chudczer (2002) and other sources as referred to in the text.

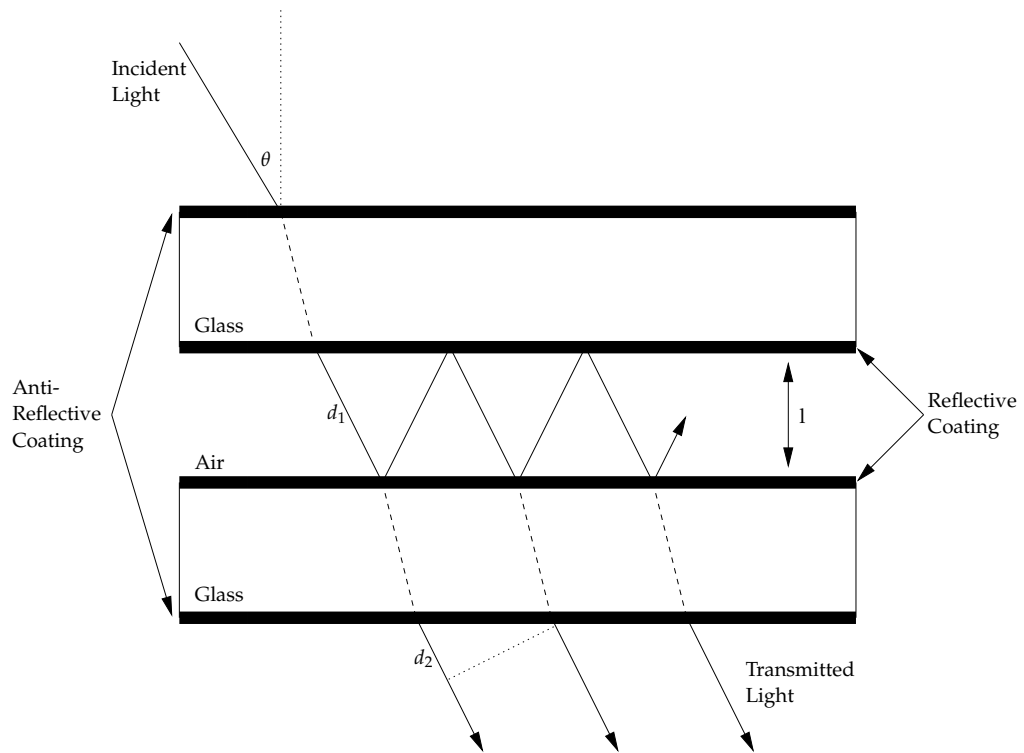


**Figure 2.1:** A diagrammatic representation of a Fabry-Pérot interferometer.

### 2.1.1 The Fabry-Pérot Interferometer

The Fabry-Pérot interferometer was first developed at the end of the nineteenth century (Pérot and Fabry, 1899; Fabry and Pérot, 1901). Its potential for astronomical observations was immediately obvious: it was used in conjunction with the 0.8 metre telescope of the Observatory of Marseilles to observe emission lines in the Orion Nebula (Fabry and Buisson, 1911). Since then, Fabry-Pérot interferometers have been in widespread use for a variety of astronomical observations (see, for example Bland-Hawthorn, 1995). We first outline the basics of operation of a Fabry-Pérot interferometer, then develop this to demonstrate how the TTF advances the state-of-the-art.

#### 2.1.1.1 Theoretical background

The key to the Taurus Tunable Filter's near-monochromatic imaging capability is the Fabry-Pérot interferometer. A clear understanding of the characteristics of this device are essen-

tial to the successful analysis of observations made with TTF.

Interferometry relies on the principle that waves which coincide with the same phase will interfere constructively, while those with opposite phases will cancel each other out. By splitting a wave and sending each component over an optical path of different length, it is possible to introduce a phase difference between the components; they can then be recombined and the relative phases determined by the form of interference. The simplest example of this is the famous Young's double slit experiment: here, the wavefront is divided by the slits, and interference is visible at recombination.

The Fabry-Pérot interferometer operates by division of amplitude, rather than wavefront. Consider the diagrammatic representation in figure 2.1. The interferometer consists of two plane parallel mirrors, illuminated at a small angle— $\theta$ —to the normal. The inner surfaces have coatings of high reflectivity, which we label  $\sqrt{\mathcal{R}}$ . Some of the light which enters the interferometer passes straight through. Most, however, is reflected. After two internal reflections, a little more is transmitted, and so on. Each set of reflections within the interferometer adds an optical path length of

$$2d_1 = 2\mu l / \cos \theta, \quad (2.1)$$

where  $l$  is the plate separation,  $\mu$  the refractive index of the medium in which the interferometer is located and  $\theta$  the angle of incidence of the light. Meanwhile the light which has left the interferometer experiences an optical path of

$$d_2 = 2\mu l \sin^2 \theta / \cos \theta \quad (2.2)$$

relative to the adjacent transmitted ray. The phase difference between light moving along these paths is then

$$\delta = \frac{2\pi(2d_1 - d_2)}{\lambda} = \frac{4\pi\mu l \cos \theta}{\lambda}, \quad (2.3)$$

where  $\lambda$  is the wavelength of the light.

The amplitude of the output wave from the interferometer is the sum of each com-

ponent of the transmitted light, thus:

$$A = 1 + \mathcal{R}e^{i\delta} + \mathcal{R}^2e^{2i\delta} + \dots \quad (2.4)$$

$$= \frac{1}{1 - \mathcal{R}e^{i\delta}}, \quad (2.5)$$

where we have normalised the amplitude of the first component output to 1. The corresponding intensity of the transmitted light is then given by

$$\mathcal{T} = A^*A = \frac{1}{1 + \mathcal{R}^2 - 2\mathcal{R} \cos \delta} \quad (2.6)$$

$$= \frac{1}{(1 - \mathcal{R}^2) + 4\mathcal{R} \sin^2(\delta/2)}. \quad (2.7)$$

We are concerned primarily with the shape, rather than the amplitude, of the output. Re-arranging equation 2.7 and discarding constants, we are left with the Airy function (Bland-Hawthorn and Cecil, 1997)

$$\mathcal{A} = \left(1 + \frac{4\mathcal{R}}{(1 - \mathcal{R})^2} \sin^2(2\pi\mu l \cos \theta / \lambda)\right)^{-1} \quad (2.8)$$

which describes the transmission profile of the interferometer. Equation 2.8 has a series of periodic maxima given by

$$m\lambda = 2\mu l \cos \theta \quad (2.9)$$

where  $m$  is the order of interference. There are, therefore, three different ways to scan the wavelength of peak transmission: by altering  $\theta$  (tilt scanning),  $\mu$  (in air this might be achieved by changing the pressure) or  $l$  (gap scanning). Recent developments—as discussed in section 2.1.3.1—have led to the performance of gap scanning surpassing the other techniques, and it is this that we use with TTF.

It is straightforward to calculate the wavelength separation of light seen at adjacent orders of interference:

$$\lambda_m - \lambda_{m+1} = 2\mu l \cos \theta (1/m - 1/(m+1)) \quad (2.10)$$

$$= (m+1)\lambda_{m+1} \left( \frac{m+1-m}{m^2+m} \right) \quad (2.11)$$

$$= \frac{\lambda_{m+1}}{m} \quad (2.12)$$

where  $\lambda_m - \lambda_{m+1}$  is the *free spectral range*. We can also consider the free spectral range in terms of the plate spacing  $l$ . On or close to the axis (that is, when  $\cos \theta \simeq 1$ ) and in air ( $\mu \simeq 1$ ), equation 2.8 reaches a maximum whenever  $\sin(2\pi l/\lambda) = 0$ —that is, when  $l = n\lambda/2$ . Hence, the free spectral range in terms of the plate separation may be written as

$$\Delta l = \frac{\lambda}{2}. \quad (2.13)$$

We demonstrate the measurement of the free spectral range in section 3.1.5.

The relative sharpness of the response function is defined by the *reflective finesse* of the interferometer; we label this  $\mathcal{F}$ . It is equivalent to the ratio of the free spectral range to the full width at half maximum of the peak transmission, which we label  $\lambda_{1/2}$ . Thus

$$\mathcal{F} = \frac{\lambda_m - \lambda_{m+1}}{\lambda_{1/2}}. \quad (2.14)$$

This, in turn, is determined by the coating reflectivities of the interferometer plates. The phase difference across the free spectral range is  $2\pi$ , while, from equation 2.7, the half maximum in terms of the phase difference occurs when

$$\frac{4\mathcal{R}}{(1-\mathcal{R})^2} \sin^2(\delta/2) = 1. \quad (2.15)$$

In the approximation of small  $\delta$ , we have

$$\delta = \frac{1-\mathcal{R}}{\sqrt{\mathcal{R}}} = \lambda_{1/2}/2 \quad (2.16)$$

and, substituting into equation 2.14, we are left with

$$\mathcal{F} = \frac{\pi\sqrt{\mathcal{R}}}{(1-\mathcal{R})}. \quad (2.17)$$

Note, however, that  $\mathcal{F}$  is susceptible to plate defects, as discussed by Atherton et al. (1981). For the TTF,  $\mathcal{F}$  is approximately 30. It is possible to combine equations 2.12 and 2.14,

producing

$$\frac{\lambda_{m+1}}{\lambda_{1/2}} = \mathcal{F}m = R, \quad (2.18)$$

where  $R$  is term the ‘spectral resolving power’ of the instrument.

### 2.1.2 Simplifying the Airy Function

For many analyses of the tunable filter transmission, the Airy function is not particularly convenient to work with. Notably, its periodic nature complicates matters. In the TTF, this is eliminated by using an order-blocking filter to select only the transmission peaks which are required: this process is discussed in section 2.1.3.3. It is, therefore, convenient to arrive at a mathematical formalism which achieves the same effect.

An examination of the Airy function (as, for example, in figure 2.2) makes it immediately clear that the profile is at least somewhat similar to the commonly-encountered (and non-periodic!) Gaussian and Lorentzian functions. We proceed, therefore, to investigate how close a correlation there is between them.

We saw in section 2.1.1.1 that the transmission of the Fabry-Pérot interferometer is given by the Airy function, equation 2.8. This, in turn, depends on the finesse  $\mathcal{F}$  (equation 2.14). We can write

$$\mathcal{A} = \left( 1 + \frac{4\mathcal{F}^2}{\pi} \sin^2(2\pi\mu l \cos \theta / \lambda) \right)^{-1}. \quad (2.19)$$

We are normally concerned with light incident on the interferometer at a small angle  $\theta$ . We therefore make the approximation  $\cos(\theta) = 1$ . For most interferometers—and certainly for TTF—the medium between the plates is air (in fact, dry nitrogen in the TTF case). Therefore, it is appropriate to also take  $\mu$ , the refractive index of the medium, to be 1. Referring to the definition of the free spectral range in equation 2.13, we have:

$$\mathcal{A} = (1 + \alpha \sin^2(\pi l / \Delta l))^{-1} \quad (2.20)$$

where  $\alpha$  is a constant.

We compare the Airy function to Gaussian and Lorentzian functions of the same full width half maximum. Because Lorentzian and Gaussian functions are not naturally periodic, we modify them just that they are cyclical over one free spectral range, as in figure 2.2. At low values of the finesse (the ratio of the full width half maximum of the transmission peaks to the interval between them) the functions are clearly quite different, as shown in figure 2.2(a). However, moving to a higher finesse as in figure 2.2(b), the Lorentzian and Airy functions become almost coincident, while the Gaussian is still quite separate.

The convergence of these three functions was investigated in detail by Jones et al. (2002). They demonstrated that, above a finesse of around 40, the Lorentzian is a near perfect match to the Airy transmission profile; it is an excellent match even at lower values of the finesse. The Gaussian, meanwhile, is an over-estimate: the normalised integral of the Gaussian is around twice as large as that of the Airy and Lorentzian functions at high finesse.

It is clear, therefore, that a Lorentzian function is a usable approximation to the Airy function at high finesse. Why is this the case? Consider equation 2.20. High finesse for a given free spectral range is equivalent to a large  $\Delta l$ . If it is sufficiently large, we may make use of the small angle approximation to re-write equation 2.20 as

$$\mathcal{A} = \left(1 + \frac{\alpha\pi^2l^2}{\Delta l}\right)^{-1}, \quad (2.21)$$

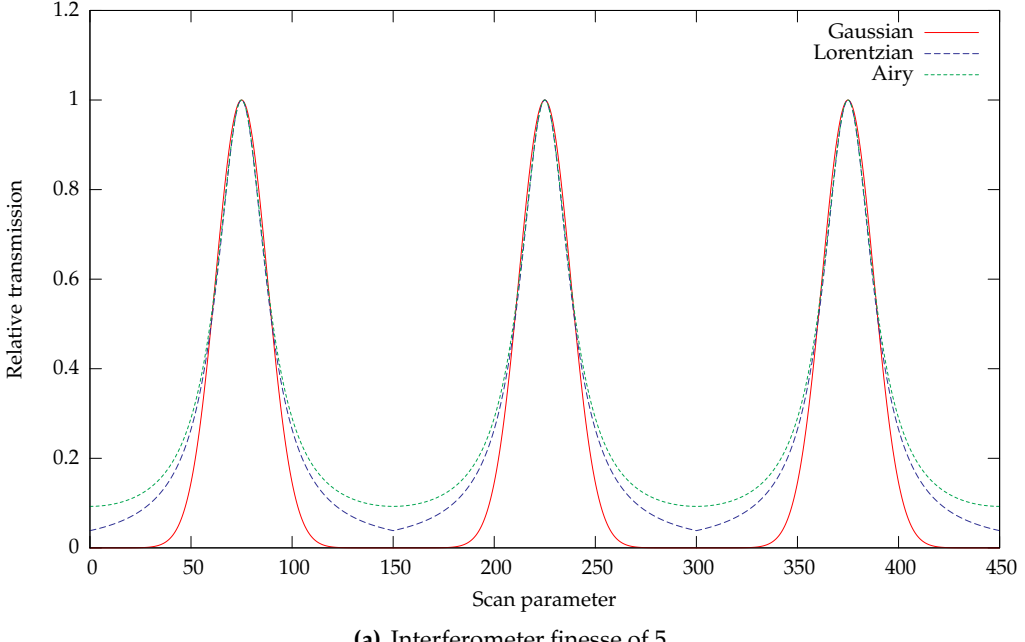
which, in turn, becomes

$$\mathcal{A} = \frac{\Delta l/\alpha\pi^2}{l^2 + \Delta l/\alpha\pi^2}, \quad (2.22)$$

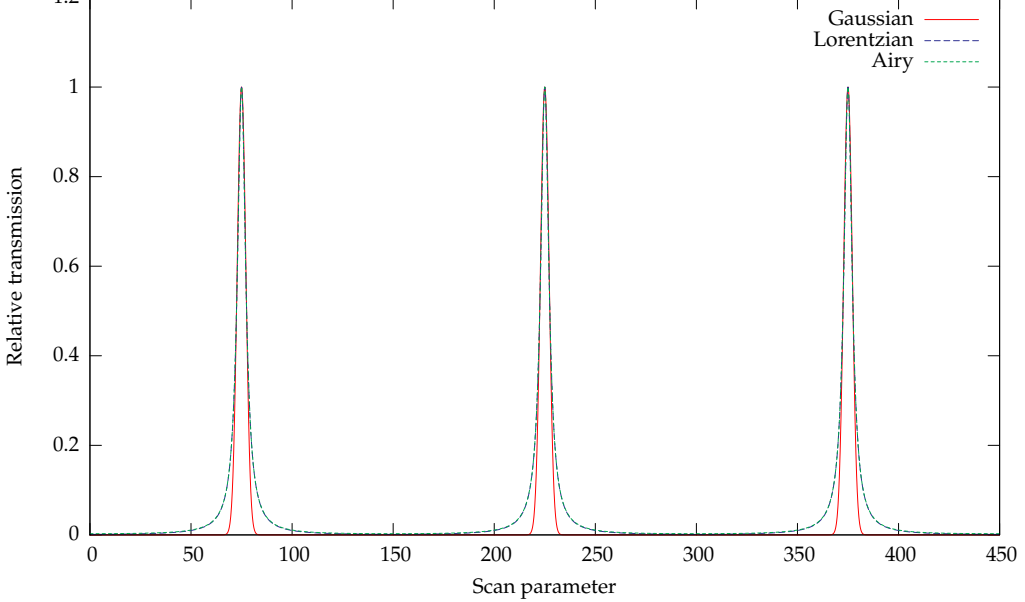
which is a Lorentzian with a full width at half maximum of  $\sqrt{\Delta l/\alpha\pi^2}$ .

### 2.1.3 Design and implementation of the Taurus Tunable Filter

The Taurus Tunable Filter is a pair of tunable Fabry-Pérot interferometers, covering 3700–6500 Å (“Blue-TTF”) and 6500–9600 Å (“Red-TTF”). Either interferometer can be used in the collimated beam of the Taurus-2 focal reducer (section 2.1.3.2), which may be placed



(a) Interferometer finesse of 5.



(b) Interferometer finesse of 30.

**Figure 2.2:** Comparison of Gaussian, Lorentzian and Airy functions. In both plots, the free spectral range has been fixed at 150 scan units; while the Airy function is naturally periodic, we wrap the other functions at the same periodicity. In 2.2(a), each curve has a full width at half maximum of 30 units, whereas in 2.2(b) the full width at half maximum is 5 units, producing the fineses stated. In the latter case, the Lorentzian and Airy functions coincide almost exactly over the majority of the curves.

at the Cassegrain foci of either the 3.9 metre Anglo-Australian Telescope (AAT) or the 4.2 metre William Herschel Telescope. All the observations recorded in this thesis were taken at the AAT. The system may be used at either  $f/8$  or  $f/15$ : this affects the coverage of the field (section 2.1.3.4).

TTF has several advantages over the traditional narrowband imaging with standard interference filters. The obvious benefit is cost: it is much cheaper to produce a tunable filter than a large number of interference filters with high performance at narrow passbands. Furthermore, the Fabry-Pérot transmission function is the same at different wavelengths and band-passes; it is straightforward to compare observations in discrete bands. Finally, the optical path through the instrument is independent of the wavelength being observed.

### 2.1.3.1 *Capabilities of the TTF*

First, we consider what attributes of the TTF differentiate it from the general class of astronomical Fabry-Pérot interferometers.

Equation 2.9 shows us that the plate spacing— $l$ —is directly proportional to  $m$ , the order of interference. At larger plate spacings, it is only possible to observe at high orders of interference—and that, in turn by equation 2.18, corresponds to a relatively high resolving power. However, Jacquinot (1954) demonstrated that a high resolving power means that only a small (near-)monochromatic region can be imaged by the interferometer: the so-called ‘Jacquinot Spot’ (Jones et al., 2002). This in turn corresponds to a small solid angle on the sky. While this is useful for imaging individual sources, it renders the instrument impractical for use as a survey tool.

Most modern Fabry-Pérot interferometers have plate spacings on the order of hundreds of microns. However, the work of Jones and Bland-Hawthorn (1998) in pioneering the design of interferometer cavities at micron spacings means that the TTF can operate in the range of  $2 \leq l \leq 13 \mu\text{m}$ . This means that, not only must the cavity be kept clear of even a single grain of dust, but great care must be taken to ensure that the interferometer plates remain parallel. Parallelism is achieved by the use of a capacitance bridge (Jones and Richards, 1973; Hicks et al., 1974, 1984); Jones (1999) documents in detail the steps that must be taken to ensure adequate parallelism at very narrow plate spacings.

This extremely narrow plate spacing makes the TTF suitable for imaging substantial solid angle, and, therefore, makes the survey of quasar environments documented here possible. Furthermore, the large dynamic range—an order of magnitude—of the TTF plate spacings is much greater than that offered by previous generations of instruments.

It is also worth noting that the TTF has the ability to switch plate spacings very rapidly: anywhere over the accessible range, at frequencies of up to 100 Hz. Furthermore, this can be synchronized with the movement of charge on the detector CCD. In section 2.1.3.5 we describe this process in more detail and give examples of its usefulness.

Finally, new developments in multilayer dielectric coatings, as documented by Jones (1999), mean that transmissions of 99% or better are achievable on interferometer plates over a range of thousands of angstroms—it would previously have been impossible to cover the wide range of wavelengths addressed by the TTF using only two interferometers. Furthermore, the coated plates can be polished to a flatness of better than  $\lambda/140$ , minimising the possible effect of defects on equation 2.17.

### 2.1.3.2 *Optical layout: Taurus-2*

As mentioned above, TTF is used in the collimated beam of the Taurus-2 focal reducer. Now decommissioned, Taurus-2 supported a variety of instrumental configurations: in addition to TTF, it was notably used to perform long- or multi-slit spectroscopy (Taurus++) or as an imaging polarimeter.

The general optical layout of the Taurus-2 system is shown in figure 2.3. It is mounted at the Cassegrain focus of the telescope; light enters from the left of the figure, is collimated and passes through the Fabry-Pérot interferometer. The field thus modulated is then reimaged by a camera, and recorded on a CCD detector. The system consists of the following optical components. Note that several of them are placed on rotating wheels: This allows us to easily choose between several different components.

The **focal plane filter wheel**, **aperture wheel** and **iris** are all placed close to the Cassegrain focus. Each of the wheels consists of eight positions into which components may be placed. The filter wheel holds 125 mm diameter filters; it is typically used to con-

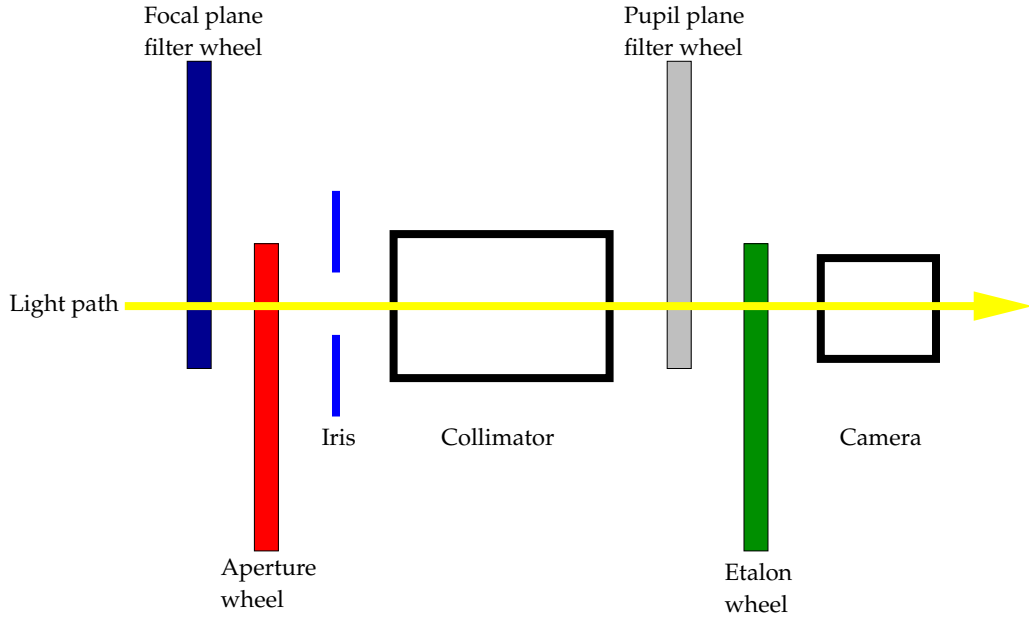


**Figure 2.3:** Optical layout of the Taurus-2 system, after Hawthorn and Kedziora-Chudczer (2002).

tain the order blocking filter, described in section 2.1.3.3. The aperture wheel, meanwhile, holds a selection of differently shaped masks. They may be used to selectively only expose portions of the field of view. One mask consists of a grid of small holes, and is used to focus the instrument; other masks are used when shuffling charge on the CCD (section 2.1.3.5). The iris determines the size of the field of view. It has a diameter of 150 mm, but note that the collimator only allows 80 mm at  $f/8$ .

The **collimator** has a focal length of 473.9 mm, and returns the beam with a diameter of 60.3 mm. It is immediately followed by the **pupil plane filter wheel**. Once again, this contains eight possible filters—this time, with a smaller diameter of 75 mm. Four of the positions are occupied by quadrant masks, which may be used to test the plate parallelism of the interferometer (an analysis which we do not perform in this work).

Perhaps the most crucial stage is the **etalon wheel**. Six slots are available here: two are occupied by Blue- and Red-TTF, and two are left clear for direct imaging. The remaining two slots may be used for gratings or prisms as required. The etalon wheel is kept within a sealed cavity, and, during use, is flushed with dry nitrogen to ensure a low humidity.

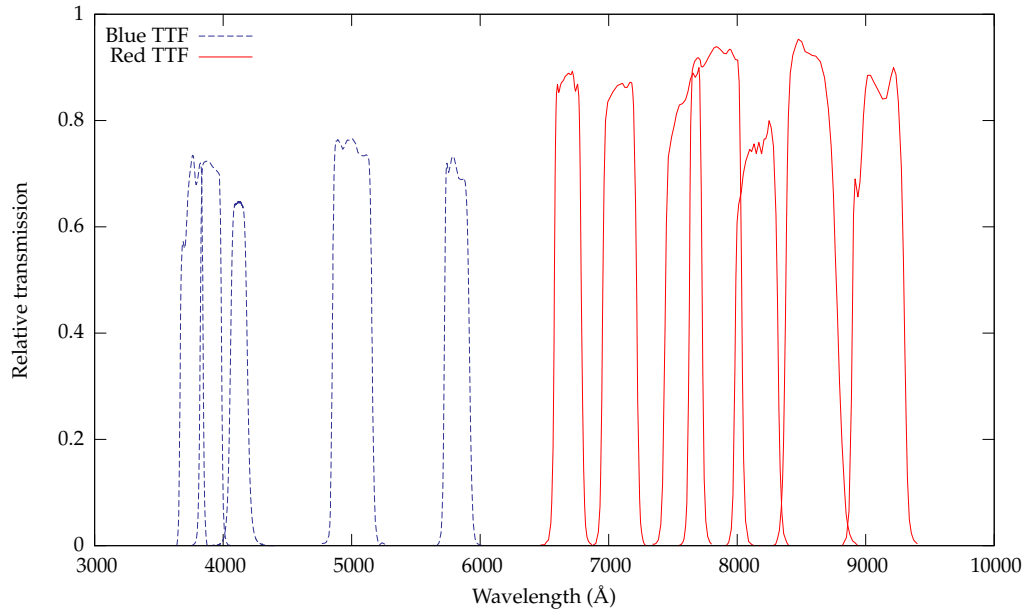


**Figure 2.4:** Intermediate-band blocking filters used with the TTF at the AAT. The profiles shown in blue are designed for use with Blue-TTF; in red, with Red-TTF. Conventionally, the filters are numbered from low to high wavelength B0–B6 (B3 and B5 are not used) and R0–R8 (R2 and R7 are not used).

Finally, the **camera** provides an image at the detector. It has a focal length of 127.8 mm and an output *f*-ratio of *f*/2.13; the scale at the detector is then 24.8''/mm and 13.1''/mm at the *f*/8 and *f*/15 Cassegrain foci respectively.

#### 2.1.3.3 Order blocking filters

The great advantage of the tunable filter is that it renders the traditional narrowband interference filter redundant: we are able to select an arbitrary wavelength to observe by setting the plate spacing. However, it is not possible to dispense with filters entirely. We have seen that the transmission of the interferometer is described by the Airy function (equation 2.8), which produces a series of *periodic* maxima. Therefore, if we observe at given interferometer settings, we run the risk of confusing light at our desired wavelength at one order of interference with another wavelength at a different order! Therefore, we introduce a ‘blocking filter’: a broad- or intermediate-band filter, which stops light of un-

**Table 2.1:** Properties of the CCD detectors used in this work.

Name	Size (pixels)	Pixel scale (''/pixel) $f/8$	Pixel scale (''/pixel) $f/15$	Readout time (seconds)	Pixel size (microns)	Sensitivity
MITLL2	$2048 \times 4096$	0.37	0.20	160	15	Red
EEV2	$2048 \times 4096$	0.33	0.18	150	13.5	Blue

wanted wavelengths entering the system.

If the interferometer is run at a sufficiently low resolution, it is possible to use the standard broad-band 'UBVRI' filters. In the case of our observations, these are not adequate: instead, we make use of a series of intermediate-band blocking filters developed for use with TTF. The profiles of these filters are shown in figure 2.4: there are five designed for use with Blue-TTF, and 7 for use with Red-TTF. They are designed to provide access to areas of the night sky free from OH night-sky emission. The filters are large enough to be mounted on the focal plane filter wheel of the Taurus-2 system without restricting the beam width.

Note that these filters do not completely cover the range of wavelengths accessible to the TTF, particularly in the blue: as we will see (section 2.2.1.2), they therefore restrict the targets available to us.

#### 2.1.3.4 Detectors

It is possible to use the TTF with any of the CCD detectors available at the AAT. In this work, we use the MITLL2 detector in the red part of the spectrum, and the EEV2 in the blue—these ranges corresponding to where the detectors display the optimal quantum efficiency, as shown in figure 2.5. The properties of the CCDs are summarised in table 2.1.

#### 2.1.3.5 Charge shuffling

Reading data from a CCD is a relatively slow process: see, for example, the read-out times in table 2.1. The delay occurs at the amplifiers as the charge in each pixel is measured; the shifting of charge over the CCD to the readout site can happen much faster: for the MITLL2 CCD in use with the TTF, each 2048-pixel column takes  $160/4096 = 40$  milliseconds to

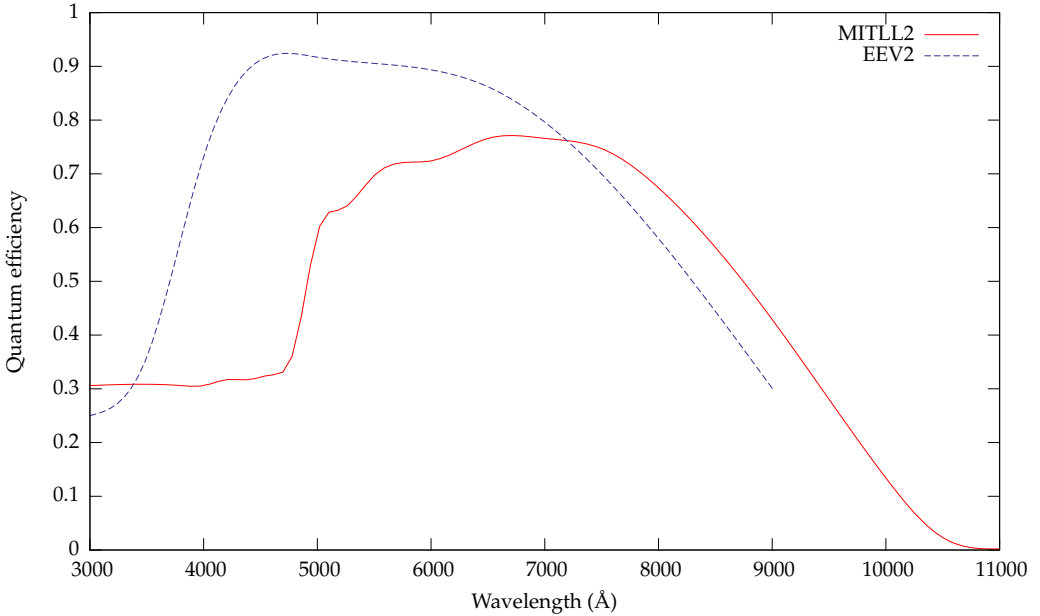


**Figure 2.5:** Quantum efficiency of the two CCDs used in our observations. Data provided by the Anglo-Australian Observatory.

amplify and read-out, but the charge takes only tens of microseconds to move between adjacent columns (based on the figure that charge can be switched over the whole CCD at rates of up to 10 Hz, provided by Hawthorn and Kedziora-Chudczer (2002)).

Charge-shuffling is the movement of charge on the surface of the CCD *without* it being read-out. This process may be synchronized both with multiple exposures of the CCD and with switching of the interferometer plate spacing. An aperture mask is held in the aperture wheel described in section 2.1.3.2 and may be used to expose only sections of the CCD at any given time.

There are several possible applications of these techniques. In this work, we use a technique referred to as ‘frequency-switching’, proceeding as follows. We configure the interferometer to transmit at some desired ‘on-band’ wavelength, and mask off a section of the CCD. The remaining part of the CCD is exposed for the required time; at the end of the exposure, the interferometer is switched to a new ‘off-band’ wavelength and charge shuffled such that our previous observation is now held in the masked section. A new exposure may now be taken. This process may be repeated, switching repeatedly between the on-

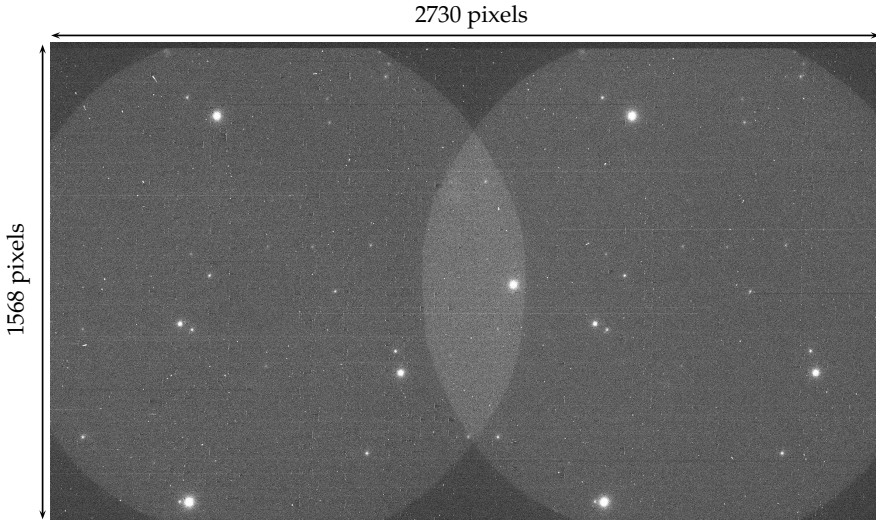


**Figure 2.6:** An example of a charge-shuffled image, this shows unreduced observations of MRC B2158-206 at two different interferometer settings, corresponding to on-axis wavelengths of 3969 Å (left) and 3959 Å (right). Each image is composed of 15 sixty-second exposures.

and off-band wavelengths, building up images of the same part of the sky at different wavelengths at (effectively) the same time—ensuring the images are easily comparable.

An example of an image taken in this way is shown in figure 2.6; charge shuffling has been used to build up simultaneous images of the field of the radio-loud quasar MRC B2158-206 at two different wavelengths.

An alternative application of charge shuffling would be to perform time-series imaging: in this case, the shuffling proceeds in one direction only and the interferometer plate spacing is not changed. Avoiding the read-out delay means that images can be very closely spaced in time.

It is worth noting that this charge shuffling technique reduces the total area of the CCD available for useful data: some must be reserved for the data shuffled off-band. The total space lost is equal to  $1/N$  of the CCD's area, where  $N$  is the number of shuffle positions.

### 2.1.4 Characteristics of tunable filter observations

The tunable filter system introduces a number of systematic effects into our observations: we must take account of these in any analysis we perform. In this section, we consider how they come about; our strategies for compensating are described in the next chapter.

#### 2.1.4.1 Variation of peak wavelength across an image

The aim of the tunable filter is to provide a monochromatic image over a large field of view. However, we have seen (equation 2.1) that the path difference between rays depends not only on the interferometer plate spacing, but also on the angle of incidence of the ray on the interferometer. This results in a position-dependent phase shift across the field of view: as  $\theta$  varies, the wavelength of peak transmission also changes.

Equation 2.9 tells us that the wavelength of maximum transmission is given by

$$\lambda = \frac{2l \cos \theta}{m}, \quad (2.23)$$

assuming the interferometer is operating in air (i.e.  $\mu = 1$ ). We make use of the small angle approximation for  $\cos \theta^*$  to write

$$\lambda(\theta) = \lambda_{\text{centre}} \times \left(1 - \frac{\theta^2}{2}\right), \quad (2.24)$$

where  $\lambda_{\text{centre}} = 2L/m$  is the wavelength on the optical axis. Therefore, as we move across the image, there is a quadratic dependence of the transmitted wavelength on position. The wavelength is longest on-axis, becoming more blue as  $\theta$  increases.

$\theta$  is the off-axis angle at the interferometer. This is not the same as the off-axis angle on the sky, which we label  $\phi$ , and this is what we actually measure on our images. The two angles are related by

$$\phi = \theta \times \frac{f_{\text{col}}}{f_{\text{tel}}}, \quad (2.25)$$

where  $f_{\text{col}}$  and  $f_{\text{tel}}$  are the focal lengths of the collimator and telescope respectively. For

---

\*That is a Taylor expansion:  $\cos \theta = \sum_{n=0}^{\infty} (-1)^n x^{2n} / (2n!)$ .

observations using TTF at  $f/8$  on the AAT, we have  $f_{\text{col}} = 473.9$  mm and  $f_{\text{tel}} = 30780$  mm; at  $f/15$  they are 473.9 mm and 57880 mm respectively. Hence

$$\lambda(\phi) = \lambda_{\text{centre}} \times \begin{cases} (1 - 2.1 \times 10^3 \phi^2) & \text{at } f/8 \\ (1 - 7.5 \times 10^3 \phi^2) & \text{at } f/15, \end{cases} \quad (2.26)$$

where  $\lambda_{\text{centre}}$  is the wavelength observed on the optical axis. The optical system of TTF allows a maximum off-axis angle at the interferometer of 0.19 radians. Therefore, the maximum possible variation of  $\lambda$  across the field is 1.8% of  $\lambda_{\text{centre}}$ . This will only be achieved if the axis lies at one edge of the field: more typically, it lies towards the centre, leading to a variation of approximately half this.

In short, then, the image provided by the TTF is not truly monochromatic: there is a systematic variation of the wavelength transmitted depending on the position in the image. When we come to analyse observations made with the TTF, it is crucial to take this into account.

#### 2.1.4.2 Night sky rings

Any spectral lines originating in the atmosphere ('night-sky lines') are detected by the TTF just as any other spectral feature. However, unlike the other features seen by the instrument, they are not localised in space: we see them wherever the interferometer transmits the appropriate wavelength.

In the last section, it was established that the interferometer transmission varies across the image about the optical axis. As we move away from the axis, the transmission peak moves to the blue. When it coincides with a night-sky line, that line appears on our image. This leads to a pattern of rings centred on the axis; an example can be seen in figure 3.14 (page 94). To a very close approximation, these rings are circular, as expected from equation 2.24: a slight (0.5%) ellipticity is due to optical imperfections within the focal reducer (Jones et al., 2002).

If our image contains these night-sky rings, it is important to fit and remove them before analysis proceeds. However, they also serve a useful function: as we demonstrate in section 3.2.3.5, they can be helpful in locating the optical axis of an observation.

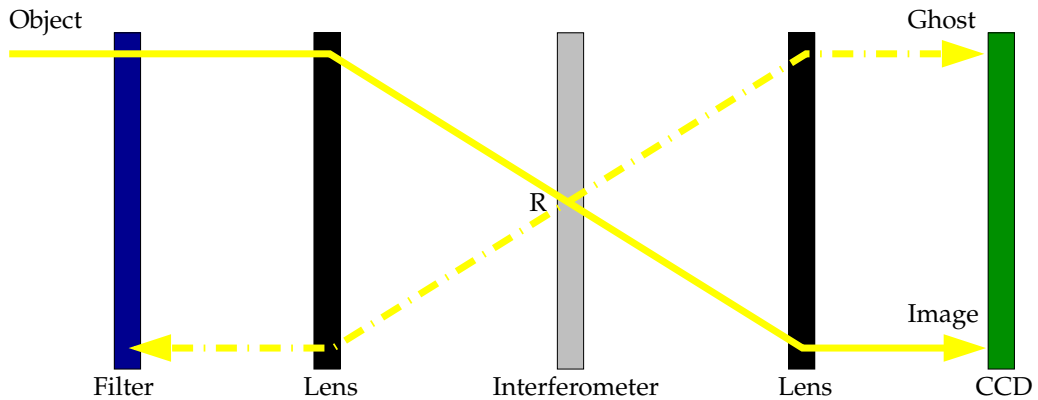


**Figure 2.7:** Formation of a diametric ghost within the optical system of a Fabry-Pérot interferometer. Light originating at the object in top left in the hope of forming an image on the CCD; however, some is reflected at R, at the filter and/or at the CCD window itself, and goes on to form a ‘ghost’ image.

#### 2.1.4.3 Ghosts

A ghost is point on the image which looks like a real object but is, in fact, due to internal reflections within the optical system of the interferometer rather than due to light arriving at the system from an external source. Such a process is illustrated in figure 2.7. An incoming ray from a real object passes through the interferometer and forms an inverted image at the CCD detector. However, some of the light reflects off the leading surface of the interferometer at the point labelled R, and passes back towards the outside of the system. However, it reflects again off the order blocking filter: the light re-enters the system, forming a secondary out-of-focus image. This secondary image passes back through the interferometer, and the object is effectively re-imaged diametrically with respect to the optical axis: a ‘diametric ghost’ has appeared.

A similar effect can be caused by light reflecting from the window of the CCD itself at the imaging point. In order to minimise this effect, modern detector windows are made of materials with low refractive indices, such as quartz (Bland and Tully, 1989). Indeed, all optically flat surfaces within the system are potential sources of reflection and hence of

spurious detections. The reflectivity  $r$  of an air-glass interface is

$$r = \left( \frac{\mu_{\text{glass}} - \mu_{\text{air}}}{\mu_{\text{glass}} + \mu_{\text{air}}} \right)^2 \simeq \left( \frac{1.5 - 1.0}{1.5 + 1.0} \right)^2 = 4\%, \quad (2.27)$$

however, this can be reduced to just a fraction of a percent by using suitable anti-reflective coatings (Jones et al., 2002).

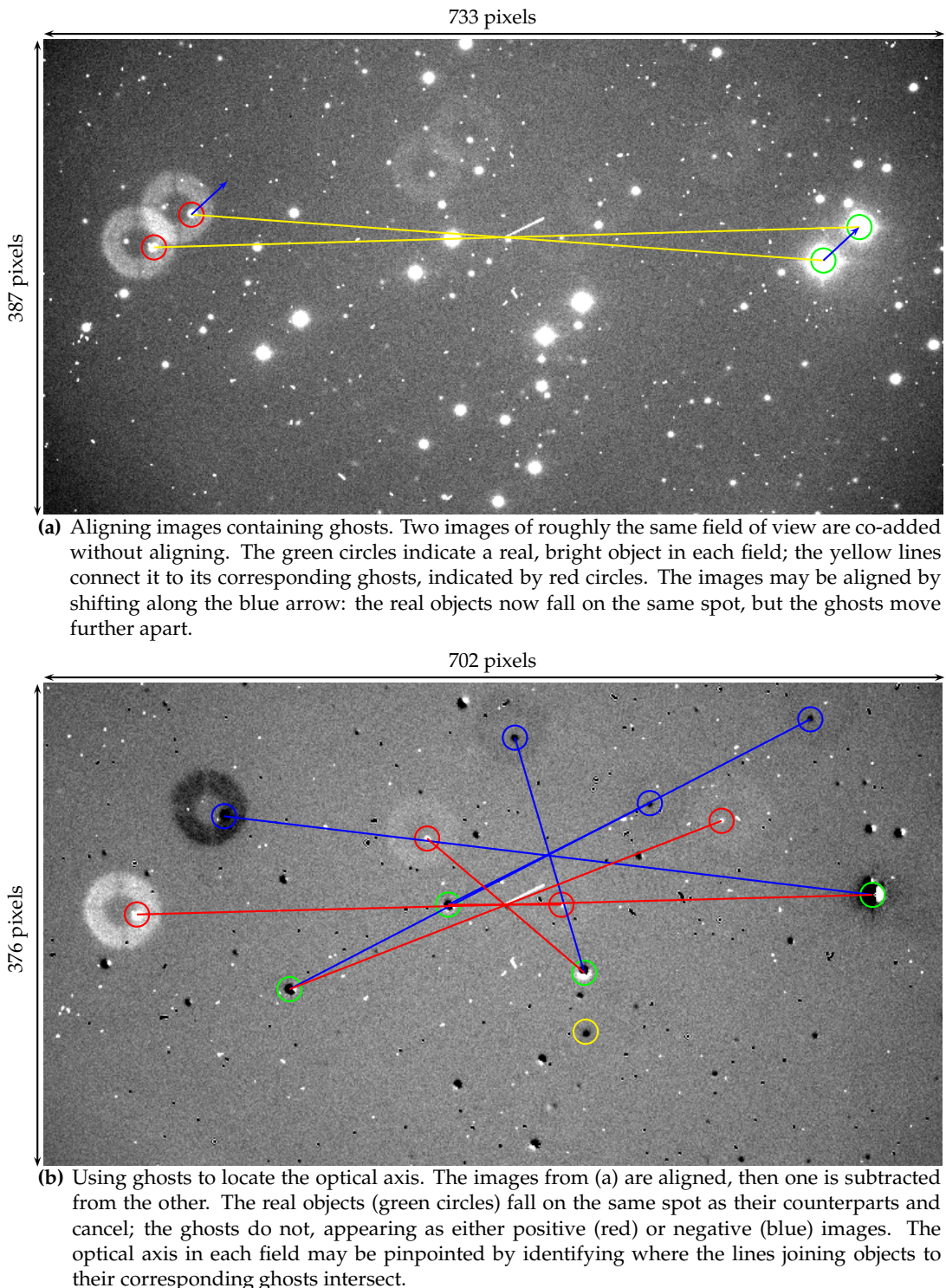
Despite these efforts, though, some ghosts are still observed: since they look very much like real objects in our images, it is important to locate them and eliminate them from our analysis. This is most conveniently achieved as follows.

When observing a given field, two images are taken at the same interferometer settings, but the pointing is shifted slightly between exposures. By considering the positions of some of the objects that appear in both images, it is possible to align the images—a procedure we consider in detail in section 3.1.4—and subtract one from the other.

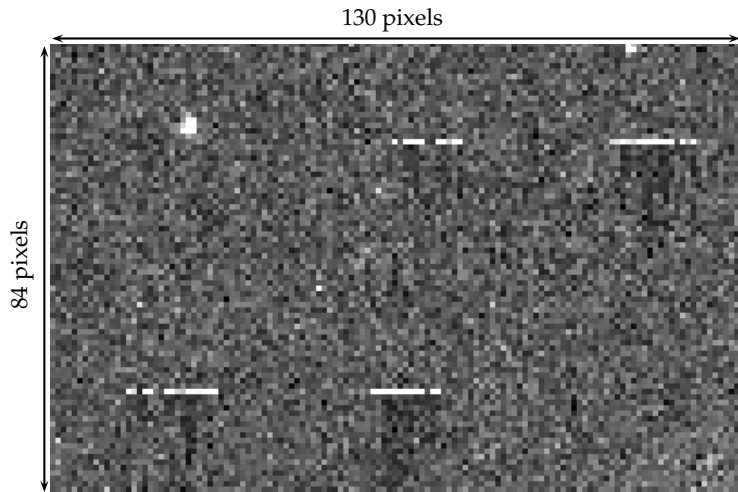
Since the images are aligned, the real objects in the field appear in the same place in the images: when we subtract one from the other, they cancel out and disappear. However, the same is not true of the ghosts: since they are diametric reflections about the optical axis, they are pulled further *out* of alignment when the images are aligned. This is demonstrated in figure 2.8(a), which shows two images of the same field at slightly different pointings after co-adding without prior aligning. All the objects within the field are duplicated, including the ghosts—but the figure shows the ghosts moving further apart as the images are aligned.

Figure 2.8 demonstrates what happens if we align the images and then subtract one from the other. The real objects cancel out: the ghosts do not. Since the ghosts are diametric about the optical axis, the position of the axis in each image may be identified by connecting the objects to their corresponding ghosts: it falls where the lines connecting each object to each corresponding ghost intersect.

We have seen that, as with night-sky rings, ghosts can prove useful in finding the optical axis. However, we must be certain that analysis of our observations is not contaminated by mis-identifying ghosts as real objects. Shifting the pointing of the telescope slightly between exposures of the same field makes it straightforward to pinpoint ghosts—and it is this technique that we will use when considering our observations in the next



**Figure 2.8:** Ghosts in a quasar field. These images of the field of PKS B1251-407—indicated by the yellow circle in (b)—demonstrate the motions of ghosts about the optical axis, and how this motion may be used to both identify the axis and the ghosts themselves.



**Figure 2.9:** Artifacts caused by charge trapping, built up over multiple shuffles on the CCD: a close-up on part of the image shown in figure 2.6.

chapter.

#### 2.1.4.4 Charge trapping

In section 2.1.3.5 we described the charge shuffling technique and outlined its usefulness. However, we must also consider its effect upon the quality of our images.

When charge is moved on the surface of the CCD, it can become ‘trapped’—electrons are not properly transferred from one pixel to the next. There are a number of possible reasons for this; for our CCDs, the most important is ‘bulk trapping’ (Janesick and Elliott, 1992). Bulk traps are due to metallic impurities or lattice defects in the silicon CCD substrate; if they lie within the charge transfer channel, they can block the transfer of charge. Janesick and Elliott quote the charge transfer efficiency of modern CCDs at upwards of 99.999%, so that charge trapping is not, in general, a significant issue if the charge is merely moved across the CCD once before read-out. However, repeated movement of charge causes the effect to build up, leading to significant degradation in the quality of images. This effect can be seen in figure 2.9.

## 2.2 Target selection

In the last section, the necessary background for understanding observations made with the TTF was developed. The remainder of this chapter is devoted to outlining how we have actually used the instrument. This section describes how our targets for observation were selected; section 2.3 goes on to explain exactly what observations were taken.

### 2.2.1 Redshift $\sim 2.2$

Observations specifically for this work were made using TTF on the Anglo-Australian Telescope in July 2003. Targets were selected from the Molonglo Quasar Sample (MQS) of Kapahi et al. (1998). In this section, we briefly consider the properties of the MQS itself, then present details of how we chose targets from it and how the observations were carried out.

#### 2.2.1.1 The Molonglo Quasar Sample

The MQS is a catalogue of 111 radio-loud quasars drawn from the Molonglo Reference Catalogue (MRC; Large et al., 1981). The MRC, in turn, is a catalogue of 12,141 radio sources with flux density greater than 0.7 Jy at 408 MHz, covering a solid angle of 7.85 steradians on the sky.

In section 1.1 we discussed the “unified scheme” of active galactic nuclei. From this model, it is immediately obvious that the orientation with which we look at an AGN has a dramatic effect on what we might expect to observe. We expect the radio spectrum of the core of a quasar to be flatter than that of the lobes, so, if we view a quasar with its jet axis close to the line of sight, Doppler boosting of the core flux density will appear to make the core flux dominate over that from the sub-relativistic lobes. Orr and Browne (1982) showed that this effect will lead to flux-limited surveys at high radio frequencies preferentially selecting core-dominated objects. In other words, high-frequency radio surveys will tend to select objects which have a particular orientation on the sky; this is not the case for lower frequency work.

Orientation effects also play a role when considering the optical depth at which quasars may be identified. As discussed, for example, by Baker (1997), optical emission from quasars is highly anisotropic, brightening by up to 5 magnitudes between lobe- and core-dominated objects. Baker goes on to argue that this is due to aspect-dependent extinction: for example, the anisotropy is more pronounced at shorter wavelengths.

The MQS was specifically designed to address these orientation effects. All of the objects in the sample have been selected from the 408 MHz MRC. All objects in the MRC with a flux density greater than 0.95 Jy in a  $10^\circ$  strip of the southern sky ( $-30^\circ < \delta < -20^\circ$ ) and with Galactic latitude  $b > 20^\circ$  but excluding the right ascension range  $14^{\text{h}}03^{\text{m}}\text{--}20^{\text{h}}20^{\text{m}}$ . By examining all objects that meet this criteria, without employing an optical flux limit, orientation effects are avoided.

Having thus produced a list of candidate objects, objects were classified as quasars based on a series of follow-up observations. These included further radio imaging (using the Molonglo Optical Synthesis Telescope and the Very Large Array), identifying the objects in the optical UK Schmidt III-aJ survey and high-resolution spectroscopy using the RGO (in the blue) and FORS (in the red) spectrographs on the Anglo-Australian Telescope.

Full details on the selection of objects for the MQS were provided by Kapahi et al. (1998); Baker et al. (1999) provides a homogeneous set of low-resolution optical spectra and further details on most of the sample.

### 2.2.1.2 MQS target selection

Six targets were chosen from the MQS. Selection was made based on three criteria:

- The quasar has a redshift of around 2;
- The quasar redshift is such that its Lyman  $\alpha$  is placed within the wavelength ranges accessible to TTF's order blocking filters (section 2.1.3.3);
- The quasar must be observable from the AAT on the nights available to us.

The objects chosen are listed in table 2.2.

We were awarded four nights of observing time at the AAT: 24–27 July 2003. However, the first three of these nights were rendered unusable to us by weather conditions. On

**Table 2.2:** Candidates for TTF observations, July 2003; the objects actually observed are listed in bold-face. Optical positions and spectroscopic redshifts are from Kapahi et al. (1998); positions have been converted to J2000 (Standish, 1982).

Object	Position (J2000)		Redshift
	R.A.	Decl.	
MRC B0136-231	01 <sup>h</sup> 38 <sup>m</sup> 57.5 <sup>s</sup>	-22°54'47"	1.895
MRC B0237-233	02 <sup>h</sup> 40 <sup>m</sup> 08.0 <sup>s</sup>	-23°09'16"	2.223
MRC B0447-230	04 <sup>h</sup> 49 <sup>m</sup> 10.3 <sup>s</sup>	-22°58'58"	2.140
<b>MRC B1256-243</b>	12 <sup>h</sup> 59 <sup>m</sup> 12.6 <sup>s</sup>	-24°36'05"	2.263
MRC B1311-270	13 <sup>h</sup> 13 <sup>m</sup> 47.3 <sup>s</sup>	-27°16'49"	2.186
<b>MRC B2158-206</b>	22 <sup>h</sup> 01 <sup>m</sup> 27.1 <sup>s</sup>	-20°25'36"	2.249

the remaining night, time constraints made it only possible to observe two of the targets: MRC B1256-243 and MRC B2158-206.

### 2.2.1.3 MRC B2158-206

MRC B2158-206 is a radio-loud quasar. Its redshift is measured in the MQS as 2.249; note, however, that Baker et al. (1995) record it at  $z = 2.272$ . It is the former that provides the best match to the wavelength of the Lyman  $\alpha$  peak observed in subsequent observations. Kapahi et al. (1998) provides details of the radio emission from the object, but not, in this case, a map. The NRAO VLA Sky Survey (NVSS; Condon et al., 1998) provides a 1.4 GHz map covering a much larger area (the entire sky north of  $\delta = -40^\circ$ ); the quasar is clearly identifiable, but there is no significant radio structure nearby.

A spectrum, including the position of the Lyman  $\alpha$  line, is given in figure 2.10; more details about the optical properties of this object are given by Baker et al. (1999).

### 2.2.1.4 MRC B1256-243

MRC B1256-243 is a radio-loud quasar, measured in the MQS to have a spectroscopic redshift of  $z = 2.263$ . Kapahi et al. (1998) presents a 4.86 GHz radio-map of the area immediately surrounding the object taken with the VLA and a summary of the radio flux density from the object—both overall, and from the core alone—at a variety of frequencies. A spec-

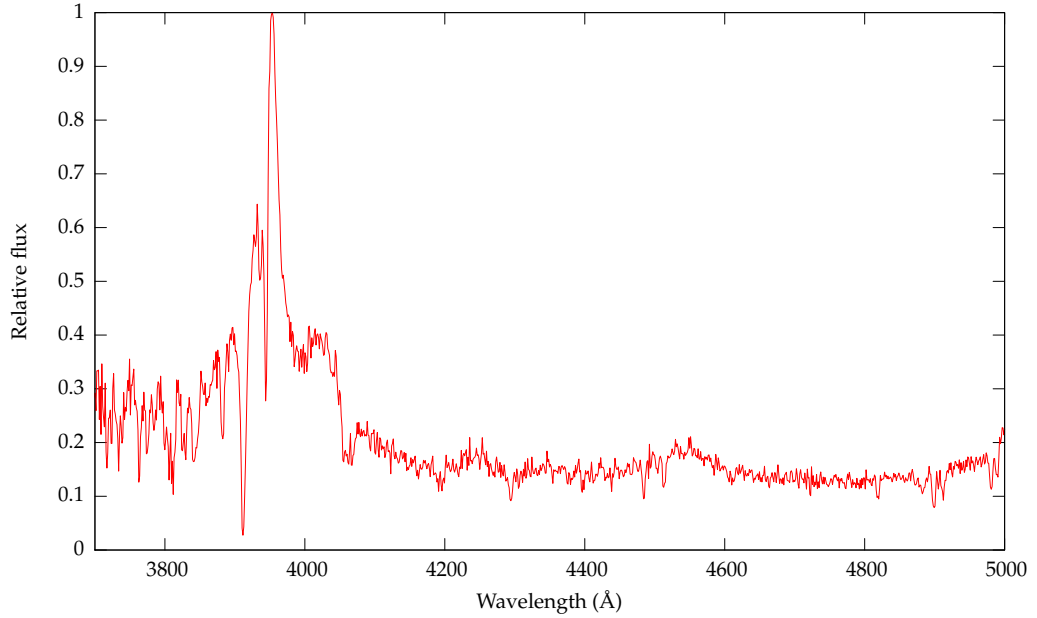


**Figure 2.10:** MRC B2158-206 spectrum. Data supplied by Joanne Baker, based on observations made at the VLT for a study of C IV absorption in radio-loud quasars (Baker et al., 2002).

trum, including the position of the Lyman  $\alpha$  line, is given in figure 2.11; more details about the optical properties of this object are given by Baker et al. (1999). Once again, the NVSS provides a 1.4 GHz map of the area, revealing no significant structure.

### 2.2.2 Redshift $\sim 4.5$

Further data used in this project was drawn from the AAT archives; unlike the  $z \sim 2.2$  data, we did not have a direct influence in choosing what should be observed. The most complete dataset available to us consists of observations of the quasar BR B0019-1522; it was this that was selected for further analysis in this thesis.

BR B0019-1522 was first discovered by the APM Color Survey (Irwin et al., 1991). This survey covered approximately 2500 square degrees from the equatorial region of the UK Schmidt Telescope. At high redshifts, the optical colours of quasars are dominated by the intervening cosmological absorption: it is possible to discriminate them from stars by considering the characteristic range they occupy in an  $B_J - R$ ,  $R - I$  colour diagram. In

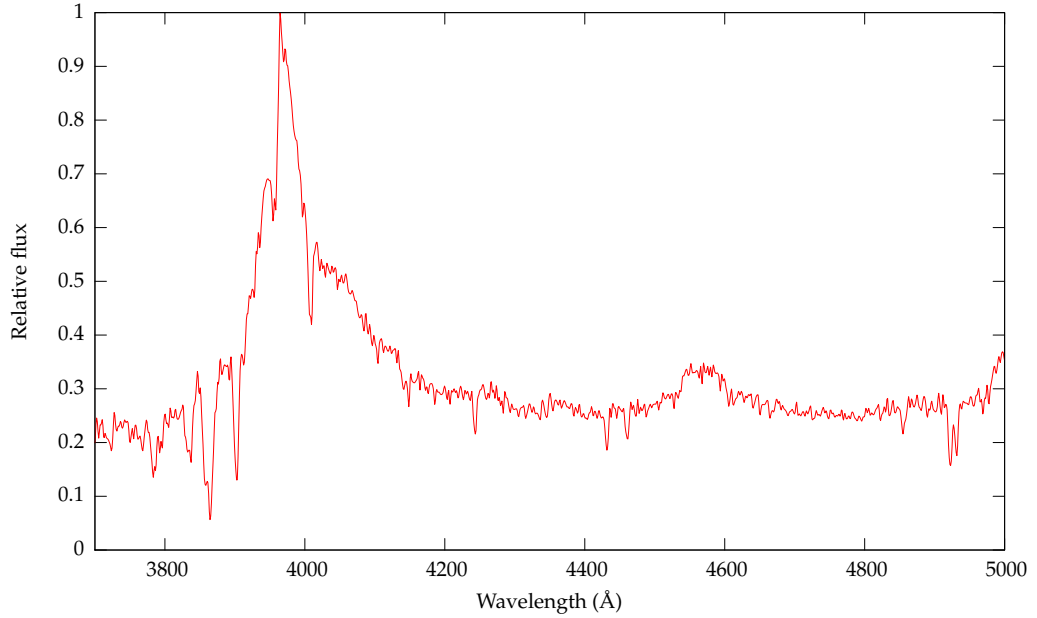


**Figure 2.11:** MRC B1256-243 spectrum. Data supplied in a private communication from Joanne Baker, based on observations made at the Anglo-Australian Observatory for a study of C IV absorption in radio-loud quasars (Baker et al., 2002). A flux calibration is not available.

total, 31 quasars at  $z \geq 4$  were discovered.

Storrie-Lombardi et al. (1996) document the results of high-resolution optical spectrophotometry of the majority of the APM quasars, including BR B0019-1522, using the ISIS spectrograph on the William Herschel Telescope. They quote the position of the object as  $00^h22^m08.0^s -15^\circ05'39''$  (converted to J2000). The spectrum they obtained for BR B0019-1522 is shown in figure 2.12. Based on their observations of the O I (rest frame 1304 Å), Si/O IV (1400 Å) and C IV (1549 Å) lines in the spectrum, Storrie-Lombardi et al. estimate the quasar redshift as  $z = 4.528$ .

BR B0019-1522 is not a radio-loud object; it is not visible in the NVSS, and there is no evidence for significant radio structure in its surroundings.

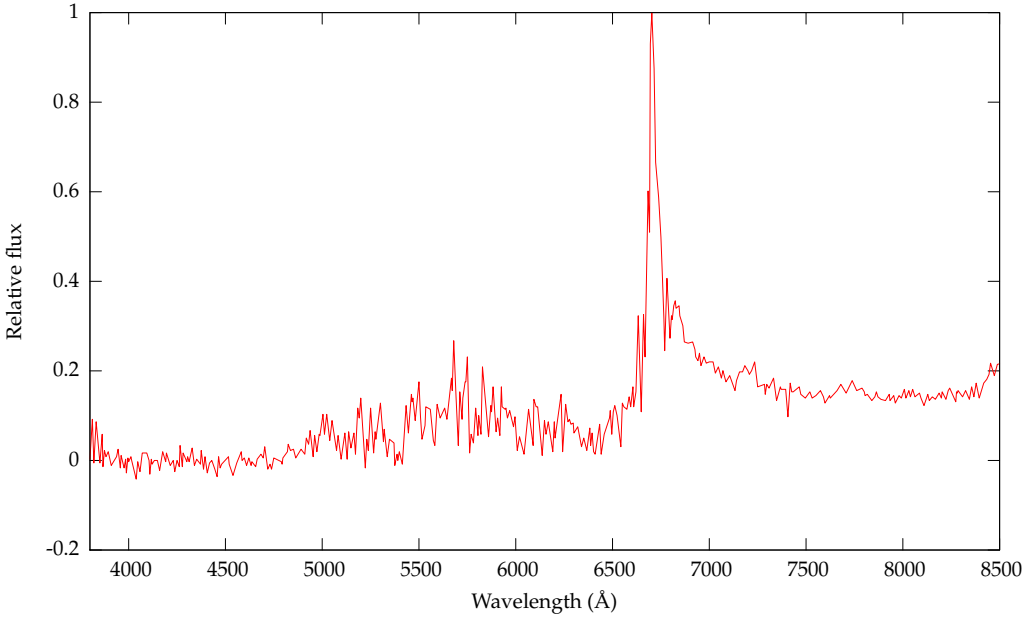


**Figure 2.12:** BR B0019-1522 spectrum. Data taken from Storrie-Lombardi et al. (1996), based on their spectrophotometry using ISIS on the William Herschel Telescope.

## 2.3 Observations

This section outlines details of the observations of our targets, thereby setting out exactly what data are available for analysis in the rest of this thesis.

### 2.3.1 Objects at $z \sim 2.2$

Both of the MRC quasars were observed on the night of 27 July 2003. The TTF was used at  $f/8$  on the AAT. At redshifts of around 2.2, Lyman  $\alpha$  occurs at approximately 4000 Å: it was therefore most appropriate to use Blue-TTF with the EEV2 CCD, with its greater sensitivity in the blue (figure 2.5). EEV2 at  $f/8$  gives a scale of 0.33''/pixel; after processing, the total useful rectangular field of view of our observations is around 7' by 5', varying slightly with the target. The use of an intermediate-band order-blocking filter was necessary, as documented in section 2.1.3.3: for the wavelengths under examination, the B1 filter was most appropriate. Observations of standard stars were made on the same night and at the same instrument settings. Conditions were photometric, and seeing was on the order of

1.5" (this is considered in more detail in the next chapter).

As we have seen, a given plate spacing corresponds to a given wavelength of transmission on the optical axis, but that wavelength varies across the field (section 2.1.4.1). Therefore, rather than labelling each field with a wavelength, we refer to it by a "Z-number". Each Z-number is mapped by the interferometer control system to a given plate spacing, and hence to a given transmission function across the field: in use, we never consider the plate spacing, but calibrate the transmission directly to the Z-number. The calibration procedure is described in section 3.1.5. A larger Z-number always corresponds to a longer wavelength. Table 2.3 lists the Z-numbers used in our observations.

The TTF, then, was configured to observe the fields at a series of interferometer plate spacings corresponding to wavelength steps of around 10 Å, the aim being to straddle the wavelength of redshifted Lyman  $\alpha$ . Figure 2.13 compares the on-axis wavelengths of our observations with the spectra of the MRC quasars. Note that although our on-axis observations fall to the red of Lyman  $\alpha$  in the MRC B2158-206 field (the observations were based on the  $z = 2.272$  quoted by Baker et al. (1995), rather than the correct value of  $z = 2.249$ ), the shift of observed wavelength to the blue as we move away from the optical axis brings it closer to our observed range. We will consider the position of the axis, and hence the range of observed wavelengths, in detail in the next chapter.

Figure 2.13 also shows the transmission profile of the AAT's B1 intermediate-band filter. Unfortunately, the transmission drops away sharply for the redder wavelengths in our observations. For MRC B1256-243, it was immediately clear when examining the reddest observations by eye that they contained no useful information: in the remainder of this work, therefore, we do not consider the MRC B1256-243 Z197 data further. Although the Z209 observations in MRC B2158-206 fall even further towards the edge of the filter, the longer exposure time means that some useful information can still be recovered from it. As we shall see in the course of the following analysis, the somewhat unfortunate choice of Z values has a significant effect on our observations.

During the course of the observations, we made use of charge shuffling on the CCD and frequency switching in the interferometer. Each data frame read out from the CCD consisted of two images of the same field at different Z settings—in the same way as the

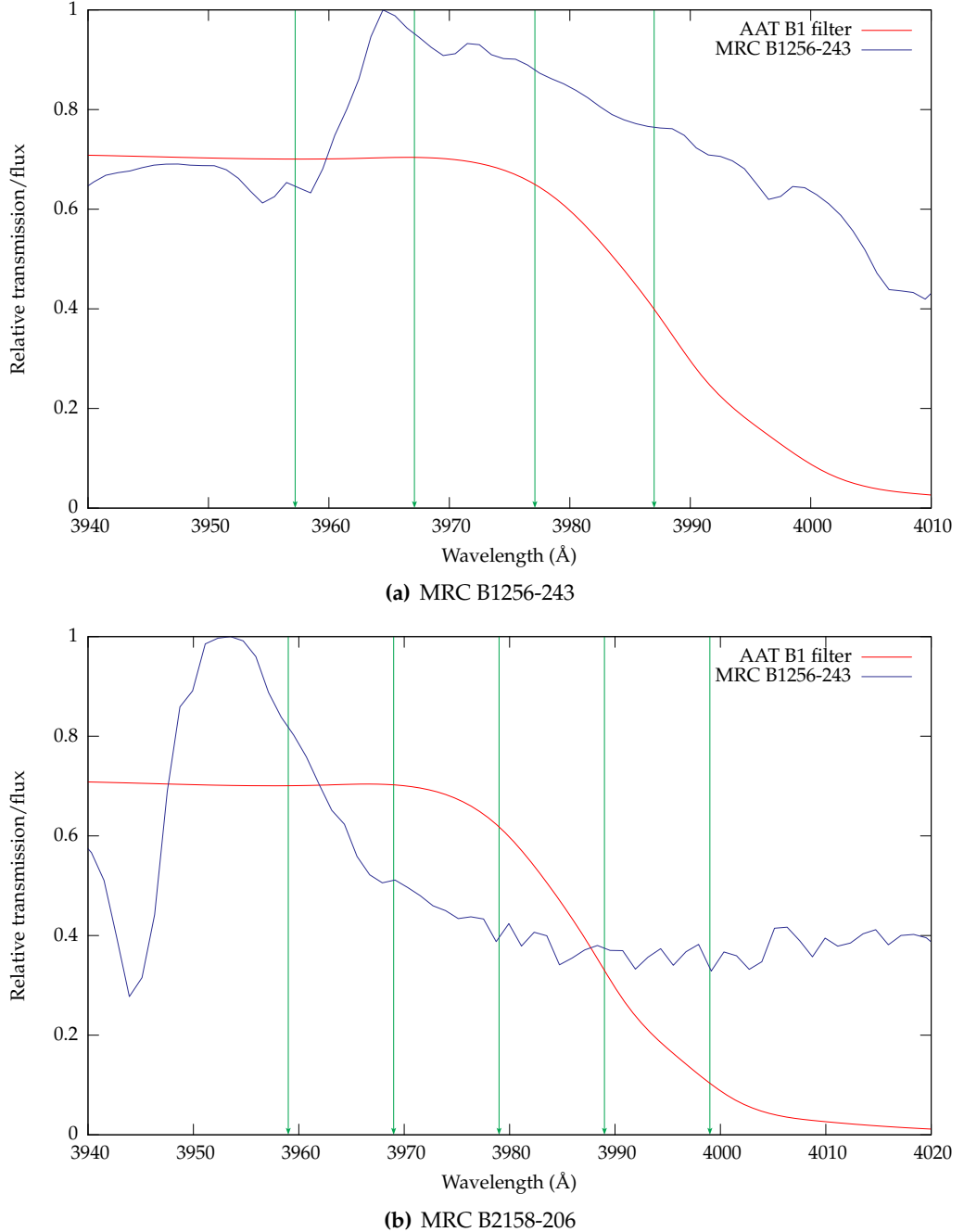


**Figure 2.13:** Wavelength coverage of our observations of the  $z \sim 2.2$  MRC quasars. The green arrows show the on-axis wavelengths of the various observations of each field; note that, as we move off axis, the observed wavelength moves to the blue. Plotted for comparison are the quasar spectra (normalised to 1), clearly showing their Lyman  $\alpha$  peaks, and the transmission profile of the AAT's B1 blocking filter.

example shown in figure 2.6. Each image consists of fifteen 60 second exposures per Z setting.

Between taking each image, the pointing of the telescope was shifted slightly. This enables the straightforward identification and subsequent elimination of ghosts from our analysis using the principles outlined in section 2.1.4.3.

Table 2.3 summarises the details of all these observations.

### 2.3.2 An object at $z \sim 4.5$

BR B0019-1522 was observed on the night of 6 November 1997. The observers were Bland-Hawthorn, Boyle and Glazebrook; the data were made available to us through the TTF archive.

At BR B0019-1522's redshift of 4.528, Lyman  $\alpha$  falls at 6722 Å. Therefore, Red-TTF was used in conjunction with the MITLL2 CCD, which is more sensitive in the red. Observations were taken at  $f/8$ , giving a scale of 0.37"/pixel. After processing, the total useful area was 9'17" by 4'10". Once again, an intermediate-band order-blocking filter was used: in this case, the R0 filter is most appropriate. Observations of a standard star were made on the same night and at the same interferometer settings. Conditions were photometric, and the seeing was on the order of 1.5".

In the same way as described above, a series of observations were taken with central wavelengths which straddle the quasar Lyman  $\alpha$  emission. In this case, the interferometer Z-number was incremented by 20 between exposures; this corresponds to a wavelength spacing of 16.4 Å. Figure 2.14 compares the on-axis wavelengths of the observations with the position of the quasar Lyman  $\alpha$  peak and the transmission profile of the R0 filter. In this case, the filter transmission is effectively flat over the range of the observations. Note once again that the observed wavelengths shown here are the upper limits in each frame: interferometer transmission shifts to the blue as we move away from the axis.

These observations also make use of charge shuffling on the CCD: each image read out from the detector includes all three Z settings that were analysed. However, only three 600 second exposures, one for each Z setting, were used for each image.

**Table 2.3:** Details of our observations using Blue-TTF at the Anglo-Australian Telescope, July 2003. The ‘interferometer Z’ is a direct but uncalibrated measure of the interferometer plate spacing; it is used to perform wavelength calibration, as described in the next chapter.

Target	Date	Exposure time (s)	Interferometer Z	On-axis wavelength (Å)	Comment
MRC B1256-243	27 July 2003	15 × 60	170 & 179	3957.2 & 3967.1	
		15 × 60	179 & 188	3967.1 & 3977.1	
		15 × 60	188 & 197	3977.1 & 3987.0	
		15 × 60	170 & 197	3957.2 & 3987.0	
EG 274	27 July 2003	30	170	3957.2	
		30	179	3967.1	
		30	188	3977.0	
		30	197	3987.0	
MRC B2158-206	27 July 2003	15 × 60	173 & 182	3959.1 & 3969.1	
		15 × 60	182 & 191	3969.1 & 3979.0	
		15 × 60	191 & 200	3979.0 & 3989.0	
		15 × 60	200 & 209	3989.0 & 3999.0	
		15 × 60	173 & 209	3959.1 & 3999.0	
		15 × 60	173 & 182	3959.1 & 3969.1	
		15 × 60	182 & 191	3969.1 & 3979.0	
		15 × 60	191 & 200	3979.0 & 3989.0	
		15 × 60	200 & 209	3989.0 & 3999.0	
		15 × 60	173 & 209	3959.1 & 3999.0	
EG 21	27 July 2003	60	173	3959.1	
		60	182	3969.1	
		60	191	3979.0	
		60	200	3989.0	
		60	209	3999.0	
		120	173	3959.1	
		120	182	3969.1	
		120	191	3979.0	
		120	200	3989.0	
		120	209	3999.0	

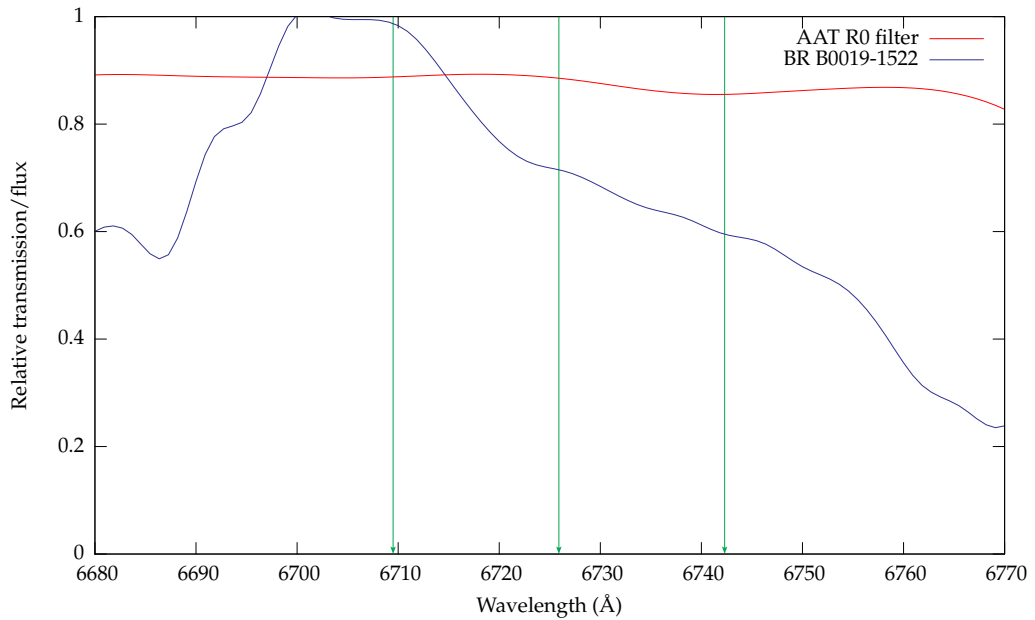


**Figure 2.14:** Wavelength coverage of the archive observations of BR 0019-1522. The green arrows show the on-axis wavelengths of our observations of each field; these set an upper limit on the observed wavelength. Plotted for comparison is the quasar spectrum (normalised to 1) and the transmission profile of the AAT’s R0 blocking filter.

After four of the total of eight data frames had been taken, the pointing of the telescope was shifted slightly. This enables the identification and subsequent rejection of ghosts from our analysis using the principles outlined in section 2.1.4.3.

Full details of the observations of BR B0019-1522 are presented in table 2.4.

## 2.4 Summary

Broadly, this chapter may be considered as two parts. In the first, we developed in some detail the background theory behind the use of a Fabry-Pérot interferometer as a tunable filter for astronomical observations, before going on to describe the specific features of an instrument build on these principles: the Taurus Tunable Filter. The second part of the chapter described how we have used the TTF: what was observed, when, and in what way.

**Table 2.4:** Details of archival observations of BR B0019-1522 using Red-TTF. The column labelled ‘Z’ records the uncalibrated interferometer plate spacing; this is converted to a wavelength calibration in the next chapter.

Target	Date	Exposure time (s)	Z	On-axis wavelength (Å)	Comment
BR B0019-1522	6 Nov 1996	600	431	6709.5	One image;
		600	451	6725.9	repeated
		600	471	6742.3	eight times.
HD49798	6 Nov 1996	600	431	6709.5	Standard.
		600	451	6725.9	One image;
		600	471	6742.3	not repeated.

The next chapter describes how the data are reduced to a form suitable for further analysis.

# Chapter 3 | *Data Reduction*

In the last chapter, we described both the properties of the TTF and it was used to make observations for this thesis. However, transforming those observations into useful information requires considerable processing; in this chapter, therefore, we outline the data reduction steps performed. This is done in two parts: first, we describe the general procedures that were performed on all of the observations. Secondly, we consider those issues which were specific to each field.

## 3.1 *General data reduction techniques*

There are a number of data reduction and analysis techniques which are common to many, or indeed all, of our images. We summarise them here, often drawing on just one or two images as examples to illustrate the working of the technique. A summary of the results for each image is presented in section 3.2. Jones et al. (2002) provide further discussion of the issues surrounding the reduction of tunable filter data.

For the purposes of this discussion, we make a distinction between a *frame* (corresponding to one set of data read off the CCD), an *image* (a number of frames at the same etalon setting which have been combined in some way) and a *field*, or a stack of images of the same area of the sky at different etalon settings.

Broadly speaking, data reduction proceeds as follows:

1. Bias correction;
2. Flat-field correction;
3. Crop data into individual frames;
4. Align and combine data frames to form images;
5. Wavelength calibration of images;

6. Photometric calibration of images;
7. Object detection and catalogue creation.

Steps 1 through 5 are carried out in the same way for all data in a given set of observations, including the standard star: the images of the standard are, of course, used in step 6 for photometric calibration of the data images.

### 3.1.1 *Bias correction*

All images taken by CCD have an offset from zero—or *bias*—in the data, even when the CCD has not been exposed to light. The first step in data reduction is to remove this offset.

This is compensated for by the use of a 20 pixel wide “overscan region” along the long dimension of the CCD: 20 extra readouts are made after all the data has been extracted from the CCD. This provides an estimate of the readout in the absence of any signal.

The bias signal does not vary significantly over the length of the overscan region. This was demonstrated as follows. For each 20 pixel wide row, we calculate the median pixel value, then calculate the standard deviation of these medians of the length of the several thousand pixel long strip. In all cases, it is found to be less than one count, and we regard it as constant. We therefore simply subtract the mean signal recorded in the overscan region from the data before proceeding.

### 3.1.2 *Flat field correction*

All CCDs have non-uniformities; equal illumination across the CCD will not generate a perfectly consistent signal. We compensate by the use of a twilight flat field.

The flat field is constructed at the start of the night’s observing: the observations are made as for data collection, but during twilight, while the sky is still bright. In this way, the CCD is uniformly illuminated.

We normalise the flat field image to a mean pixel value of 1, then divide the bias-corrected data by it.

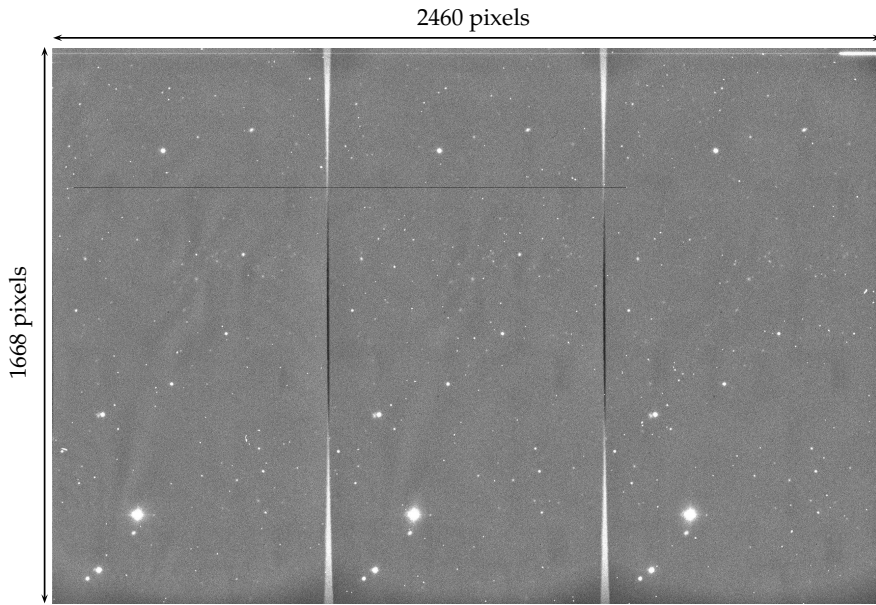


**Figure 3.1:** Unreduced observations of BR B0019-1522; compare with figure 2.6. By including three different Z settings in the data, the total area available to each observation is decreased. An aperture mask is used to prevent the data from overlapping.

### 3.1.3 Data cropping

As described, observations were made at various different Z settings in one CCD read-out, with charge-shuffling used to separate the various frames. The data produced by the instrument is therefore in the form shown in figure 2.6 (page 40) in the case of MRCs B1256-243 and B2158-206; BR B0019-1522 includes all three Z settings on one image, as shown in figure 3.1.

In order to produce frames at individual Z, therefore, the relevant pixels must be cropped out of the larger datasets. Sections were chosen to maximise the number of useful pixels extracted from the data; no effort was made to ensure all sections were the same size and shape. In the next section, we consider how the cropped frames may be aligned and trimmed to a consistent size.

### 3.1.4 Aligning and combining frames

As recorded in section 2.3, the pointing of the telescope was shifted slightly between observations. Furthermore, section 3.1.3 records that the data were cropped from each read-out individually, without reference to how it might align with other frames of the same field. Before the analysis proceeds, we must ensure that each frame shows the same field of view.

The IRAF (Tody, 1986, 1993) task cl.images.immatch.imalign was used to align the images as follows. For each complete image (that is, for a given etalon Z pointing at a given quasar), a reference frame was chosen from the available data. A selection of six objects which were clearly visible in each frame to be aligned were chosen, and their coordinates within the reference image noted. A rough estimate as to the shifts between the images was made by comparing the positions of one of these objects in each of the frames using SAOImage DS9 (Joye and Mandel, 2003).

Based on the above information, IRAF performs a marginal centroid fit (see appendix A) with up to seven iterations for each of the specified objects. The fit is taken as converging when the calculated position of the centroid is in the middle of the centring region. The overall shift in  $x$  and  $y$  coordinates to bring each frame into line with the reference frame is then calculated by combining the shifts for each object. This procedure assumes that the shifts are linear in  $x$  and  $y$ ; this is borne out by the error in the centring process (based on the discrepancies between the shifts generated for each object) being  $\leq 0.3$  pixels.

The signal in the image is binned into pixels. When a fractional pixel shift is calculated, it is necessary to consider how the shifted image should be binned. Two possibilities present themselves: either the data can be rebinned by interpolating between neighbouring bins, or the shift can be limited to an integral number of pixels.

Rebinning the signal has the side-effect of smoothing out noise in the images: since a good understand of the noise is essential when considering the significance of any objects we detect in the image, this is something to be avoided if possible. Further, we have seen that the errors in the aligning process are around 0.3 pixels: aligning to the nearest pixel should be accurate to a maximum error of 0.5 pixels—a difference of only 0.2 pixels or

significantly less than 0.1''. To check, we used the IRAF task `noao.digiphot.apphot.fitsf` compare the full width at half maximum of a selection of objects in the images by fitting them with a radial Gaussian profile. There was no detectable difference in the size of unresolved sources between the rebinned and the nearest-pixel images. From this point onwards, therefore, we align all our images to the nearest pixel. After alignment, the images are trimmed so that they all have the same field of view.

Post alignment, the individual frames are combined to make an image at each  $Z$  value. We do this by taking the median of all the images: this increases the signal to noise ratio (section 3.1.8), while simultaneously eliminating artifacts such as cosmic rays, which appear in only one frame, and ghosts, which shift position when the pointing of the telescope is changed slightly (section 2.1.4.3). A complete discussion of the removal of these artifacts in each field is given later in this chapter, when we consider the individual fields in detail.

#### 3.1.5 *Wavelength calibration: the ‘sausage cube’*

Wavelength calibration is achieved by means of a procedure known in the TTF jargon as making a ‘sausage cube’.

In this process, the instrument is exposed to light from an arc lamp of known spectrum. The CCD is masked off, such that data are only recorded from a region of nine pixels around the optical axis—such a small region avoids the problem of the peak transmission varying across the field of view. The etalon plate spacing,  $Z$ , is then changed in small increments and, at each spacing, an image is recorded.

A series of such measurements are carried out, spanning the range of  $Z$  for which a wavelength calibration is to be performed. It is then possible to measure the relative flux recorded in each exposure, and plot this against the etalon plate spacing, parameterized by  $Z$ . An example of such a plot is shown in figure 3.2: here, a neon arc lamp is observed through the TTF’s R0 blocking filter. Three neon lines may be identified by comparing this with the documented spectrum for the AAT’s neon arc lamp.

Due to the cyclical nature of the interferometer transmission (as discussed in section

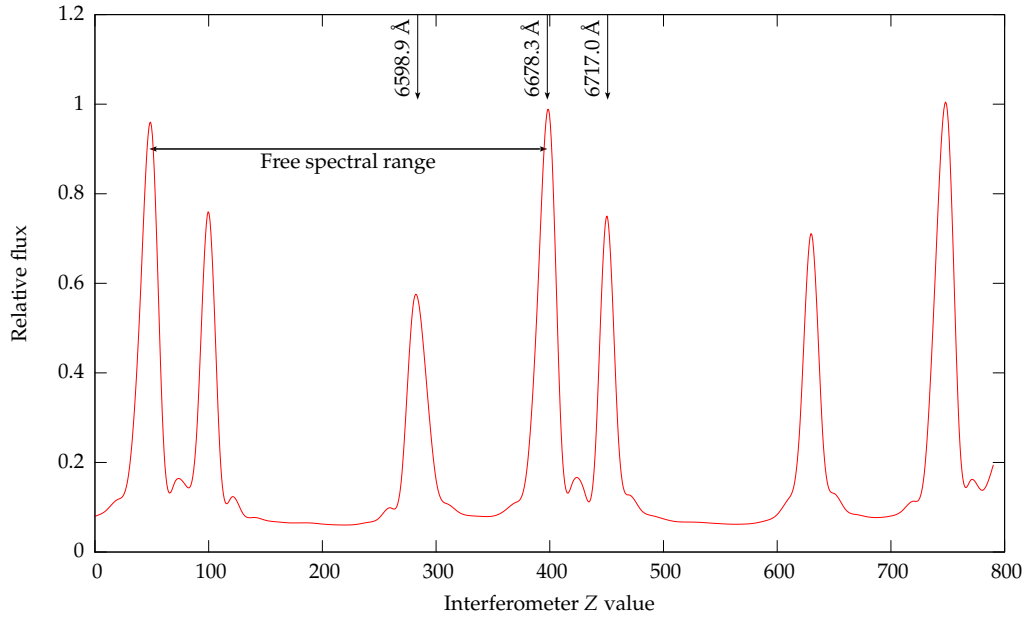


**Figure 3.2:** A ‘sausage cube’ based on a neon arc lamp. The positions of three spectral lines are marked. Note that the pattern is cyclical with a period equal to the free spectral range: the  $6678.3\text{ \AA}$  line is visible in three different orders of interference at the left, centre and right of the plot.

2.1.1.1), we see the same small portion of the arc lamp spectrum repeated several times, with each order of interference separated by the free spectral range. As shown in figure 3.2, it is therefore possible to measure the free spectral range (in units of  $Z$ ) from a ‘sausage cube’ spectrum which covers several orders.

With the help of the IRAF routine `noao.onedspec.splot`, we fit Lorentzians to the peaks in the sausage cube spectrum using a least squares method (Marquardt, 1963) and therefore determine the position of their centre as a function of  $Z$ . Since the relationship between plate spacing and the wavelength of peak transmission is linear (equation 2.9), we then use a linear regression analysis (courtesy of IRAF’s `cl.utilities.polyfit`) to determine a relationship between  $Z$  and  $\lambda$ .

As we have established, though, the wavelength of peak transmission varies across the image (section 2.1.4.1). The wavelength at any given point on the image may be calculated by the above calibration combined with equation 2.26 once the position of the optical axis has been determined.

Finally, note that the wavelength calibration obtained in this way is stable: Francis and Bland-Hawthorn (2004) report it varying by less than 1 Å throughout the night for their observations centred on 3851 Å.

### 3.1.6 *An introduction to SExtractor*

SExtractor—“Source Extractor”—is a software tool for building catalogues of objects in an image (Bertin and Arnouts, 1996). In addition, it can perform various sorts of analysis, including photometry, on the result. This project makes extensive use of it: this section, therefore, briefly outlines the principles of its operation and its capabilities. We go on to discuss its use in photometry in section 3.1.7 and catalogue creation in section 3.1.9.

Broadly, SExtractor operates in five stages: background estimation, thresholding, deblending, filtering and photometry. Many aspects of the software are specifically developed to deal with conditions that we do not experience here (for example, extremely crowded fields): this discussion will skip rapidly over them.

#### 3.1.6.1 *Background estimation*

The flux recorded in each pixel of the image is the sum of a night-sky background and any signal from an object which falls in that pixel. In order to identify objects and measure how bright they are, it is therefore necessary to remove the background signal. SExtractor therefore constructs a ‘background map’: a precise estimate of the background signal at each point in the image. There are various ways of building up such a map; the algorithm used by SExtractor is based on that used by DAOPHOT (Stetson, 1987).

The image is divided into a grid with a user-defined mesh size (controlled by the SExtractor parameter `BACK_SIZE`; we use a value of 64, which is comfortably bigger than the largest sources in our image), the mean and the standard deviation ( $\sigma$ ) of the pixel values are computed. The most divergent pixels are discarded, and the computation performed again; this process is repeated until all the remaining pixels are within  $\pm 3\sigma$  of the mean. If  $\sigma$  changes by less than 20% over the course of this process, the field is considered ‘uncrowded’, and the (clipped) mean is regarded as the background signal. In the alter-

native ('crowded') case, the background is estimated as  $2.5 \times \text{median} - 1.5 \times \text{mean}$ . The resulting background map is then a bilinear interpolation between the meshes of the grid.

As well as using the background map internally for detection and photometry, SExtractor can save a copy for further analysis. This is how figure 4.1 was produced, for example.

### 3.1.6.2 Detecting, deblending and filtering objects

The algorithm SExtractor uses to identify an object is, in principle, straightforward: it simply searches for a contiguous group of pixels each of which is at least some threshold above the background. Both the number of pixels in the group and the required threshold are defined by the user (the relevant parameters being `DETECT_MINAREA` and `DETECT_THRESH` respectively); the threshold may be specified in terms of data units, surface brightness or, as we shall always use, relative to the background RMS.

Before thresholding, it is possible to filter the image by convolving it with an arbitrary mask. In order to best detect faint objects, the appropriate mask is a Gaussian point spread function matched to the seeing, as described by Irwin (1985). Such a convolution is performed as a matter of course during all the SExtractor analysis in this thesis. The convolved image is, of course, only used for object detection: subsequent analysis is performed on the original data.

We chose the appropriate values of these parameters for our observations based on a combination of an automatic optimisation approach (described in section 4.3.1) and individual fine-tuning on an image-by-image basis.

A problem with the above technique is dealing with objects which are so close together that their pixels appear contiguous: they are merged. SExtractor calls the process of separating such objects 'deblending'. In summary, SExtractor fits a 'tree' pattern to all the pixels forming the object, branching wherever there is a local minimum in the object. When the tree is complete, major branches—those containing more than a certain fraction of the counts—are regarded as independent objects. Note that our fields are not crowded, so that this is not an issue in our analysis.

A potential pitfall with the system as described so far is the influence of objects on their close neighbours. Therefore, the list of detections is ‘cleaned’: each object is examined to see if it would have been detected if its neighbours did not exist. Contributions from neighbouring objects are estimated by fitting a Moffat (1969) profile of the form

$$I(r) = \frac{I(0)}{(1 + kr^2)^\beta} \quad (3.1)$$

to each of the neighbours, where  $\beta$  is a user-supplied parameter (CLEAN\_PARAM) which determines the brightness of profile wings (and hence the efficiency of the cleaning). Once again, though, although it is important to be aware of SExtractor’s cleaning, it is not, in general, an issue in our relatively uncrowded fields.

### 3.1.6.3 *SExtractor as a photometric tool*

SExtractor provides a variety of methods for performing photometry. However, we make use of the simplest form: simply placing fixed apertures over the objects in our field and calculating flux based on the number of counts within the aperture after the background has been subtracted off. The size of the apertures used is chosen to optimise the signal to noise ratio, as described in section 3.1.8.4.

It is worth noting that SExtractor provides further capabilities for, for example, distinguishing between stars and galaxies. However, in this work we do not make use of them.

### 3.1.7 *Photometry*

Section 3.1.6 referred to SExtractor’s ability to perform photometry. In fact, it provides a variety of photometric tools, but, in this work, we make use of only the simplest form: placing fixed apertures over the objects in our field and calculating flux based on the number of counts within the aperture after the background has been subtracted. The size of the apertures used is chosen to optimise the signal to noise ratio, as described in section 3.1.8.4. The raw count provided by SExtractor needs calibrating before it can be used for useful measurements. In this section, we outline how this might be done.

### 3.1.7.1 Magnitude calibration

For a given count  $C$  as produced by SExtractor, a corresponding magnitude is given by

$$m = C_0 - 2.5 \times \log_{10} C \quad (3.2)$$

where  $C_0$  is a zero-point offset. In order to calibrate the system, we must calculate  $C_0$ . In order to do this, we use a standard star. For all our observations, standards were observed at the same time and the same etalon settings as our data: see tables 2.3 and 2.4 (pages 56 and 58 respectively). The standards are chosen such that their AB magnitude (defined in section 3.1.7.2) at the wavelengths of our observations is known, and the data are reduced in exactly the same way as the data frames.

SExtractor is now used to perform aperture photometry on the standard frame. A large (24 pixel diameter) aperture is used, to ensure that all the counts from the standard are collected. We record the number of counts as  $C_s$ .

Aperture photometry is also performed on the image to be calibrated with this standard. A smaller aperture is used here, ensuring the best possible signal to noise characteristics and minimising the chance of confusion between objects: for a full discussion, see section 3.1.8.4. For each object in the field, a count  $C_{\text{Obj}}$  is recorded.

Now, take the (known) magnitude of the standard to be  $m_s$ , and the magnitude of the object to be  $m_{\text{Obj}}$ . The exposure time for the standard observations is  $t_s$ , and for the data  $t_{\text{Obj}}$ . Then

$$m_{\text{Obj}} = m_s - 2.5 \times \log_{10} \left( \frac{C_{\text{Obj}} t_s}{C_s t_{\text{Obj}}} \right) \quad (3.3)$$

gives us the magnitude of the object in the field. By comparison with equation 3.2, it is then possible to calculate  $C_0$ , and hence obtain a calibration.

Note that this discussion assumes that  $C_0$  is constant across the image. In practice, this is not always the case: the change of wavelength across the field, together with the variation of blocking filter transmission seen in some observations, causes  $C_0$  to vary. We return to this topic in sections 3.2.1.8 and 3.2.2.8.

Note further that we used a different aperture size to measure the counts in the standard and the data frames. This leads to a systematic offset in our calibration which we calculate later in this chapter for each field (sections 3.2.1.7, 3.2.2.7 and 3.2.3.7).

Finally, note that the airmass was effectively constant throughout the course of each set of observations. Therefore, we do not take further account of it in this calibration.

### 3.1.7.2 Conversion between magnitude and flux

The above procedure produces a calibrated AB magnitude for each object detected. However, in order to investigate the properties of the objects—for example, to calculate their luminosities, and hence star formation rate as described in section 6.2—it is necessary to determine the flux coming from each object.

The AB magnitude system (Oke, 1974; Oke and Gunn, 1983) is defined by

$$m_{\text{AB}} = -2.5 \log_{10} f_{\nu} - 48.60 \quad (3.4)$$

where  $f_{\nu}$  is the flux in  $\text{ergs cm}^{-2} \text{s}^{-1} \text{Hz}^{-1}$ . The constant 48.60 is chosen such that  $m_{\text{AB}}$  is equal to the V band magnitude for an object with a flat spectrum. We work in monochromatic flux  $f_{\lambda}$  with units  $\text{ergs cm}^{-2} \text{s}^{-1} \text{\AA}^{-1}$ , so rewrite equation 3.4 as

$$m_{\text{AB}} = -2.5 \log_{10} \left( \frac{f_{\lambda} \times \lambda^2}{c} \right) - 48.60 \quad (3.5)$$

and hence

$$f_{\lambda} = \frac{c \times 10^{-(m_{\text{AB}}+48.60)/2.5}}{\lambda^2} \quad (3.6)$$

gives the flux  $f_{\lambda}$  in terms of  $m_{\text{AB}}$ .

In order to determine the total flux in the band, it is now necessary to multiply by an effective width. In the simple case of a sharp-sided square transmission band, we could simply multiply by the band width. However, the pass-bands of the TTF interferometer do not conform to such a straightforward model. Instead, following section 2.1.2, we model them as Lorentzians, normalised to 1 at the wavelength of peak transmission thus:

$$T(\lambda) = \frac{\lambda_{1/2}^2 / 4}{(\lambda - \lambda_c)^2 + \lambda_{1/2}^2 / 4} \quad (3.7)$$

where  $\lambda$  is the wavelength,  $\lambda_c$  the central wavelength of the band and  $\lambda_{1/2}$  the full width at half maximum of the band. Integrating, we have:

$$\int_0^\infty T(\lambda) d\lambda = \left[ -\frac{1}{2} \lambda_{1/2} \tan^{-1} \left( \frac{2(\lambda_c - \lambda)}{\lambda_{1/2}} \right) \right]_0^\infty \quad (3.8)$$

$$\simeq \frac{\pi \lambda_{1/2}}{2}, \quad (3.9)$$

where we make the assumption that  $\lambda_c \gg \lambda_{1/2}$ . Hence, combining equations 3.6 and 3.9 we measure the total flux  $f_{\text{total}}$  with units ergs cm<sup>-2</sup> s<sup>-1</sup> in the band as

$$f_{\text{total}} = \frac{\pi c \lambda_{1/2} \times 10^{-(m_{AB} + 48.60)/2.5}}{2 \lambda_c^2} \quad (3.10)$$

for an object with measured AB magnitude  $m_{AB}$  in a band with full width at half maximum  $\lambda_{1/2}$ , where we have made the assumption that the band is narrow and hence replaced  $\lambda$  from equation 3.6 with  $\lambda_c$ .

Note that this treatment assumes that the flux comes from a flat spectrum source, like the standard. When measuring emission lines, this is obviously not the case: an offset must be applied to the magnitude before the correct flux can be calculated. This is considered in section 4.2.2.2.

### 3.1.8 Uncertainties and signal to noise ratio

As discussed, we perform photometry on our images by laying down a circular aperture of given radius on the image, calculating the total number of counts that fall within that radius, and subtracting from it the estimated background level. It is then necessary to make an estimate of how uncertain such a measurement might be. First, we consider the various routes by which statistical noise might be introduced to our measurements.

#### 3.1.8.1 CCD readout noise

CCD readout noise is introduced as the charge is extracted from the CCD and converted to data units: conversion of the same pixel with the same charge do not yield absolutely reproducible results, as the sensor and electronics may inject unwanted random signals

which end up being digitised. The readout noise in the TTF system is dependent on the CCD being used: 2.7 electrons per pixel with the EEV CCD, or 2.0 for MITLL2.

### 3.1.8.2 Shot noise

Shot noise is introduced whenever that finite number of particles that carry information—such as photons hitting our CCD—is small enough to give rise to detectable statistical fluctuations in the measurement. It is a Poisson process; the number of photons detected will follow a Poisson distribution.

We must take account of the general shot noise in the background across the whole image, and also the shot-noise induced uncertainty in the counts detected for sources.

### 3.1.8.3 Combining noise

It is now necessary to combine these sources of noise to estimate the total uncertainty in our measurements.

The readout noise and the shot noise in the background are present all across the field; they simply cause a variation in the background signal. Conveniently, SExtractor measures the root mean square variation across the image: for any given aperture laid down on the image, we can use it to extract the noise in the included background pixels and hence calculate the average RMS background noise per pixel in the aperture,  $R$ . We label the background noise  $\sigma_{\text{BG}}$ , given by

$$\sigma_{\text{BG}} = \sqrt{\pi \times r^2 \times R^2}, \quad (3.11)$$

where  $r$  is the radius of the photometry aperture in pixels.

Next, we consider the shot noise in a given object. If  $N$  electrons are recorded on the CCD, the associated Poisson noise is  $\sqrt{N}$ . However, each electron read from the CCD does not map directly to one count in the image; rather, the signal is amplified—for a  $N$  electrons, we record  $g \times N$  “analogue to digital units”, or ADUs. We call  $g$  the gain of the readout process; more usually, though, we deal in terms of the inverse gain  $\mathcal{G} = 1/g$ . The

inverse gain is dependent on the CCD being used: 0.32 in the electrons per ADU for the EEV CCD, or 1.1 using MITLL2.

Now, the signal to noise ratio in terms of ADUs must be the same as that in terms of the raw electrons. Thus, having scaled the number of electrons  $N$  by  $g$ , we simply do the same for the noise;  $\sigma_S$ , the error on the number of ADUs is then

$$\sigma_S = g \times \sqrt{N} = g \times \sqrt{\frac{g \times N}{g}} = \sqrt{\frac{C}{g}} \quad (3.12)$$

where  $C$  is the total number of ADUs recorded in the source.

This, of course, holds true for a single exposure. However, we typically take the median of two or more raw images before analysing: in this way, we can eliminate features such as ghosts and cosmic rays (as discussed in section 3.1.4). What does this do to our noise estimates?

Since the noise in the background is directly measured from the combined image we are processing, it is not necessary to calculate the effect of taking the median here. However, it is worth noting that care must be taken when combining images: if the images are aligned by shifting a fractional pixel distance and then rebinned before combining, noise can be artificially smoothed out of the resultant image. Therefore, when building noise maps of our data, images are only shifted by integral numbers of pixels.

The same happy situation does not apply to the shot noise in the sources, however. We calculate this based on the number of counts in the object; our calculation must therefore be modified to take account of the extra information. Combining images by taking the median reduces the noise by  $1/\sqrt{n}$ , where  $n$  is the number of images combined.

Finally, then, we add the errors from the background and the source in quadrature, to produce an overall  $\sigma$  for the aperture:

$$\sigma = \sqrt{\pi r^2 \times R^2 + \frac{C}{Gn}}. \quad (3.13)$$

### 3.1.8.4 Choosing the best aperture size

As recorded in section 3.1.7, we perform fixed aperture photometry on our objects. For best performance, it is important to optimise the signal to noise ratio in the apertures we use.

We model the flux from each object as distributed on the image with a Gaussian point spread function of full width at half maximum equal to the seeing in the image. Consider an object which produces a total of  $C_t$  counts. We have

$$C_t = 2\pi \times C_p \times \int_0^\infty x \exp\left(\frac{-4x^2 \ln 2}{s^2}\right) dx \quad (3.14)$$

where  $C_p$  is the height of the object peak and  $s$  the full width at half maximum of the seeing. This enables us to calculate  $C_p$  for an assumed  $C_t$ . The total flux collected over an aperture of radius  $r$  is then

$$C = 2\pi \times C_p \times \int_0^r x \exp\left(\frac{-4x^2 \ln 2}{s^2}\right) dx. \quad (3.15)$$

Noise in the aperture is given by equation 3.13; if  $C$  counts are measured within the aperture, then the signal to noise ratio is  $C/\sigma$ , and the aim is to maximise this. This is a function of several image properties—the gain, the readout noise, the number of exposures, the RMS noise in the background, the seeing and the number of counts in an object—so it must be optimised on a case-by-case basis (sections 3.2.1.7, 3.2.2.7 and 3.2.3.7). In general, the optimal aperture diameter is slightly bigger than the full width at half maximum of the seeing.

Note that the the above discussion makes the assumption that the observed distribution of flux from an object may be accurately represented by a Gaussian point spread function corresponding to the seeing: that is, that the objects are unresolved. Extended sources are not accurately accounted for by the above: a larger fraction of the flux from the object will fall outside our measurement aperture.

How accurate is this assumption? In sections 3.2.1.4, 3.2.2.4 and 3.2.3.4 we consider the magnitude of the seeing in each of the images: in general, it is equivalent to a full width half maximum of around 1.5''. Further, In section 6.1.1 (page 154) we derive angular scales

for these objects on the order of 8 kpc per arcsecond: in other words, our seeing scale is roughly comparable to the expected angular size of a 12 kpc diameter galaxy.

Given that we are observing at high redshift, we would expect the galaxies seen to be relatively small: hierarchical merging has not yet had chance to build them up into the massive galaxies in the local universe. This model is supported by the data of Bouwens et al. (2004b): in their study of galaxies observed in the Hubble Ultra Deep Field (Beckwith et al., 2006), they quote average half-light diameters of  $\sim 4$  kpc at  $z \sim 2.2$  and  $\sim 2.2$  kpc at  $z \sim 4.5$ , while noting that large galaxies (diameters over 6 kpc) are rare. While it is worth noting that their observations are considerably deeper than ours (and hence sensitive to smaller, fainter galaxies than we see), it seems safe to make the assumption that our candidate objects are unresolved. This is supported when our detections are examined by eye (chapter 5): no extended structure is visible.

### 3.1.9 *Object detection and catalogue creation*

At this stage, barring the caveats to be discussed in section 3.2, the images are reduced, calibrated and ready for analysis. Detecting and building catalogues of all the objects within an image is performed using SExtractor: this process is described in section 5.1.

## 3.2 *Specifics of each field*

In addition to the general data reduction procedures outlined so far in this chapter, the unique characteristics of each field required special treatment.

### 3.2.1 *MRC B2158-206*

The majority of our observing time at redshift  $z \sim 2.2$  was expended on MRC B2158-206. In this section, we outline in detail the results of all the data reduction steps.

### 3.2.1.1 Charge trapping

The repeated shuffling of charge during the exposures on this field caused a large number of defects in the data frames due to charge trapping; see, for example, figure 2.9 (page 46). Ideally, these could be subtracted using a ‘dark’ image; however, dark images were not available for these data. Instead, another technique was adopted, and is described here.

The charge-trapping sites appear at the same pixel coordinates in the raw data read out from the CCD in every exposure. Meanwhile, the pointing of the telescope is shifted slightly between exposures, so that objects (and ghosts) do not fall at the same point.

After subtraction of the overscan bias, all the raw frames were combined by taking their median. This median displays all the charge-trapping artifacts, but not the objects. Dividing our data by this median image reduced all the charge-trapping sites to undetectable levels. Although this successfully produced a very clean-looking image, its statistical implications for the data are undesirable: a better method would have been to mask out the trapping sites. This is considered in some detail in appendix B.

However, this method also divides out any systematic variation in illumination across the data frames, which might not be appropriate here: the effect may be due to variations in filter transmission, for example, which are corrected for elsewhere. Therefore, we use SExtractor to fit the background signal in the median image, effectively reproducing the same pattern but without the charge-trapping sites. We multiply the data by this background fit, restoring its original illumination patterns.

It should be noted that the elimination of objects by taking the median is not perfect. Bright stars may subtend a distance on the data frames larger than the change in the pointing between exposures. When the median is taken, they do not disappear perfectly, but remain as bright patches on the median image. Therefore, in a small area around bright stars in our reduced data, the signal is slightly suppressed. We recognise this effect, but note that all the objects we go on to detect are sufficiently far from bright stars that this does not compromise our results.

An example section of a median image used in this process is shown in figure 3.3; it shows both the clearly defined charge-trapping sites and the remnant of a bright star.

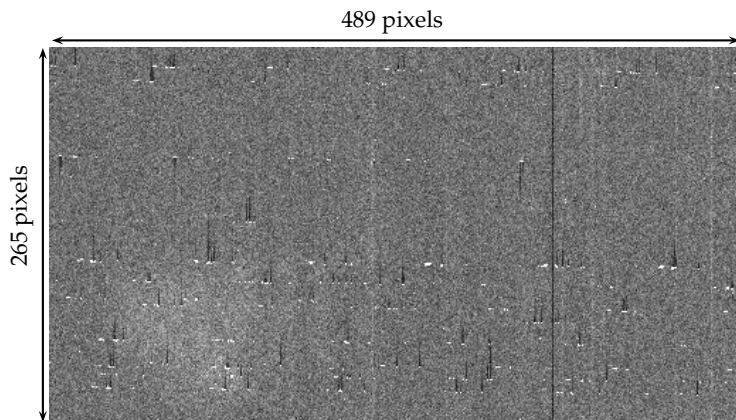


**Figure 3.3:** A close up section of a median through all our MRC B2158-206 data frames. Note the clearly visible charge-trapping defects. Almost all objects have been removed, the patch at lower left being the remains of a bright star.

### 3.2.1.2 Cropped image dimensions

After the alignment and cropping procedures outlined in section 3.1.3 were followed, each reduced image of the MRC B2158-206 field has pixel dimensions 1237 by 863, corresponding to 6'48" by 4'45".

### 3.2.1.3 Ghosts, night-sky rings and cosmic rays

A check for ghosts (section 2.1.4.3) was carried out by using SAOImage DS9 to blink back and forth between aligned frames, watching for objects which appear to change position. None were seen.

There was also no evidence of circular patterns on the image that might be attributed to night-sky rings (section 2.1.4.2).

Each reduced image consists of the median of four independent data frames as calculated by the IRAF routine cl.images.immatch.imcombine; in situations (such as this) with an even number of frames, this consists of taking the mean of the two central values. A cosmic ray strike produces a very intense signal in only one frame. By taking the median of all four, then, cosmic rays are eliminated.

**Table 3.1:** The seeing in our observations of MRC B2158-206. The seeing is reported as the mean full width at half maximum of an arbitrary selection of five star-like objects across the field; the uncertainties are the standard deviation of the distribution.

Image	FWHM (pixels)	FWHM (arcsec)
z173	$4.75 \pm 0.33$	$1.57 \pm 0.11$
z182	$4.92 \pm 0.17$	$1.62 \pm 0.06$
z191	$4.87 \pm 0.16$	$1.61 \pm 0.05$
z200	$4.60 \pm 0.15$	$1.52 \pm 0.05$
z209	$5.02 \pm 0.44$	$1.66 \pm 0.15$

### 3.2.1.4 Seeing

The overall seeing in each image was measured by choosing a random selection of five star-like objects across the image and fitting a Gaussian to the flux profile of each object using the IRAF task noao.digiphot.apphot.fitspsf. The results are shown in table 3.1.

### 3.2.1.5 Optical axis

As described in section 2.1.4.1, the wavelength of peak transmission of the etalon varies quadratically with distance from the optical axis. In order, therefore, to establish the observed wavelength at a given point on the image, it is essential to know what the position of the axis within that image is. This is doubly significant in the case of objects such as those in the field of MRC B2158-206, which are observed towards the extremities of the blocking filter (figure 2.13(b)): not only the wavelength but also the photometric calibration varies with distance from the axis!

For a given configuration of the Taurus-2 system, the axis falls on the same location in the data frame. This location is, in general, recorded: establishing the position of the axis is performed on an ad-hoc basis using the properties of the recorded images. For this field, the most convenient image characteristic to use is the background signal.

The sky background is transmitted through the etalon in the same way as any other signal. Therefore, in the case of images which fall at the long wavelength limit of the blocking filter, the background will be lowest on the optical axis, increasing in the shorter

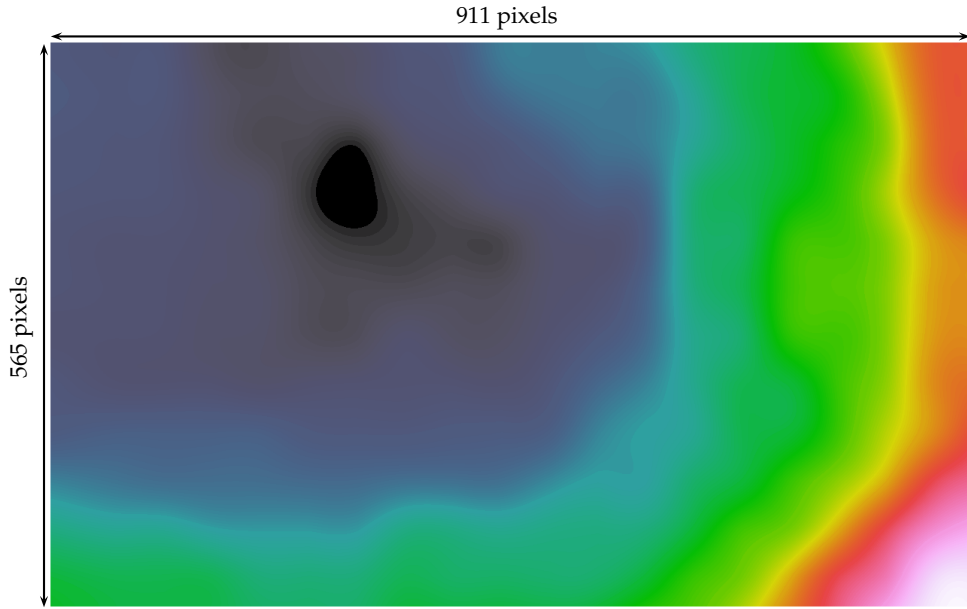


**Figure 3.4:** Locating the optical axis of MRC B2158-206. The plot shows a background map with SExtractor (section 3.1.6); the colour is proportional to the background signal at each pixel, ranging from black (lowest) to white (highest). On the optical axis transmission is lowest, resulting in the black spot which identifies the axis.

wavelength parts of the image.

In the case of MRC B2158-206, there are two images which are severely affected by the blocking filter: Z200 and Z209. We work, therefore, from an average of these two frames. We fit the background in the averaged frame using SExtractor, as described in section 3.1.6: it is immediately possible to observe the position of the optical axis by simply examining the background image using a visualization tool such as SAOImage DS9—see, for example, figure 3.4. We confirm that the estimated position of the axis does not shift significantly from image to image by identifying it in each field.

In order to precisely determine the location of the axis, we took the reciprocal of the background image and used the IRAF task `noao.digiphot.apphot.qphot` to fit the peak. This uses a marginal centroid algorithm (appendix A) to determine the precise pixel position of the peak: it was found to lie at a pixel position of 422, 622. The inverse signal in the surrounding pixels as determined by IRAF is shown in figure 3.5.

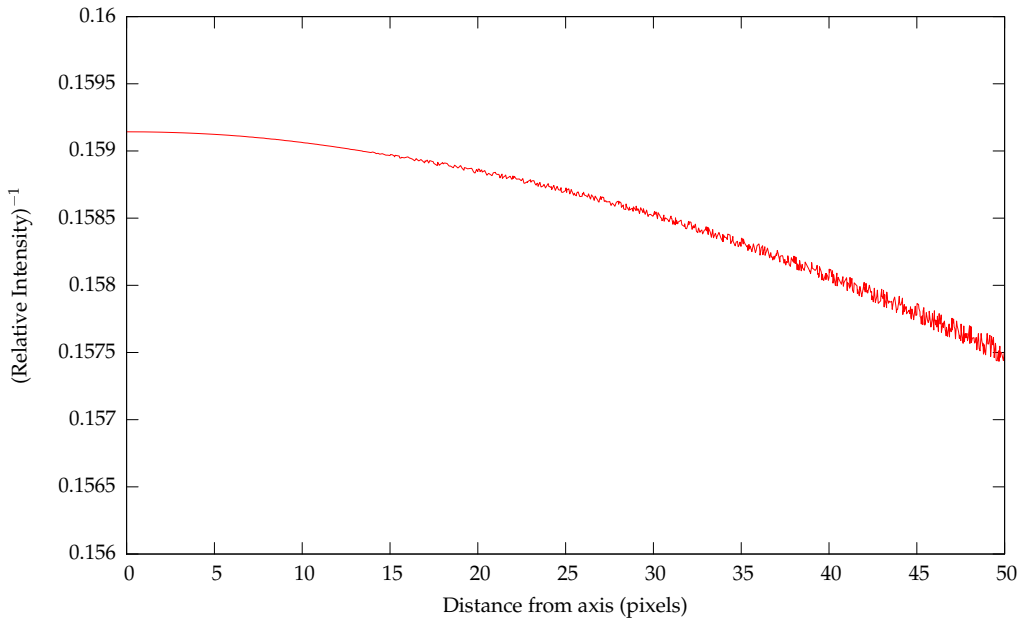


**Figure 3.5:** The variation of intensity (in uncalibrated units) in a reciprocal background image with distance from the position of the optical axis in the MRC B2158-206 field. The curve is smoothed by averaging the values of reciprocal intensity at given pixel distance.

Note that the above analysis does not account for the shifting of the telescope pointing between observations, used to identify ghosts. This causes the position of the axis in the combined images to be slightly ‘smeared’ out, and hence introduces an error to the wavelength transmitted at a given position.

The dithering takes place on scales of the order 10 pixels. Due to the quadratic nature of the wavelength dependence, the divergence in wavelengths will be greatest at the furthest point from the axis; in this field, that is at a pixel coordinate of 1237, 0: a ten pixel inter-frame discrepancy in the position of the axis corresponds to a maximum wavelength divergence of 0.4 Å between the frames here. This is sufficiently small as to not compromise our results.

### 3.2.1.6 Wavelength calibration

Wavelength calibration was performed using the ‘sausage cube’ method described in section 3.1.5. In this case, two calibration lamps were used: xenon and copper-helium. They

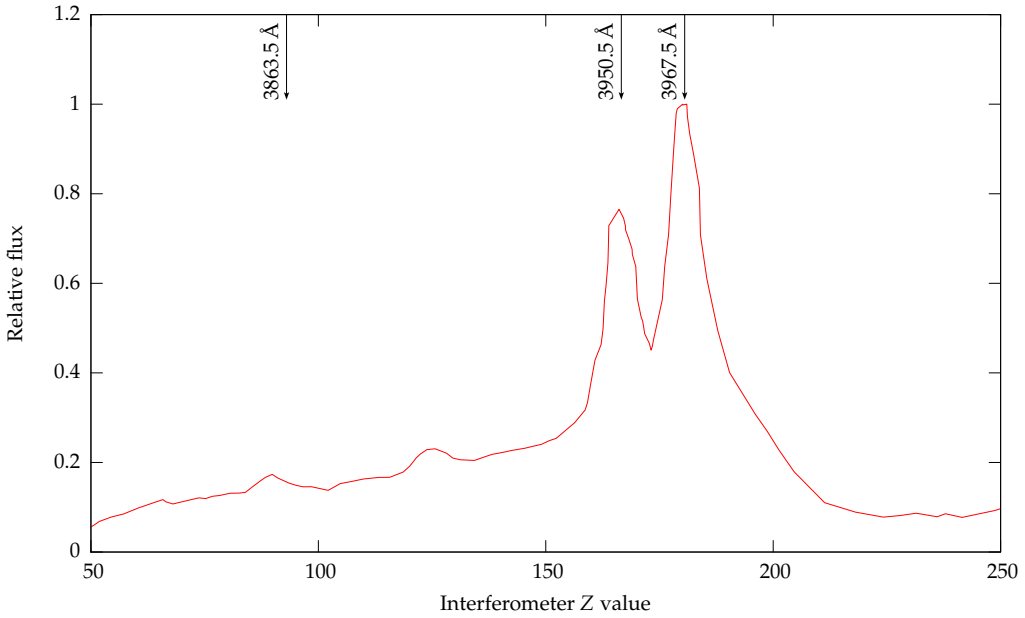


**Figure 3.6:** MRC B2158-206 sausage cube based on a xenon lamp. The spectral lines used for wavelength calibration have been marked.

were both sampled at the rate of one measurement for every three steps in  $Z$ . Figure 3.6 shows the three lines used in the xenon lamp; a single line at 3888.65 Å was used from the copper-helium spectrum.

We use the IRAF task cl.utilities.polyfit to fit a straight line through the  $Z-\lambda$  pairs reached in this way using a linear regression analysis. The best fit is found to be

$$\lambda = 3767.41 + 1.108 \times Z. \quad (3.16)$$

This corresponds to observed on-axis wavelengths of 3959.1 Å, 3969.1 Å, 3979.0 Å, 3989.0 Å and 3999.0 Å with increasing  $Z$  in our data frames.

### 3.2.1.7 Aperture size

The most appropriate aperture size for each image is chosen by optimising the signal to noise ratio  $C/\sigma$ , as described in section 3.1.8.4. The relevant parameters vary from frame to frame: they are listed in table 3.2.

The signal to noise ratio was calculated based on a range of aperture sizes and ob-

**Table 3.2:** Optimal photometric apertures for MRC B2158-206. The seeing is taken from table 3.1; the RMS noise per pixel is the average measured by SExtractor across the whole image. The optimal aperture diameter is chosen based on figure 3.7, and the magnitude correction reflects the fraction of flux lost due to falling outside the aperture.

Etalon Z	Number of exposures	Seeing FWHM (pixels)	RMS noise per pixel	Aperture diameter (pixels/”)	Magnitude correction
173	4	4.75	4.92981	6/1.98	0.44
182	4	4.92	4.81124	6/1.98	0.48
191	4	4.87	4.61603	6/1.98	0.47
200	4	4.60	4.35852	6/1.98	0.40
209	4	5.02	4.32911	6/1.98	0.51

ject brightnesses (parameterised as the total number of counts received from the object). The results for each frame are shown in figure 3.7. Based on these results, an aperture of diameter six pixels was chosen as most appropriate in each frame.

The aperture diameter is, in each case, slightly bigger than the full width at half maximum of the point spread function of the objects. Therefore, a fraction of the flux falls outside the aperture and is lost. The proportion of the flux collected is given by  $C/C_t$ , where  $C$  is the number of counts collected and  $C_t$  is the total number of counts from the object over the whole image. This may be calculated using equations 3.14 and 3.15, and then converted to a correction which should be applied to the magnitude measured in the aperture. This correction is tabulated in table 3.2.

### 3.2.1.8 Photometric calibration

Photometric calibration was carried out following the general principles laid down in section 3.1.7. The standard star used was EG 21, observed on the same night and with the same instrumental settings as the quasar field. Calibration data was taken from Hamuy et al. (1992): the relevant part of the stellar spectrum is shown in figure 3.8. The zero-points obtained in this way are shown in table 3.3.

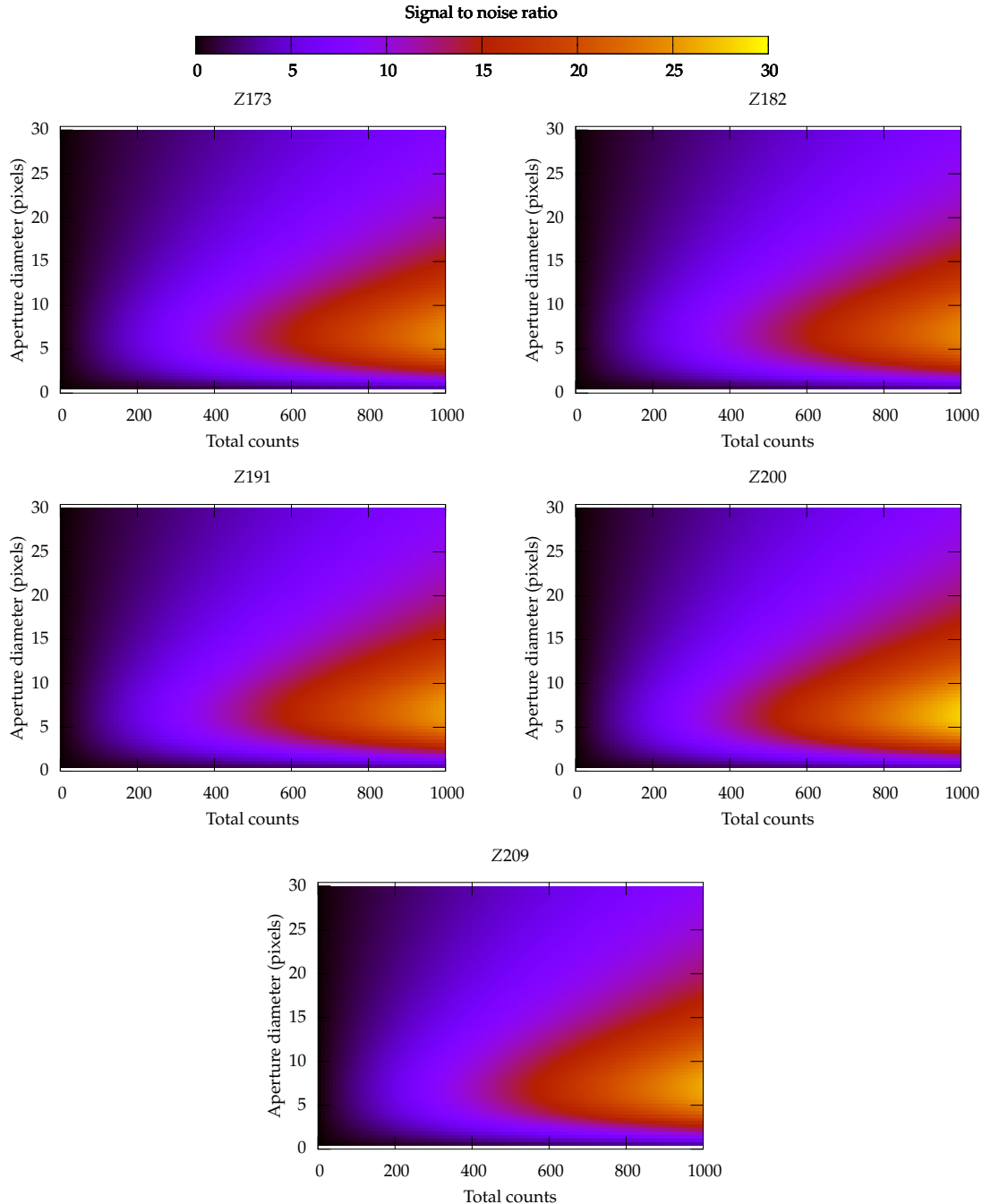


**Figure 3.7:** Variation of signal to noise ratio with aperture size and number of counts in objects in the various MRC B2158-206 images.

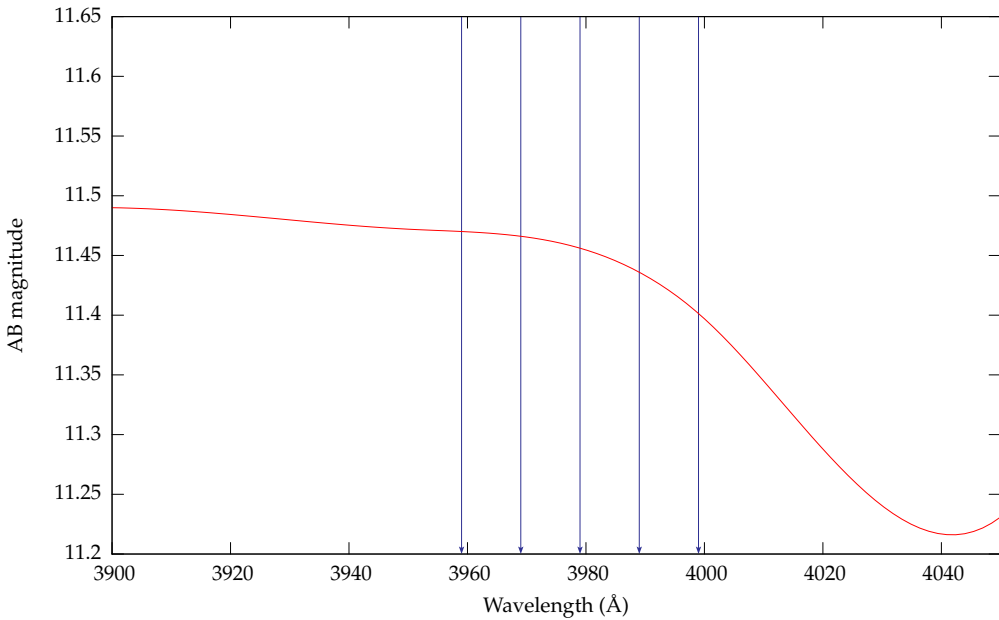


**Figure 3.8:** A section of the spectrum of the standard star EG 21, based on data from Hamuy et al. (1992). The vertical lines indicate the on-axis wavelengths of our observations.

### 3.2.1.9 The effects of the blocking filter on photometry

Section 3.2.1.8 describes photometric calibration of this field. However, it is necessary to consider how this might be influenced by the order-blocking filter.

We have seen that the observed wavelength varies quadratically with distance from the optical axis. In those frames (notably Z200 and Z209) which lie towards the limits of the filter, the filter transmission therefore varies significantly across the field.

Assuming our calibration is accurate for an object which lies on the axis (an issue we will return to shortly), it *overestimates* the magnitude of an object away from the axis: for objects of the same flux incident on the filter, more counts are received from those objects which lie off-axis.

For a given position on the field, the wavelength of transmission may be calculated from equation 2.26. This is then combined with the known transmission profile of the B1 filter (figure 2.4) to calculate a correction factor to the AB magnitude of each object observed.

**Table 3.3:** Magnitude zero-points (see section 3.1.7) for observations of MRC B2158-206. Note the systematic decrease in the zero-point with increasing Z: this is due to the throughput of the blocking filter dropping (see figure 2.13 (page 54)).

Etalon Z	Magnitude zero-point
173	27.8172
182	27.6537
191	27.2554
200	26.5030
209	25.7538

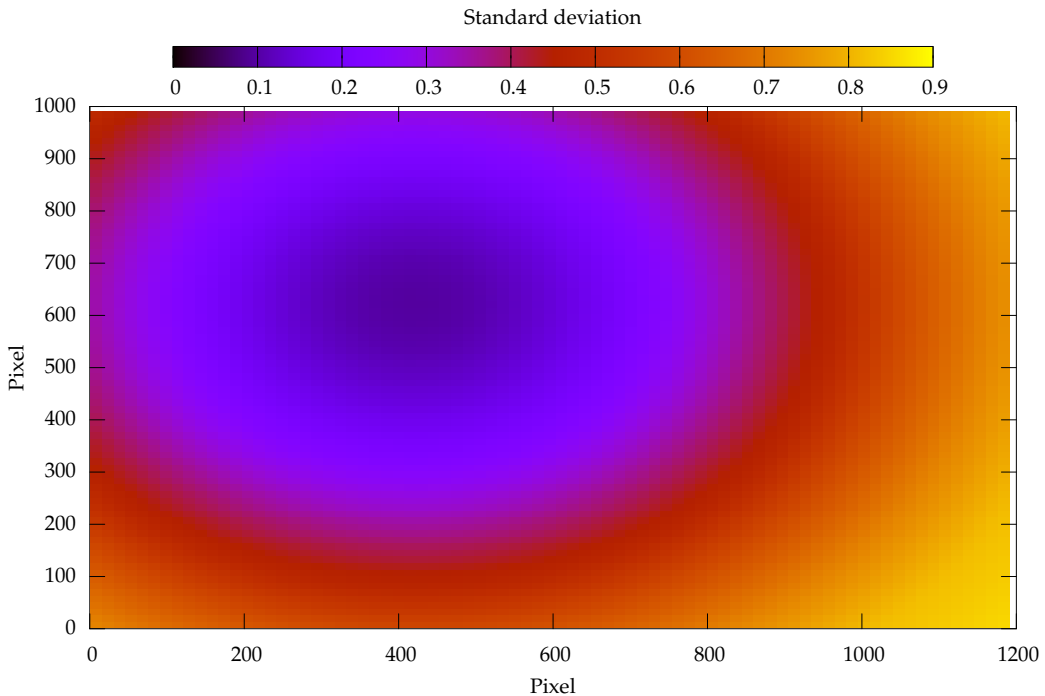


**Figure 3.9:** Determining the offset of the standard star relative to the optical axis in MRC B2158-206. The standard deviation is that of the magnitudes of a flat-spectrum source observed in each frame, if the standard was observed at a position corresponding to the given pixel coordinates. The axis lies at the position 422,622.

The above discussion makes the assumption that the correct calibration is obtained for objects which lie on the axis. This, in turn, assumes that the standard star was observed on the axis—an assumption it is necessary to verify. The short exposure time used when observing the standard renders the background faint and hard to fit; the method described in section 3.2.1.5 is therefore inadequate.

Consider a bright foreground object in the field of the quasar. To a good approximation, we would expect it to have a flat spectrum over the wavelength range we are considering. Considering the spectra of a variety of these objects, then, can be used to estimate the consistency of our calibration.

The transmission of the B1 filter over the range covered by the lower wavelength observations is effectively constant: the position of the standard relative to the axis here therefore has little effect. However, if the standard was observed off-axis in a high Z frame, we would *underestimate* the magnitude of objects observed on-axis. Foreground objects would therefore not have flat spectra, but tend to appear dimmer in frames with higher Z.

This procedure is illustrated in figure 3.9. The optical axis lies at a position of 422,622; for each pixel in the image, we apply a photometry correction to the flat spectrum objects on the assumption that the standard was observed at that pixel. The position at which the standard was observed, then, is at the point where the spectra are flat—that is, the standard deviation of the magnitudes is at a minimum. As can be seen from the figure, this coincides with the optical axis.

In summary, then, the standard was observed on-axis; no correction need be applied to compensate for its position.

### 3.2.1.10 Etalon pass-band width

Equation 2.14 (page 30) tells us the full width at half maximum of the etalon transmission bands ( $\lambda_{1/2}$ ) as a function of the free spectral range (in units of Å) and the etalon finesse. At 4000 Å, the free spectral range is recorded in the TTF documentation (Hawthorn and Kedziora-Chudczer, 2002) as 205 in units of Z; given the wavelength calibration of equation 3.16, this is equivalent to 227 Å, and hence  $\lambda_{1/2}$  is 7.5 Å.

### 3.2.2 MRC B1256-243

The data for MRC B1256-243 follows a very similar pattern to that of MRC B2158-206: the most notable difference is that only half the number of exposures were taken. The data reduction techniques used are therefore very similar to those outlined in section 3.2.1.

#### 3.2.2.1 Charge trapping

As described in section 3.2.1.1, all the raw data frames were combined by taking the median to produce an image which clearly identified the trapping sites. They were then eliminated in the same way as in the MRC B2158-206 observations.

#### 3.2.2.2 Cropped image dimensions

After alignment and cropping, each image of MRC B1256-243 had pixel dimensions of 1276 by 889, corresponding to 7'11" by 4'53".

#### 3.2.2.3 Ghosts, night-sky rings and cosmic rays

A check for ghosts (section 2.1.4.3) was carried out by using SAOImage DS9 to blink back and forth between aligned frames, watching for objects which appear to change position. None were seen.

There was also no evidence of circular patterns on the image that might be attributed to night-sky rings (section 2.1.4.2).

Each image of MRC B1256-243 consists of only two data frames. This means that the median is equivalent to the mean and hence does not effectively remove cosmic rays. In order to exclude cosmic rays, the lower of the two values at any given point was chosen. Statistically, this procedure is incorrect: a better approach would have been to mask out the affected pixels only (appendix B).

**Table 3.4:** The seeing in our observations of MRC B1256-243. The seeing is reported as the mean full width at half maximum of an arbitrary selection of five objects across the field; the uncertainties are the standard deviation of the distribution.

Image	FWHM (pixels)	FWHM (arcsec)
z170	$4.43 \pm 0.60$	$1.46 \pm 0.20$
z179	$4.91 \pm 0.38$	$1.62 \pm 0.13$
z188	$4.68 \pm 0.62$	$1.54 \pm 0.21$

### 3.2.2.4 Seeing

As usual, seeing was measured by fitting Gaussians to a selection of five objects across the field by using IRAF’s noao.digiphot.apphot.fitsf and measuring their full pixel widths at half maximum. The results are shown in table 3.4.

### 3.2.2.5 Optical axis

The optical axis for MRC B1256-243 is determined in the same way (observing the variation in the background) as for MRC B2158-206 (section 3.2.1.5). Note, however, that only one of the Z-settings (Z188) in our MRC B1256-243 was seriously affected by filter transmission, and there are only two exposures at that setting due to time constraints.

A fit to the reciprocal of the background signal in the average of these two exposures is shown in figure 3.10: the optical axis was found to be at a pixel position of 487, 570. Effects due to the change in telescope pointing between observations are of the same sub-0.5 Å order as reported for MRC B2158-206.

### 3.2.2.6 Wavelength calibration

Wavelength calibration was performed in the same way, and with the same lamps and spectral lines, as described in section 3.2.1.6. The ‘sausage cube’ measurement was, however, repeated between observations to compensate for any variation in the system; an updated wavelength calibration of

$$\lambda = 3769.37 + 1.105 \times Z \quad (3.17)$$

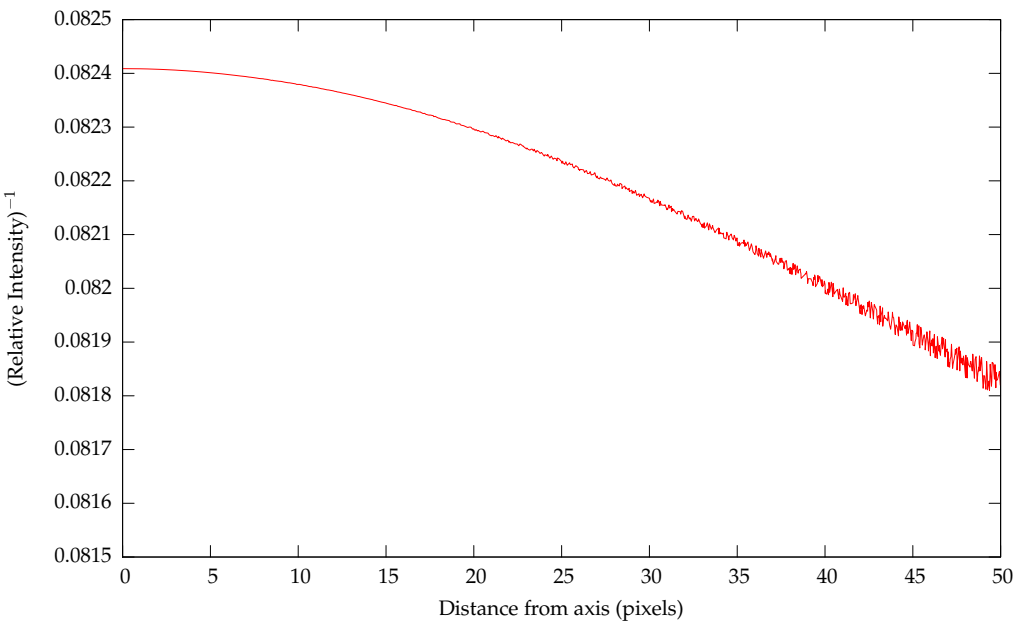


**Figure 3.10:** The variation of intensity (in uncalibrated units) in a reciprocal background image with distance from the position of the optical axis in the MRC B1256-243 field; the equivalent of figure 3.5 for this field.

was arrived at. As might be expected, this is very close, but not identical, to the calibration obtained on the same evening for observations of MRC B2158-206. The corresponding wavelengths for our observations are 3957.2 Å, 3967.1 Å and 3977.1 Å.

### 3.2.2.7 Aperture size

The optimal aperture size was chosen in the same way as for MRC B2158-206 (section 3.2.1.7). Full details are shown in table 3.5 and figure 3.11.

### 3.2.2.8 Photometric calibration

Photometric calibration was carried out following the general principles laid down in section 3.1.7. The standard star used was EG 274, observed on the same night and with the same instrumental settings as the quasar field. Calibration data was taken from Hamuy et al. (1992): the relevant part of the stellar spectrum is shown in figure 3.12. The zero points obtained in this way are shown in table 3.6.

**Table 3.5:** Optimal photometric apertures for MRC B1256-243. The seeing is taken from table 3.4; the RMS noise per pixel is the average measured by SExtractor across the whole image. The optimal aperture radius is chosen based on figure 3.11, and the magnitude correction reflects the fraction of flux lost due to falling outside the aperture.

Etalon Z	Number of exposures	Seeing FWHM (pixels)	RMS noise per pixel	Aperture diameter (pixels/”)	Magnitude correction
170	2	4.43	6.88762	6/1.98	0.36
179	2	4.91	6.91791	6/1.98	0.48
188	2	4.68	6.51542	6/1.98	0.42

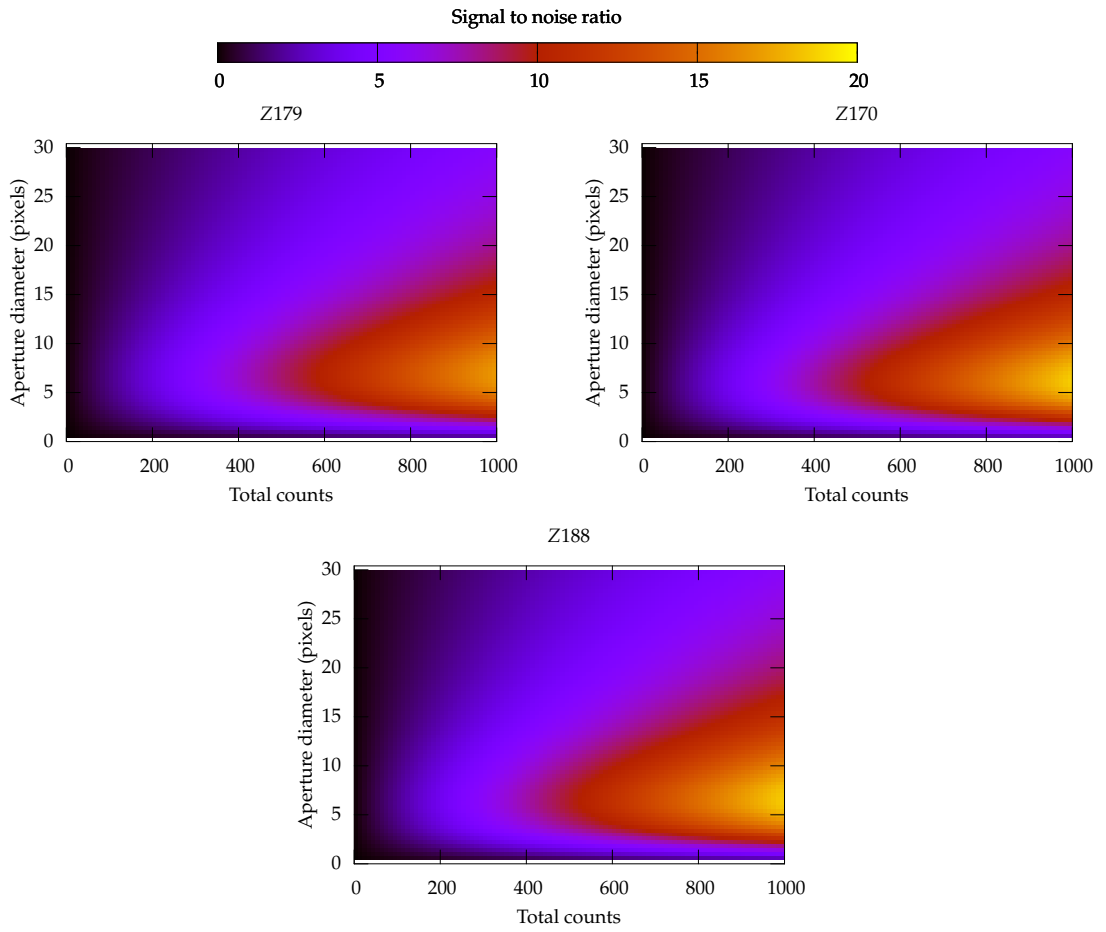


**Figure 3.11:** Variation of signal to noise ratio with aperture size and number of counts in objects in the various MRC B1256-243 images.

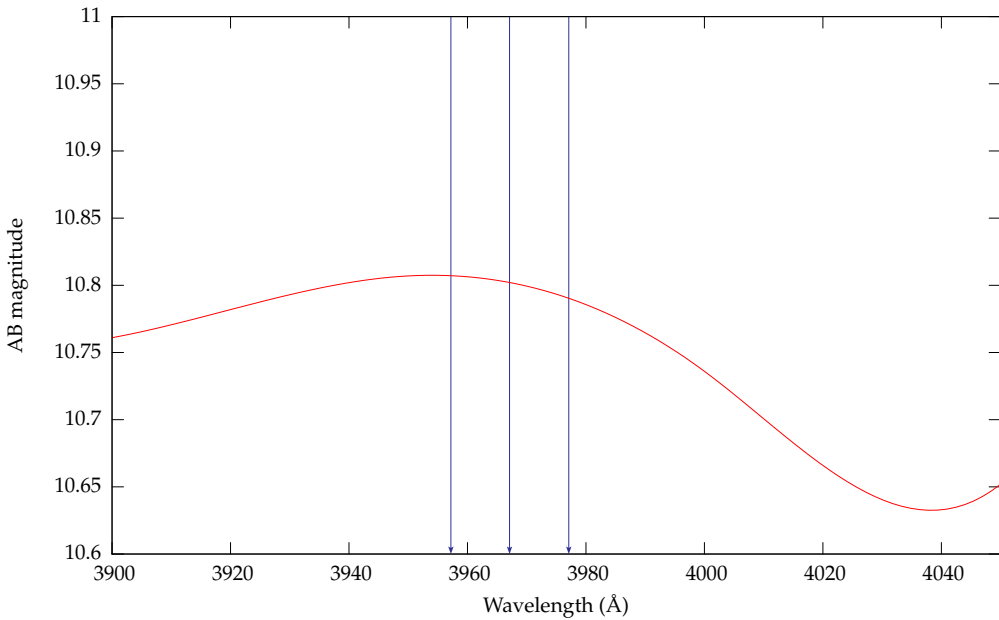


**Figure 3.12:** A section of the spectrum of the standard star EG 274, based on data from Hamuy et al. (1992).

**Table 3.6:** Zero-point magnitudes (see section 3.1.7) for observations of the field MRC B1256-243.

Etalon Z	Magnitude zero-point
170	27.2039
179	27.0975
188	26.7443

### 3.2.2.9 The effects of the blocking filter on photometry

The same considerations surround the effects of the blocking-filter transmission as discussed for MRC B2158-206 in section 3.2.1.9. Given that the position of the axis has been established, it is again possible to calculate a magnitude correction for each object which lies off axis using the same method as previously.

Furthermore, we show that the standard was observed on axis in the same way as before. Frames Z170 and Z179 are sufficiently well exposed through the blocking filter that the position of the axis makes relatively little difference to their photometry. Therefore, we consider the difference between them and frame Z188, varying the position of the

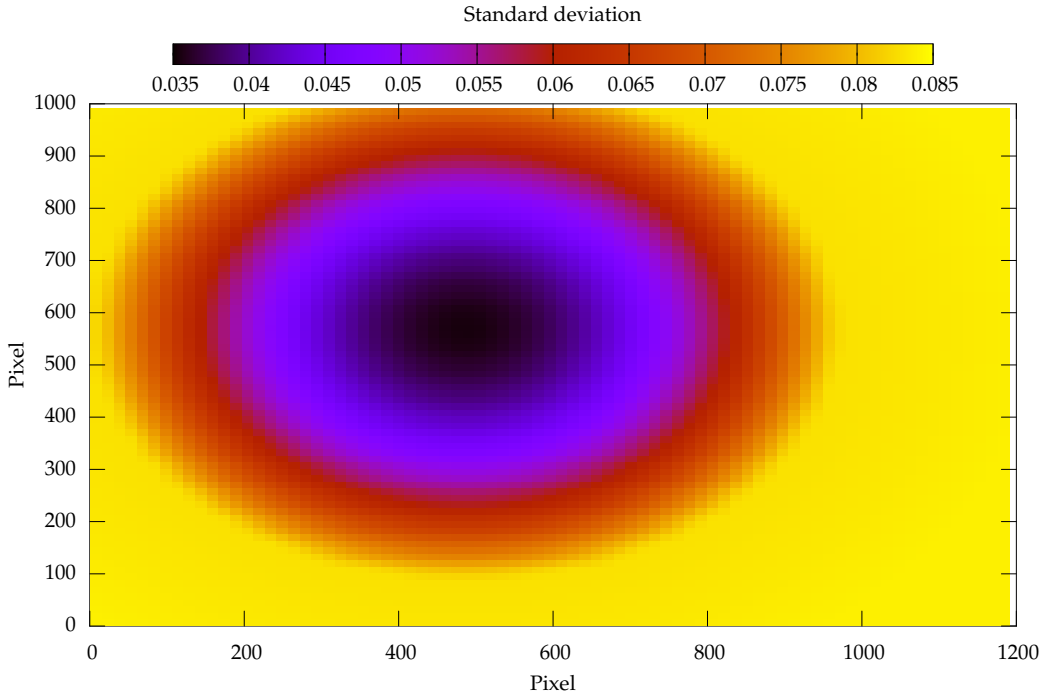


**Figure 3.13:** Determining the offset of the standard star relative to the optical axis in MRC B1256-243. The standard deviation is that of the magnitudes of a flat-spectrum source observed in each frame, if the standard was observed at a position corresponding to the given pixel coordinates.

standard so as to make the calibrated magnitudes recorded for bright stars in the quasar field consistent from image to image. The results are shown in figure 3.13. This is broadly equivalent to figure 3.13; note, though, that the standard deviation is lower. This is because the difference between the frames is considerably smaller: Z170 and Z179 record effectively the same transmission, while even Z188 is less suppressed than, say, Z209 was in the case of MRC B2158-206.

Once again, we see that the most consistent results are obtained when we assume the standard was observed on-axis.

#### 3.2.2.10 Etalon pass-band width

Using exactly the same argument as section 3.2.1.10, the width of the etalon pass-band in this field is 7.5 Å.

### 3.2.3 BR B0019-1522

Since the BR B0019-1522 data were retrieved from the AAT archive, they were not taken under exactly the same conditions as our observations. The data reduction procedures therefore differ in some details.

#### 3.2.3.1 Charge trapping

Unlike our observations, charge-shuffling was not used on the CCD when these data were taken. There are, therefore, no charge-trapping artifacts in evidence on the images.

#### 3.2.3.2 Cropped image dimensions

After alignment and cropping, each reduced image of the BR B0019-1522 field has pixel dimensions 1506 by 676, corresponding to 9'17" by 4'10".

#### 3.2.3.3 Ghosts, night-sky rings and cosmic rays

There was no evidence of the characteristic circular pattern of night-sky rings on the images.

For each etalon Z setting, eight different images were available. Combining them all by taking the median simultaneously eliminates cosmic rays and increases the signal-to-noise ratio.

Data frames of the field were taken at two slightly different pointings. All the data frames were aligned using IRAF, then the frames from each pointing were combined into two different images by taking the median. When one of these median images is subtracted from the other, all the real objects cancel out and disappear, but ghosts are clearly visible (for a more comprehensive discussion, see section 2.1.4.3). Using this method, one ghost was identified in the field. Its position was recorded and it was eliminated from further analysis.

**Table 3.7:** The seeing in our observations of BR B0019-1522. The seeing is reported as the mean full width at half maximum of an arbitrary selection of five star-like objects across the field; the uncertainties are the standard deviation of the distribution.

Image	FWHM (pixels)	FWHM (arcsec)
Z431	$4.14 \pm 0.36$	$1.53 \pm 0.13$
Z451	$4.29 \pm 0.51$	$1.56 \pm 0.19$
Z471	$3.89 \pm 0.27$	$1.44 \pm 0.10$

### 3.2.3.4 Seeing

The seeing was measured as in the previous fields (sections 3.2.1.4 and 3.2.2.4). The results are shown in table 3.7.

### 3.2.3.5 Optical axis

The optical axis in the field of BR B0019-1522 cannot be discovered in the same way as in our  $z \sim 2.2$  fields. This is because the wavelengths covered by these fields lie well within the transmission range of the order blocking filter: there is not any significant variation.

Another possibility for finding the axis is to search for diametric ghosts in the field. These are discussed in section 2.1.4.3. However, in this field, only one ghost image can be identified: this is not sufficient to uniquely locate the axis.

There remains a further way to locate the optical axis. As discussed in section 2.1.4.2, the variation of the wavelength of peak transmission with radial distance from the optical axis produces a series of (almost perfectly) circular ‘rings’ in the image due to the imaging of atmospheric phenomena. The axis, therefore, lies at the centre of these rings: if we can identify and fit them, we find the location of the optical axis.

Unfortunately, there are no such rings to be observed in the field of BR 0019-1522! However, on the same night and with the same settings as these observations, some other fields were observed with exactly the same settings. In particular, PKS B0511-220, a  $z = 1.3$  AGN (Stickel et al., 1989), was observed immediately following our observations: the optical axis should fall in the same place, and it *does* display skyline effects—as shown in

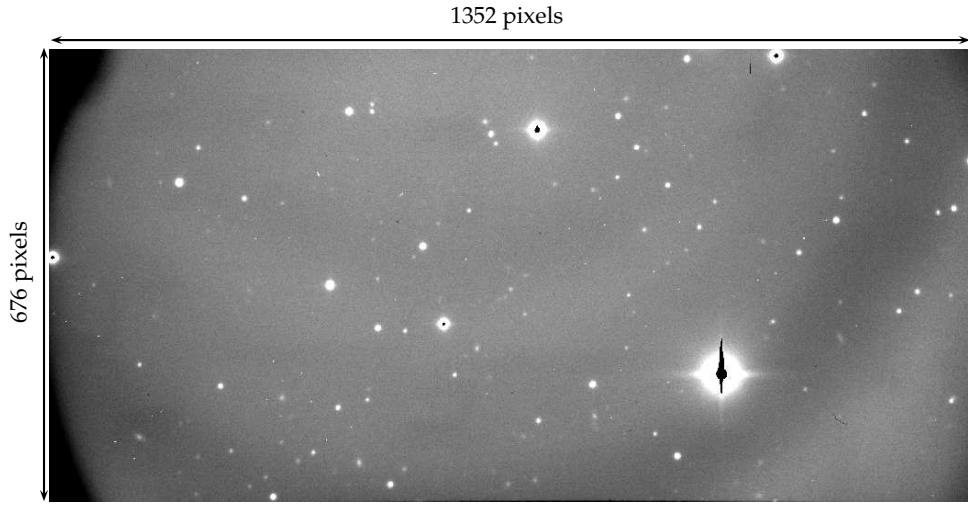


**Figure 3.14:** An unreduced image of PKS B0511-220. Skylines are visible both as the broad, dark rings across the whole image, and also as faint narrow fringes around the top centre.

figure 3.14.

The problem, then, is how best to find the centre of these rings. It is, of course, easy to read X-Y positions for points which lie on a given ring directly off the image. A least-squares algorithm was then used to locate the centre, as follows.

An initial estimate of the position of the centre and the radius of the circle is made:  $x_0, y_0, R_0$ . For each of the observed points  $x, y$ , the difference between the estimated radius and the distance of the point from the estimated centre is calculated:

$$\delta = R_0 - \sqrt{(x - x_0)^2 + (y - y_0)^2}. \quad (3.18)$$

A the error on our estimate is then computed as the sum over all measured points:

$$\sigma = \left( \sum_{i=0}^n \delta_i^2 \right)^{1/2} \quad (3.19)$$

The aim is then to minimise  $\sigma$ . An algorithm optimised for speed would then intelligently update the values of  $x_0, y_0$  and  $R_0$  to this effect. However, in this case we can easily see where the location of the axis is to within a relatively small range. Therefore, for simplicity, we simply iterate over the whole possible range of locations and radii, calculating  $\sigma$  for

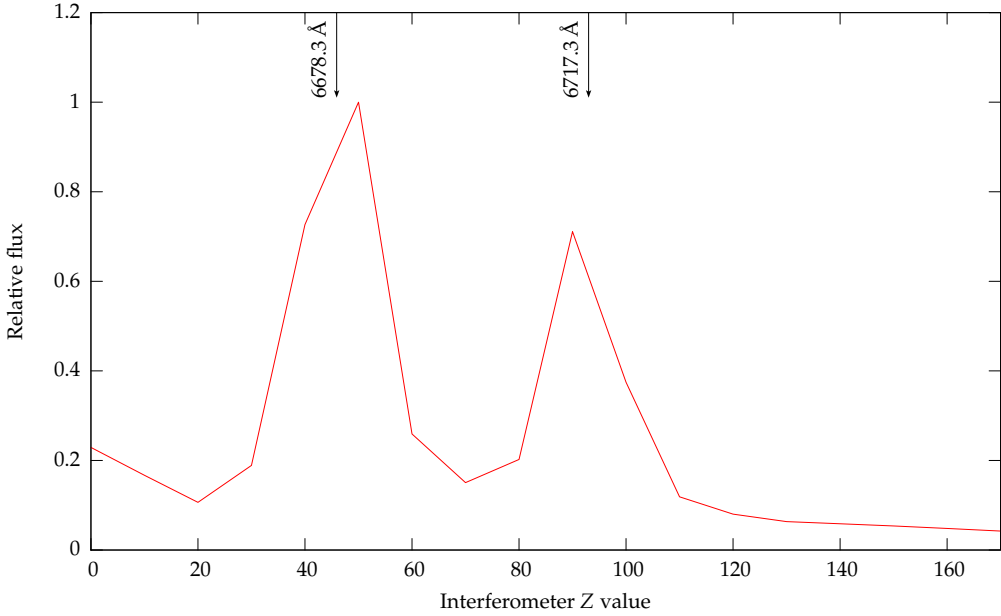


**Figure 3.15:** BR B0019-1522 sausage cube based on a neon arc. The spectral lines used for wavelength calibration have been labelled.

each one, and then choose as our best estimate the values which correspond to the lowest  $\sigma$ .

Effects due to the change in telescope pointing between observations are of the same sub-0.5 Å order as reported for MRC B2158-206.

Following this method, we arrive at a pixel position of 665, 806 for the optical axis in our BR B0019-1522 images. Note that this falls slightly outside the imaged area.

### 3.2.3.6 Wavelength calibration

Broadly, wavelength calibration for BR B0019-1522 proceeded as outlined in section 3.1.5. However, there are some considerations which are unique to this field.

No wavelength calibration ('sausage cube') images were made on the same night as the observations of the quasar field. However, two nights earlier (4 November 1997) a sausage cube was taken at appropriate etalon settings and wavelength. This situation is not ideal; however, we know (section 3.1.5) that the interferometer calibration is relatively

stable—these data should enable us to make a reasonable wavelength estimate.

A neon arc lamp was used in the calibration. the data available, however, were taken at a low resolution: only 18 exposures are available, covering etalon Z values of 0 to 170 in steps of 10. This obviously limits the precision of the calibration we can perform. Figure 3.15 shows the extracted spectrum. The two spectral lines visible can be identified by comparison with the documented spectrum for the lamp. Fitting Lorentzians to the observed spectrum enables us to match the lines to Z value, as shown in table 3.8. With only two low-resolution lines, our fitting is necessarily limited, but we arrive at the expression

$$\lambda = 6678.3 + 0.82 \times (Z - 45.9) \quad (3.20)$$

for the observed wavelength  $\lambda$  at given Z.

Our observations, however, were made at Z values 431, 451 and 471, which do not lie within the range of this sausage cube. We know that the etalon transmission is periodic over a free spectral range. Furthermore, equation 2.13 shows us that the free spectral range in terms of the plate spacing is directly proportional to the wavelength. Measurements of the free spectral range at given wavelengths are available in the TTF documentation (Hawthorn and Kedziora-Chudczer, 2002), which, for example, quotes it as 340 Z units at H $\alpha$  (6560 Å), and it can also be read directly from our own results, for example in figure 3.2. For our measurements at around 6700 Å, we therefore arrive at a free spectral range of 347 Z. Our sausage cube observations should, therefore, be repeated over the Z-range 347–517; taking this into account, we modify equation 3.20 to become

$$\lambda = 6678.3 + 0.82 \times (Z - 392.9). \quad (3.21)$$

With this calibration, the three different Z settings with which BR B0019-1522 was observed—431, 451 and 471—correspond to on-axis wavelengths of 6709.5, 6725.9 and 6742.3 Å respectively.

### 3.2.3.7 Aperture size

The optimal aperture size was chosen in the same way as for MRC B2158-206 (section 3.2.1.7). Full details are shown in table 3.9 and figure 3.16.

**Table 3.8:** Wavelength calibration data for BR B0019-1522.

Wavelength (Å)	Etalon Z
6678.3	45.9
6717.0	93.0

**Table 3.9:** Optimal photometric apertures for BR B0019-1522. The seeing is taken from 3.7; the RMS noise per pixel is the average measured by SExtractor across the whole image. The optimal aperture radius is chosen based on figure 3.16, and the magnitude correction reflects the fraction of flux lost due to falling outside the aperture.

Etalon Z	Number of exposures	Seeing FWHM (pixels)	RMS noise per pixel	Aperture diameter (pixels/”)	Magnitude correction
431	8	4.14	3.27863	6/2.22	0.29
451	8	4.29	3.30348	6/2.22	0.33
471	8	3.89	3.18101	6/2.22	0.24

### 3.2.3.8 Photometric calibration

Photometric calibration was carried out using the standard star HD 49798, observed with the same instrumental settings and on the same night as the quasar field. Data were taken from the online ESO standard star database; the relevant part of the stellar spectrum is shown in figure 3.17. The calculated zero-point offsets are listed in table 3.10.

### 3.2.3.9 The effects of the blocking filter on photometry

As seen in figure 2.14, the transmission of the R0 filter is effectively constant across the range of our observations. Its effect on our photometry is therefore negligible.

**Table 3.10:** Zero-point magnitude offsets (see section 3.1.7) for observations of BR B0019-1522.

Etalon Z	Magnitude zero-point
431	27.8857
451	27.7589
471	27.7270

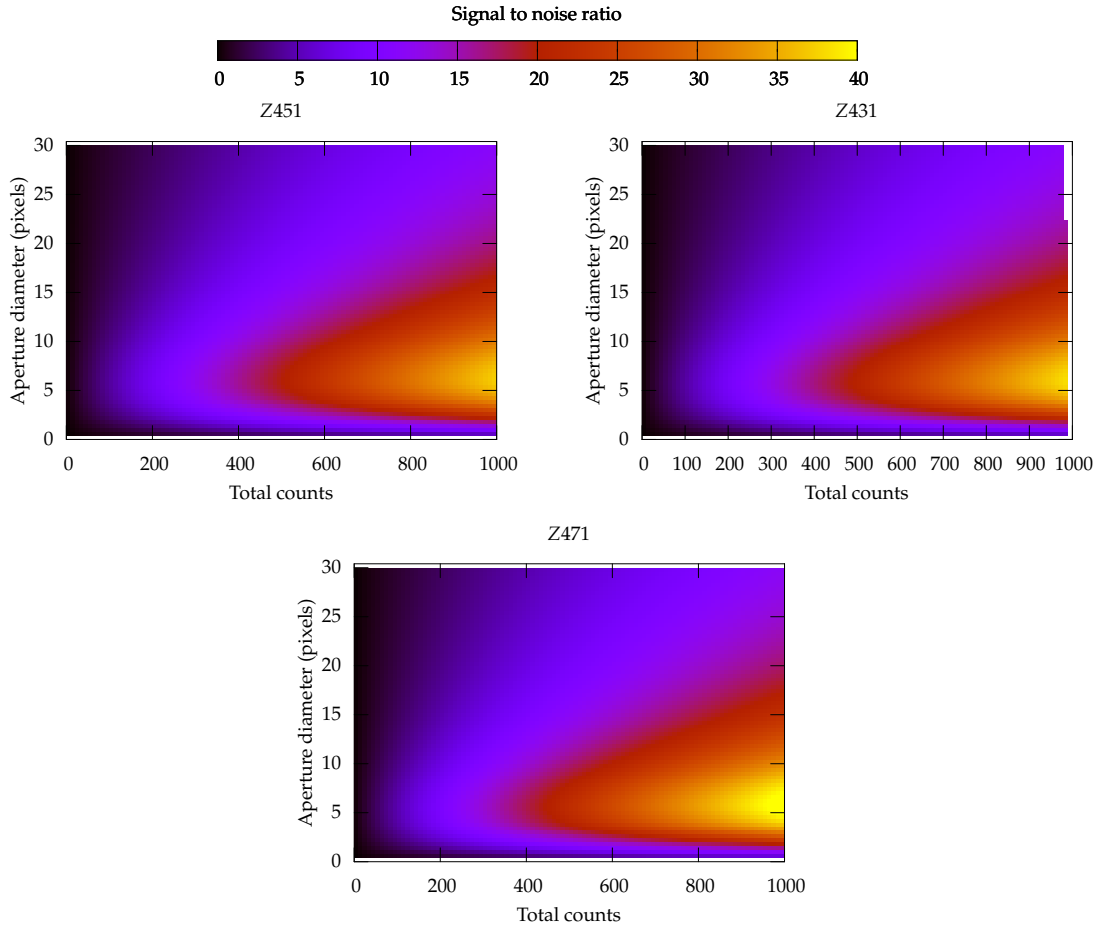


**Figure 3.16:** Variation of signal to noise ratio with aperture size and number of counts in object in the various BR B0019-1522 images.

### 3.2.3.10 Etalon pass-band width

In section 3.2.3.6, we established that the free spectral range of our observations is 347 Z; this is equivalent to 285 Å. Equation 2.14 therefore tells us that the etalon transmission bands have a full width at half maximum of 9.5 Å.

## 3.3 Summary

In the previous chapter, we described the observations available for the purposes of this thesis, including the selection of the objects under examination and how the data was collected. This chapter went on to present a detailed consideration of how the data was

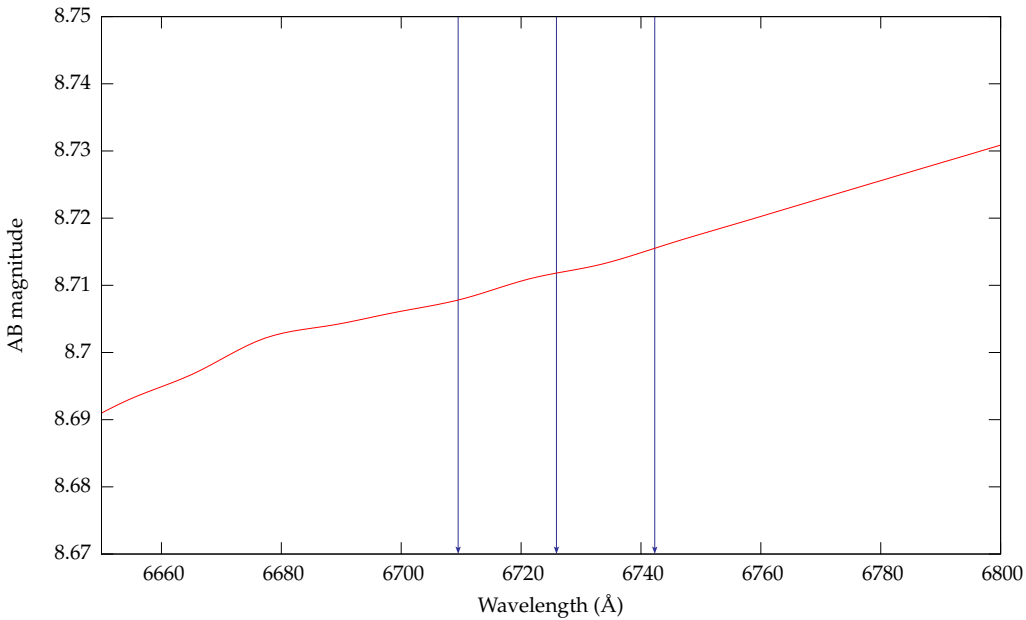


**Figure 3.17:** A section of the spectrum of the standard star HD 49798, taken from the ESO standard stars database.

reduced in order to extract the greatest possible amount of information from it.

The reduced data may now be searched for evidence of emission line galaxies, a process which is considered in chapter 5. First, though, the next chapter describes the use of simulated data to ascertain the limits of that analysis.

# Chapter 4

## *Simulations*

In order to best understand and most effectively analyse our observations, a thorough understanding of their characteristics is necessary. In this chapter, we build up a system of modelling what we might observe with the TTF given a known population of objects and use it to investigate the properties of our data.

### 4.1 *Aims of the simulation process*

We aim to build a series of simulated images: data with properties similar to our observations, but containing a known population of objects. By analysing these, we are able to gain a great deal of insight into the results of our observations. Throughout the following discussion we maintain the terminology established in section 3.1, distinguishing between an *image*, corresponding to the data observed through one etalon pass-band, and a *field*, or stack of images concentrated on a given area.

Specifically, our simulated data enables us to address the following questions:

- To what depth is each individual image complete?
- What are the most appropriate SExtractor parameters for extracting useful data from our images?
- To what depth is the whole field complete—and how does that depth vary over the field?
- To what extent can a photometry correction be applied to take account of losses within the observations, such as emission lines falling between etalon passbands?
- To what extent is our analysis prone to mis-identifying spurious, ‘noisy’ features within the image as candidate emission line galaxies?

## 4.2 Building simulated images

The aim of our simulation process is to produce data that mimic that recorded from the telescope as closely as possible. Broadly, therefore, we consider this in two ways: the background statistical properties of the simulated images should match those of the ‘genuine’ data, and the objects with which we populate the fields should imitate the properties of emission line galaxy observations as closely as possible. In this section, we explore how both these aims can be achieved.

The ultimate goal of this process is to produce an image which is very similar to our data—in terms of the image dimensions, background statistics, object properties, position of the optical axis, wavelength coverage—but which contains a known population of objects.

### 4.2.1 Background simulation

The aim here is to mimic two distinct, albeit intimately linked, aspects of the observations—the strength of background signal (that is, how many counts are recorded in parts of the image which do not contain objects) and the noise in the background (that is, the variation in the background signal from pixel to pixel).

A naive approach is to simply measure the average background and root-mean-square pixel to pixel variation in an image, and then produce a blank frame which matches those properties. SExtractor produces these measurements when it is run on an image, using the methods described in section 3.1.6: they can simply be read directly from the SExtractor output. However, this approach is flawed: it does not take account of the variation of these properties across the image. This is particularly an issue for those images which fall at the edge of the blocking filter, as described in section 2.3.

In order to ensure that we match the properties of the data, then, it is not possible to simply read average values over the whole image. Instead, we split each image into a grid 100 by 100 pixel blocks, and use SExtractor to measure the average background signal and associated noise in each block. For each of these blocks, we then generate an associated simulated block. The new block is first created with a constant background

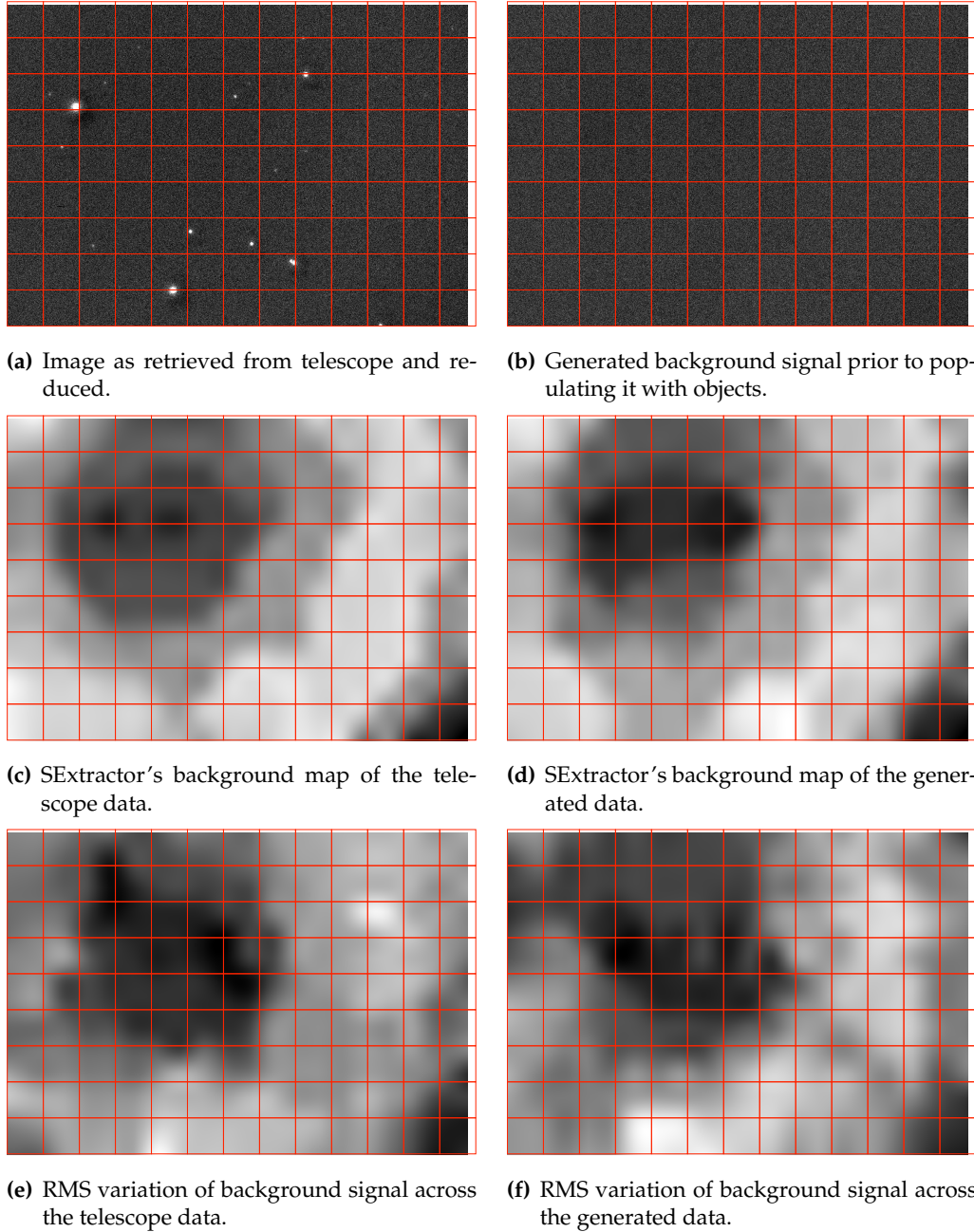


**Figure 4.1:** Building a simulated background. (a) shows the image we attempt to mimic; as described in the text, it is divided into 100 by 100 pixel sections. The resultant background is shown in (b), while (c)–(f) demonstrate demonstrate the close match between the images. Images are not calibrated or colour-matched, but, in each case, a light colour corresponds to a high value in a given pixel.

**Table 4.1:** A comparison of the statistics of the ‘real’ data, as collected from the telescope, and our attempt to generate a simulated image with similar properties. The ‘background’ and ‘RMS noise’ properties refer to the fits to the image produced by SExtractor (section 3.1.6); ‘data’ corresponds to the unprocessed input image and the final output. Values given are raw counts per pixel and are averaged across each image. The numbers given are for one generated field only; in practice, we create many hundreds using the same method.

Image	Property	Mean	Std. Dev.
Real	Data	9.11	12.59
	Background	9.73	0.45
	RMS noise	5.76	0.08
Generated	Data	9.69	5.78
	Background	9.71	0.42
	RMS noise	5.72	0.08

signal equal to the average in the real data. Gaussian random numbers of mean zero and standard deviation equal to the RMS noise we require are then added to each pixel in the block using the IRAF task noao.artdata.mknoise. Finally, we join all these generated blocks in the appropriate positions to produce an overall blank field; since its dimensions are necessarily a multiple of 100 pixels, it is trimmed to match our data images.

How successfully does this process work? An example is shown in figure 4.1; in this case, we generate a background designed to match that in our Z188 observation of MRC B1256-243 (as described in section 2.2.1.4). In figure 4.1(a), we show the genuine data; our eventual aim is to simulate this as accurately as possible. It is shown sub-divided into a grid of 100 by 100 pixel blocks, as described. The results of the simulation process, are shown in figure 4.1(b); this, of course, looks effectively like a constant grey field, with no bright objects.

We then use SExtractor to produce a map of the variation of the background (figures 4.1(c) & 4.1(d)) and noise (figures 4.1(e) & 4.1(f)) in the two images. These are, of course, not identical—the simulation process injects random noise!—but are clearly a close match. The statistical properties of each of these images are recorded in table 4.1; the simulated image is a very close match to the real data, with one exception: the actual observations have a higher standard deviation due to the presence of objects in the image.

### 4.2.2 Constructing objects

Having thus constructed a background image which closely mimics that which might be observed, it is next necessary to superimpose a series of objects on it which are designed to mimic the properties of those we might expect to observe. In this section, we first consider what those properties should be, and then move on to consider how we might emulate them.

#### 4.2.2.1 Object properties

There are several properties of emission line galaxies that we aim to emulate:

- Spatial distribution of flux on the image;
- Continuum flux;
- Emission line flux;
- Emission line wavelength;
- Emission line profile;
- Emission line width.

The first two items in this list are straightforward to address. High-redshift galaxies are not resolved in our observations: we simply observe a point spread function due to the instrument and the atmospheric seeing. Therefore, we model the spatial distribution of flux on the object as a Gaussian, with full width half maximum chosen to match the seeing in the image being simulated (as listed in tables 3.1, 3.4 and 3.7).

Le Delliou et al. (2006) modelled the properties of Lyman  $\alpha$  emitters at a variety of redshifts using a semi-analytical galaxy formation model. They consider specifically the ratio of broad-band magnitude to Lyman  $\alpha$  flux. Based on their results, in combination with the predicted depths of our observations (a topic to which we return later in this chapter), we conclude that our observations are not sensitive to the continuum flux of typical Lyman  $\alpha$  emitters at the redshifts we consider. We do not, therefore, attempt to simulate continuum emission from our objects.

The aspect of high- $z$  emission line galaxies which we do hope to observe is their Lyman  $\alpha$  flux. It is important, therefore, that our model of this emission line is robust and realistic.

Perhaps the primary goal of the simulations is to understand to what emission line flux our observations are sensitive. Therefore, in each simulation, we will simulate objects with fluxes covering a wide range, from the very bright to the relatively dim, and examine which objects are detected.

Our instrument is tuned to observe emission lines corresponding to the wavelength of Lyman  $\alpha$  at around the quasar redshift. One of the the goals of the simulation is to investigate the dependence of completeness depth on wavelength: therefore, we simulate objects with a range of emission line peak wavelengths, but within some tens of Å of the wavelength range we might plausibly expect to observe.

Modelling a realistic line profile for a high- $z$  ELG is awkward: observations do not show a consistent shape which can be modelled. For example, Dawson et al. (2004) display a variety of spectra with different shapes from their survey of  $z \sim 4.5$  Lyman  $\alpha$  emitters with the Low Resolution Imaging Spectrometer on the Keck Telescope; typically, Lyman  $\alpha$  absorption causes a sharp blue cut-off with a red wing. This is in contrast to, for example, the distinctive double-peaked relatively symmetric profile presented by Tapken et al. (2004) for the  $z = 3.304$  emission line galaxy FDF-4691.

Code was developed, therefore, that enables the easy insertion of any line profile required. During the course of this analysis, we have assumed a Gaussian profile; however, it is easy to change this and recompute should a preferred model become available. In general, though, the results are not sensitive to line profile: given that we observe with a relatively generous passband at intervals which are widely spaced compared to the expected width of the emission line, it is unlikely that modifications to the lineshape would significantly alter our results.

Likely to have a more significant effect on our results is the width of the emission line profile. Once again, though, there is a wide variety in observed linewidths. Dawson et al. (2004) performed spectroscopy on a variety of  $z \sim 4.5$  emission lines; eleven of them at high resolution. They record a variety of velocity widths ( $\Delta v$ ) in the range

$190 \leq \Delta v \leq 460 \text{ km s}^{-1}$ . However, others have recorded rather larger widths: for example, Tapken et al. (2004) records a full width at half maximum for FDF-4691 of  $\sim 1000 \text{ km s}^{-1}$ . As described below, we aim to account for all these possibilities by simulating a wide range of lineshapes in the range  $100\text{--}1000 \text{ km s}^{-1}$ .

#### 4.2.2.2 Software modelling of emission lines

In this section, we consider in detail exactly how a given emission line might interact with the TTF as a prelude to section 4.2.2.3, which describes in detail the code which was written to generate a field of simulated objects.

For each object we simulate, a variety of properties are chosen based on the criteria outlined in the last section: a peak AB magnitude, the wavelength of the peak and the width of the spectral line. In addition, the object is assigned a position relative to the optical axis. The goal is to translate these characteristics into a number of counts which might be received by the detector.

There are two factors which act on light at different wavelengths in different ways to control how much flux reaches our detector: the order-blocking filter and the etalon itself. We use the same flux calibration for the simulated data as was derived from our real observations (sections 3.2.1.8, 3.2.2.8 and 3.2.3.8), so that the on-axis magnitudes simulated for each object are consistent with those measured in our observations. Since we have also chosen the position of the object relative to the axis, it is straightforward to use equation 2.26 (page 42) to calculate the observed wavelength, and hence relate that to the blocking filter transmission (figure 2.4 on page 37). Taking the on-axis filter transmission to be unity, we multiply the flux in the object by a constant to compensate for the different transmission off-axis.

The second—and more complex—factor is the transmission of the etalon itself. This is fundamentally the convolution of the etalon transmission function with the spectral line profile. First, it is necessary to establish exactly what that profile is.

As established in section 4.2.2.1, we model emission lines using a Gaussian profile of width  $100 \leq \Delta v \leq 1000 \text{ km s}^{-1}$ . Making a non-relativistic approximation—which is rea-

sonable, since even for the highest velocities  $\Delta v \ll c$ —we use the Doppler effect in the form

$$\Delta\lambda \simeq \frac{\lambda\Delta v}{c} \quad (4.1)$$

to convert this to the full width at half maximum of the spectral energy distribution in wavelength space. Over the range of data we consider, this corresponds to a range of simulated widths between 1.3 Å (a 100 km s<sup>-1</sup> line at 3900 Å) and 22.3 Å (a 1000 km s<sup>-1</sup> line at 6700 Å).

As discussed in section 2.1.2, we model the interferometer pass-bands as having a Lorentzian profile. The width of this profile is set by equation 2.18, and was calculated for each of our datasets in chapter 3: in each case, it is somewhat less than 10 Å.

The interaction between the etalon and the object is illustrated in figure 4.2. Of course, this figure can only illustrate one of many possible permutations of etalon and object properties. In this case, we show an ELG with a Gaussian peak of 6.7 Å full width half maximum. It is observed through two etalon pass-bands, each of FWHM 8.2 Å and separated by 20 Å. In figure 4.2(a), the peak of the emission line coincides exactly with a peak in the etalon transmission: most of the flux is transmitted, but even here some of the flux is lost due to the etalon profile. Some flux is collected in the wing of the other etalon transmission band, although this is a relatively tiny fraction.

Contrast this with the situation illustrated in figure 4.2(b). Here, the emission line falls half way between the two etalon transmission peaks. Both of them record a small signal—around 20% of the total flux—from the peak, but most of it is lost. Were we to observe an object such as this, it would either fall completely beneath our detection threshold, or we would underestimate its total flux substantially, recording only one fifth of the true value.

There are other ways in which the total flux might be underestimated. When we observe an object, we have no way of measuring its true emission line width: we can only record the amount of flux which falls within one of our transmission bands, as described in section 3.1.7.2. As mentioned in that section, our photometry rests on the assumption that the object we are observing has a flat spectrum. Hence, a bright, narrow emission line

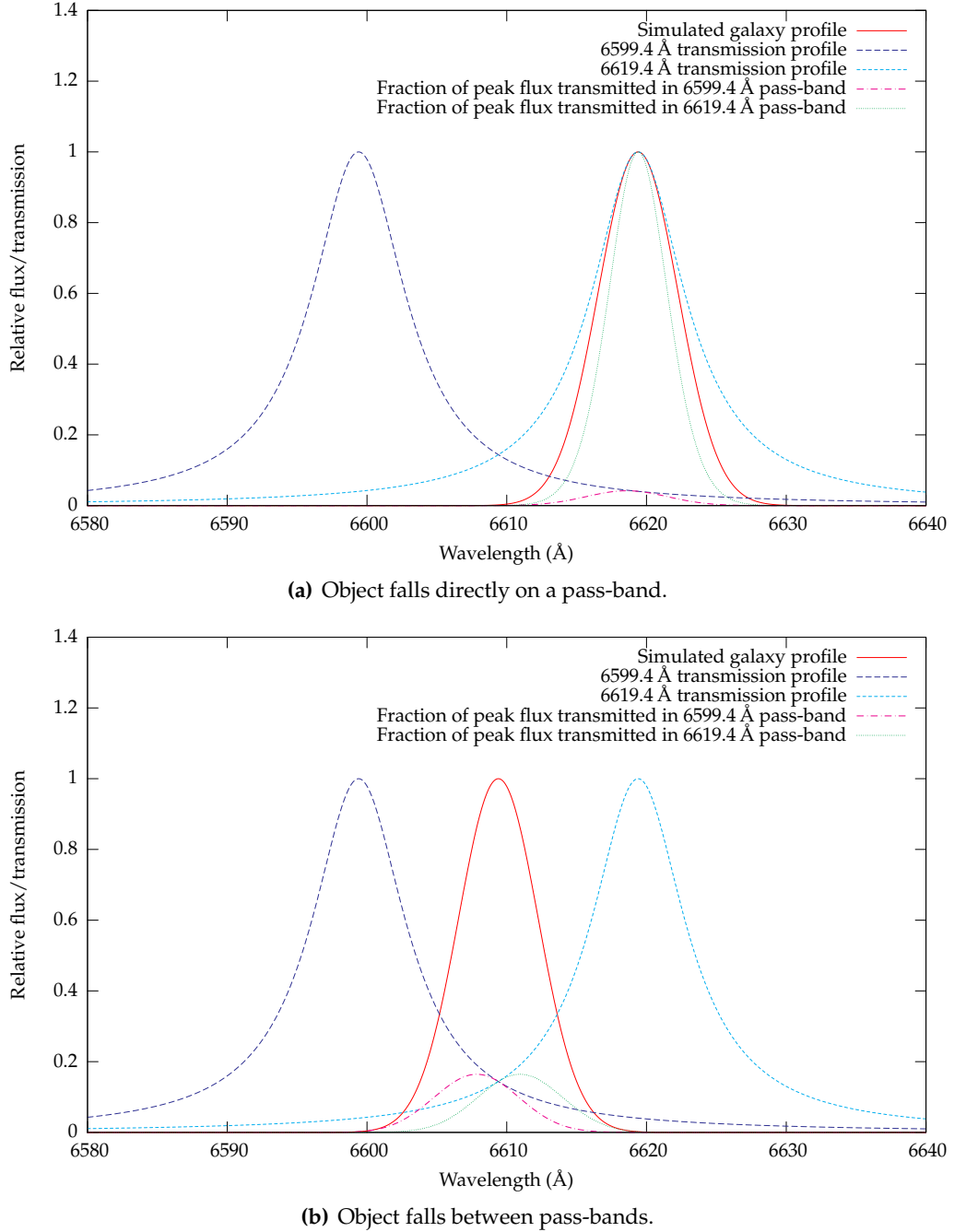


**Figure 4.2:** The change in transmitted flux with position of the peak wavelength of an ELG candidate is graphically demonstrated. In (a), the peak wavelength of the ELG lies directly on the pass-band and almost all flux is transmitted; in (b), however, it falls between the interferometer pass-bands, and most flux is lost. In this example, the full width at half maximum of the interferometer pass-bands is 8.2 Å and of the simulated ELG is 6.7 Å.

will have its total flux underestimated even if it falls centrally in an etalon transmission band. This situation is mitigated substantially for objects with wider profiles.

On the other hand, in many cases our etalon transmission bands are separated by less than 20 Å. In these cases, the opportunity for objects ‘disappearing’ between the bands is much reduced.

It would be useful to be able to estimate what fraction of the flux of each object might be lost in this way—in other words, to calculate a correction which might be applied to a measured magnitude to produce the magnitude which was actually incident on the instrument. However, in general this is not possible: we simply do not know whether we are observing a bright object off-band or a dim object on-band, for example.

That having been said, it is possible to estimate the order of magnitude of the corrections that might be applied. As shown in figure 4.2(a), some flux is lost even when an object falls directly on a passband. This causes the least possible impact to the total measured magnitude when the object line-width is a maximum. Here, we take the maximum velocity widths to be  $1000 \text{ km s}^{-1}$ . At redshift  $\sim 2.2$ , this corresponds to an offset of 0.44 magnitudes; at  $z \sim 4.5$ , both the etalon passbands and the object linewidth is greater: the offset falls to 0.33 magnitudes. The opposite situation occurs when a narrow line falls half-way between passbands; here, several magnitudes worth of flux are lost, often rendering the object undetectable.

In summary, though, there are too many variables which may change from object to object to be able to make an accurate measurement of the true properties of each one. However, by applying the principles set forth in this section to a large number of objects, we can estimate some of the bulk effects over the whole field. The next section describes how many thousands of objects may be generated for analysis.

#### 4.2.2.3 Generating simulated objects

Code to generate catalogues of simulated objects was written using Ruby, a dynamic, object-oriented, general purpose interpreted programming language (Matsumoto, 2001). The general structure of the code is shown in figure 4.3; in this section, we elaborate on

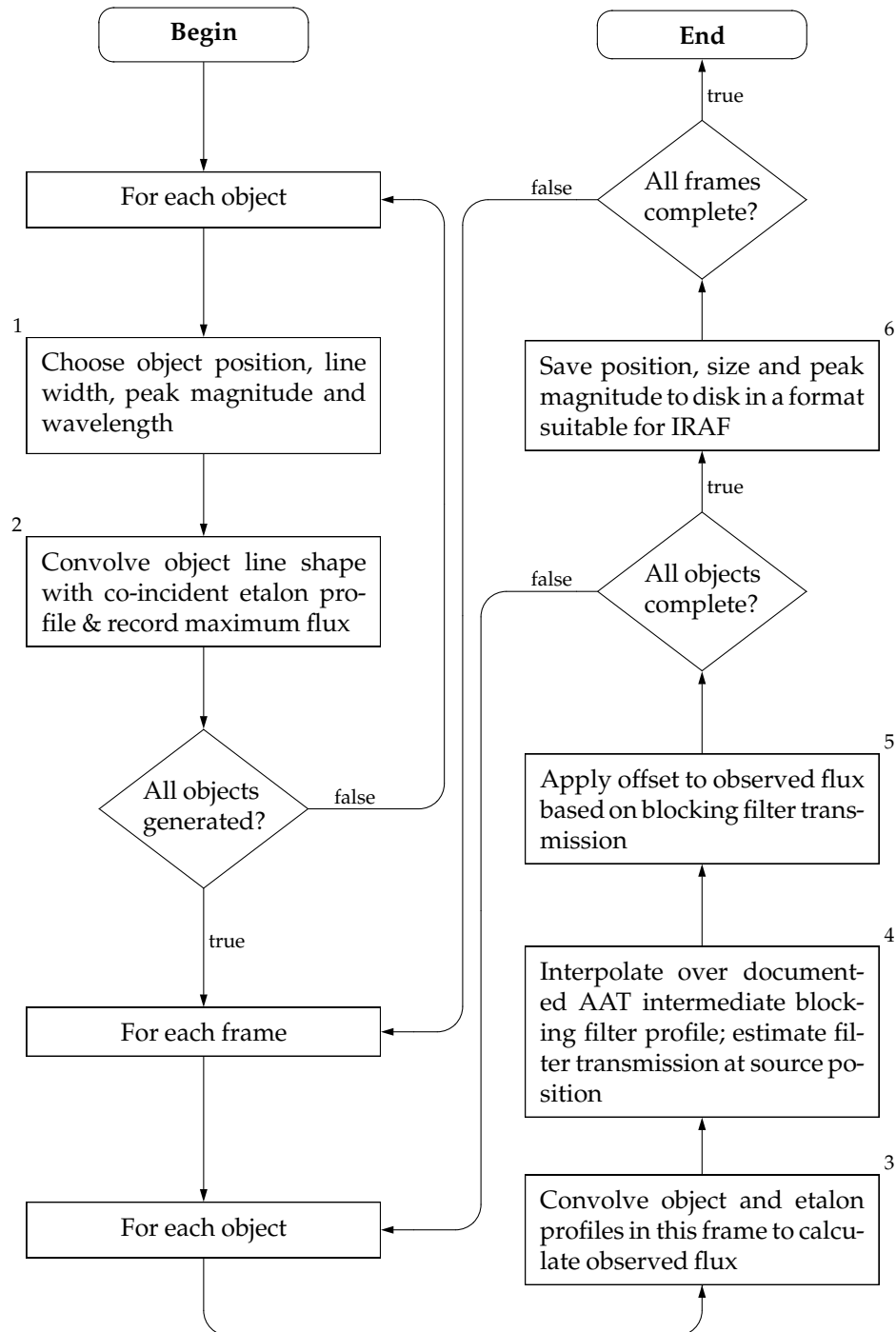


**Figure 4.3:** Structure of the code used for generating simulated fields. The numbered boxes are referred to in the text of section 4.2.2.3.

that description, referring to the numbered boxes in that figure.

Broadly, the program executes in two main loops. In the first loop, including figure 4.3 boxes 1 and 2, the characteristics of all the objects to be simulated are chosen; in the second (boxes 3–6) the appearance of each object after observation is modelled.

In box 1, the position of the object within the field, its peak AB (monochromatic) magnitude, the wavelength at which that peak is to be found, and the width of the spectral line are all determined. Positioning is simply carried out by choosing random pixel co-ordinates within the defined limits of the field we are simulating. In order to ensure that objects are clearly distinguishable by position, the co-ordinates are rejected if they lie too close to another object. This limit is set (fairly arbitrarily) at 27 pixels; this provides a compromise between packing objects into the field (allowing for several hundred to be simulated in a field the size of a typical TTF observation) but ensuring they are clearly distinct. This does not, of course, correspond to a physically likely distribution of objects: this is not important, as the aim is not to simulate a plausible looking quasar field. Indeed, given that the aim of this project is to investigate what a quasar field looks like, we do not have enough information to simulate one!

Purely random selections are made for the peak magnitude and the central wavelength of the line, within limits defined in the code to correspond to the discussion in section 4.2.2.1.

Box 2 refers to convolving our chosen object line shape—usually chosen to have a Gaussian profile, as discussed in section 4.2.2.1—with a coincident etalon transmission profile (i.e. assuming the peak of the etalon transmission is co-incident with the peak of the line). The etalon profile is approximated by a Lorentzian. The maximum possible flux from the object that can be detected from an object of given spectral energy distribution is thus recorded; as illustrated in figure 4.2, this is less than the total flux received even under ideal conditions when the pass-band and emission line peaks coincide.

The above procedure is repeated for each object that is to be simulated. The second part (boxes 3–6) of the procedure translates the properties of the objects which have now been established to a format which can be usefully applied to our blank data fields, generated as described in section 4.2.1.

In the first step, box 3, we convolve the object profile with the etalon transmission for that frame. This is different from the convolution above, as here we do not assume the etalon and the object peaks coincide; rather, the peak of the etalon transmission at the given pixel coordinate is calculated based on equation 2.26. This step gives us the flux we might expect to observe in this pass band were it not for the variation in transmission of the TTF's order-blocking filter.

In boxes 4 and 5, we correct for the effect of the filter. As described in section 4.2.2.2, this is done by multiplying the recorded flux by a constant to account for the filter transmission at the observed wavelength, where the wavelength is calculated based on equation 2.26 and the filter transmission is displayed in figure 2.4.

After this procedure has been completed for each object, the details of everything in the frame is saved to disk in a format suitable for insertion into the blank frame, using standard IRAF tasks as described in section 4.2.3 and the procedure is then repeated for the next frame in the simulation.

### 4.2.3 *Image production*

At this point, a list of the positions and observed magnitudes of objects has been generated, as well as a suitable background image upon which the objects can be superimposed. A resultant image is produced by using the IRAF task `noao.artdata.mkobjects`. This is configured to add each object to the image with a Gaussian point spread function designed to match the seeing in the observed data, as discussed in section 4.2.2.1.

The above procedure may be repeated, each time generating a new field for analysis—as many as can be produced are required to provide solid statistics. Generally, several hundred simulated fields were generated for each one observed.

## 4.3 *Individual image analysis*

We perform simulations in two distinct, but complementary, ways: in the first instance, we consider each individual *image* in isolation; in the second, we move on to consider the

properties of the whole *field*. In this section, we consider the former approach.

For each of our data images (that is, five times in the case of MRC B2158-206, three times each for MRC B1256-243 and BR B0019-1522), six hundred simulated images were produced. Each of those images was populated by five hundred simulated objects—a total of 2,750,000 objects simulated. The properties of each object were chosen following the procedure outlined in the preceding sections with one exception: the peak of each emission line was chosen to coincide precisely with the peak in the etalon transmission at the position of the object.

### 4.3.1 Optimising detection parameters

Section 3.1.6 described the SExtractor tool, which is used for identifying objects in the images and performing photometry on them. Although most of the algorithm used by SExtractor operates without manual interference, there are two user-supplied parameters which must be selected for best performance with the data under analysis. These are DETECT\_MINAREA and DETECT\_THRESH: in brief, objects are regarded as significant by SExtractor if they consist of at least DETECT\_MINAREA contiguous pixels at a level of at least DETECT\_THRESH times the noise in the background.

In addition to this definition of an object used by SExtractor, we also compute the signal to noise ratio for every potential object. The noise in a given aperture is calculated based on equation 3.13 (page 72).

These three parameters are chosen in conjunction with the aim of extracting the greatest possible number of genuine objects, while excluding any contamination from noisy artifacts.

First, the individual background noise images—generated as described in 4.2.1—are analysed with SExtractor. Since these images have not been populated with objects, in the ideal case there are no objects detected; in practice, however, fluctuations in the background mean that some ‘spurious’ detections take place. In each of our images, it was found that the parameters DETECT\_MINAREA = 6 and DETECT\_THRESH = 1.3 produced a small number of detections (between 0 and 2 per image) in each of the background fields.

**Table 4.2:** SExtractor settings used for the analysis in this chapter.

Parameter	Value
DETECT_MINAREA	6
DETECT_THRESH	1.3
BACK_SIZE	64
PHOT_APERTURES	6

Any reduction of either of the parameters (to 5 or 1.2 respectively) causes an order of magnitude increase in the number of spurious detections. Further, all of the spurious detections found were at an aperture signal to noise ratio of less than 5.

SExtractor was then used to build catalogues of each of the populated images. Objects which were observed at a signal to noise ratio of less than 5 were discarded: in this way, any spurious detections were removed. The total number of objects detected in each image was recorded—the completeness of each image is considered in more detail in section 4.3.2. Relaxing the SExtractor detection parameters produced only a small increase—on the order of a few percent—in the number of objects detected in this way in each image.

Based on the above analysis, as well as the discussion in chapter 3, the SExtractor settings listed in table 4.2 were chosen as most appropriate for all the analysis in this chapter. They represent a good compromise between incorrectly detecting noisy artifacts from the background and maximising the number of genuine objects detected.

### 4.3.2 Aperture corrections redux

As an initial check on the simulation system, it was used to calculate photometric aperture corrections. These have already been evaluated theoretically (sections 3.2.1.7, 3.2.2.7 and 3.2.3.7); by comparing the simulated results with the calculated values, we check the consistency of the simulation process.

SExtractor was run on each of the simulated images. The SExtractor settings used are shown in table 4.2. The SExtractor catalogue for each image was then correlated by position with the known objects simulated in the field; for each detected object, its simulated counterpart was determined. The total flux simulated for each object was recorded

**Table 4.3:** Comparison of aperture corrections measured from simulations with theoretical values. The simulated values are the mean calculated across all objects; the corresponding error is the standard deviation of the distribution.

Field	Image	Aperture correction	
		Theoretical	Simulated
MRC B2158-206	Z173	0.44	$0.45 \pm 0.09$
	Z182	0.48	$0.49 \pm 0.09$
	Z191	0.47	$0.48 \pm 0.09$
	Z200	0.40	$0.40 \pm 0.09$
	Z209	0.51	$0.52 \pm 0.10$
MRC B1256-243	Z170	0.36	$0.37 \pm 0.10$
	Z179	0.48	$0.49 \pm 0.10$
	Z188	0.42	$0.42 \pm 0.10$
BR B0019-1522	Z431	0.29	$0.30 \pm 0.09$
	Z451	0.33	$0.35 \pm 0.09$
	Z471	0.24	$0.24 \pm 0.08$

during the simulation process (figure 4.3 box 2; recall that in this simulation etalon and line profiles are always co-incident).

The flux simulated is converted to a magnitude, and compared with that recorded by SExtractor in the image. Any disparity between the two is due to flux which falls outside the photometry aperture—in other words, this is the aperture correction. The mean correction for each image is recorded in table 4.3, together with the theoretical values: the agreement is good, validating the simulation process.

### 4.3.3 Depth of individual images

It is also possible to use these simulations to assess the sensitivity of each individual image. In this section, this problem is addressed in two ways.

Firstly, we have simulated a wide variety of objects of known wavelength and magnitude. For a given wavelength and magnitude, we aim to establish what fraction of the total number of objects are detected. Once again, we apply SExtractor to the images as described in the previous section. From the SExtractor catalogue, we select those objects which are detected a signal to noise ratio of at least 5—the details of our procedure for

detecting objects are discussed in section 5.1. This catalogue of detected objects is then correlated with the known output from the simulation: for each simulated object, we record whether or not a detection has been made. This having been done, the dataset is binned into 3,600 wavelength-magnitude bins: each bin spans around 0.1 magnitudes and 1 Å, and on average contains about 80 individual simulated objects. We then calculate what fraction of the simulated objects in each bin are observed in the catalogues produced by SExtractor. This enables us to put a fractional completeness on the image for a given magnitude and wavelength.

An alternative way of addressing a similar problem is as follows. We know that the wavelength being probed varies across the image as a function of the pixel position in relation to the optical axis. It is, therefore, instructive to consider how the depth to which the image is sensitive varies as a function of position. In this case, we define a “50% completeness depth”—that is, the dimmest magnitude at which 50% of the objects simulated are detected. The simulated objects are sorted into 1,600 bins; this time, however, they are binned by pixel coordinate on the image. Within each of these spatial bins, the data are sorted into bins of size 0.25 magnitudes. For each spatial bin, then, the dimmest magnitude range which is 50% complete is recorded.

The results of this procedure are illustrated in figures 4.4 (MRC B2158-206), 4.5 (MRC B1256-243) and 4.6 (BR B0019-1522).

There are a number of characteristics of the data which are notable from this simulation. Perhaps the most striking is the influence of the blocking filter on the simulations of MRC B2158-206: in the case of Z173, the depth of the observations is constant across the field. However, at longer wavelengths, the depth tails away rapidly—a process which is most pronounced in Z209. The position of the axis is immediately obvious on the map showing 50% completeness depth as a function of position on the field.

This effect is not in evidence to the same degree in the other fields. The BR B0019-1522 observations all fall well within the range of the filter (figure 2.14 on page 57); hence, the observations are all to approximately constant depth. The filter begins to play only a marginal role at the long wavelength end of the Z188 observations of MRC B1256-243.

Also strikingly displayed in this simulation are the relative depths to which we have

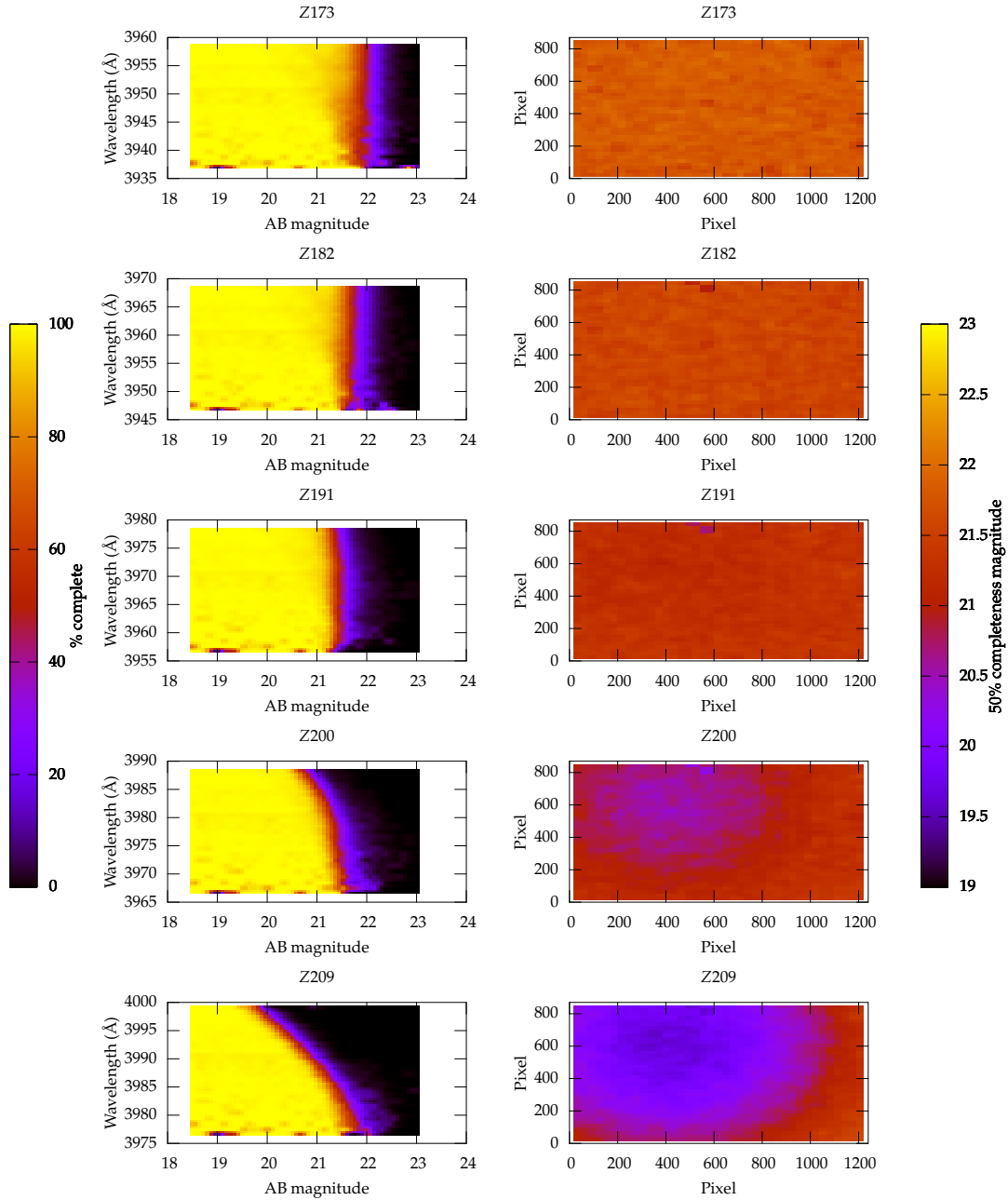


**Figure 4.4:** Analysis of simulations of individual images in the field of MRC B2158-206. The left hand column shows the total percentage of simulated objects at a given AB magnitude and wavelength which are recovered by our analysis; the right hand column the depth (in AB magnitudes) to which 50% of the objects are recovered as a function of position in the image.

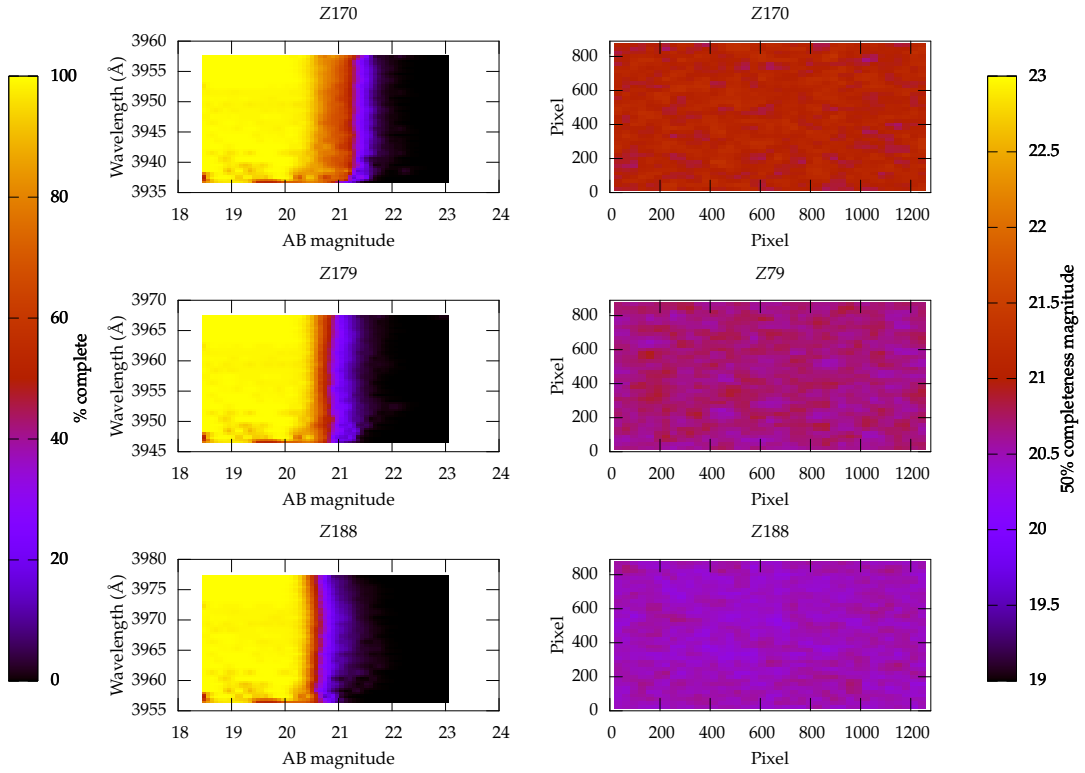


**Figure 4.5:** Analysis of simulations of individual images in the field of MRC B1256-243; the figure is structured in the same way as 4.4.

observed the various fields. In our July 2003 observations, twice as much integration time was spent on MRC B2158-206 as on MRC B1256-243 (table 2.3, and this is immediately reflected in figures 4.4 and 4.5. BR B0019-1522 was exposed for even longer—4800 seconds per image—and consequently the images are deeper still.

There are some slight variations of depth from image to image. This is perhaps most obvious in MRC B1256-243: despite equal integration times and a minimal influence from the blocking filter, Z188 is notably less deep than Z170. This is due to the seeing, as reported in table 3.4: poorer seeing spreads the flux over a larger area of the image, so that the faintest objects are lost.

Finally, note that all these simulations suffer from poorer statistics at shorter wavelengths. This is due to the nature of the simulations: at the shortest wavelengths, we probe only the part of each image which is furthest from the axis, necessarily covering a small area. It is straightforward to improve the statistics by simulating more images: we are limited only by computer time.

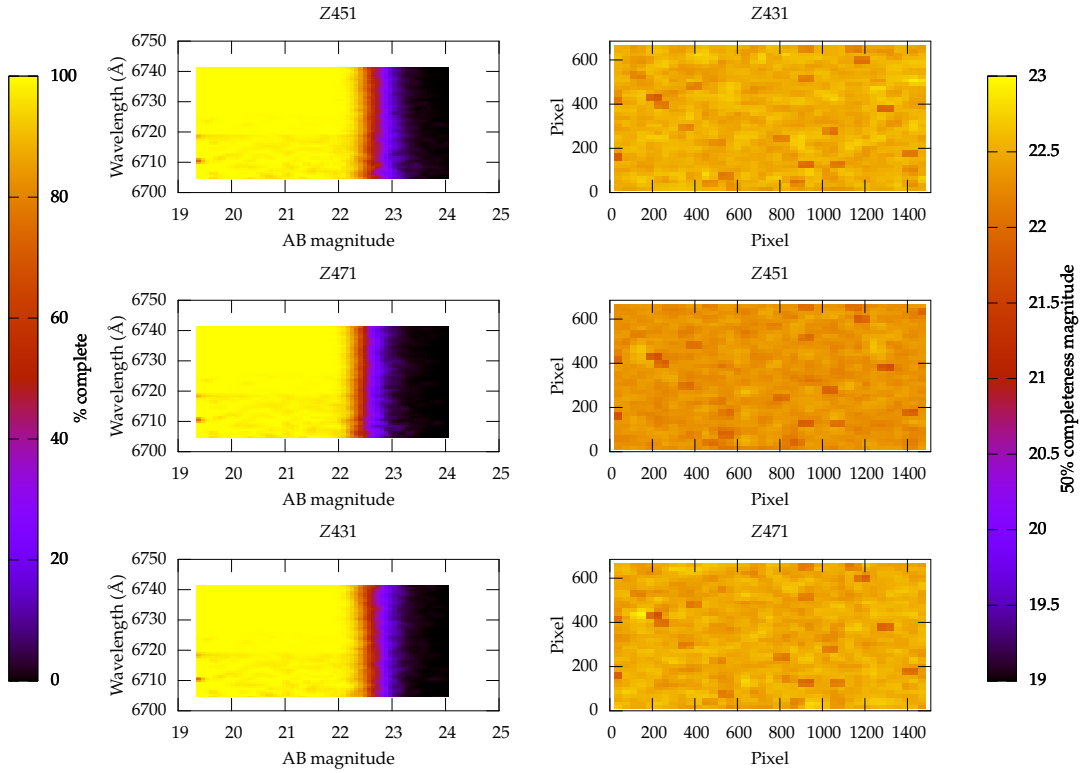


**Figure 4.6:** Analysis of simulations of individual images in the field of BR B0019-1522; the figure is structured in the same way as 4.4, but note that the AB magnitude scale in the left column is different as these images are somewhat deeper.

#### 4.4 Overall field analysis

In the last section, we considered simulations of each individual image in our data. We now combine these to form stacks covering a whole field, and assess the properties of our data as a whole.

Simulation data was prepared in a manner similar to that described in section 4.3, but this time the peak wavelength of each object was allowed to vary arbitrarily over a range of values covering the wavelengths we calculate that our observations probe. Once again, five hundred simulations were run for each field; each of those simulations consisted of five hundred objects.

#### 4.4.1 Overall field completeness

It is now possible to consider the overall completeness of our observations. In effect, the aim is to answer the question: given an object of known peak brightness and wavelength falling somewhere within a field, how likely are we to observe it?

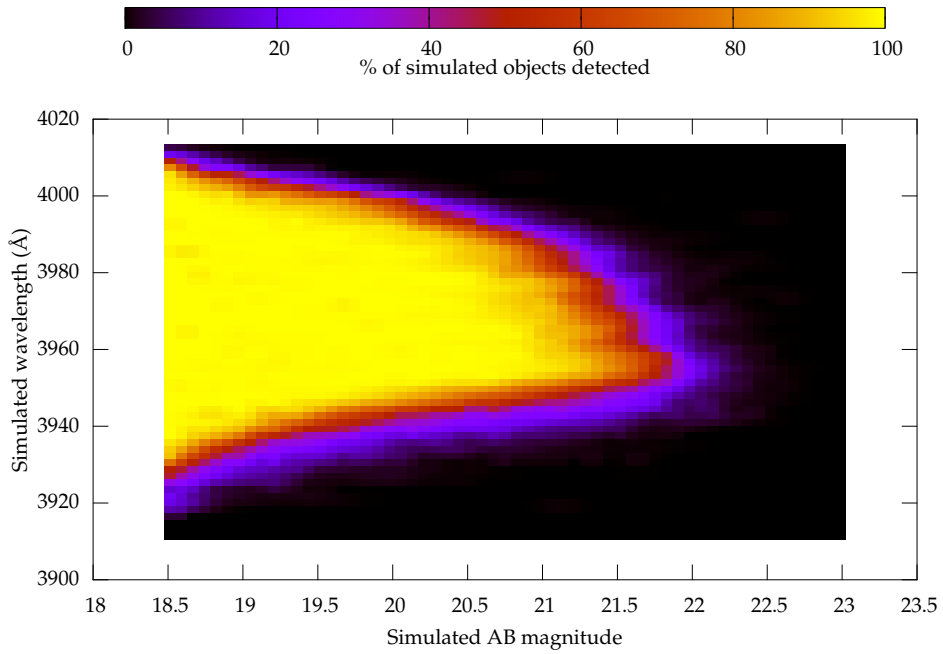
Once again, we use SExtractor to build catalogues of each simulated field; the configuration parameters used are listed in table 4.2. We select only those objects from the catalogue which are detected at a signal to noise ratio of at least 5, using the definition of noise given in equation 3.13 (page 72) compared to the total number of counts in the aperture. Note that  $R$ , the RMS noise in the background, varies with the number of counts in the background—and that, in turn, can vary across the field due to filter transmission, as discussed in section 4.2.1 (and clearly illustrated in figure 4.1(e)). In order to enable us to calculate  $\sigma$  at any given position in the field, we fit a polynomial to the RMS background as a function of distance from the axis.

The list of all the objects in the image is then compared to the list of objects which included in the simulation; whether each of the simulated objects was detected is recorded. For each of the objects, a variety of properties are known from the simulation:

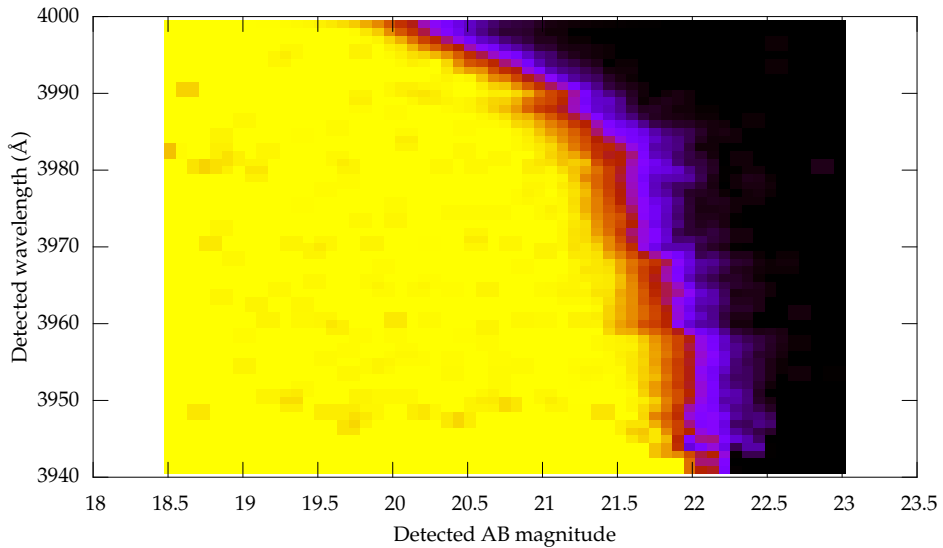
- Simulated wavelength of the peak;
- Peak AB magnitude of the object;
- Maximum possible detected magnitude—that is, calculated from the flux as recorded in figure 4.3 box 2 combined with equation 3.10 (page 70).

In addition, we have measured the actual detected magnitude (which is less than the ‘true’ simulated magnitude) and the detected wavelength. The detected wavelength is taken as the wavelength of peak transmission at the pixel coordinate of the image in which the object is detected. If the object is seen in more than one image, its wavelength and magnitude are measured from the image in which it is brightest.

It is, therefore, possible to consider the completeness of the field in terms of various sets of parameters. In figures 4.7, 4.8 and 4.9 the completeness is presented both in terms of the *simulated* quantities—that is, the chosen peak wavelength of the emission and the maximum possible detected magnitude—and the *detected* quantities, as measured from the

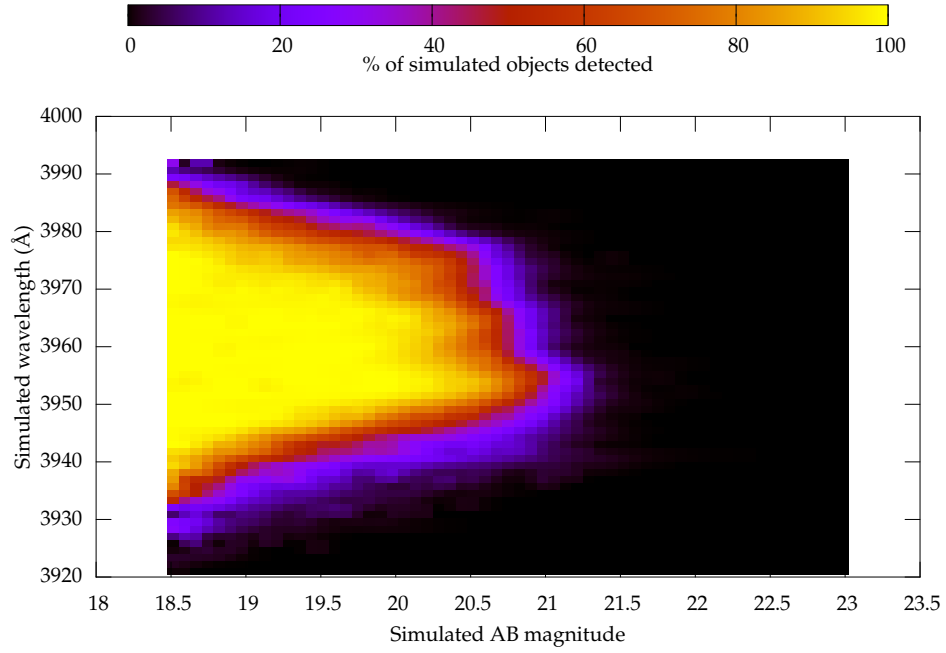


(a) Completeness of the field as a function of simulated magnitude and wavelength.

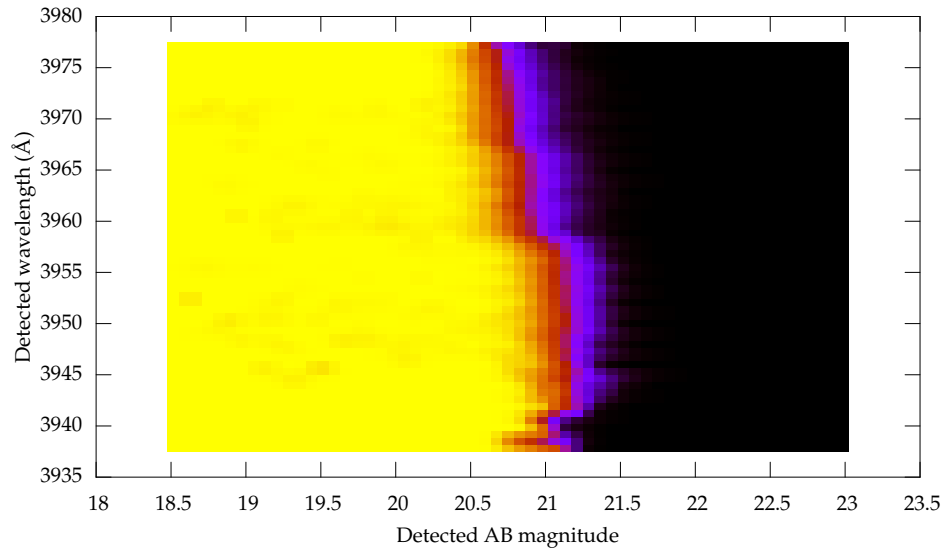


(b) Completeness of the field as a function of detected magnitude and wavelength.

**Figure 4.7:** Completeness of the overall field of MRC B2158-206 as a function of wavelength and AB magnitude. In (a), the data are plotted in terms of the known variables as used in the simulation input; in (b) in terms of those we measured from the image.

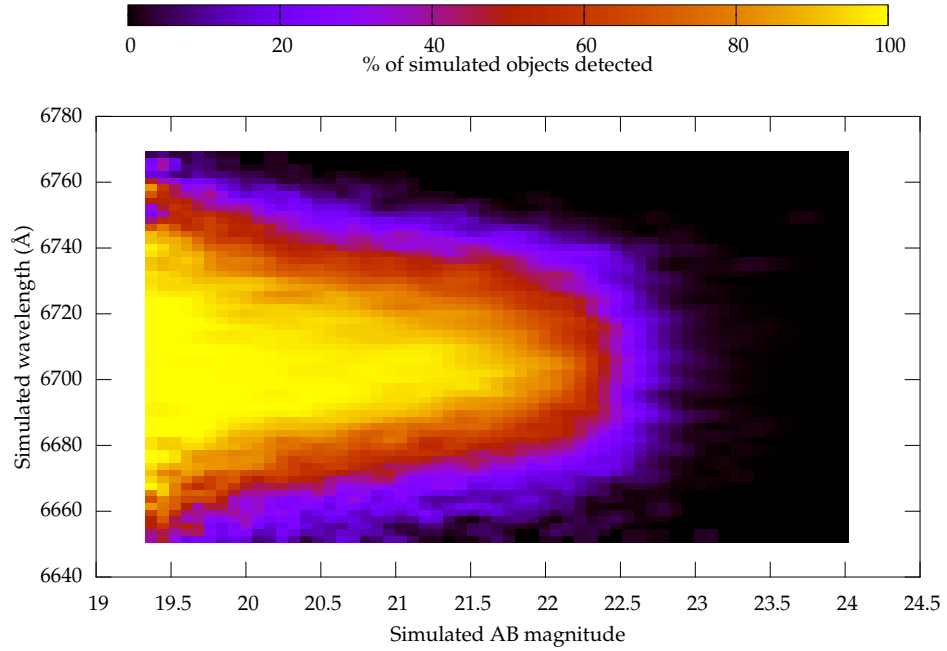


**(a)** Completeness of the field as a function of simulated magnitude and wavelength.

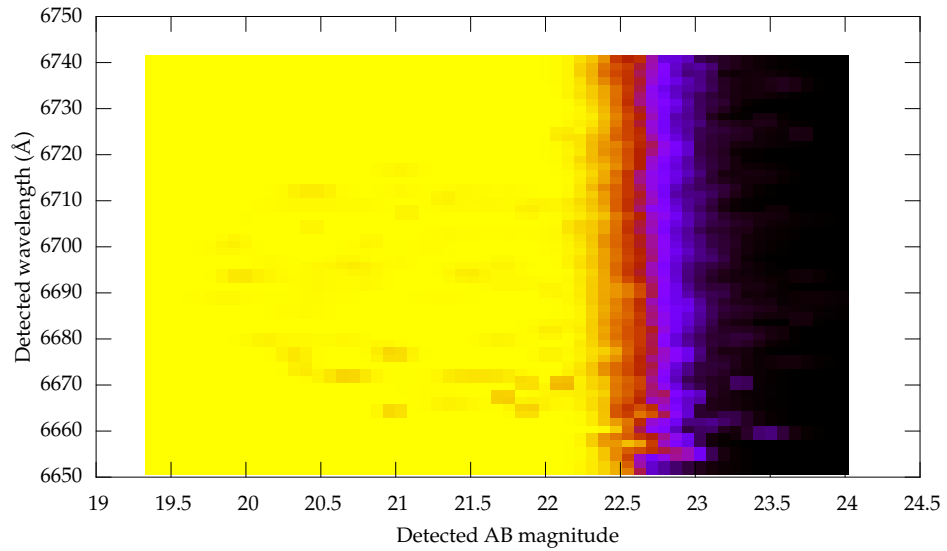


**(b)** Completeness of the field as a function of detected magnitude and wavelength.

**Figure 4.8:** Completeness of the overall field of MRC B1256-243 as a function of wavelength and AB magnitude. The data are presented in the same way as figure 4.7.



(a) Completeness of the field as a function of simulated magnitude and wavelength.



(b) Completeness of the field as a function of detected magnitude and wavelength.

**Figure 4.9:** Completeness of the overall field of BR B0019-1522 as a function of wavelength and AB magnitude. The data are presented in the same way as figure 4.7.

images. Note that, in this definition, the simulated magnitude is *not* the true source magnitude, but includes a minimal offset due to etalon effects (as discussed in section 4.2.2.2). This is more convenient when correcting our observations for completeness, a process we consider in some detail in chapter 6, but means that an offset must be applied before the simulated magnitude can be converted to a source luminosity. This offset varies with line width (which we do not know), but may be conservatively estimated 0.44 magnitudes in the MQS fields, and 0.33 magnitudes in the BR B0019-1522 field following section 4.2.2.2.

Note also that, in general, the different etalon transmission bands are not clearly distinguished in these figures. This is because the band is not well localised in terms of wavelength: each one covers a considerable range in wavelength space (on the order of tens of Å; a maximum of 1.8% of the central wavelength, as discussed in section 2.1.4.1) to the extent that they overlap.

Finally, figure 4.10 displays the 50% completeness depth (in terms of the simulated magnitude) as a function of wavelength for each of the fields. This clearly illustrates how bright an object would have to be to be detected at a given wavelength.

The results presented in this section are used in the next chapter to determine and correct for the overall completeness of our observations.

## 4.5 Summary

This chapter has presented a system for simulating tunable filter observations. This is useful both for tuning our detection procedure by selecting the optimal settings for use in software and, even more importantly, for assessing the overall sensitivity and significance of our results—a procedure to which consideration is given later in this thesis.

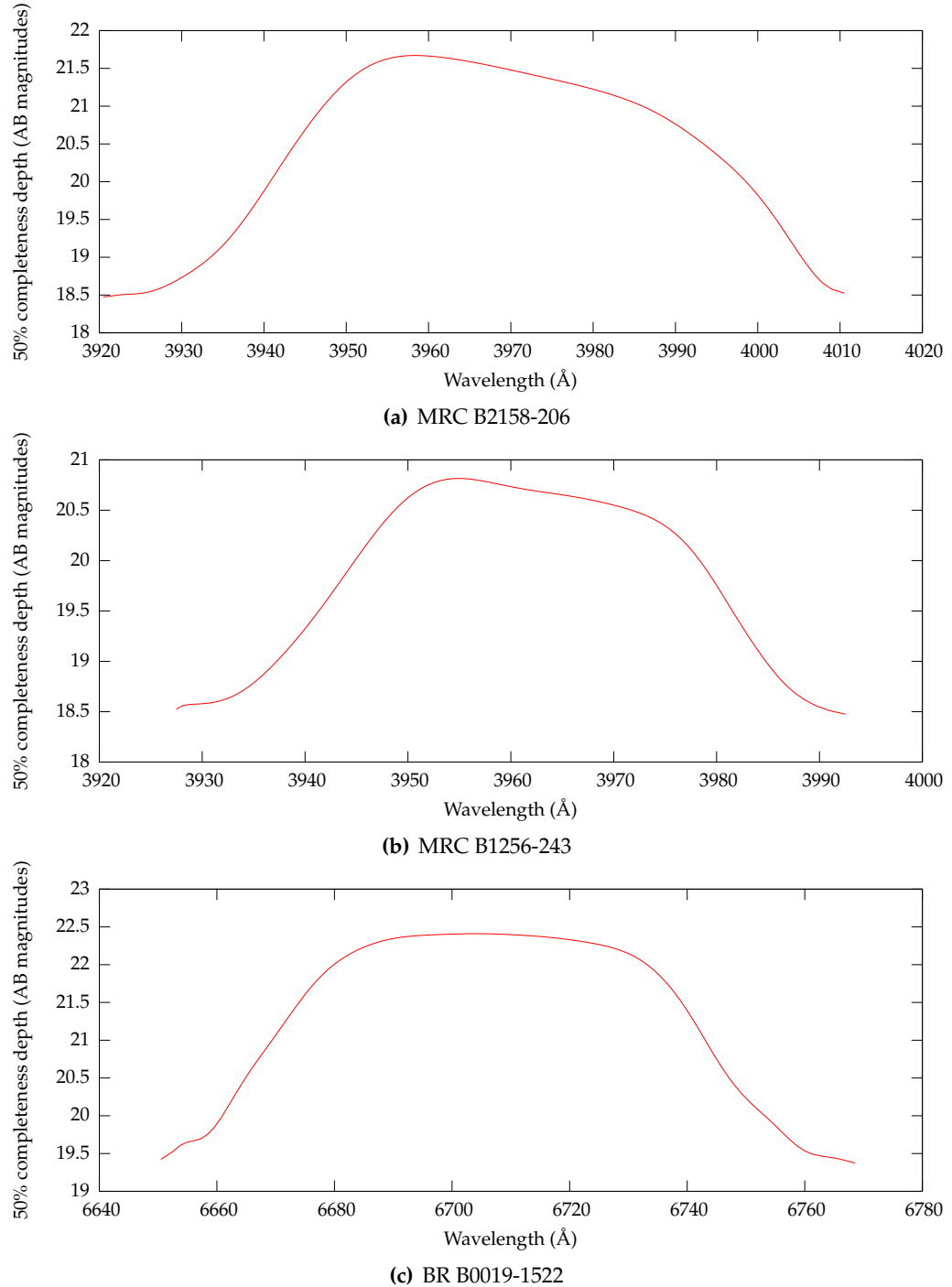


**Figure 4.10:** 50% completeness depth as a function of wavelength in each of the three overall quasar fields. The AB magnitude recorded here is the *simulated* magnitude, as plotted in figures 4.7(a), 4.8(a) and 4.9(a).

# Chapter 5

## *Identifying candidate galaxies*

This chapter describes the method by which potential emission line galaxies were identified in the quasar fields. It goes on to provide full details of all of the detections, in preparation for further analysis in the next chapter. Finally, consideration is given to the possibility of contamination of the sample by false detections.

### 5.1 *Object detections*

The procedure used for detecting candidate emission line galaxies is described in this section. Subsequent sections describe the objects identified on a field-by-field basis.

The data were first completely reduced, as described in chapter 3. SExtractor was then used to build a catalogue of each image in the field. The parameters used were those discussed in section 4.3.1 and listed in table 4.2 (page 114). For each image, SExtractor produced a catalogue containing the pixel coordinates of the centre of each detected object, the background-subtracted (as described in section 3.1.6) number of counts falling within the photometry aperture, and the measured AB magnitude of the object (section 3.1.7). The catalogue for each image is saved into a separate ASCII text file.

Ruby code was written to analyse the catalogues. Objects in each catalogue were associated by position, with a match being made for objects with central coordinates within three pixels of each other in each frame.

As discussed in section 4.2.2.1, based on the results of Le Delliou et al. (2006) we do not believe that our observations are deep enough to observe the continuum flux from a typical Lyman  $\alpha$  emitting galaxy. Further, considering figure 4.2, it is clear that an object which falls directly on one passband is unlikely to record a strong signal in the others—

although it is possible that an object which falls between two bands will be detected in both (recall that the bands in figure 4.2 are separated by 20 Å, which is a wider separation than our  $z \sim 2.2$  observations). In short, therefore, emission line galaxies should be detected in either one or two of our passbands, but not in the other one (in the case of MRC B1256-243 and BR B0019-1522) or three (in the case of MRC B2158-206).

Therefore, the procedure for identifying objects is to look for objects which are detected at a  $5\sigma$  (as defined by equation 3.13 on page 72) level in at least one and at most two of the frames. There is still some risk of contamination by noisy artifacts (section 5.2.1); in order to minimise this, all of the flagged objects are checked by eye for plausibility. This check consisted of two parts: first, the appearance of the objects was considered—they were rejected if they could not be clearly picked out by eye, or had unphysical looking structure (such as, for example, an extended line of bright pixels, rather than a circular patch). Secondly, they were compared to the original data frames to check for a correspondence between detections and sites of particularly heavy cosmic ray or charge trapping activity. This procedure obviously relies to an extent on individual judgement; to minimise the risk of spurious detections, a conservative approach was adopted and several of the very faintest detections were rejected.

After objects have been identified following the above procedure, the area where the objects would be expected to appear in the frames in which it was *not* detected is examined in more detail: detections were recorded as low as the  $1\sigma$  level. Often, although it failed to meet the  $5\sigma$  criterion above, some trace of the object is still detected. These measurements were not used in the automatic object selection routine, but were used when assessing the detections by eye. They are useful for assessing the validity of our detections against the contaminants set forth in section 5.2. Firstly, a faint detection lends legitimacy to a real signal in an adjacent frame: the chances of a noisy artifact appearing at the same place in two frames is small. Secondly, they lend some guidance as to the probability of an object being a mis-identified flat-spectrum source.

After objects had been identified, their precise positions were calculated as follows. A selection (13 in the case of MRC B2158-206; 12 in both MRC B1256-243 and BR B0019-1522) of objects randomly scattered across each field were identified in the U.S Naval Ob-

servatory “B” catalogue of astrometric standards (Monet et al., 2003). The IRAF task `images.imcoords.ccmap` was then used to compute a plate solution for each field: in this way, arbitrary pixel coordinates can be converted to right ascension and declination, taking account of both a linear shift and a distortion.

The following sections describe in detail the objects which were identified in each of the quasar fields. Throughout, the fluxes referred to are computed directly from the AB magnitude calculated by SExtractor using equation 3.10; no correction has been made for galactic extinction or etalon transmission characteristics.

### 5.1.1 MRC B2158-206

As a preliminary check to make sure that Lyman  $\alpha$  peaks could be identified in the data, the flux attributed to the quasar MRC B2158-206 itself was measured in each band. This is shown in figure 5.1. The peak in the quasar's spectrum is clearly visible at a position consistent with the value taken from the literature (Kapahi et al., 1998).

**Two** candidate emission line galaxies were identified in this field using the method outlined above. Each object was assigned an alphabetic identifier. Details of the detection of both of the objects are presented in table 5.1, while figure 5.2 graphically displays the flux measured in each etalon transmission band together with thumbnail images of both objects. The positions of the objects in the field are shown in figure 5.3.

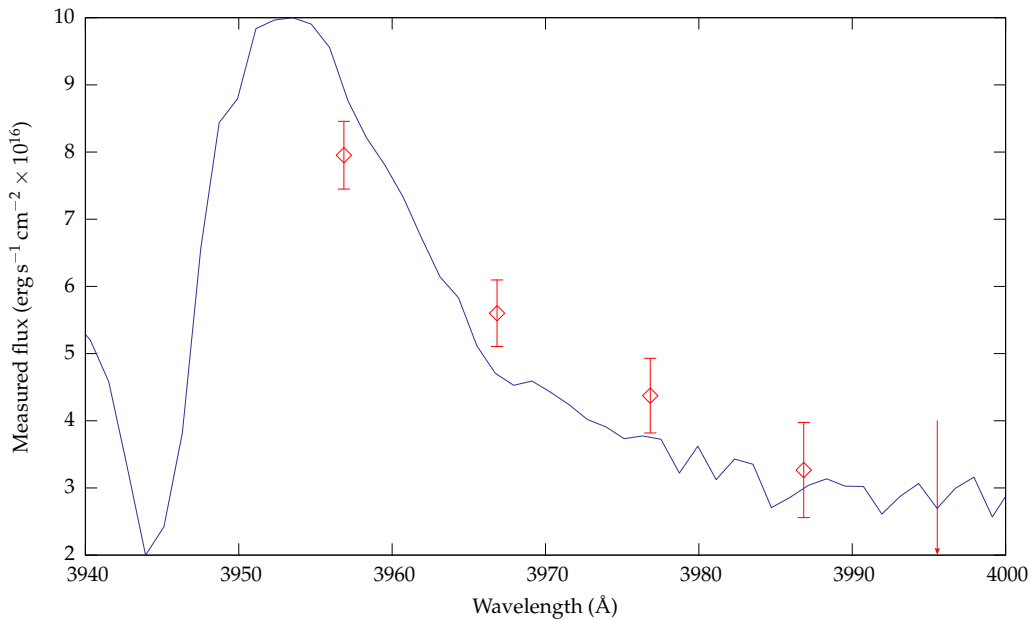


**Figure 5.1:** A comparison of our (four-point) “spectrum” of MRC B2158-206 (in red) with the (normalised) spectrum provided in figure 2.10 (blue). The quasar is not detected in the final (Z209) frame: the wavelength at which it would have appeared is shown by an arrow.

**Table 5.1:** ELG candidates in the field of MRC B2158-206. The alphabetic identifiers correspond to those shown in figures 5.3 and 5.2; the AB magnitude is that measured in the peak frame with no correction for galactic extinction or etalon transmission. Projected distances are based on a conversion factor of 8.235 kpc per arcsecond (section 6.1.1).

Identifier	Position (J2000)		Projected distance from Quasar (Mpc)	Lyman $\alpha$ peak:		
	R.A.	Decl.		Frame	Wavelength (Å)	AB magnitude
A	$22^h 01^m 26.0^s$	$-20^\circ 25' 08.0''$	0.263	Z173	3956	21.7
<i>6.6<math>\sigma</math> in Z179. Falls to 2/3 of the flux and 3.7<math>\sigma</math> in Z182, and not above 1<math>\sigma</math> in other images.</i>						
B	$22^h 01^m 41.7^s$	$-20^\circ 24' 03.5''$	1.986	Z173	3971	21.5
<i>5.5<math>\sigma</math> in Z191. Not detected in other images.</i>						

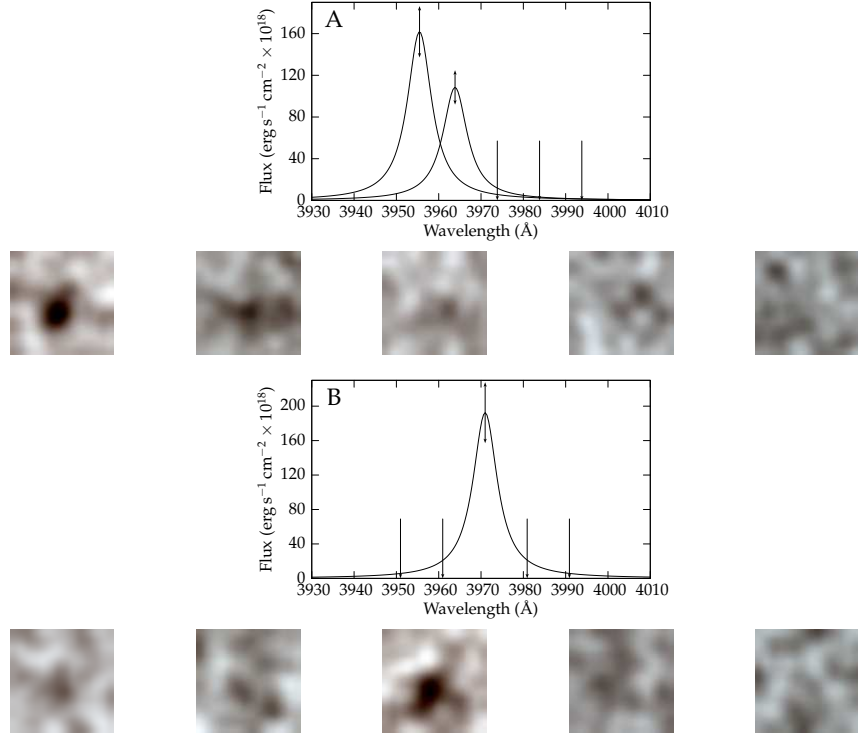


**Figure 5.2:** ELG candidates in the field of MRC B2158-243. For each object, the graph shows the flux recorded in and the wavelength at each etalon transmission band. The width of the curves indicated the etalon transmission profile. Error bars are calculated based on equation 3.13. 14 pixel (4.6 arcsecond) square thumbnail images are displayed of the object as seen in each band; the thumbnail greyscales are matched, and they have been smoothed with a Gaussian kernel chosen to match the seeing.

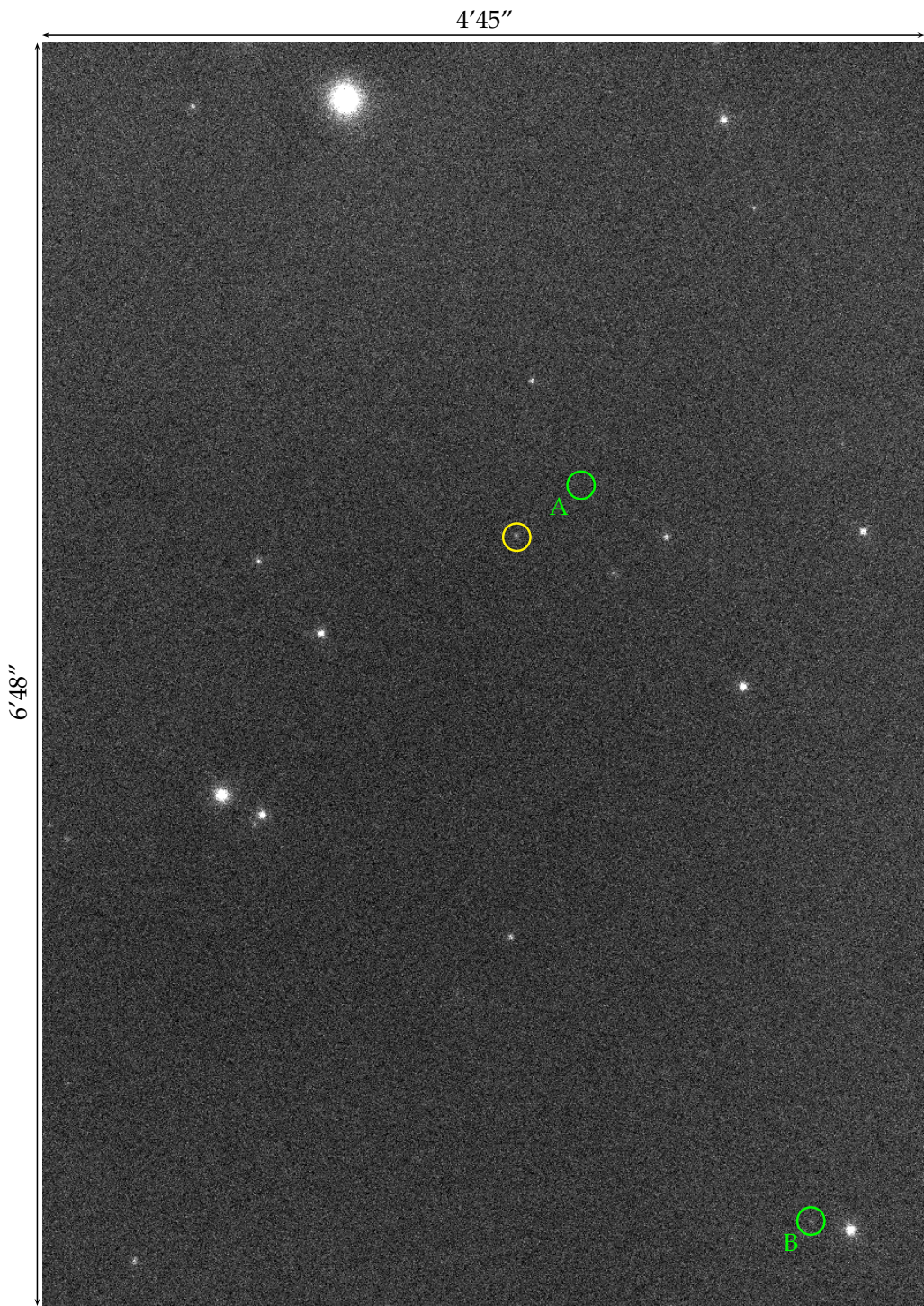


**Figure 5.3:** Positions of candidate emission line galaxies in the field of MRC B2158-206. North is right and east is down. Candidate galaxies are marked by green circles; the position of the quasar is marked by a yellow circle. The letters refer to ELG designations used throughout the text.

### 5.1.2 MRC B1256-243

As a preliminary check to make sure that Lyman  $\alpha$  peaks could be identified in the data, the flux attributed to the quasar MRC B1256-243 itself was measured in each band. This is shown in figure 5.4. The peak in the quasar's spectrum is clearly visible at a position consistent with the value taken from the literature (Kapahi et al., 1998) (although it is notable that we detect more flux at short wavelengths than expected).

**Four** candidate emission line galaxies were identified in this field using the method outlined above. Each object was assigned an alphabetic identifier. Details of the detection of each object are presented in table 5.2, while figure 5.5 graphically displays the flux measured in each etalon transmission band together with thumbnail images of each object. The positions of the objects in the field are shown in figure 5.6.

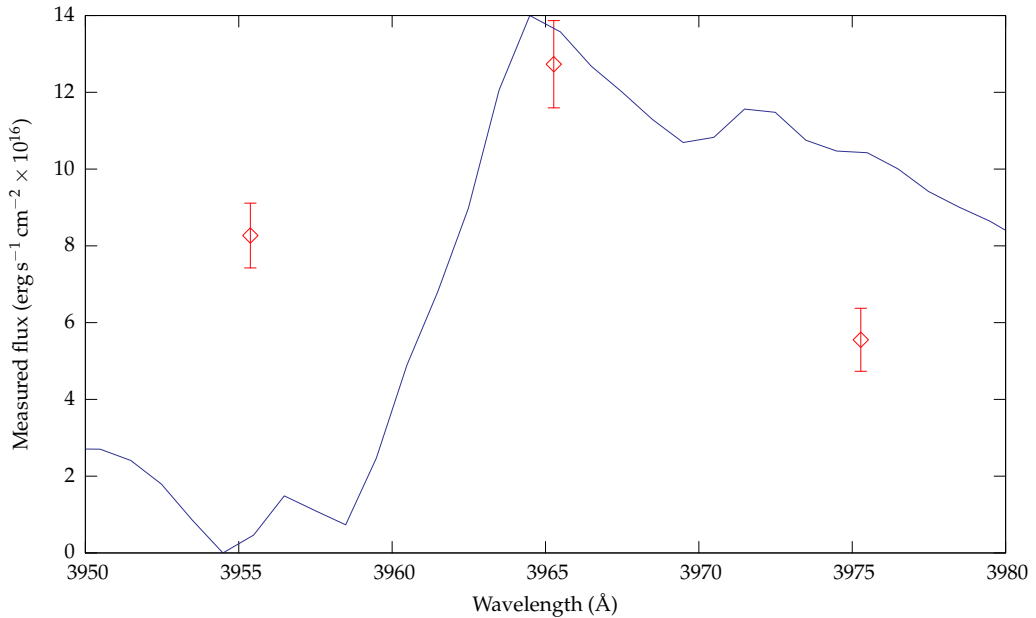


**Figure 5.4:** A comparison of our (three-point) “spectrum” of MRC B1256-243 (in red) with the (normalised) quasar spectrum as displayed in 2.11 (blue). The wavelength of the peak is clearly determined; it is noteworthy, however, that, we detect more flux than might be expected short of the Lyman  $\alpha$  wavelength.

**Table 5.2:** ELG candidates in the field of MRC B1256-243. The alphabetic identifiers correspond to those shown in figures 5.6 and 5.5; the AB magnitude is that measured in the peak frame with no correction for galactic extinction or etalon transmission. Projected distances are based on a conversion factor of 8.227 kpc per arcsecond (section 6.1.1).

Identifier	Position (J2000)		Projected distance from Quasar (Mpc)	Lyman $\alpha$ peak:		AB magnitude
	R.A.	Decl.		Frame	Wavelength (Å)	
A	$12^h 59^m 23.2^s$	$-24^\circ 37' 32.9''$	1.428	Z179	3970	20.8
	5.3 $\sigma$ in Z179. Not detected in other images.					
B	$12^h 59^m 15.7^s$	$-24^\circ 37' 40.7''$	0.871	Z179	3966	21.0
	5.0 $\sigma$ in Z179. Not detected in other images.					
C	$12^h 59^m 02.7^s$	$-24^\circ 37' 15.1''$	1.257	Z179	3957	20.8
	5.8 $\sigma$ in Z170, 5.2 $\sigma$ in Z179. The total flux in Z179 is greater, though. Not detected in Z188.					
D	$12^h 59^m 05.3^s$	$-24^\circ 37' 31.3''$	1.085	Z179	3960	20.6
	6.0 $\sigma$ in Z179, 4.9 $\sigma$ in Z188. Not detected in Z170.					

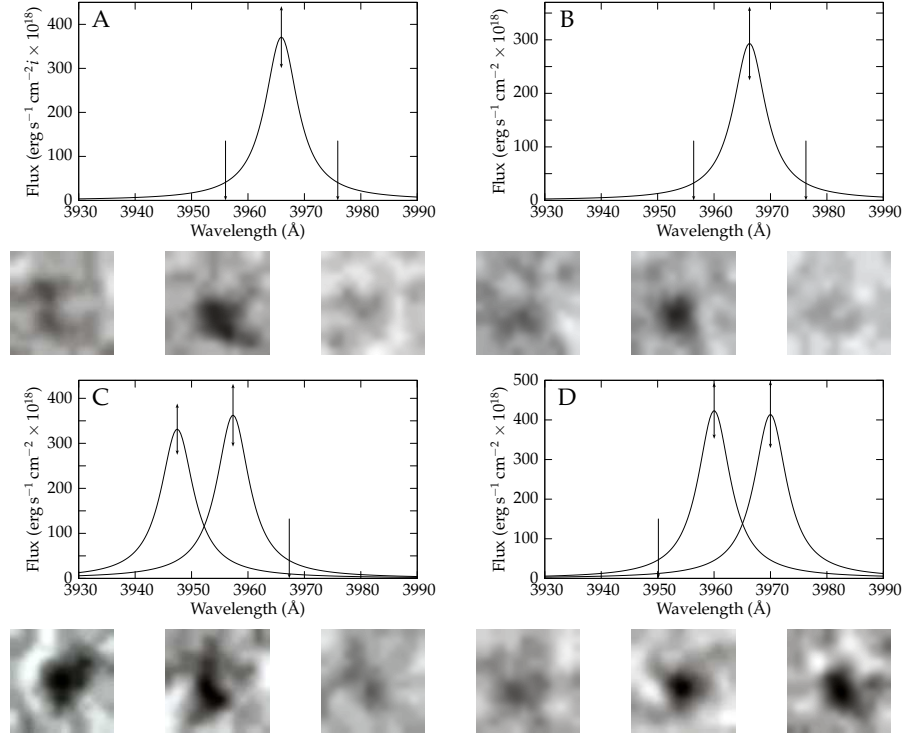


**Figure 5.5:** ELG candidates in the field of MRC B1256-243. For each object, the graph shows the flux recorded in and the wavelength at each etalon transmission band. The width of the curves indicated the etalon transmission profile. Error bars are calculated based on equation 3.13. 14 pixel square thumbnail images are displayed of the object as seen in each band.

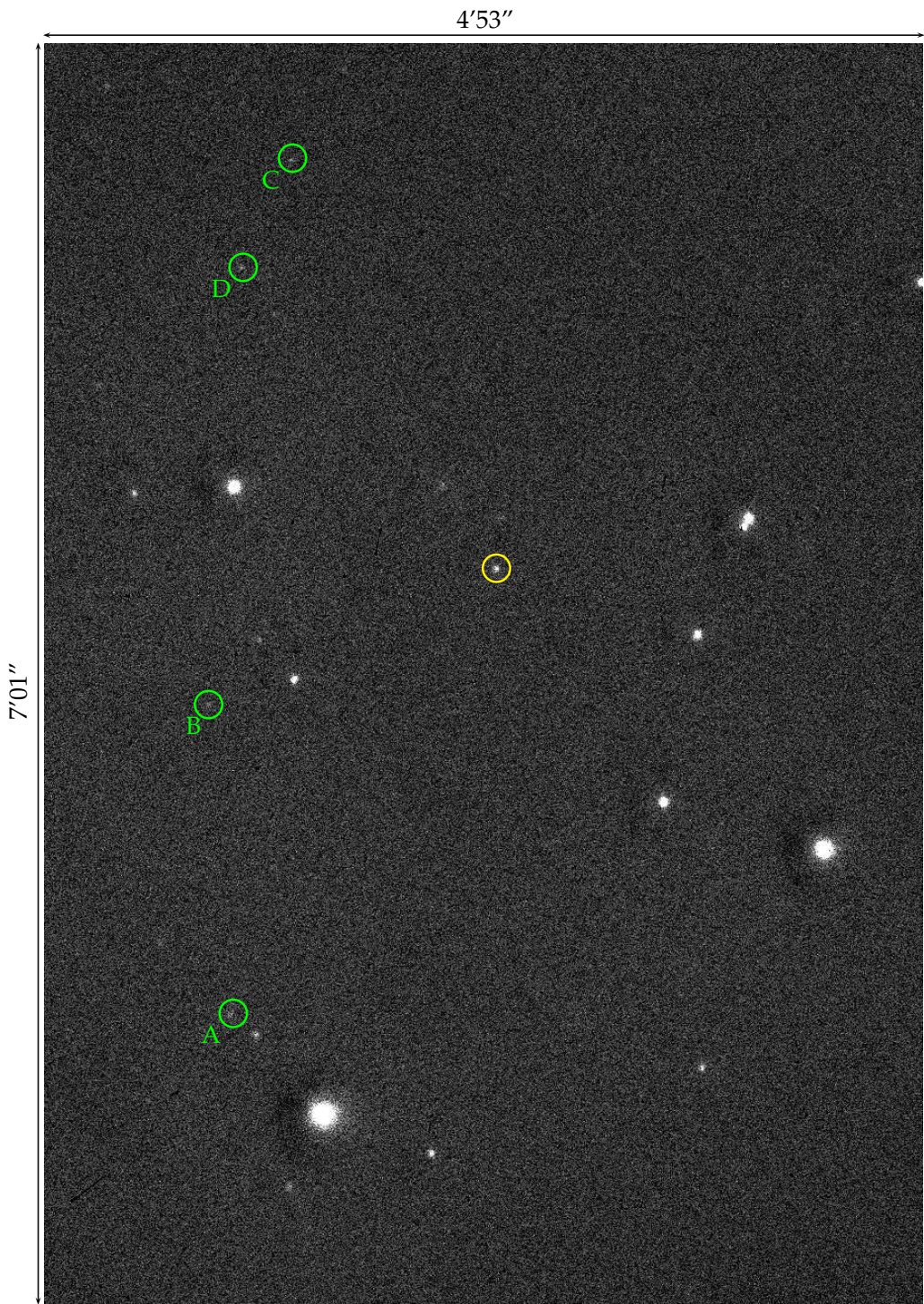


**Figure 5.6:** Positions of candidate emission line galaxies in the field of MRC B1256-243. North is right and east is down. Candidate galaxies are marked by green circles; the position of the quasar is marked by a yellow circle. The letters refer to ELG designations used throughout the text.

### 5.1.3 BR B0019-1522

As a preliminary check to make sure that Lyman  $\alpha$  peaks could be identified in the data, the flux attributed to the quasar BR B0019-1522 itself was measured in each band. This is shown in figure 5.7. The peak in the quasar's spectrum is clearly visible at a position consistent with the value taken from the literature (Irwin et al., 1991).

**Seventeen** candidate emission line galaxies were identified in this field using the method outlined above. Each object was assigned an alphabetic identifier. Details of the detection of each object are presented in table 5.3, while figure 5.8 graphically displays the flux measured in each etalon transmission band together with thumbnail images of each object. The positions of the objects in the field are shown in figure 5.9.

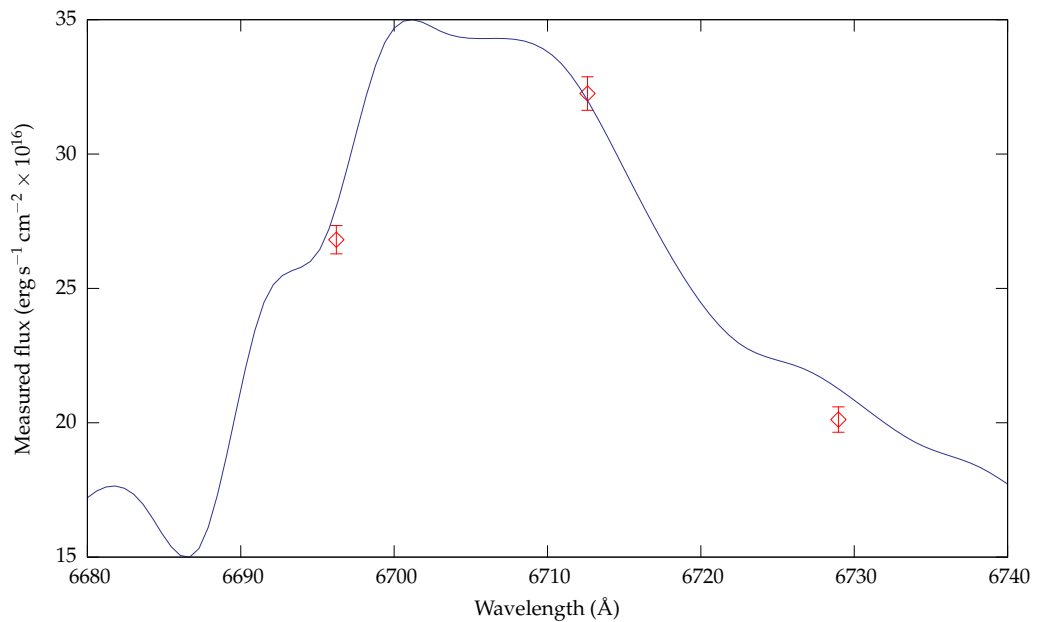


**Figure 5.7:** A comparison of our (three-point) “spectrum” of BR B0019-1522 (in red) with the (normalised) spectrum provided in figure 2.12 (blue). The peak falls between the etalon transmission peaks, but is still discernible in the data.

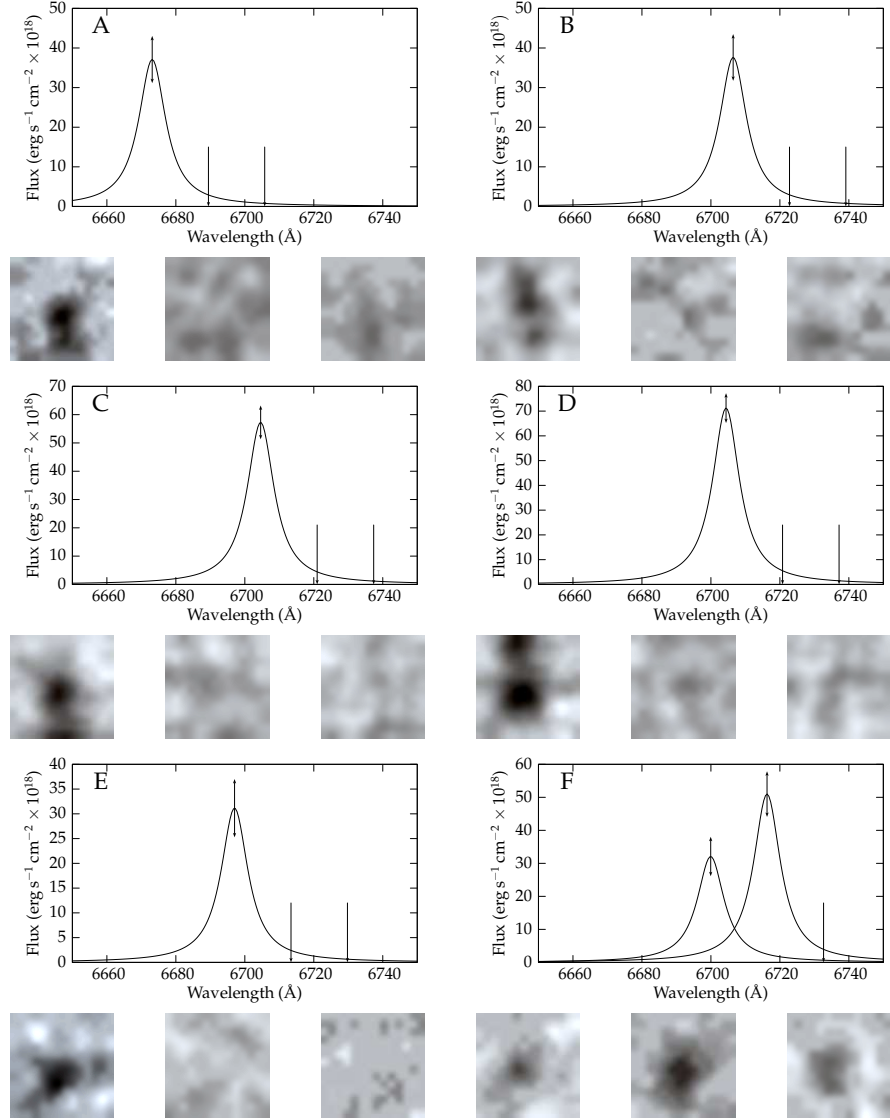
**Table 5.3:** ELG candidates in the field of BR B0019-1522. The alphabetic identifiers correspond to those shown in figures 5.9 and 5.8; the AB magnitude is that measured in the peak frame with no correction for galactic extinction or etalon transmission. Projected distances are based on a conversion factor of 6.585 kpc per arcsecond (section 6.1.1)

Identifier	Position (J2000)		Projected distance from Quasar (Mpc)	Lyman $\alpha$ peak:		AB magnitude
	R.A.	Decl.		Frame	Wavelength (Å)	
A	$0^h 21^m 58.4^s$	$-15^\circ 08' 20.3''$	1.427	Z431	6673	22.5
	6.2 $\sigma$ in Z431. Not detected in other images.					
B	$0^h 22^m 03.8^s$	$-15^\circ 07' 41.2''$	0.907	Z431	6706	22.5
	6.4 $\sigma$ in Z431. Not detected in other images.					
C	$0^h 22^m 08.8^s$	$-15^\circ 06' 58.8''$	0.525	Z431	6705	22.0
	9.6 $\sigma$ in Z431. Not detected in other images.					
D	$0^h 22^m 08.8^s$	$-15^\circ 06' 56.3''$	0.508	Z431	6704	21.8
	11.8 $\sigma$ in Z431. Not detected in other images. Very close in position to object C, but clearly distinct in the images.					
E	$0^h 21^m 57.8^s$	$-15^\circ 06' 58.7''$	1.087	Z431	6697	22.7
	5.3 $\sigma$ in Z431. Not detected in other images.					
F	$0^h 22^m 14.5^s$	$-15^\circ 06' 42.6''$	0.743	Z451	6716	22.1
	7.4 $\sigma$ in Z451 and 5.3 $\sigma$ in Z431. Not detected in Z471, but discernible in the thumbnail image.					
G	$0^h 22^m 12.4^s$	$-15^\circ 06' 17.8''$	0.487	Z431	6716	22.1
	7.8 $\sigma$ in Z431 and 7.3 $\sigma$ in Z451. Not detected in Z471.					
H	$0^h 22^m 12.7^s$	$-15^\circ 06' 01.4''$	0.464	Z431	6697	22.5
	6.3 $\sigma$ in Z431. Not detected in other images, but probably visible.					
I	$0^h 22^m 07.6^s$	$-15^\circ 05' 27.1''$	0.094	Z431	6694	22.4
	6.6 $\sigma$ in Z431, 5 $\sigma$ in Z451. Not detected in Z471.					

Continued overleaf...

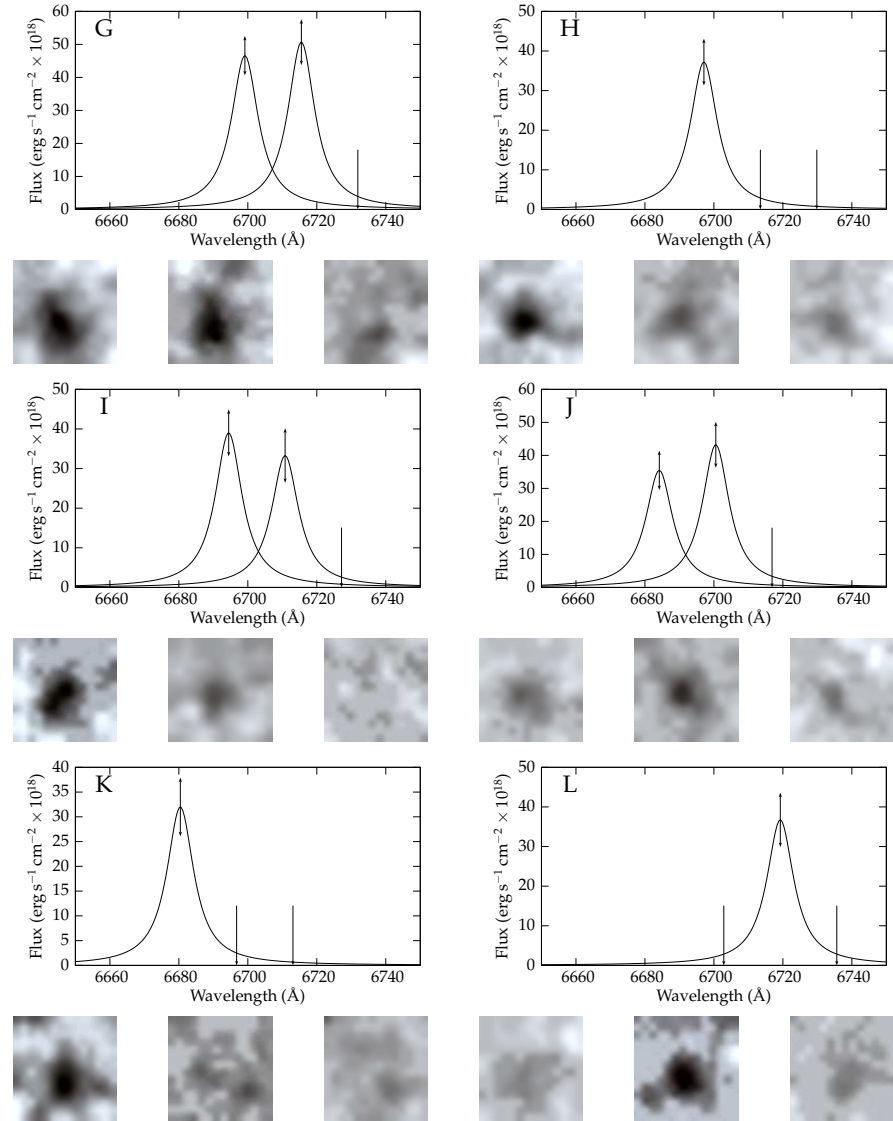
**Table 5.3:** ELG candidates in the field of BR B0019-1522, continued from previous page.

Identifier	Position (J2000)		Projected distance from Quasar (Mpc)	Lyman $\alpha$ Peak		AB magnitude
	R.A.	Decl.		Frame	Wavelength (Å)	
J	$0^h 21^m 58.6^s$	$-15^\circ 04' 56.2''$	0.941	Z451	6701	22.3
	6.2 $\sigma$ in Z451, 5.9 $\sigma$ in Z431. Not detected in Z471, but probably discernible in the thumbnail image.					
K	$0^h 22^m 14.2^s$	$-15^\circ 04' 20.6''$	0.791	Z431	6680	22.6
	5.4 $\sigma$ in Z431. Not detected in other images.					
L	$0^h 22^m 14.8^s$	$-15^\circ 07' 22.1''$	0.925	Z451	6719	22.5
	5.4 $\sigma$ in Z451. Not detected in other images.					
M	$0^h 22^m 15.3^s$	$-15^\circ 06' 52.7''$	0.846	Z471	6716	22.2
	7.7 $\sigma$ in Z471, 7.1 $\sigma$ in Z451. Not detected in Z431.					
N	$0^h 22^m 11.5^s$	$-15^\circ 05' 04.1''$	0.408	Z451	6706	22.3
	6.2 $\sigma$ in Z451, 4.0 $\sigma$ in Z471. Not detected in Z431, but discernible in the thumbnail image.					
O	$0^h 22^m 18.0^s$	$-15^\circ 04' 36.8''$	1.050	Z451	6694	22.4
	5.6 $\sigma$ in Z451. Not detected in other images.					
P	$0^h 21^m 53.9^s$	$-15^\circ 05' 58.2''$	1.364	Z431	6685	22.4
	6.8 $\sigma$ in Z431, 5.8 $\sigma$ in Z451. Not detected in Z471.					
Q	$0^h 22^m 13.9^s$	$-15^\circ 05' 08.8''$	0.607	Z431	6689	22.5
	6.0 $\sigma$ in Z431, 2.7 $\sigma$ in Z451. Not detected in Z471; not clear in thumbnail.					



*Continued overleaf...*

**Figure 5.8:** ELG candidates in the field of BR B0019-1522. For each object, the graph shows the flux recorded in and the wavelength at each etalon transmission band. The width of the curves indicated the etalon transmission profile. Error bars are calculated based on equation 3.13. 14 pixel square thumbnail images are displayed of the object as seen in each band.



*Continued overleaf...*

**Figure 5.8:** ELG candidates in the field of BR B0019-1522, continued from previous page.

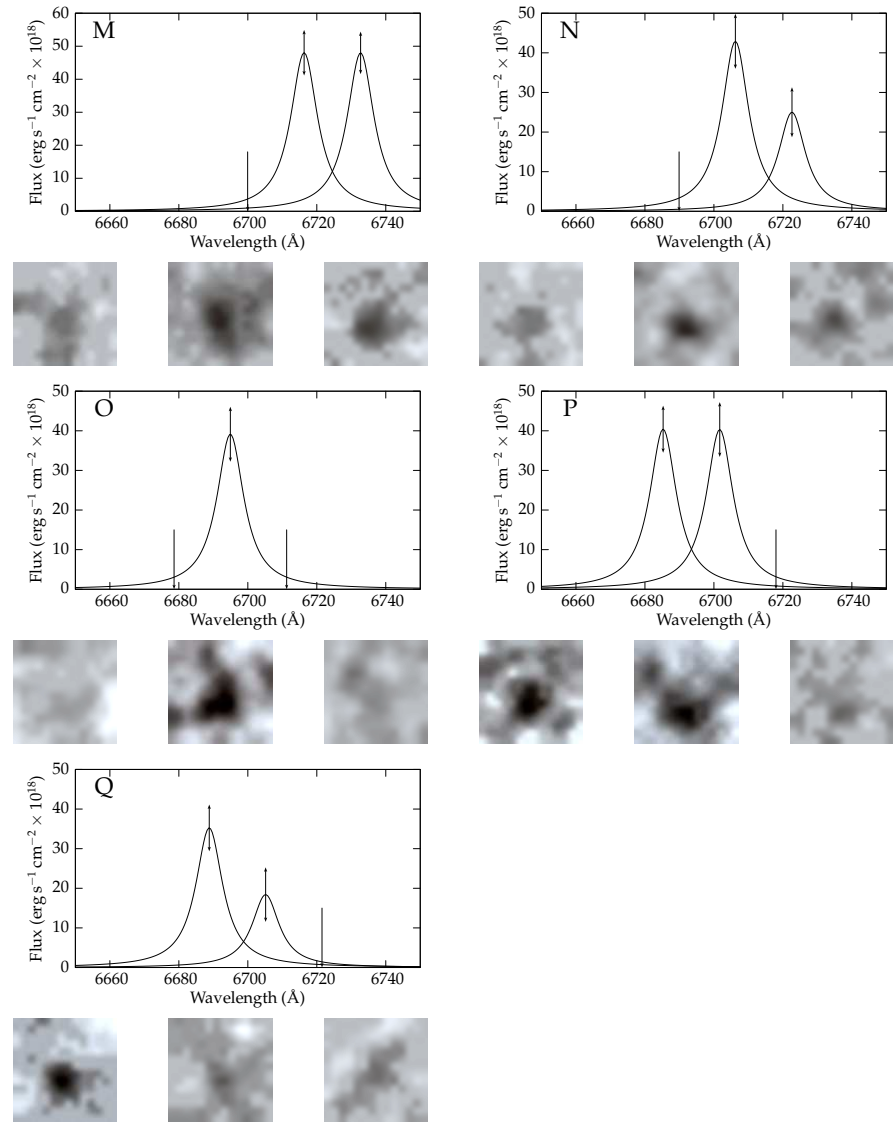


**Figure 5.8:** ELG candidates in the field of BR B0019-1522, continued from previous page.

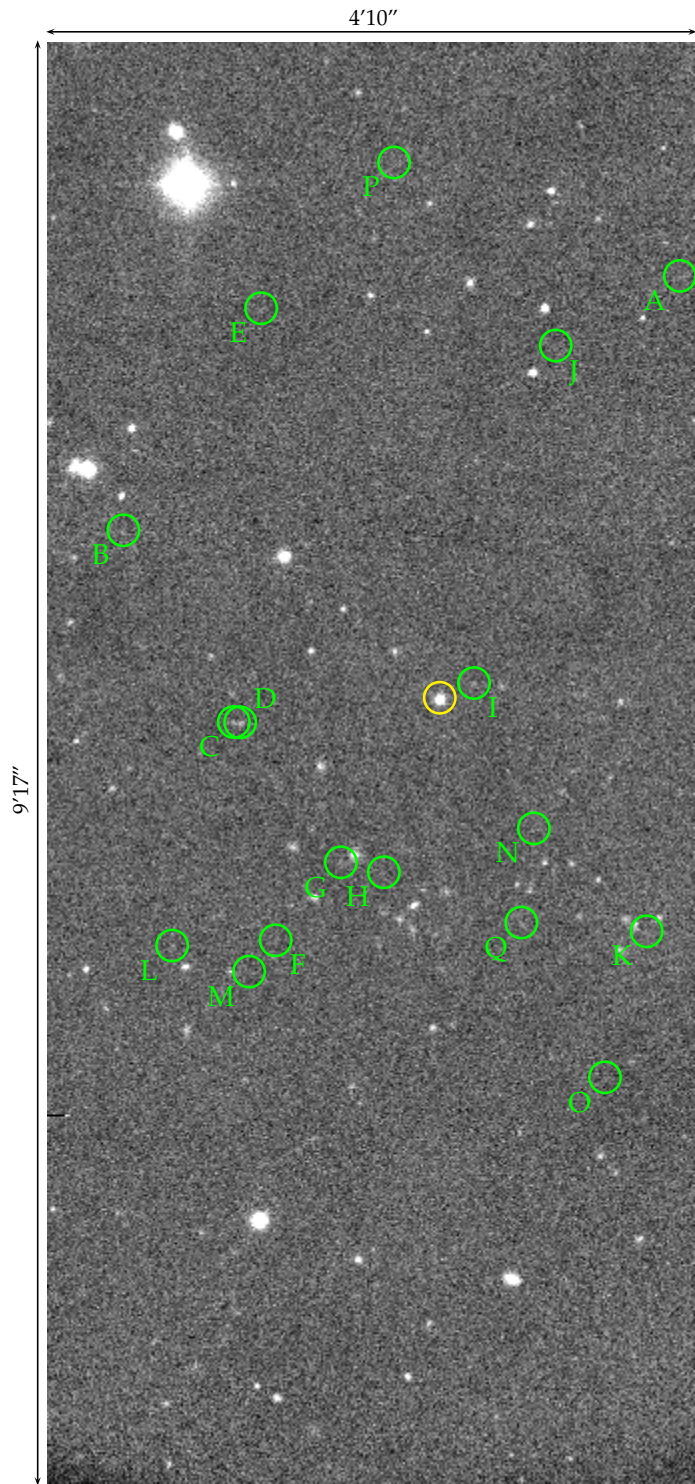


**Figure 5.9:** Positions of candidate emission line galaxies in the field of BR B0019-1522. North is right and east is down. Candidate galaxies are marked by green circles and the associated letters; the position of the quasar is marked by a yellow circle. The letters refer to ELG designations used throughout the text.

## 5.2 *Contaminants*

There are a variety of other effects which might incorrectly be identified as potential emission line galaxies in our observations. This section identifies the possible sources of confusion and discusses the steps taken to account for them.

### 5.2.1 *Noise artifacts*

As discussed in section 4.3.1, the selection criteria used when building lists of objects with SExtractor were chosen to minimise the number of false detections due to noise artifacts in the data. However, this was carried out using simulated data: although it provides a useful guide, the simulation may be less prone to some types of noise than others. For example, improperly subtracted ghosts, charge trapping artifacts or cosmic rays could be misconstrued as objects in the real data, but do not appear in the simulations at all.

Substantial lengths have been gone to to ensure that such artifacts do not occur. For example, in chapter 3 we discussed the filtering procedure for eliminating charge trapping and ghosts, while taking a median pass through the data rejected as many cosmic rays as possible. In addition, as described in section 5.1, each object was examined by eye in both the overall image and each individual frame to ensure it looked physically plausible. However, our detections are pushing at the limit of the sensitivity of the observations: it is impossible to rule out the possibility of some contamination.

### 5.2.2 *Continuum objects*

In section 5.1, potential emission line galaxies were identified by the characteristic shape of their spectrum—in other words, by searching for a peak that is visible in only one or two of the stack of images of a given field. However, as discussed in chapter 3 (and graphically demonstrated in chapter 4), the sensitivity of the observations varies from image to image within a field: see, for example, figures 4.4 (MRC B2158-206) and 4.5 (MRC B1256-243). There is, therefore, the possibility that a flat-spectrum source will *appear* to be peaked in more sensitive frames, while, in fact, the data were simply not deep enough to detect it in

the others.

In order to assess the probability of this occurring, we turn to the simulations of individual fields, as documented in section 4.3. Each of the individual objects is sorted into 3,600 bins by wavelength and magnitude—each bin covering 1 Å and 0.1 magnitudes, and containing around 80 simulated objects on average. It is possible to calculate a percentage completeness for each bin: the fraction of the simulated objects that are detected at a given significance level.

Each of the objects identified in section 5.1 can be assigned to a bin. It is then possible to check the equivalent bins (that is, corresponding to the same magnitude and pixel coordinate on the image) for completeness: if all of the objects in the bin are detected, it is unlikely that a flat spectrum could be misconstrued as a peak, but if the completeness varies significantly from image to image the potential for confusion is significant.

Taking this into consideration, the following objects are called into question: A in the field of MRC B2158-206, B in the field of MRC 1256-243 and E and K in the field of BR B0019-1522. These sources were carefully examined by eye, but there is no indication of a faint detection in the crucial frame. Therefore, they were not excluded from this analysis, but we note that there exists a question mark over their validity which can only be resolved by follow-up observations.

### **5.2.3 Lower redshift interlopers**

Our observations do not include any information about the spectrum of the object under examination, beyond the presence (or otherwise) of an emission line. There is, therefore, no way to be certain that we are observing Lyman  $\alpha$  at the target redshift: it is possible that we might be observing a longer wavelength line from a lower-z emission line galaxy. This section quantifies the number of such ‘interlopers’ which might be observed in each of our fields.

As well as Lyman  $\alpha$ , a variety of other spectral lines are produced by star-forming galaxies. A list of the most prominent is displayed in table 5.4, which is based on spectroscopy of galaxies in the local universe documented by Kennicutt (1992a). The table also

**Table 5.4:** Emission lines which have the potential to appear as ‘interlopers’ in our observations, together with the redshifts at which they might appear. The flux of each line relative to H $\alpha$  in a “typical” galaxy is given, based on the observations of Kennicutt (1992a).

Line	Rest-frame wavelength	Flux Ratio	Relevant redshift		
			MRC B1256-243	MRC B2168-206	BR B0019-1522
[O II]	3727 Å	0.41 ± 0.21	0.065	0.060	0.803
H $\beta$	4860 Å	0.14 ± 0.06	-	-	0.383
[O III]	5007 Å	0.20 ± 0.15	-	-	0.342
H $\alpha$	6548 Å	1.00 ± 0.00	-	-	0.027
[N II]	6583 Å	0.43 ± 0.16	-	-	0.021

lists the approximate redshift at which each line could be confused with our data, and gives the typical ratio of the line flux to H $\alpha$  in a given galaxy. This ratio is based on the data provided by Kennicutt (1992a); however, many of the fluxes—and particularly that of [O III]—show a very wide dispersion, so that these numbers should not be regarded as accurate. They do, though, enable us to make good estimate, if not a precise count, of the number of interlopers.

Cowie et al. (1997) and Gallego et al. (1995) provide number density counts for star forming galaxies as a function of star formation rate at a (complementary) range of redshifts. In section 6.2, we consider the relationship between line luminosities and star formation rates in some detail; for now, suffice it say that equation 6.2 makes it straightforward to calculate the expected H $\alpha$  luminosity from a galaxy of given star formation rate, and, using the flux ratios in table 5.4, this may be extended to include all of the listed lines. This calibration may then be used to calculate the potential number of each type of interloper in each field, as described below.

Note that Mg and C IV lines may also be observed in the spectra of star forming galaxies. They are, however, likely to be weaker than the lines listed above, and a convenient luminosity function was not readily available. We do not, therefore, consider them further here, but note their existence as a possible source of confusion.

### 5.2.3.1 Adapting a luminosity function to our cosmology

As described above, we make use of the number counts of galaxies at a given star formation rate provided by Gallego et al. (1995) and Cowie et al. (1997). However, there is a complexity: Gallego et al. and Cowie et al. both adopt an  $H_0 = 50 \text{ km s}^{-1} \text{ Mpc}^{-3}$ ,  $\Omega_\Lambda = 0$ ,  $\Omega_M = 1$  cosmology, in contrast to the  $H_0 = 70 \text{ km s}^{-1} \text{ Mpc}^{-3}$ ,  $\Omega_\Lambda = 0.7$ ,  $\Omega_M = 0.3$  system adopted by this thesis. It is therefore necessary to adapt their luminosity function to match ours. In addition, Gallego et al. assume a Scalo (1986) IMF\*, which is inconsistent with the assumptions made in section 6.2 of this thesis; Cowie et al. provide a conversion of the results of Gallego et al. to a Salpeter (1955) IMF: it is this conversion that is used here, and, for simplicity, we refer only to Cowie et al. from this point onwards.

Cowie et al. provide a luminosity function in terms of the number of galaxies with a given star formation rate per cubic megaparsec over a given redshift range. They estimate star formation rates in two ways (using the [O II] and 2500 Å luminosities): in both cases they are directly proportional to the observed flux from the galaxy.

The change in cosmology necessitates an adjustment of their results in two ways. Firstly, the redshift range surveyed now equates to a different volume. Given that the total number of galaxies observed remains constant, we can write

$$\rho(L_1, z) \frac{\partial V_1}{\partial z} = \rho(L_2, z) \frac{\partial V_2}{\partial z}. \quad (5.1)$$

That is, the product of the space density of galaxies of equivalent luminosity and the volume observed is a constant. In other words, a change in the volume observed necessitates a change in the space density to compensate. Secondly, the luminosity distance corresponding to a given redshift changes, and, with it, the calculated star formation rate. Cowie et al. bins their objects by star formation rate; consequently, the change in cosmology causes these bins to shift along the star formation rate axis.

Each of these is compensated for by a correction factor, which we go on to calculate. A volume correction factor, labelled  $\mathcal{F}_1$ , accounts for the first effect; a luminosity correction

---

\*That is, of the form  $\xi(M_*) = \xi_0 M_*^{-x}$ , where  $\xi(M_*)$  is the number of stars formed per unit mass range and  $M_*$  is the mass of a star. Salpeter (1955) adopted the model  $x = 2.35$ ; Scalo (1986) had it vary with  $M_*$ .

factor,  $\mathcal{F}_2$ , for the second. Relating this to equation 5.1, we have

$$\rho(L_2, z) = \rho(L_1, z) \times \frac{\partial V_2}{\partial z} / \frac{\partial V_1}{\partial z} \quad (5.2)$$

$$\simeq \rho^{(L_2/\mathcal{F}_2, z)} \times \mathcal{F}_1, \quad (5.3)$$

where the calculation of  $\mathcal{F}_1$  and  $\mathcal{F}_2$  is described below.

Both of the cosmologies under consideration have no spatial curvature: in other words,  $\Omega_k = 0$ . In such a case, Pen (1999) showed that the luminosity distance  $d_L$  may be conveniently approximated by

$$d_L = \frac{(1+z)c}{H_0} [\eta(1, \Omega_M) - \eta(1/(1+z), \Omega_M)] \quad (5.4)$$

$$\eta(a, \Omega_M) = \frac{2\sqrt{s^3 + 1}}{\left[ \frac{1}{a^4} - \frac{0.1540s}{a^3} + \frac{0.4304s^2}{a^2} + \frac{0.19097s^3}{a} + 0.066941s^4 \right]^{\frac{1}{8}}} \quad (5.5)$$

$$s^3 = \frac{1 - \Omega_M}{\Omega_M}, \quad (5.6)$$

where  $d_L$  is defined such that an object with luminosity  $L$  has flux  $F = L/(4\pi d_L^2)$ . Further, in a flat universe, the comoving volume from the present to a redshift  $z$  is

$$V = \frac{4\pi \times d_L^3}{3(1+z)^3} \quad (5.7)$$

(Carroll et al., 1992; Hogg, 2000). It is, therefore, straightforward to take a given redshift  $z$  and set of cosmological parameters— $H_0$ ,  $\Omega_M$ —and, in the assumption that  $\Omega_k = 0$ , calculate both the luminosity distance and the total comoving volume from the present to that redshift.

Cowie et al. provide a luminosity function over four redshift ranges covering the range  $0 \leq z \leq 1.6$ . Equation 5.7 may be used to calculate the total comoving volume in each of those ranges under both cosmologies: the results, and their ratio—which we label  $\mathcal{F}_1$ —are shown in table 5.5. At high redshift, each cubic megaparsec in their cosmology is equivalent to a larger volume in ours; at low redshift, this situation is reversed.

Now, the differing cosmologies adopted by this work and that of Cowie et al. mean

**Table 5.5:** Data required for the conversion of luminosity functions from the cosmology of Cowie et al. (1997) to that of this thesis.

Redshift		Volume (Gpc <sup>3</sup> )			Luminosity distance
Min.	Max.	Cowie et al.	This work	Ratio ( $\mathcal{F}_1$ )	correction factor ( $\mathcal{F}_2$ )
0.0	0.1	0.7	0.3	2.39	0.55
0.1	0.4	26.1	15.3	1.68	0.65
0.4	0.8	92.6	75.5	1.23	0.77
0.8	1.6	277.1	299.4	0.93	0.92

that an object they calculated a luminosity distance  $d_{L1}$  corresponding to a redshift  $z$ , while, for the same redshift, we calculate  $d_{L2}$ . From the definition of the luminosity distance above, it is clear that an object which has luminosity  $L_1$  calculated from its flux on the assumption that its luminosity distance is  $d_{L1}$  will have a new luminosity  $L_2 = (d_{L1}^2/d_{L2}^2) \times L_1$  calculated if that luminosity distance is subsequently re-calculated as  $d_{L2}$ . However, the ratio of  $d_{L1}$  to  $d_{L2}$  is not constant across the redshift ranges considered: it ranges from 1.33 at  $z = 0.1$  to 1.06 at  $z = 1.6$ .

Cowie et al. does not provide enough detail about the distribution of objects within the bins to enable us to apply a correction on a per object level. We therefore calculate a weighted average correction for each redshift range, which we label  $\mathcal{F}_2$ ; the corrected star formation rate over the range  $z_1$  to  $z_2$  is thus calculated as  $\mathcal{F}_2 \times \dot{M}$ , where  $\dot{M}$  is the star formation rate quoted by Cowie et al. and

$$\mathcal{F}_2 = \frac{\int_{z_1}^{z_2} \frac{dV(z)}{dz} \times (d_{L1}(z)/d_{L2}(z))^2 dz}{\int_{z_1}^{z_2} \frac{dV(z)}{dz} dz} \quad (5.8)$$

where  $V(z)$  is the total comoving volume in the cosmology of Cowie et al.: this is appropriate as it was in this cosmology that the distribution of objects was originally measured. The values of  $\mathcal{F}_2$  for each redshift range under consideration are tabulated in table 5.5.

In summary, then, in order to convert a point in the galaxy number density versus star formation rate plots of Cowie et al. to our cosmology, we multiply the number density by the factor  $\mathcal{F}_1$  and the corresponding star formation rate by  $\mathcal{F}_2$ . The data thus corrected are plotted in figure 5.10.

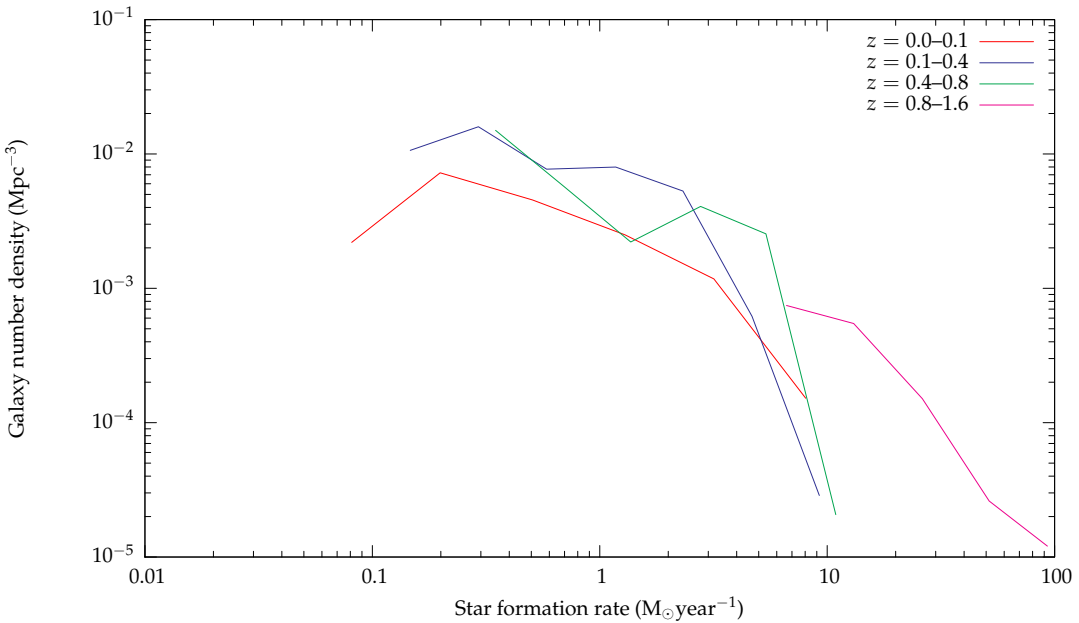


**Figure 5.10:** Number densities of star forming galaxies, as a function of star formation rate and redshift. Based on data taken from Cowie et al. (1997) and Gallego et al. (1995), but adapted to our cosmology as described in section 5.2.3.1.

### 5.2.3.2 Number of interlopers

In the last section, a relationship between the number density of galaxies of a given star formation rate and redshift was arrived at. In order to translate this number density to a number of objects which might be observed in our fields, it is therefore necessary to calculate the volumes over which interlopers may be observed.

Calculation of the survey volume is not immediately straightforward, as it depends on the magnitude of the objects being surveyed. Consider, for example, figure 4.7(a). This illustrates the fraction of objects detected in the field of MRC B2158-206 as a function of their wavelength and AB magnitude. A bright object—19<sup>th</sup> magnitude, say—may be detected at a range of wavelengths, from around 3920 Å to 4010 Å. A fainter object at, for instance, 22<sup>nd</sup> magnitude is only detected if it lies within a much smaller wavelength range: around 3940 Å to 3960 Å. These wavelength ranges correspond directly to the redshift windows over which objects may be observed and, therefore, to the volume surveyed.

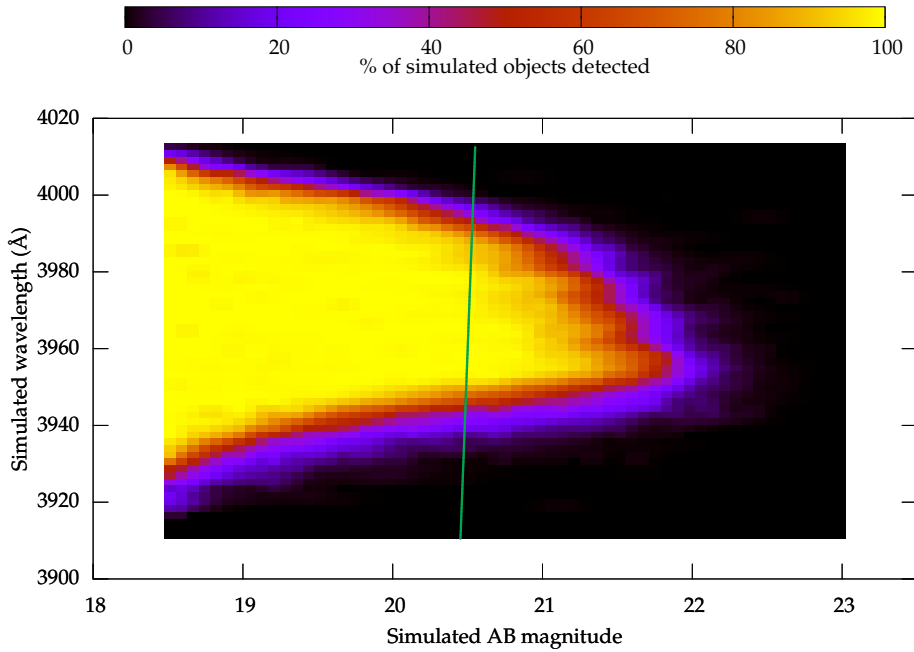


**Figure 5.11:** The locus of points which correspond to an object of a certain emission line luminosity—and hence star formation rate—is shown as a green line overlaid on a plot of the completeness of the MRC B2158-206 frame (figure 4.7(a)). In this illustration, the locus of points shown corresponds to an object forming stars at a rate of  $\sim 50 \text{ M}_\odot \text{ year}^{-1}$ .

Consider an object of given star formation rate. It is possible to convert this star formation to an H $\alpha$  luminosity. This is an issue which we discuss at some length in section 6.2.1; for now, suffice it to say that we use the calibration of Kennicutt (1998):

$$\text{SFR}(\text{M}_\odot \text{year}^{-1}) = 7.9 \times 10^{-42} L(\text{H}\alpha)(\text{erg s}^{-1}). \quad (5.9)$$

Combined with equation 5.4, it is therefore possible to calculate the H $\alpha$  flux from such a galaxy when observed at a given redshift, and hence to estimate the AB magnitude we might expect to observe (equation 3.10). After applying an appropriate correction for etalon effects (section 4.2.2.2) and galactic extinction (Schlegel et al., 1998), a locus of points in the magnitude-wavelength completeness diagram (figures 4.7(a), 4.8(a) and 4.9(a)) within which such an object could lie may be determined.

Using the flux ratios given in table 5.4, a similar locus may also be defined for emission from the other spectral lines.

The next step is to calculate the volume corresponding to such a locus. This is done

**Table 5.6:** Calculated numbers interloping low-redshift emission line galaxies which might be observed in each of the observed quasar fields. A superscript  $\ell$  indicates that the functions shown in figure 5.10 do not reach a sufficiently low star formation rate to make the analysis exhaustive—an issue which is discussed further in the text.

Line	Estimated number in field		
	MRC B2158-206	MRC B1256-243	BR B0019-1522
[O II]	0.05 $^\ell$	0.02	1.93
H $\beta$	-	-	1.68
[O III]	-	-	1.41
H $\alpha$	-	-	0.01 $^\ell$
[N II]	-	-	0.01 $^\ell$

by determining the area observed in each frame and then integrating along the line (we use steps of 1 Å; smaller intervals were found to increase the computation time without significantly altering the results), using equation 5.7 to calculate the total volume observed. In each wavelength bin, the volume is multiplied by the fractional completeness at that position, as read from figure 5.11. In this way, an “accessible volume” for objects of the given star formation rate is calculated. This accessible volume is multiplied by the space density of objects at the given star formation rate as read from the appropriate curve in figure 5.10 to estimate the total number of such objects we might observe. Finally, we integrate over the full length of the curves in figure 5.10, performing the above calculation at each point. In this way, the total number of interlopers which might be observed is calculated.

The results of this process are shown in table 5.6. Note that for some low-redshift interlopers, the minimum observable star formation is very low, so that the curves of figure 5.10 do not reach low enough star formation rates to enable the calculation to be carried out in full. These cases are indicated in the table. Note, however, that in these cases the galaxies are sufficiently nearby, and the contrast between the peak and the continuum magnitude is sufficiently low, that these would not display a peak satisfying the conditions for detection as a potential high- $z$  emission line galaxy.

In the case of the  $z \sim 2.2$  MQS fields, effectively no interlopers are likely to be observed in these fields, and we do not consider them further. However, we might expect as

many as five to appear in the observations of BR B0019-1522. This is a substantial fraction of the 17 ELG candidates we have identified. It is not possible from the data available to us to pick out which they are, so we do not attempt to exclude any of the 17 objects: from this point onwards, the analysis is presented including all of them. However, it should be borne in mind that there is a possible overestimate of quoted densities in this field by a factor of somewhat less than one third.

### **5.3 Summary**

In this chapter, we have identified candidate emission line galaxies in all three of the quasar fields: two in the field of MRC B2158-206, four in that of MRC B1256-243 and seventeen around BR B0019-1522. We have presented full details of each galaxy candidate, including thumbnail images and an indication of its position within the quasar field. We have also considered the possibility of contamination of our sample from a variety of sources, and taken steps to estimate its extent and, where possible, eliminate it.

In the next chapter, we will assess the properties of the galaxies and the field, estimating their star formation rates and searching for evidence of structure around the quasars.

# Chapter 6

## *Distribution and properties of galaxy candidates*

The aim of this thesis is not merely to identify emission line galaxies, but to set them in the context of the broader quasar environment. In this chapter, we investigate the objects previously identified, searching for evidence of visible structure or galaxy overdensities around the quasars. We move on to consider the star formation rates of galaxies in the quasar environments.

### 6.1 *Clustering of ELG candidates*

In this section, we consider the distribution of the candidate emission line galaxies around the quasar: the aim is to determine whether the quasar lies in an identifiable overdensity of galaxies relative to the field.

We have two pieces of information about the positions of the ELGs relative to the quasars. First, their pixel positions on the detection images, relating directly to their position on the sky, and secondly the wavelength at which they are detected, corresponding to their position and relative velocity along our line of sight. We consider each of these separately.

#### 6.1.1 *Distribution on the sky*

The projected distribution on the sky of the ELG candidates is considered separately for the  $z \sim 2.2$  MQS fields and for the higher-redshift BR B0019-1522.

Over the course of this section, we make repeated reference to the projected distance

on the sky of an object from the quasar. This distance is calculated based on the angle subtended. Recall that these images have a pixel scale of either 0.33 (MQS objects) or 0.37 (BR B0019-1522) arcseconds. Given that the angular size distance  $d_A$  may be written as  $d_L / (1 + z)^2$  (Carroll et al., 1992), equation 5.4 (page 148) may be used to calculate the distance scale of the images. At the redshifts of these quasars, one arcsecond corresponds to 8.235 kpc (MRC B2158-206), 8.227 kpc (MRC B1256-243) or 6.585 kpc (BR B0019-1522).

### 6.1.1.1 Redshift $\sim 2.2$

The distribution of ELG candidates on the sky with respect to the two Molonglo quasars is shown in figures 5.3 and 5.6 (pages 132 and 136), while the projected distances of each object from the quasar recorded are in tables 5.1 and 5.2 (pages 130 and 134).

The number of objects detected in each of these fields is low—a total of only six objects, roughly evenly distributed across both fields. This low count necessarily makes any statistical analysis performed on the fields unreliable. In an attempt to mitigate this, and because the fields appear similar, we consider both the fields as one unit in this section.

In figure 6.1, the number of candidate emission line galaxies is plotted as a function of their distance from the quasar. Both the total number of galaxies in each 0.25 Mpc distance bin is shown and, in figure 6.1(b), the number is normalised according to the visible area on the sky in the distance bin. This area consists of a series of concentric annuli: the area small in those nearest the quasar (due to their small radius), increasing with distance but then, at the largest radii, being truncated by the edge of the visible field.

There is no evidence for any clustering based on these figures: the number of ELG candidates per square megaparsec on the does not vary significantly with distance from the quasar. It is, however, worth noting once again that this analysis is plagued by poor statistics and the attendant large margin of error. A close examination of figures 5.3 and 5.6 is not encouraging: only one of the objects (MRC B2158-206 object A) is seen in close proximity ( $\sim 260$  kpc) to its associated quasar, the other objects falling at the edges of typical cluster scale lengths observed around AGN by other work (a comparison is drawn in the next chapter). It is noteworthy that all four objects observed in the field of MRC B1256-243 appear at approximately the same projected distance to the south of the quasar, spread

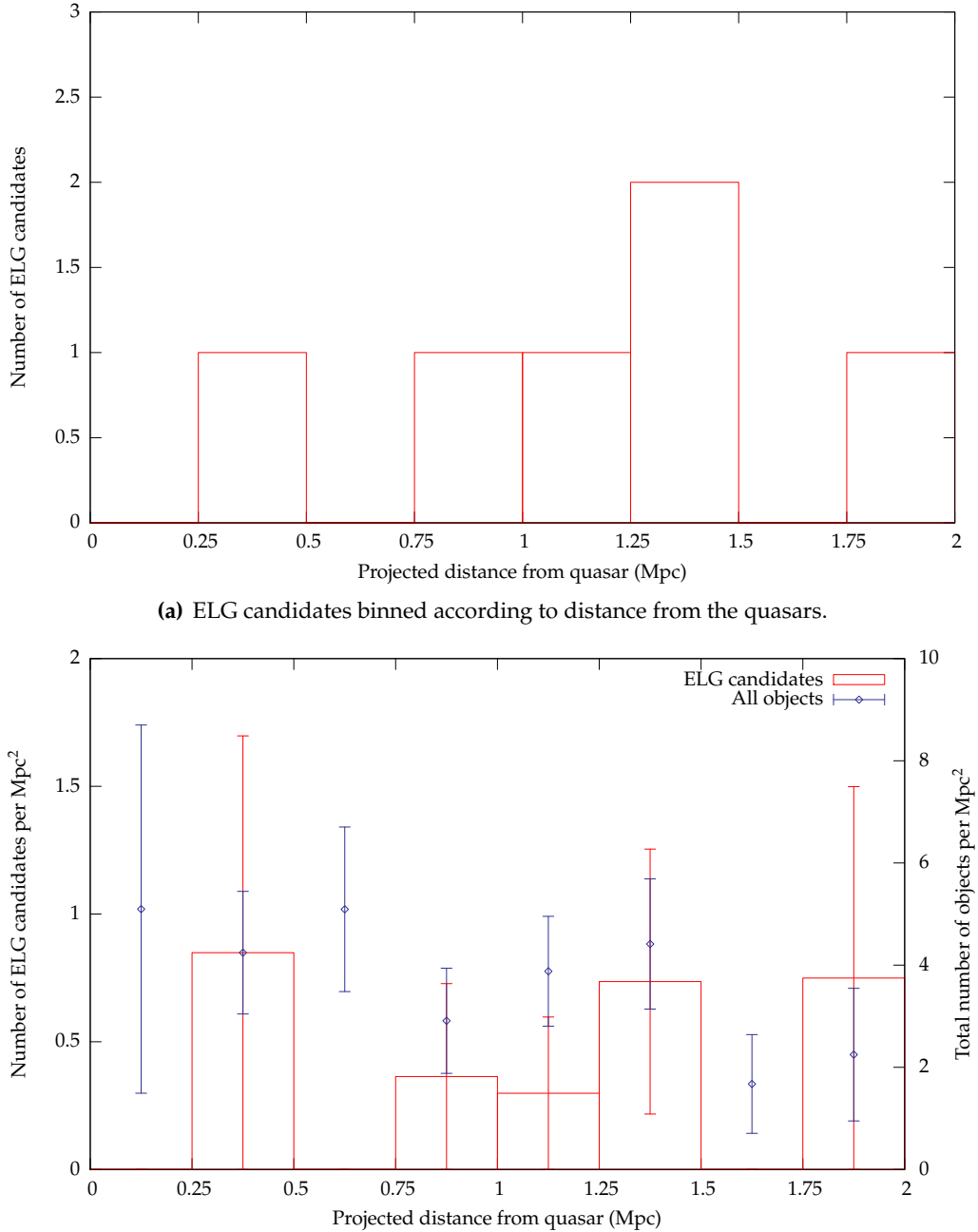


**Figure 6.1:** Variation of the number of ELG candidates detected with distance from the quasar in the redshift  $\sim 2.2$  fields. In (a) raw object counts are shown; in (b), the number of objects is normalised by the total visible area on the sky at a given distance. Objects are sorted into bins of width 0.25 Mpc. For comparison, the density of all other objects detected in the field at a  $5\sigma$  level but not classified as potential ELGs is also plotted in (b)—note that the vertical scales are different.

fairly equally along the east-west dimension of the field. There is, perhaps, a suggestion of filamentary structure here, but, once again, we are stymied by low number counts.

### **6.1.1.2 Redshift $\sim 4.5$**

The distribution of ELG candidates on the sky with respect to BR B0019-155 is shown in figure 5.9 (page 143); their projected distances from the quasar are recorded in table 5.3 (page 138). Conversion of angle to projected distance is carried out as described in previously, but note that the pixel scale is now 0.37 arcseconds, and that, at a redshift  $z = 4.528$  the angular scale is 6.585 kpc to the arcsecond.

This field is considerably richer than those at lower redshift. To some extent, this may be attributed to longer exposure times making it sensitive to fainter magnitudes (figure 4.10 on page 125, although note that the peaks of figures 4.10(a) and 4.10(c) actually correspond to very similar source luminosities).

Figure 6.2 is the equivalent of figure 6.1 for this field. This figure has substantially more tightly constrained errors than in the previous field, due to the larger number of objects. It also provides much more convincing evidence for clustering: the number of objects per square megaparsec clearly tails off with distance from the cluster, moving from a peak of around  $9 \text{ Mpc}^{-2}$  to no objects detected further than 1.5 Mpc away. This is similar to the scale lengths observed in other fields, to which we will compare it in section 7.2.2.

It is also informative to examine figure 5.9: there is considerable evidence for structure in the distribution of the objects about the quasar. There is one object—I—in relatively close proximity to the quasar, at less than 100 kpc. There is a substantial grouping of 9 objects at around 0.5–1.0 Mpc east of the quasar, which may indicate richer clustering slightly offset from the position of the quasar itself. Further east in the field there are no detections, while to the west of the quasar there are some well spaced objects, with little evidence of any structure.

In short, there is a definite suggestion of clustering in this field. Later in this thesis we will consider how it compares to both blank field studies and other work on the environments of AGN.

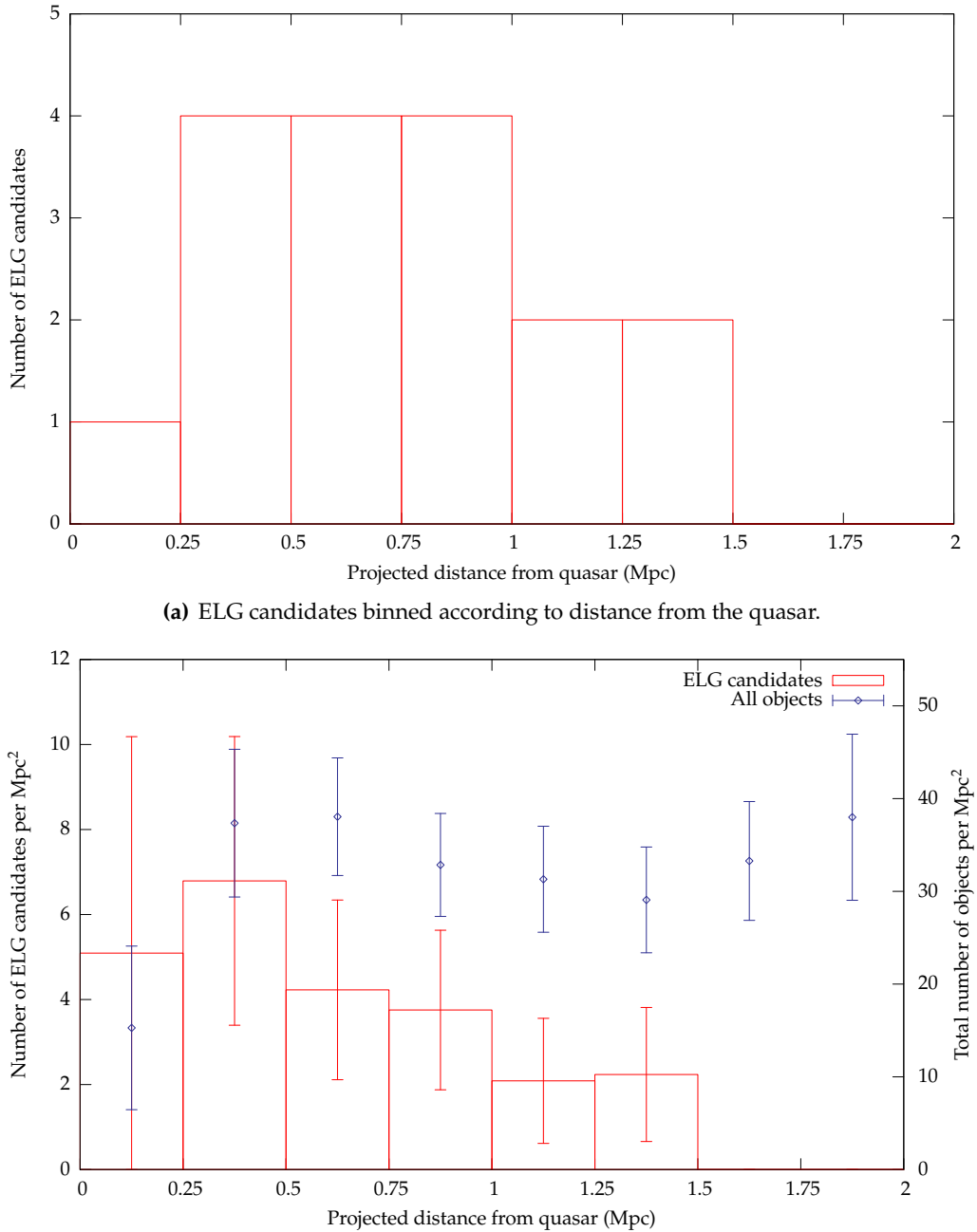


**Figure 6.2:** Variation of the number of ELG candidates detected with distance from the quasar BR B0019-1522. In (a) raw object counts are shown; in (b), the number of objects is normalised by the total visible area on the sky at a given distance. Objects are sorted into bins of width 0.25 Mpc. For comparison, the density of all other objects detected in the field at a  $5\sigma$  but not classified as potential ELGs is also plotted in (b)—note that the vertical scales are different.

### 6.1.2 *Distribution along the line of sight*

Once again, the MQS fields are considered separately from the BR B0019-1522 data.

#### 6.1.2.1 *Redshift $\sim 2.2$*

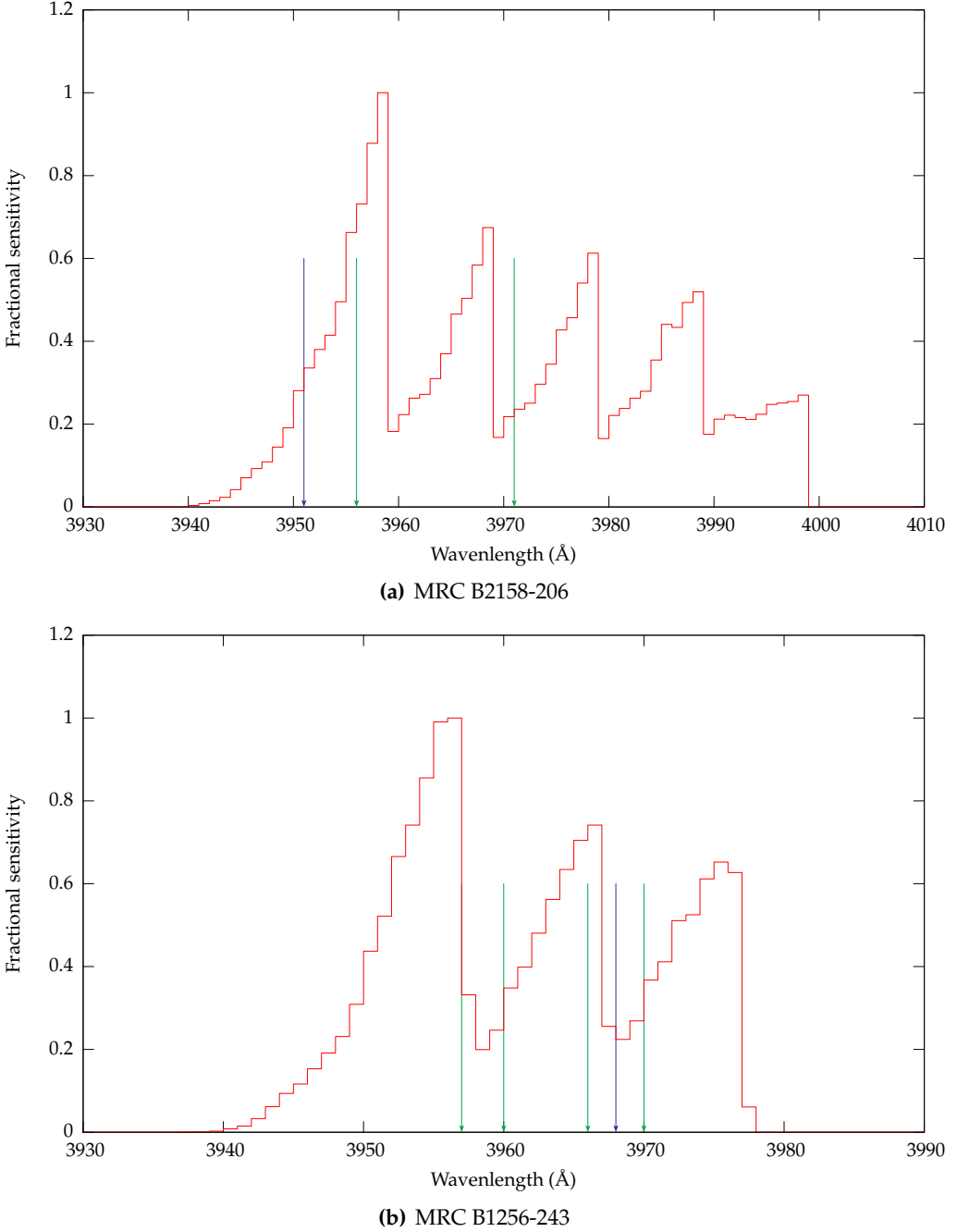
The wavelength at which each of the candidate ELGs was detected is recorded in tables 5.1 (MRC B2158-206 field) and 5.2 (MRC B1256-243). Note that the detected wavelength is taken as the wavelength of peak transmission in the image which recorded the maximum signal at the pixel coordinates of the object: it does not necessarily coincide exactly with the actual peak of the emission (which is not measured by our observations).

Figure 6.3 shows the detected wavelength of each ELG candidate with respect to the expected wavelength of the quasar's Lyman  $\alpha$  emission, the latter being calculated based on its documented redshift. It is important to note, however, that not all wavelengths are equally likely: there are more detector pixels that correspond to some wavelengths than others.

Consider the simulations of the overall field, as described in chapter 4. In each field, 300,000 objects were simulated, covering all possible wavelengths that we might detect: 3900–4020 Å in the case of MRC B2158-206, 3920–4000 Å for MRC B1256-243 and 6640–6790 Å for BR B0019-1522. The objects were randomly spread over the wavelengths: there are (within Poisson errors) the same number of objects simulated at each wavelength.

However, the number of objects *detected* at each wavelength is not a constant: it depends on how much of the detector area is sensitive and on the overall throughput of the instrument at that wavelength. We quantify this by measuring the number of simulated objects detected at a given wavelength. This is also shown in figure 6.3 for comparison with the wavelengths of the detected objects. Note that this selection function modulates any clustering observed in the figure.

Figure 6.4 shows the velocity dispersion of ELG candidates about the quasars. Data are shown both in terms of raw number counts, and also normalised to reflect the wavelength sensitivity in the bin. Since a total of only seven objects were detected in the MQS



**Figure 6.3:** Distribution of ELG candidates along the line of sight to the quasar in each of the  $z \sim 2.2$  MQS fields. The blue arrows show the wavelength of the quasar Lyman  $\alpha$  peak (based on the catalogue redshift); the detected ELG wavelengths are shown in green. For comparison, the likelihood of detecting objects at a given wavelength is also shown (in red); see the text for a discussion..

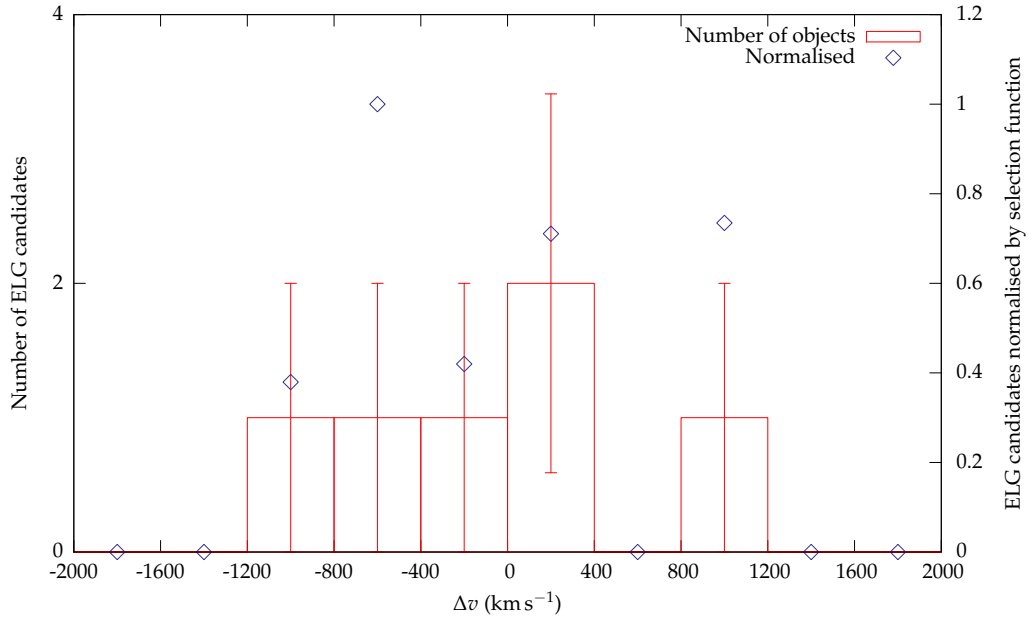


**Figure 6.4:** Relative velocities of all the ELG candidates detected in both the MQS fields with respect to the quasars. The data are plotted for both raw number counts (in red, with Poissonian error bars) and normalised in terms of the sensitivity to the range in question (blue).

fields, the statistics are of poor quality. In order to help offset this, the data from both fields was combined in one plot—note that the error bars are still of the same order as the data, so it is impossible to use this figure to draw firm conclusions.

Based on these figures, the evidence for an overdensity along the line of sight to these quasars is inconclusive. The uncertainties in figure 6.4 render it of little value; however, it is noteworthy that all the objects fall within roughly  $1000 \text{ km s}^{-1}$  of the quasar. This is of the same order as clusters observed around other AGN, a matter we discuss more fully in section 7.2.2.

Figure 6.3 is also inconclusive, but holds out some prospect of clustering. Both of the objects detected in the MRC B2158-206 field lie within  $20 \text{ \AA}$  of the quasar, and none are detected in the nearly  $30 \text{ \AA}$  surveyed (albeit with less sensitivity) longwards of this. It is unfortunate that we are not sensitive in any useful volume short of the quasar in this field.

A similar state exists in the MRC 1256-243 field. The objects are all observed within  $15 \text{ \AA}$  of the quasar, and, furthermore, not necessarily falling in the wavelength ranges to

which we are most sensitive. Once again, we are left with a tantalising prospect, but are frustrated by poor survey depth.

#### **6.1.2.2 BR B0019-1522**

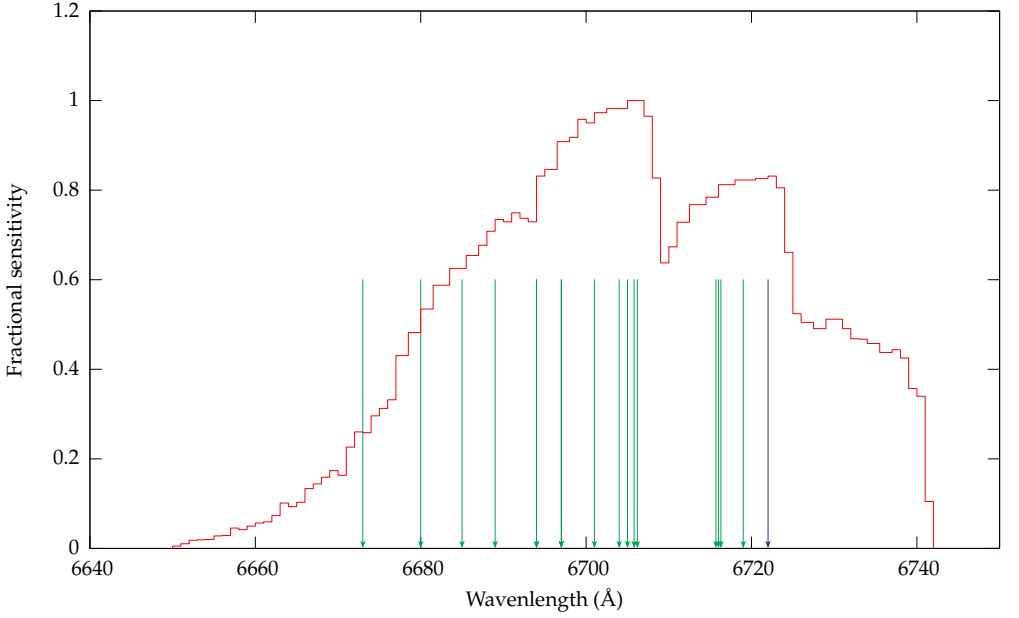
The detected wavelengths of candidate ELGs in the field of BR B0019-1522 are recorded in table 5.3; note once again the limited wavelength resolution of our measurements.

Figure 6.5 displays the equivalent information for this field as figures 6.3 and 6.4 did for the MQS fields. Some structure is immediately evident: there are no objects detected redward of the quasar. This is not because we are not sensitive in this range: as seen in figure 6.5(a), there is a range of almost 20 Å over which we might expect to detect redder objects (albeit a range with slightly reduced sensitivity).

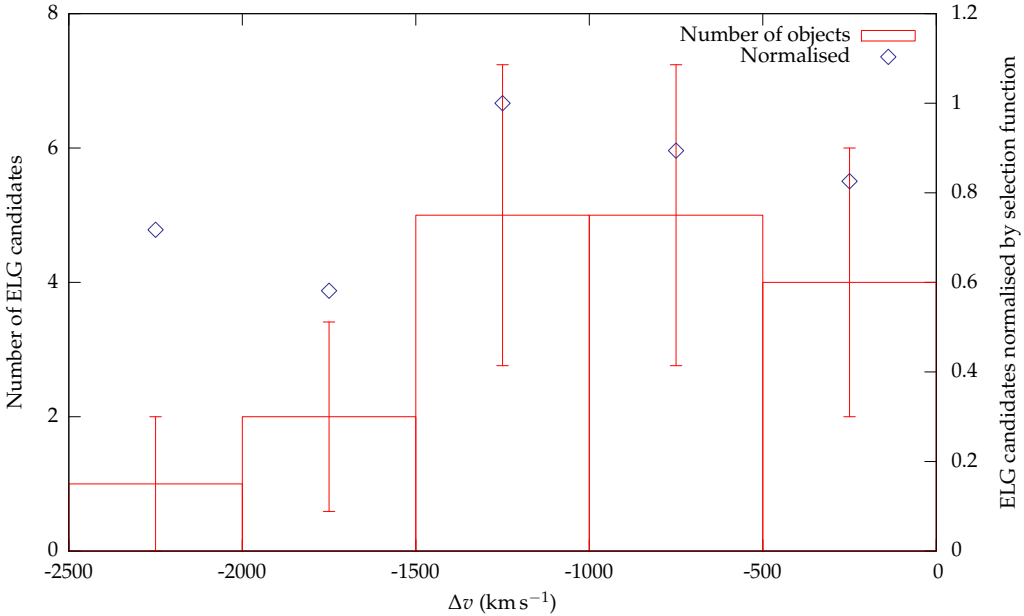
There is also a cluster of four objects within a few Å of the quasar. These are objects F, G, L and M: note from figure 5.9 that these objects all appear in a tight group around 0.75 Mpc south-east of the quasar position. The other objects do not follow the same pattern: there is no correspondence between observed wavelength and position on the field.

Figure 6.5(b) displays the velocity dispersion of the objects about the quasar, both in terms of raw counts and normalised by the wavelength sensitivity. Again, the lack of objects redward of the quasar (that is with a positive relative velocity) is striking. Shortward of this, the raw number counts do show a peak within  $1500 \text{ km s}^{-1}$  of the quasar, tailing away at greater velocities. However, this is not so clearly reflected in the normalised count rate; it is impossible to be sure if this structure is real, or is simply due to the lower number of pixels on the detector sensitive to the bluest wavelengths.

Once again, then, the evidence for an overdensity along the line of sight to this object is best described as equivocal. There is certainly some encouraging suggestion of structure (perhaps most notably in the dearth of objects redward of the quasar), but the density of objects seen at shorter wavelengths than the Lyman  $\alpha$  emission from the quasar cannot be definitively said to be decreasing with distance from the quasar wavelength.



(a) Wavelengths of the quasar (blue arrow) and those measured for ELG candidates (green); the red curve indicates the volume sampled at each wavelength in terms of the number of pixels.



(b) Relative velocities of the ELG candidates with respect to the quasar, shown for both raw object counts (red) and normalised to the number of pixels sensitive in each range (blue).

**Figure 6.5:** Distribution of ELG candidates along the line of sight to the quasar in the field of BR B0019-1522. In (a), the relative wavelengths of the quasar and the ELG candidates are displayed. Note that all the ELGs are observed bluer than the quasar. In (b), the objects are binned by velocity relative to the quasar.

### 6.1.3 Space density of galaxies

Perhaps the most convincing way of identifying a protocluster is to observe an overdensity of galaxies in three-dimensional space. In order to determine whether such an overdensity has been observed, it is first necessary to arrive at a definition of the volume surveyed by our observations.

#### 6.1.3.1 Volumes and completeness correction

In section 5.2.3.2, the issues surrounding measurement of the survey volume were touched upon. The idea of introducing an accessible volume—the comoving volume over which an object of given luminosity might be observed—was introduced. We make use of much the same concepts here.

If the volume surveyed depends on magnitude, then it is different for each of the detected objects in each field. We cannot, therefore, arrive at a density of objects by simply dividing the total number of objects by a single depth for the field. Instead, in a field containing  $n$  objects, we define the density  $\rho_n$  as

$$\rho_n = \frac{1}{V_1} + \frac{1}{V_2} + \dots + \frac{1}{V_n}, \quad (6.1)$$

where  $V_n$  is the comoving volume corresponding to the properties of the  $n^{\text{th}}$  object observed.

The problem, therefore, is reduced to calculating an accessible volume for each object detected, a task we approach as follows. Each object is detected at a given wavelength and magnitude, as recorded in section 5.1.

Now the object can be mapped onto the plot of completeness as a function of (simulated) wavelength and AB magnitude (figures 4.7(a), 4.8(a) and 4.9(a) on pages 121–123). Recall that the AB magnitude in these plots already includes a conservative correction for etalon effects, of the order discussed in section 4.2.2.2: the plotted magnitude corresponds to that we observe if the emission line is coincident with the etalon transmission. Of course, this is not in general the case, and it is important not to underestimate the offset here, or we will underestimate the accessible volume for the object and hence calculate incorrectly

high densities. Therefore, we apply a further correction, making the approximation that objects will be evenly spread in wavelength space around the etalon peaks. This means that the observed magnitudes are taken as being 0.23 (in the MQS fields) or 0.27 (in the BR B0019-1522 field) brighter than observed for the purposes of the following calculation.

The original wavelength is now converted to a redshift ( $z + 1 = \lambda / 1216$ ), which is, in turn, used to calculate the luminosity distance (equation 5.4). The luminosity distance is calculated similarly for each wavelength, and thus used to map the given source luminosity to an apparent magnitude at each wavelength. The locus of points occupied by such a source is thus defined in much the same way as for objects of given star formation rate in section 5.2.3.2. Figure 5.11 (page 151), indeed, shows the locus of points corresponding to an object observed with an AB magnitude of 20.5 and recorded wavelength 3960 Å in the field of MRC B2158-206.

In order to estimate the comoving volume over which such an object might be observed, we calculate the area observed in each frame, and then integrate over all wavelengths covered by the observations, much as described in section 5.2.3.2. The integration was performed numerically in 1 Å steps: smaller intervals increase the computation time without significantly altering the results. Each step was weighted by the fractional completeness of the observations at that point.

In short, then, we calculate an effective accessible volume for each object, taking into account the range of wavelengths surveyed and the fractional completeness at each wavelength. It is these volumes, calculated individually for each object, which are used in equation 6.1 to estimate the total space density of objects.

### **6.1.3.2 Calculated number densities**

Accessible survey volumes were computed for each of the objects detected in each field, following the method described above. They are presented for each object in tables 6.1 (MRC B2158-206), 6.2 (MRC B1256-243) and 6.3 (BR B0019-1522); the total number densities are  $9.52 \pm 6.77$  for MRC B2158-206,  $22.48 \pm 11.64$  for MRC B1256-243 and  $49.08 \pm 12.21$  for BR B0019-1522.

**Table 6.1:** Accessible volumes for each of the objects in the field of MRC B2158-206. The volumes are then used to calculate a total number density using equation 6.1.

Object	Accessible volume ( $V \text{ Mpc}^3$ )	$1/V (\text{Mpc}^{-3} \times 10^4)$
A	1887	5.30
B	2637	4.22
Total	-	$9.52 \pm 6.77$

**Table 6.2:** Accessible volumes for each of the objects in the field of MRC B1256-243. The volumes are then used to calculate a total number density using equation 6.1.

Object	Accessible volume ( $V \text{ Mpc}^3$ )	$1/V (\text{Mpc}^{-3} \times 10^4)$
A	1959	5.10
B	1232	8.12
C	1929	5.18
D	2450	4.08
Total	-	$22.48 \pm 11.64$

**Table 6.3:** Accessible volumes for each of the objects in the field of BR B0019-1522. These comoving volumes are used to calculate a total number density using equation 6.1.

Object	Accessible volume ( $V \text{ Mpc}^3$ )	$1/V (\text{Mpc}^{-3} \times 10^4)$
A	3097	3.23
B	3197	3.13
C	4629	2.16
D	4998	2.00
E	2076	4.82
F	4414	2.27
G	4414	2.27
H	3178	3.15
I	3539	2.83
J	3893	2.57
K	2669	3.75
L	3223	3.10
M	4180	2.39
N	3901	2.56
O	3539	2.83
P	3535	2.83
Q	3138	3.19
Total	-	$49.08 \pm 12.21$

In all cases—and particularly the MQS fields, which have a smaller number of detected objects—the uncertainties on these results are large. It is immediately noteworthy, though, that the field of MRC 2158-206 is significantly the poorest, while BR B0019-1522 is the richest, with around twice the density of MRC 1256-243 and five times that of MRC 2158-206. Note from section 5.2.3 that it is also most susceptible to low-redshift interlopers; they may constitute on the order of one third of the total number density. Further, note that the objects detected in the field of MRC B1256-243 are considerably more luminous than those in the other fields (see, for example, the peaks in figure 4.10). In order to compare the fields more directly, both with each other and with the results of other work, it is necessary to take the difference in luminosity ranges into account. This is done in the next section.

In order to assess whether these results constitute a significant overdensity, it is necessary to compare them to equivalent surveys of field galaxies. This is a topic to which we return in the next chapter.

## **6.2 Star formation rates**

As discussed in chapter 1, the AGN activity and star formation in its environment are hypothesised to be intimately linked. In this section, we turn to discussing the star formation properties of our candidate emission line galaxies.

### **6.2.1 Lyman $\alpha$ calibration**

Apart from simple flux and position of candidate ELGs, the other property of emission galaxies that Lyman  $\alpha$  opens for investigation is their star formation rates. This was first postulated by Partridge and Peebles (1967); the fundamental idea being that ionising radiation from young stars prompts the recombination of hydrogen in the interstellar medium.

How, then, can we calibrate Lyman  $\alpha$  luminosity to star formation rates? The starting point is to build a model of the luminosity of a typical galaxy, using the technique of “population synthesis modelling”. A set of model stars is produced for a variety of different stellar masses, using standard stellar atmosphere models and spectral libraries. These models are then summed together and weighted by a given initial mass function

(IMF) to estimate the properties—luminosity, colour, spectrum—of stellar populations as a function of age. It is then possible to add the various isochrones to simulate the spectrum of a galaxy with an arbitrary star formation history. This technique has been used to build models which are in very close agreement with observation: see, for example, Charlot and Bruzual (1991). A wide variety of synthesis models have been produced based on the technique outlined above: a compilation is provided by Leitherer et al. (1996).

Nebular recombination lines effectively re-emit the integrated luminosity of galaxies shortward of the Lyman limit. Since our population synthesis model tells us that this is where the youngest stars tend to dominate the galactic emission, this tells us that we can use these nebular lines as a sensitive probe of the star formation rate, independent of any previous star formation history.

Kennicutt et al. (1994) developed a population synthesis model based on H $\alpha$  and UV observations of 210 nearby galaxies, together with the stellar evolution tracks of Schaller et al. (1992). Assuming solar abundances and a Salpeter IMF in the range 0.1–100 M $_{\odot}$ , Kennicutt (1998) used this model to derive the relationship

$$\text{SFR}(\text{M}_{\odot}\text{year}^{-1}) = 7.9 \times 10^{-42} L(\text{H}\alpha)(\text{erg s}^{-1}), \quad (6.2)$$

linking the star formation rate (in solar masses per year) directly to the H $\alpha$  luminosity of a galaxy.

Kennicutt et al. does not reach an equivalent calibration between Lyman  $\alpha$  luminosity and star formation rate. However, Brocklehurst (1971) and Hu and McMahon (1996) provide us with a relationship between H $\alpha$  and Lyman  $\alpha$  luminosities. Assuming “case B” recombination—that is, that the rate of depopulation of an excited state by the emission of Lyman quanta is balanced by the rate of population due to absorption of Lyman quanta—a ratio of Ly  $\alpha$  to H $\alpha$  of 8.2 applies.

Combining these results, we estimate the total star formation rate based on Lyman  $\alpha$  emission as

$$\text{SFR}(\text{M}_{\odot}\text{year}^{-1}) = 0.91 \times 10^{-42} L(\text{Ly}\alpha)(\text{erg s}^{-1}). \quad (6.3)$$

It is worth noting that this is in very good agreement with Le Delliou et al. (2006), who

reach their relationship for a similar IMF based on a semi-analytical galaxy formation model (“Galform”, described in detail by Cole et al., 2000), if we assume the escape fraction of Lyman  $\alpha$  from the galaxy is unity. The weaknesses of this assumption are discussed in the next section.

### **6.2.2 Weaknesses of Lyman $\alpha$ as a star formation diagnostic**

Lyman  $\alpha$  emission is the only diagnostic method available to us from our observations, so we persist with the technique above. However, we should consider the drawbacks to this approach.

The observed Lyman  $\alpha$  luminosity naturally depends on what fraction of the Lyman  $\alpha$  produced within that galaxy escape from the system. Lyman  $\alpha$  photons are resonantly scattered by neutral hydrogen; this scattering increases the path length and hence their chance of being absorbed by dust within the galaxy: see, for example, Haiman and Spaans (1999). Early models of this process such as that of (such as that of Charlot and Fall, 1991) indicated that only a very small fraction of the Lyman  $\alpha$  photons would escape from a galaxy with even a relatively small amount of dust. Indeed, it was even argued that the observations of Lyman  $\alpha$  emission was evidence for a very low dust content in the interstellar medium (Neufeld and McKee, 1988).

However, more recent observations have shown that many galaxies do emit substantial amounts of Lyman  $\alpha$ ; as observed, for example, by Pettini et al. (2000). This situation might be explained by the presence of galactic winds in such systems (Kunth et al., 1998): the idea here is that outflowing gas would affect photons at shorter wavelengths than Lyman  $\alpha$ , thus dramatically reducing the number of resonant scatterings which our photons must undergo. Encouragingly, radiative transfer calculations of such a process also produce a good match with observed Lyman  $\alpha$  lineshapes (Ahn, 2004).

Lyman  $\alpha$  may also be attenuated in the intergalactic medium (IGM). If the IGM was mostly neutral, it could in principle strongly suppress the Lyman  $\alpha$  flux; however, reionization occurred at redshifts higher than those of our observations (Miralda-Escude, 1998). We do not, therefore, attempt to make any correction this effect. Some suppression due to clouds of neutral hydrogen will, however, still occur en route.

There is another subtlety to calculating star formation rates based on Lyman  $\alpha$ . Valls-Gabaud (1993) argued that Ly  $\alpha$  emission in starbursts is a strong function of the age of the burst due to the large equivalent width for Lyman  $\alpha$  absorption of late B-type stars. The suggestion is that anomalous ratios of Ly  $\alpha$  to H  $\beta$  flux appear around  $10^7$  years after the start of a burst; from this point, the calibration of equation 6.3 is unreliable. Spectroscopic observations of our targets would enable us to estimate the timescale of star formation in our galaxies and hence assess the likely impact of this effect on our results; however, such observations are not currently available.

In short, therefore, we believe that identifying high redshift star forming galaxies by their Lyman  $\alpha$  emission is not precluded by extinction. However, the fraction of Lyman  $\alpha$  which might escape from a galaxy is not a well understood quantity. Any calculation of star formation rate based on equation 6.3 should be regarded as a lower limit, based on the assumption that all photons escape. Furthermore, we are aware of potential inaccuracies introduced by burst ages.

### 6.2.3 Calculated star formation rates

For each candidate emission line galaxy, a star formation rate is calculated using equation 6.3. The AB magnitude for each object (recorded in tables 5.1, 5.2 and 5.3) is first corrected for galactic extinction in the field (Schlegel et al., 1998) and a minimal correction for etalon losses is applied (as discussed in section 4.2.2.2). It may then be converted to a flux  $f_{\text{total}}$  by equation 3.10 (page 70), and the flux is converted to a luminosity  $L$  by

$$L(\text{Ly } \alpha) = 4\pi d_L^2 \times f_{\text{total}} \quad (6.4)$$

where  $d_L$  is the luminosity distance (equation 5.4).

We calculate the total star formation rate per unit accessible volume as follows. We modify equation 6.1 to become

$$\rho_{\text{SFR}} = \frac{SFR_1}{V_1} + \frac{SFR_2}{V_2} + \dots + \frac{SFR_n}{V_n} \quad (6.5)$$

where  $SFR_n$  is the star formation rate (in  $M_\odot \text{ year}^{-1}$ ) associated with object  $n$ . This calculation makes no attempt to estimate the total star formation rate recorded below our

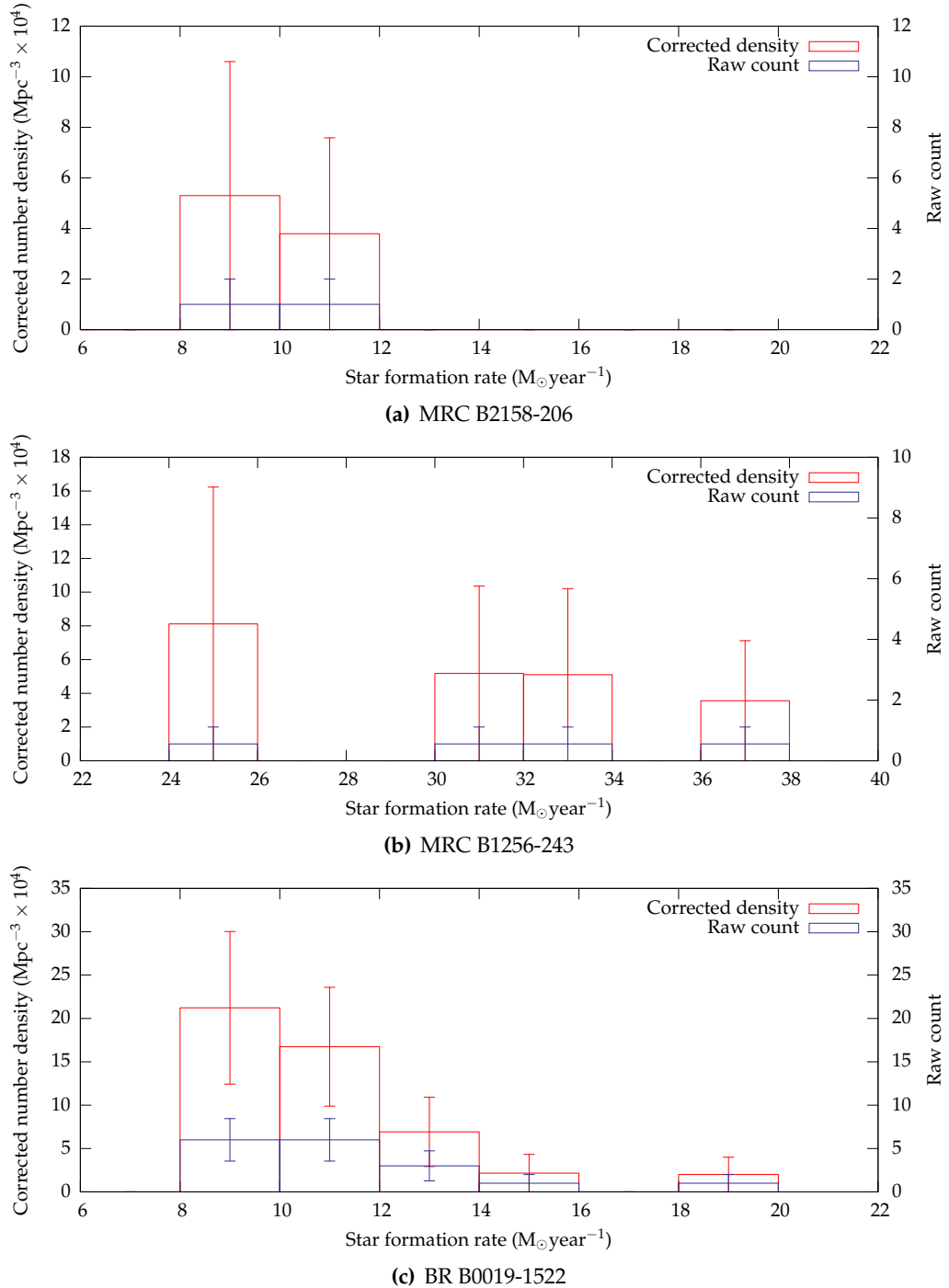


**Figure 6.6:** The number of objects per cubic megaparsec of comoving volume with given star formation rates falling in bins of width  $2 M_\odot \text{year}^{-1}$  in each of the three quasar fields. The error bars are Poissonian.

detection thresholds. Indeed, the detection thresholds themselves for each field are not well defined, varying as they do with wavelength (see figure 4.10 on page 125 for example). In order to estimate an appropriate limit, we bin the data (as shown in figure 6.6) and choose the mid-point of the populated bin corresponding to the lowest star formation rate in the field.

The approach adopted here is merely an approximation, and it is important to emphasise its weaknesses. Each detection we make is the result of the application of a Poisson process to an underlying smoothly varying galaxy population. Such a detection only samples the population at one point in redshift-luminosity space. We have made the assumption that the population may be divided into groups, or bins: those objects detected in a bin are representative of all the objects contained within it. However, this, in turn, relies on the assumption that populations within each bin are consistent: in practice, they may well vary dramatically. We believe the errors introduced by this method are relatively small: a better approach, though, to deriving a luminosity function—and hence the star formation rate density) would be to use a maximum likelihood method (Murdoch et al., 1973; Marshall et al., 1983) to fit a smooth function to the data available.

The rate per unit comoving volume, together with the corresponding star formation rate limit for the field, is tabulated in table 6.4. It is noteworthy that the fields of MRC B1256-243 and BR B0019-1522 display similar total densities. However, the former is composed of a few very luminous objects, and hence has a much larger uncertainty than the second, which is based on a greater number of less luminous objects—this is clearly seen by comparing their detection limits. Further, the BR B0019-1522 field is susceptible to interlopers; the true value may be only around two thirds of that recorded here. The rate in the MRC B2158-206 field is substantially lower, and once again the uncertainty is high due to the limited number of objects.

Figure 6.6 shows a histogram of the number of objects per star formation rate in each of the fields. This, in itself, is not a particularly useful measure, since the comoving volume surveyed changes with star formation rate. Therefore, the same figure also shows the the number of objects per cubic megaparsec of effective accessible volume: this plot is corrected for completeness and volume effects, so is directly comparable from bin to bin

**Table 6.4:** Star formation rate per unit accessible comoving volume in each of the three quasar fields, calculated as per equation 6.5. As discussed in the text (section 6.2.3), our observations are valid only to approximately defined lower limits of star formation: these are also recorded in the table.

Field	SFR detection limit ( $M_{\odot} \text{ year}^{-1}$ )	Star formation rate density ( $M_{\odot} \text{ year}^{-1} \text{ Mpc}^{-3}$ )
MRC B2158-206	9	$0.0094 \pm 0.0067$
MRC B1256-243	25	$0.0683 \pm 0.0344$
BR B0019-1522	9	$0.0543 \pm 0.0132$

of star formation rate.

Once again, the MQS fields are limited by extremely low count rates, particularly MRC B2158-206, which contains only two objects. The corrected version of the plot is potentially a section of a plausible luminosity function, but the uncertainties in each bin are the same size as the total bin population.

It is immediately obvious that the star formation rates in MRC B1256-243 are significantly (a factor of 2 to 3) higher than for any objects detected in the other fields. Note that our observations would not be sensitive enough to detect fainter objects in this field. There are, therefore, two possibilities: we may be sampling the peak of a rich cluster of star forming objects, the rest of which fall below the detection threshold—or these objects are due to contamination of the forms discussed in section 5.2. It is not possible to clarify further from these results.

Figure 6.6(c), shows the most convincing distribution of objects, particularly after correction. This luminosity function is similar to that observed in other work (section 7.2.2), although we do not reach the same depths of sensitivity.

It is particularly worthwhile to compare the results in the field of MRC B2158-206 and BR B0019-1522. They are sensitive to very nearly the same levels of star formation—the peaks in figures 4.10(a) and 4.10(c) correspond to the same luminosity—but the BR B0019-1522 observations cover a substantially larger comoving volume, especially considering the rapid decrease in depth with wavelength seen in figure 4.10(a). Their correct luminosity functions follow a similar shape, but there are clearly far fewer objects detected

in the lower redshift field. It seems likely, therefore, that they are sampling very similar distribution patterns, but that the field around BR B0019-1522 is significantly richer.

It is possible to use these results to make some estimate of the star formation that falls below our detection limits. Malhotra and Rhoads (2004) fit a Schechter (1976) function to field populations of Ly  $\alpha$  emitters at  $z = 5.7$ . Although this is significantly higher than any of our observations, there is little evidence for significant evolution in the luminosity function to much lower  $z$  (Rhoads and Malhotra, 2001; Hu et al., 2004); it should, therefore, be adequate to provide at least approximate results at the redshift we consider.

Due to a lack of constraints from the data, Malhotra and Rhoads provide three alternative fits, depending on the assumed shape of the faint end of the luminosity function. We adopt

$$\phi dL = \phi_*(L/L_*)^\alpha \exp(-L/L_*) dL/L_* \quad (6.6)$$

where  $\phi$  is the galaxy number density at luminosity  $L$ , and  $\alpha = -1.5$ ,  $L_* = 10^{43.0}$  and  $\phi_* = 10^{-4.0}$ .

As discussed in chapter 1 (and, as we will see in the next chapter, confirmed by this data), it is expected that quasars will fall in environments of above average galaxy density. Therefore, it is not appropriate to directly apply the above luminosity function. Instead, we normalise it to our data for each of the three fields—integrating upwards from the lower limit of our detections (as recorded in table 6.4) and inserting a constant such that the calculated and measured star formation rate densities are the same. Integrating upwards to the minimum and applying the same normalisation, it is thus possible to estimate the total star formation in these fields.

This procedure results in estimates of  $0.025 M_\odot \text{ year}^{-1} \text{ Mpc}^{-3}$  for the field of MRC B2158-206,  $1.2 M_\odot \text{ year}^{-1} \text{ Mpc}^{-3}$  for that of MRC B1256-243 and  $0.13 M_\odot \text{ year}^{-1} \text{ Mpc}^{-3}$  for BR B0019-1522. It should be noted that these numbers are extremely speculative: in all cases, the luminosity function is ill defined, and, particularly in the case of MRC B1256-243, the total number is heavily influenced by just a few very luminous candidate galaxies.

### 6.3 Summary

Potential emission line galaxies have been identified in all three of the quasar fields investigated in this thesis. The total number of objects identified varied from field to field: two in MRC B2158-206, four in MRC B1256-243 and seventeen in BR B0019-1522. Our identifications are not conclusive, due to the limited sensitivity of our data and possible contamination by mis-identified noisy artifacts, continuum objects and lower-redshift emission lines, and should therefore be regarded as candidates for further investigation.

Investigation of the properties of the lower redshift MQS fields is very much limited by poor statistics due to the relatively low number of objects identified. There is no real evidence for a cluster projected on the sky around the quasar within our field of view of these fields, although there may be a hint of filamentary structure in the field of MRC B1256-243. There is, however, some evidence for a cluster in terms of the velocity dispersion of ELG candidates along the line of sight to the quasar: we observe all objects with  $-1200 < \Delta v < 1200 \text{ km s}^{-1}$  of the quasar redshift.

The higher redshift field, BR B0019-1522, is rather more richly populated. There is structure in terms of both the line of sight velocity dispersion and the projected distribution of objects around the quasar, with particular evidence for clustering within a megaparsec to the south of the quasar itself. Further the projected distribution of objects on the sky shows a steady decline in object density over a projected distance of around 1.5 Mpc, as shown in figure 6.2.

It is possible to estimate star formation rates for all the candidate emission line galaxies based on their observed Lyman  $\alpha$  flux. We note, however, that there are significant weaknesses to this technique due to the nature of the Lyman  $\alpha$  emission and subsequent extinction. MRC B1256-243 and BR B0019-1522 both display significantly higher star formation rates than the field of MRC B2158-206. In the case of MRC B1256-243, this is due to a few extremely luminous objects, which fall at the limit of our detection sensitivity: it is possible we are sampling the peak of a much more extensive distribution. The field of BR B0019-1522 contains a larger number of less luminous objects, more typical of those seen in the field and providing better statistical constraints.

In the next chapter, all these results will be put in context with other observations, both of high redshift galaxies in the field and, more specifically, in the environments of active galaxies.

# Chapter 7 | *Conclusions*

In this chapter, we consider what conclusions can be drawn from the work described in this thesis, setting our results in the broader context of the study of AGN environments and considering future work in the field.

## 7.1 *Our results*

We have examined the fields of three quasars using the Taurus Tunable Filter: those of MRC B2158-206 ( $z = 2.429$ ), MRC B1256-243 ( $z = 2.263$ ) and BR B0019-1522 ( $z = 4.528$ ). In total, we have identified twenty three candidate emission line galaxies. Chapter 5 presented full details of each of these. They were not uniformly distributed from field to field: seventeen of the detections were made in the higher-redshift BR B0019-1522 field, compared to two in the field of MRC B2158-206 and four around MRC B1256-243.

These raw number counts are not directly comparable, however: differences in redshift, instrument characteristics and exposure times cause substantial differences in the volumes being surveyed. The TTF itself has a relatively complex design, described in chapter 2, which further complicates the analysis. In order to assess the significance of our results, therefore, a comprehensive system of simulating observations was developed. We modelled the characteristics of the instrument, calculating what we might expect to detect when observing a field containing known objects designed to imitate the targets we were searching for. The results were used to estimate the magnitude depths and wavelength ranges to which our observations are sensitive. These simulations were described in some detail in chapter 4; they offer a vital insight into tunable filter observations of this nature, without which much of the rest of this analysis would have been impossible.

## 7.2 Placing our results in context

The goal of this work is to enhance our understanding of the cluster environments of AGN. It is necessary, therefore, to consider these results in the context of other studies of similar environments. In this section, we briefly outline how our results compare to work carried out by other groups. We are interested in both how the environments of AGN differ from blank field studies, and on how our quasar fields compare to other observations of AGN.

### 7.2.1 Emission line galaxies in the field

Section 5.2.3 discussed the work of Cowie et al. (1997), which provides blank-field number counts of star forming galaxies at a range of redshifts. In that section, the data was used to estimate the number of lower-redshift interlopers which might be observed in the field. However, they also provide a measurement over the range  $z = 1.6\text{--}3.2$ , which covers at least our lower redshift observations. In this redshift range, their results are sensitive to star formation rates from  $10 M_{\odot} \text{ year}^{-1}$  upwards. Using the same methodology as employed for determining the potential number of interlopers in the field, these results are used to estimate the number of Lyman  $\alpha$  emitters which might be observed. Using the same technique to estimate the number of galaxies we might observe as described in section 5.2.3, these results suggest we might expect on average 0.86 galaxies in the field of MRC B2158-206, 0.25 in the field of MRC B1256-243 and 1.3 in the field of BR B0019-1522. We find significantly in excess of this for all but the first case.

At higher redshift, Hu et al. (1998) report the use of narrowband imaging and spectroscopy with LRIS on the Keck telescope (Oke et al., 1995) to identify Lyman  $\alpha$  emitters in blank fields at redshifts of 3.4 and 4.5. In the higher redshift field (which is at a directly comparable redshift to our BR B0019-1522 observations), they report a lower limit on the star formation density of  $0.005 M_{\odot} \text{ year}^{-1} \text{ Mpc}^{-3}$  (corrected to our cosmology), where they reach a very similar depth to our observations. This is an order of magnitude less than the completeness-corrected results detected in our fields of MRC B1256-243 and BR B0019-1522, and half that observed in the field of MRC B2158-206.

An alternative approach is taken by Haiman and Spaans (1999). Rather than direct

observation, they model star-forming galaxies by combining the formalism of Press and Schechter (1974) (a system for describing formation of structure through gravitational condensation from statistical perturbations among self-gravitating masses) with a consideration of the dust distribution inside galaxies. From this basis, they predict the surface density of Lyman  $\alpha$  emitters observable at a given redshift and flux limit. They present a “standard model”, demonstrating that it is consistent with the results of Hu et al. (1998) at  $z \sim 4.5$ . Applying this model to our  $z \sim 2.2$  observations predicts only one detectable Lyman  $\alpha$  emitter in the MRC B2158-206 field, with a one-third chance of the MRC B1256-243 containing an object which we might detect.

It is also worth considering the results of the LALA (“Large Area Lyman  $\alpha$ ”) survey. Rhoads et al. (2000) identified thousands of potential Lyman  $\alpha$  emitters at a redshift of  $z \sim 4.5$  using narrowband imaging. They estimate a surface density of 4,000 genuine objects (after eliminating low-redshift contaminants) per square degree per unit redshift covering a star formation range of  $5\text{--}10 \text{ M}_\odot \text{ year}^{-1}$ . Their objects are, therefore, rather fainter than ours. If we were able to see to an equivalent depth over the wavelength ranges of peak transmission in our survey (3955–3990 Å for MRC B2158-206, 3952–3977 Å for MRC B1256-243 and 6680–6740 Å for BR B0019-1522)—and assuming that the density of Lyman  $\alpha$  emitters is similar at  $z \sim 2.2$  to that observed at  $z \sim 4.5$ —we might expect to observe 1.1 objects in the field of MRC B2158-206, 0.8 in the field of MRC B1256-243 and 2.1 in the field of BR B0019-1522. These results are quite similar to the field estimates above, and, again, rather lower than the numbers we actually observe—an especially significant result when it is borne in mind that LALA probes a slightly fainter portion of the luminosity function than this work.

### **7.2.2 *The environments of AGN***

As outlined in chapter 1, there have been several other investigations of the environments of AGN. In this section, we discuss how our results compare to some of the most significant of these.

### 7.2.2.1 Projected distribution and velocity dispersion

There was no conclusive evidence for a projected galaxy overdensity in the lower- $z$  MQS fields. However, in the field of BR B0019-1522, there was evidence for a peak in the surface density of galaxy candidates about the quasar within a distance of around 1.5 Mpc. This distance is consistent with the scale lengths observed in clusters around other AGN (Venemans et al., 2002; Bremer et al., 2002; Barr et al., 2004). However, it is notable that the distribution we observe is significantly less sharply peaked around the quasar than those reported by others: Barr et al. (2004), for example, saw dramatic peaks within 250 kpc of the quasars in their observations.

We do see, though, a potentially rich environment—both in terms of projected positions and velocity dispersion along the line of sight—within a megaparsec to the east of the quasar. It is particularly interesting to draw a comparison with the observations of the  $z \sim 1.1$  quasar MRC B0450-221 made by Baker et al. (2001). They reported that the greatest concentration of [O II] emitting star forming galaxies were detected in a group lying 200–700 kpc from the quasar, which was more directly surrounded by an overdensity of passively evolving red galaxies (which this work would not detect).

A similar effect is observed in the field of the  $z = 4.1$  radio galaxy TN J1338-1942 observed by Venemans et al. (2002) and with followup by Overzier et al. (2006b). Overzier et al. reported that the radio galaxy itself falls in relatively small region containing bright Lyman-break galaxies. An overdensity of Lyman  $\alpha$  emitters is also observed in the quasar field, but they tend to be grouped together away from the quasar, in regions which are poorer in the more luminous Lyman-break galaxies.

Similar comparisons can be drawn with respect to the velocity dispersion of ELG candidates. In the MQS fields, all the objects were found within  $-1200 < \Delta v < 1200 \text{ km s}^{-1}$  of the quasar redshift. This compares well to the velocity dispersion observed by Barr et al. (2004), particularly among their objects known to exist in clusters. Venemans et al. (2002) measured a similar, albeit slightly narrower, distribution, with objects detected within  $600 \text{ km s}^{-1}$  of the quasar. All of these numbers are consistent with the velocity dispersions for Abell class 2 clusters—not selected for their AGN associations—measured by Yee and Ellingson (2003).

### 7.2.2.2 Space density

In terms of the space density of ELG candidates, perhaps the closest comparison to our  $z \sim 2.2$  MQS fields is the work of Pentericci et al. (2000) and Kurk et al. (2001), who investigated the environment of the  $z = 2.16$  radio galaxy PKS B1138-262. They found a space density of Lyman  $\alpha$  emitters of  $0.01 \text{ Mpc}^{-3}$  with a sensitivity of  $1 \text{ M}_\odot \text{ year}^{-1}$ . The same result was obtained in by Venemans et al. (2002) studying a  $z = 4.2$  radio galaxy. This space density is twice that observed in our richer MRC B1256-243 and BR B0019-1522 fields, and almost an order of magnitude higher than the field of MRC B2158-206: however, they also probe to star formation rates an order of magnitude lower than this work.

Barr et al. (2004) found similar results— $0.01 \text{ Mpc}^{-3}$  to a depth of  $1 \text{ M}_\odot \text{ year}^{-1}$ —in their study of radio loud quasars at  $z \sim 1$ . Excluding those objects with star formation rates less than  $10 \text{ M}_\odot \text{ year}^{-1}$  from their analysis, however, produces a space density of  $0.002 \text{ Mpc}^{-3}$ —very much the same order as our results. Barr et al. also report a similar range of star formation rates to those observed here: they follow a near-identical distribution above  $10 \text{ M}_\odot \text{ year}^{-1}$  as shown in figure 6.6(c), with the addition of a single luminous object at  $\sim 40 \text{ M}_\odot \text{ year}^{-1}$ : this rate is comparable with that we measure for the objects in the field of MRC B1256-243.

It is also interesting to compare our measured star formation rates with those observed by Overzier et al. (2006b) in the  $z = 4.1$  radio galaxy field. They investigate 12 Lyman  $\alpha$  emitters, calculating star formation rates of  $\leq 14 \text{ M}_\odot \text{ year}^{-1}$ . These results are comparable with our measurements in the fields of MRC B2158-206 and BR B0019-1522, but have no equivalent to the luminous galaxies in the MRC B1256-243 field.

In short, then, these results are broadly consistent with those observed by others: we see evidence for a density of star forming galaxies in the vicinity of our quasars which is significantly higher than that in the field. However, the limited sensitivity of our observations places the fainter reaches of the luminosity function probed by other work beyond our reach.

### **7.2.3 The star formation history of the universe**

Section 1.3 (page 11) briefly outlined the importance of understanding the history of star formation in the universe, as well as the current picture of how it has evolved. How consistent is this picture with our results?

Figure 7.1 presents a compilation of the results of a number of different measurements of the star formation rate density covering a wide range of redshifts: from the local universe to  $z = 6.57$ . These results are based on several different measurement techniques (as described in chapter 1). The characteristic pattern of a plateau starting around  $z \sim 1$  is clearly visible, as is a decline in the high-redshift universe.

The results of this work are also plotted in figure 7.1, and may be regarded as broadly consistent with the other measurements. The estimate of the total star formation rate density in our MRC B1256-243 field is clearly abnormally high; this is likely due to the presence of a few luminous galaxies being causing excessive normalisation as discussed in section 1.3. MRC B2158-206 seems perfectly average for its redshift: there is certainly no evidence of an overdensity here. BR B0019-1522 falls somewhat above its peers: this may be taken as further evidence that it is, indeed, a rich protocluster.

#### **7.2.3.1 The broader picture**

Perhaps the most significant result of this thesis is the detection of a probably cluster of Lyman  $\alpha$  emitting galaxies around the  $z = 4.528$  radio-quiet quasar BR B0019-1522. The main concentration of Lyman  $\alpha$  emitters is located between 0.5 and 1.0 Mpc east of the quasar, although objects are detected throughout the field. The projected space density of object falls off with distance from the quasar to a radius of 1.5 Mpc.

This is among the highest-redshift clusters detected around a radio quiet quasar (Stiavelli et al., 2005, tentatively report clustering around a radio-quiet quasar at  $z = 6.28$ , observed by searching for red galaxies). The uncertainty inherent in identifying emission lines and measuring their fluxes with TTF means that questions remain to be answered; however, even taking that into account, there is a striking similarity between the potential cluster we observe and those observed at lower redshift. The scale length of the cluster-

ing is similar to that observed around other AGN, as is the grouping of Lyman  $\alpha$  emitters slightly offset from the quasar itself. The space density of objects and of star formation is also similar to that observed by others, although we do not probe so far down the luminosity function.

It is particularly informative to compare our results to the investigation of the  $z = 4.1$  radio galaxy TN J1338-1942 documented by Venemans et al. (2002). They report similar star formation rates and clustering structure, bearing in mind that their results are nearly an order of magnitude deeper in terms of star formation rate. There is certainly little evidence here to support the hypothesis that radio quiet quasars inhabit poorer environments than their radio-loud brethren or radio galaxies.

The fields of MRC B2158-206 and MRC B1256-243 are, perhaps, less interesting. In the latter case particularly, our observations lack depth: we make no detections of objects with calculated star formation rates less than  $24 \text{ M}_\odot \text{ year}^{-1}$ . This is unfortunate, as this field is tantalising—the relatively large number of luminous galaxies detected implies that we may be detecting the peak of a very rich distribution. This, combined with the odd structure observed in the field, makes this object a prime target for future investigation. However, it is very hard to draw conclusions from the limited data available to us here.

Only two candidate galaxies were detected in the field of MRC B2158-206. Although a smaller volume is sampled than for BR B0019-1522, we do reach an equivalent depth here (albeit over a smaller volume): this is not simply due to the truncation of the luminosity function seen in MRC B1256-243. In short, there is very little evidence for structure or a galaxy overdensity around the AGN. Such poor fields have certainly been found in other work: for example, although documenting several overdensities in other fields, Barr et al. (2004) find a similar lack of structure around the radio-loud quasar MRC B2037-234 ( $z = 1.15$ ). The obvious comparison is to the work of Francis and Bland-Hawthorn (2004), who detected no Lyman  $\alpha$  emission around the extremely luminous  $z = 2.159$  radio-loud quasar PKS B0424-131.

The most immediate predecessor of this work was that of Barr et al. (2004). They observed the fields of six radio-loud quasars at  $z \sim 1$ . It is noteworthy that their results were, for the most part, rather similar to those documented here—and, indeed, very comparable

to the studies of higher redshift radio galaxies made by the Leiden group, as discussed in section 1.5.1. This thesis, therefore adds to the evidence that quasars—both radio loud and quiet—and radio galaxies inhabit qualitatively similar environments over an extremely wide range of redshifts. However, this still relies on a very small number of samples, particularly at higher redshifts.

### 7.3 Future work

In common with all such work, this thesis raises as many questions as it answers. Here, we discuss the potential for further investigations.

#### 7.3.1 Spectroscopy of ELG candidates

Throughout this thesis, objects have been identified as “candidate” emission line galaxies, based on an increase of the observed flux at a wavelength we expect to correspond to Lyman  $\alpha$ . The possibilities for misidentification are potentially significant: for example, in section 5.2.3 we considered a number of possible lower-redshift lines that might appear as “interlopers” in our fields. Further, Lyman  $\alpha$  itself is not a particularly reliable indicator of star formation, as discussed in section 6.2.2.

The next stage in this investigation, therefore, is to follow-up all the ELG candidates we have identified with spectroscopy. As well as validating our ELG detections—by confirming the presence (or otherwise) of Lyman  $\alpha$  and other emission lines—such spectroscopy would be useful in manifold ways. A more accurate estimate of the star formation rate could be obtained by considering the blue spectral slope or spectral lines other than Lyman  $\alpha$ . Spectroscopy would also enable a detailed study of the distribution of galaxies about the AGN as a function of star formation rate and metallicity. Finally, it would tell us more about the dynamical state of the cluster (but not the total cluster mass, as such structures at high redshift are not expected to be virialised).

### 7.3.2 *Further imaging of these fields*

All three of the fields presented here prompt questions which could be answered with deep broadband imaging. Such imaging would both confirm the existence of the galaxy candidates identified in this work and enable us to estimate the equivalent width of their Lyman  $\alpha$  emission. Surprisingly, such data are not available from observatory archives; there is certainly potential for further work here.

MRC B2158-243 provides the least evidence for a cluster of Lyman  $\alpha$  emitters in this investigation. It would be an interesting exercise to see if the quasar is indeed solitary, or if a population of galaxies which are not bright in Lyman  $\alpha$  could be detected. I am involved with further observations of this field using GMOS-S, the Gemini Multi-Object Spectrograph, in an attempt to identify cluster members using the method suggested by Adelberger et al. (2004) (which we consider in more detail in section 7.3.3.2). Some data from this investigation is now becoming available, but it has not yet been analysed.

BR B0019-1522 provides the most direct evidence of clustering in this work. It seems likely that we have identified the high redshift precursor of a substantial cluster in the present universe. Further investigation of this field could confirm this, and also investigate the structure of the protocluster. For example, in their  $z = 4.1$  cluster, Overzier et al. (2006b) observed that Lyman  $\alpha$  emitters tended to be slightly separated from the AGN, which was itself surrounded by more luminous Lyman-break galaxies. We have seen evidence for a similar pattern here; it would be fascinating to investigate further.

Most curious of these fields is that of MRC B1256-243. Our observations here did not have enough sensitivity to do more than provide a glimpse at what might be. It seems possible that we have sampled the peak in an extremely rich population of galaxies; however, it is impossible to confirm that based on our results. This field cries out not just for broad-, but also narrowband investigation pushing to a fainter sample than investigated in this work. Unfortunately, the TTF has now been decommissioned, but this field is surely a promising candidate for investigation using another instrument.

### 7.3.3 Future surveys of AGN environments

This work has demonstrated the potential of tunable filter imaging of quasar environments at high redshift. In this section, we consider the prospects of building on this success in the future.

#### 7.3.3.1 Tunable filter imaging

Unfortunately, the TTF was decommissioned some years ago. Therefore, although we have demonstrated its usefulness as a probe of quasar environments, the opportunity to take advantage of its potential is now past.

However, the future for tunable filter observations is rosy, particularly due to the potential of OSIRIS, the “Optical System for Imaging and low Resolution Integrated Spectroscopy”, a day one instrument destined for the Gran Telescopio Canarias (Cepa et al., 2000). OSIRIS incorporates many of the technologies that were pioneered by TTF, including the use of charge shuffling on the CCD and two Fabry-Pérot etalons as narrowband tunable filters, covering the range 3965–10000 Å. This is the first instrument on an 10 metre class telescope to incorporate this tunable filter technology: it has the potential to carry out work similar to that documented here, but with far greater sensitivity.

Other new tunable filters are also in development. Notable is the FGS-TFI (“Fine Guidance Sensor—Tunable Filter Imager”), destined for use on the James Webb Space Telescope. Once again based on a Fabry-Pérot etalon and a suite of order blocking filters, it will image a square of sky 2.2 arcminutes to the side at wavelengths between 1.5 and 5  $\mu\text{m}$ . This is a rather smaller field of view than that offered by ground based instruments such as TTF, but the wavelength range available opens the possibility of investigating [O II] 3727 Å emission from very high redshift galaxies.

#### 7.3.3.2 Current techniques

As we saw in section 1.5, there have historically been three methods that have been successful in identifying high- $z$  clusters around AGN. As well as the tunable filter technique

discussed above, the combination of narrow- and broad-band imaging used by the Leiden Group has seen considerable success, and it is very likely that it will continue to do so in future. The same can also be said of the searches for red objects described in section 1.5.3: at the moment, these provide access to the very highest redshifts available.

Another technique that bears mentioning is that of Adelberger et al. (2004). They propose a technique for identifying star-forming galaxies in the redshift range  $1.0 < z < 3.0$ , based on the colours measured in just three optical bands by ground-based telescopes. Their approach is similar to that taken by Lyman-break surveys, but, since the Lyman-break is below optical wavelengths in this redshift range, they focus on other spectral features, most notably the 3700 Å Balmer break.

The redshift range that Adelberger et al. focus on is one of particular importance: it is here that we expect to see the peak in both AGN activity (Wolf et al., 2003) and in the growth of galaxies and clusters (Murali et al., 2002). A programme of observations using this technique in an attempt to identify star forming galaxies in protoclusters around AGN at  $z \sim 2$  was undertaken in 2006 using GMOS-S (PI Barr; the team includes the present author). One of the quasars under investigation in this survey is MRC B2158-206: it will be particularly interesting to compare their results for this field to those documented here.

### 7.3.3.3 *New instrumentation*

We have seen, then, that further extension of the techniques outlined elsewhere in this thesis is possible. However, new instrumentation is in development which holds out great promise for detecting high-redshift star formation.

DAzLE, the Dark Ages  $z$  Lyman  $\alpha$  Explorer (Horton et al., 2004) is a near-infrared narrowband differential imager, designed for use on the 8 metre ESO Very Large Telescope (VLT). It is designed to detect Lyman  $\alpha$  emitters at redshifts above  $z = 7$ . Over the range of wavelengths in question, OH emission in the atmosphere renders conventional broadband imaging useless; instead, DAzLE uses ultra-narrowband (10 Å) interference filters, specifically targeted to windows in the atmospheric emission (Cianci et al., 2004). The filters are arranged in pairs; they identify Lyman  $\alpha$  emitters by their brightening in one filter, but not its companion, much as in this work. With a field of view comparable to our

TTF observations, they will survey a comoving volume of  $1600 \text{ Mpc}^{-3}$  per pointing, with a 10 hour integration time probing star formation rates of just a few solar masses per year.

Our observations built up a crude—just three or five point—spectrum of all the objects in the field, with the aim of identifying a Lyman  $\alpha$  peak. A rather more reliable identification of Lyman  $\alpha$  emitters could be made with better spectroscopy of each object. This would be possible if observations were made using an integral wide-field spectrograph, such as MUSE (the Multi Unit Spectroscopic Explorer), also destined for the VLT (Bacon et al., 2006). Previous generations of integral field units have been too limited in terms of their field of view to act as survey tools; MUSE goes some way to overcoming this limitation, providing a grid of 90,000 “spaxels” (spectral pixels, each containing a 3000 element spectrum over the range 4650–9300 Å) in a square arcminute field. Such a field of view is substantially smaller than that used in this work, but still provides much potential both in its own right and as a possible harbinger of future instruments yet to come.

In short, then, the future for studies of star formation at high redshifts may certainly be described as rosy. The traditional methods still have much utility left in them, while the latest generation of instrumentation, both in terms of tunable filter imaging and other techniques, offer great promise for the years to come.

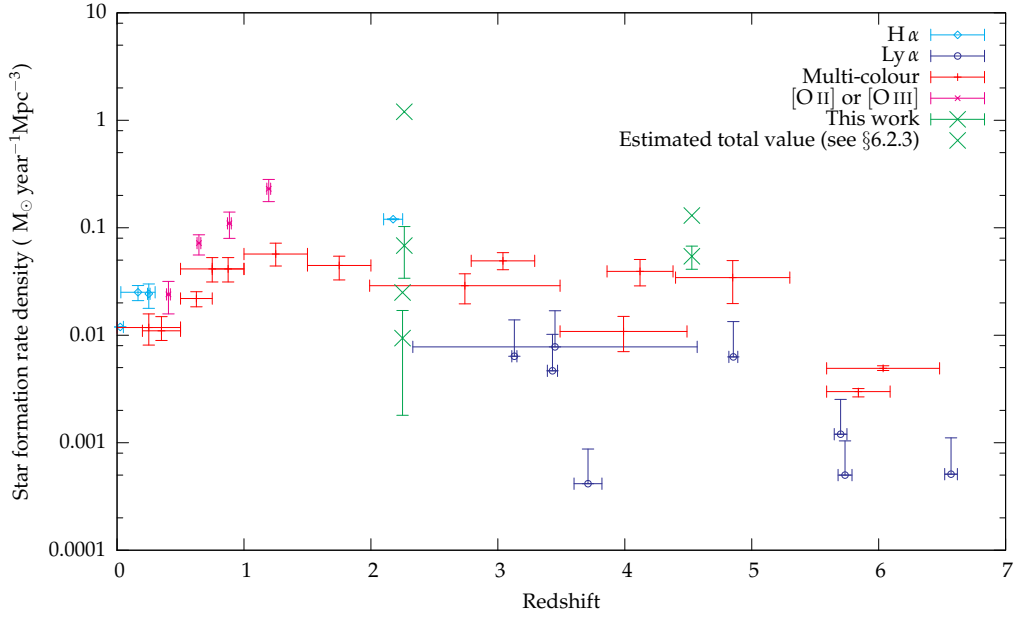


**Figure 7.1:** Star formation rate per unit volume as a function of redshift. Based on data compiled by van Breukelen et al. (2005). A number of different survey types are included: H $\alpha$  (Gallego et al., 1996; Tresse and Maddox, 1998; Moorwood et al., 2000; Hippelein et al., 2003), multi-colour (Lilly et al., 1996; Connolly et al., 1997; Madau et al., 1998; Treyer et al., 1998; Steidel et al., 1999; Iwata et al., 2003; Bunker et al., 2004; Stanway et al., 2004), [O II] and [O III] (Hippelein et al., 2003) and Ly $\alpha$  (Cowie and Hu, 1998; Kudritzki et al., 2000; Ajiki et al., 2003; Fujita et al., 2003; Kodaira et al., 2003; Ouchi et al., 2003; Rhoads et al., 2003; van Breukelen et al., 2005). Redshift error bars are indicative of the survey ranges. The results of this study are plotted on the same axes; we include both the raw results to the limits given in table 6.4 (page 173) and the estimated total levels calculated in section 6.2.3 (page 170).

# Appendix A

## *Locating the centre of an object*

It is often necessary to precisely locate the position of the peak of an object within an image. The technique used throughout this thesis is referred to be IRAF “marginal centroid fit”, described by Stone (1989) as the “moment method” and based on the work of Auer and van Altena (1978).

We consider each dimension of the image individually: the discussion that follows refers to  $x$ , but exactly the same procedure is followed for  $y$ .

We start with some initial estimate of the position of the centre of the object: call its  $x$  coordinate 0. The image is then collapsed along the  $y$  direction—we define the ‘marginal’ at position  $x$  relative to the estimated centre as

$$M(x) = \sum_y I(x, y) \tag{A.1}$$

where  $I(x, y)$  is the intensity at some position in the image. Given some estimate of the background signal,  $B$ , the moment of the distribution is then given by

$$x_c = \frac{\sum_x x \times [M(x) - B]}{\sum_x [M(x) - B]}. \tag{A.2}$$

If this moment is zero, we have found the centre of the distribution. If not, we perform another iteration of the procedure, shifting our estimate of the position of the centre appropriately.

This method is sensitive to variations in the image: since the marginal is weighted with distance from the estimated centre, a spuriously high value at the edge of the region being fitted introduces significant error. To compensate for this, we perform our fit only within a small number of pixels of the estimated position of the centre: this distance is chosen such that no other sources intrude into the region being fitted.

# Appendix B

## *Data reduction revisited*

In chapter 3 the techniques used for reducing the data used throughout this thesis were described. This approach was based on that described in the literature (notably Jones et al., 2002; Francis and Bland-Hawthorn, 2004). However, it may not produce the most statistically accurate or sensitive results. In this appendix, therefore, we consider some of the possible drawbacks to the approach taken and the alternatives which might be applied.

Throughout this section, we consider the data relating to our observations of MRC B2158-206. It provides the most appropriate platform for testing our techniques: MRC B1256-243 was not median combined (since it consisted of only two frames per image), while BR B0019-1522 did not display charge trapping artifacts.

### **B.1** *The removal of charge trapping artifacts*

The method used to eliminate charge trapping artifacts from our data frames was based on that developed by (Francis and Bland-Hawthorn, 2004), and is described in section 3.2.1.1. However, the risk with this technique is that it will significantly alter the statistical properties of the image background. Therefore, it was considered wise to consider alternative techniques.

If the charge trapping sites cannot be corrected in the way described above, they must be excluded from the data altogether. This is achieved by building a ‘bad pixel mask’—simply a list of all the pixels in each frame which should be considered unusable.

Once again, all the raw frames were combined by taking their median. This median displays all the charge trapping artifacts, which appear in the same place in each frame, but not the objects themselves (or other defects such as cosmic rays), which do not. This

median image, therefore, provides an ideal ground for identifying those pixels affected by charge trapping.

The construction of the mask itself was performed in two stages. First, a simple high-pass filter was used to remove all those pixels which recorded more than 20 counts above the mode for the image. This removed many of the visible charge trapping sites, but there was still a pattern of elevated bands of charge across the image. These were found to be most effectively identified and removed by the IRAF task noao.imred.ccdred.ccdmask.

The resultant mask was successful in identifying most of the charge trapping artifacts, when judged by eye. Some were still in evidence, however: these were eliminated when combining the images, as described below.

## **B.2** *Distribution of frames contributing to the median*

Combining observations by taking the median runs the risk of excluding some valid data which was recorded with slightly lower than average counts—for example, because of a transitory atmospheric effect, such as a cloud passing overhead during the observation. Such a process could, therefore, cause a systematic bias in our results.

As an experiment to determine whether this effect was important, consider the observations of MRC B2158-206. Each of the five images of this field was produced by taking the median of four separate data frames. In other words, each pixel on the resultant image consists of the mean of two source frame pixel values, while two further values—the maximum and minimum from the source frames—have been rejected. If there is no statistical bias in this process, the same fraction of pixels should be rejected from each frame.

The results for our data are shown in table B.1. The 1237 by 863 pixel images of MRC B2158-206 each contain 1,065,531 individual pixels. For each pixel in the image, two pixels from the raw data frames have been rejected: a total of 2,135,062 rejects. The fraction of this total coming from each of the constituent frames is tabulated.

If the data were composed of a uniform background with random noise, the expected reject fraction from each image would be  $25 \pm 0.04\%$ . Hence, the data presented

**Table B.1:** The fraction of the 2,135,062 of rejected pixels drawn from each frame in our images of MRC B2158-206.

Etalon Z	% pixels excluded in frame			
	1	2	3	4
173	24.5	24.2	24.2	27.0
182	24.7	24.9	25.5	24.9
191	24.9	25.1	25.2	24.8
200	25.0	25.9	24.5	24.6
209	25.1	24.9	24.2	25.8

here indicates that there are systematic differences in brightness from frame to frame—most notably, one frame of the Z173 image is excluded at the 27 % level. This will lead to a reduction in the overall signal-to-noise level in the resultant image, but should not fundamentally compromise our results.

As an experiment, the Z173 frames were scaled by multiplying each by a constant factor such that their median flux levels were the same. In this way, the same fraction of pixels would be rejected from each. After median combining, SExtractor was run over both the scaled and the unscaled images. The catalogues produced were nearly identical: there were two objects which did not appear in both, and they were far below the  $5\sigma$  level used for selecting objects for inclusion in this work.

### B.3 A comparison of mean and median combining

In the previous section it was established that there was no obvious bias between the frames when combining by taking the median. In this section, we go on to compare the actual results obtained when using the mean as compared to the median.

Two of the MRC B2156-206 images were chosen: those corresponding to etalon settings of Z173 and Z182. The data frames were cropped and aligned as described in chapter 3, then combined using the IRAF task cl.images.immatch.imcombine.

When combining by taking the median, cosmic rays (and residual charge trapping artifacts) are automatically excluded since they appear in different places on each frame. This is not, however, the case when taking the mean: a cosmic ray in one data frame can

appear much like a potential object in the resultant image.

The imcombine procedure includes various rejection algorithms which can be used to exclude spurious data and hence eliminate this effect. For this work, an ‘averaged sigma clipping’ algorithm was used (imcombine’s AVSIGCLIP). This assumes that  $\sigma$  about the median at a given point is proportional to that median, and then rejects any pixels more than  $0.5\sigma$  away from that median. This sigma threshold was found by experimentation to be necessary to exclude most of the obviously visible traces of artifacts from the resultant image: the low value necessary must be attributed to the poor quality of the available data.

After the images had been prepared in this way, they appeared effectively identical when compared by eye. SExtractor was then used to build catalogues of sources within each images, as described in section 5.1, and the catalogues were then compared.

Four sources were recorded by SExtractor in the mean image for Z173 that did not appear in the median image. One of these fell right on the edge of the image, and would therefore have been discounted in our analysis. Two of the others could be directly attributed to inadequately subtracted cosmic rays in the input frames. The remaining source could not be so easily dismissed, but fell below the  $5\sigma$  threshold for inclusion in this analysis.

Three sources were detected in the median image for Z173 that were not seen in the mean. One of these was due to a bright star which had become segmented and was thus detected twice by SExtractor. Another was part of a larger, extended bright patch that was visible on both the mean and median images, and was thus discounted. Finally, there was one object which, once again, fell below the  $5\sigma$  threshold.

The situation in the Z182 image was very similar. Five images were detected in the mean, but not the median. Two of these were badly subtracted cosmic rays. The remaining three either fell below the  $5\sigma$  threshold or could be sensibly rejected after examination under the criteria laid down in section 5.1. Three sources were detected in the median but not the mean: one was rejected as an edge effect, while the others were once again rejected after checking by eye.

It bears adding that the total number of sources detected in each image was around

50; the variation from image to image was at the 10% level or less. Further, the measured fluxes for sources detected in both the mean and the median images were almost identical, with no evidence of systematic variation.

#### **B.4** *Conclusions*

It is recognised that the data reduction procedures adopted in chapter 3 of this thesis had some statistical weaknesses. However, based on the analysis presented in this appendix, it seems unlikely that those weaknesses would have significantly prejudiced the results presented in this thesis.

# The | Bibliography

- Abell, G. O. "The distribution of rich clusters of galaxies". *The Astrophysical Journal Supplement Series*, 3:211–288, 1958.
- Adelberger, K. L., Steidel, C. C., Shapley, A. E., Hunt, M. P., Erb, D. K., Reddy, N. A., and Pettini, M. "Optical selection of star-forming galaxies at redshifts  $1 < z < 3$ ". *The Astrophysical Journal*, 607:226–240, 2004.
- Ahn, S.-H. "Singly peaked asymmetric Ly  $\alpha$  from starburst galaxies". *The Astrophysical Journal*, 601:L25–L28, 2004.
- Ajiki, M. et al. "A Subaru search for Ly  $\alpha$  emitters at redshift 5.7". *The Astronomical Journal*, 126:2091–2107, 2003.
- Antonucci, R. "Unified models for active galactic nuclei and quasars". *Annual Review of Astronomy and Astrophysics*, 31:473–521, 1993.
- Appenzeller, I. et al. "Successful commissioning of FORS1—the first optical instrument on the VLT". *The Messenger*, 94:1–6, 1998.
- Aragón-Salamanca, A., Ellis, R. S., Couch, W. J., and Carter, D. "Evidence for systematic evolution in the properties of galaxies in distant clusters". *Monthly Notices of the Royal Astronomical Society*, 262:764–794, 1993.
- Atherton, P. D., Reay, N. K., Ring, J., and Hicks, T. R. "Tunable Fabry-Perot filters". *Optical Engineering*, 20:806–814, 1981.
- Auer, L. H. and van Altena, W. F. "Digital image centering. II". *The Astronomical Journal*, 83:531–537, 1978.
- Bacon, R. et al. "Probing unexplored territories with MUSE: a second generation instrument for the VLT". In McLean, I. S. and Iye, M., editors, *Astronomical telescopes and instrumentation*, volume 6265 of the *Proceedings of SPIE*, 2006.
- Bahcall, J. N. and Sarazin, C. L. "Parameters and predictions for the X-ray emitting gas of Coma, Perseus, and Virgo". *The Astrophysical Journal*, 213:L99–L103, 1977.
- Bahcall, N. A. et al. "A merged catalog of clusters of galaxies from early Sloan Digital Sky Survey Data". *The Astrophysical Journal Supplement Series*, 148:243–274, 2003.
- Baker, J., Hunstead, R., Athreya, R., Barthel, P., de Silva, E., Lehnert, M., and Saunders, R. "Associated absorption in radio quasars. I. C IV absorption and the growth of radio sources.". *The Astrophysical Journal*, 568:592–609, 2002.

- Baker, J., Hunstead, R., Kapahi, V., and Subrahmanya, C. "The Molonglo Reference Catalog 1 Jy radio source survey. IV. Optical spectroscopy of a complete quasar sample". *The Astrophysical Journal Supplement Series*, 122:29–50, 1999.
- Baker, J. C. "Origin of the viewing-angle dependence of the optical continuum emission in quasars". *Monthly Notices of the Royal Astronomical Society*, 286:23–37, 1997.
- Baker, J. C., Hunstead, R. W., Bremer, M. N., Bland-Hawthorn, J., Athreya, R. M., and Barr, J. "Tunable-filter imaging of quasar fields at  $z \sim 1.1$ . I. A cluster around MRC B0450-221". *The Astronomical Journal*, 121:1821–1839, 2001.
- Baker, J. C., Hunstead, R. W., and Brinkmann, W. "Radio and X-ray beaming in steep-spectrum quasars". *Monthly Notices of the Royal Astronomical Society*, 277:553–560, 1995.
- Barr, J. *The environments of radio-loud quasars*. PhD thesis, University of Bristol, 2003.
- Barr, J., Baker, J., Bremer, M., Hunstead, R., and Bland-Hawthorn, J. "Tunable-filter imaging of quasar fields at  $z \sim 1$ . II. The star forming galaxy environments of radio-loud quasars". *The Astronomical Journal*, 121:2660–2676, 2004.
- Beckwith, S. V. W. et al. "The Hubble Ultra Deep Field". *The Astronomical Journal*, 132:1729–1755, 2006.
- Bertin, E. and Arnouts, S. "SExtractor: Software for source extraction". *Astronomy and Astrophysics Supplement Series*, 117:393–404, 1996.
- Bland, J. and Tully, R. B. "The Hawaii imaging Fabry-Perot interferometer (HIFI)". *The Astronomical Journal*, 98:723–735, 1989.
- Bland-Hawthorn, J. "Tridimensional spectroscopic techniques: conference summary". In Comte, G. and Marcellin, M., editors, *Tridimensional Optical Spectroscopic Methods in Astrophysics*, number 71 in the A.S.P. Conference Series, pages 369–381, 1995.
- Bland-Hawthorn, J. and Cecil, G. "Classical spectroscopy". In Dunning, F. and Hulet, R., editors, *Atomic, Molecular and Optical Physics: Atoms and Molecules*, volume 29B, chapter 18. Academic Press, New York, 1997.
- Bland-Hawthorn, J. and Jones, D. H. "Taurus Tunable Filter: A flexible approach to narrowband imaging". *Publications of the Astronomical Society of Australia*, 15:44–49, 1998.
- Born, M. and Wolf, E. *Principles of Optics*. Cambridge University Press, seventh edition, 1999.
- Bouwens, R. J. et al. "Galaxies at  $z \sim 7$ –8:  $z_{850}$ -dropouts in the Hubble Ultra Deep Field". *The Astrophysical Journal*, 616:L79–L82, 2004a.
- Bouwens, R. J., Illingworth, G. D., Blakeslee, J. P., Broadhurst, T. J., and Franx, M. "Galaxy size evolution at high redshift and surface brightness selection effects: Constraints from the Hubble Ultra Deep Field". *The Astrophysical Journal*, 611:L1–L4, 2004b.
- Bower, R. G., Lucey, J. R., and Ellis, R. S. "Precision photometry of early-type galaxies in the Coma and Virgo clusters: A test of the universality of the colour-magnitude relation. I—The data". *Monthly Notices of the Royal Astronomical Society*, 254:589–600, 1992a.

- Bower, R. G., Lucey, J. R., and Ellis, R. S. "Precision photometry of early-type galaxies in the Coma and Virgo clusters: A test of the universality of the colour-magnitude relation. II—Analysis". *Monthly Notices of the Royal Astronomical Society*, 254:601–613, 1992b.
- Bremer, M. N. and Baker, J. C. "Radio-loud quasars in distant groups and clusters". In Röttgering, H. J. A., Best, P. N., and Lehnert, M. D., editors, *The Most Distant Radio Galaxies*, pages 425–436. Royal Netherlands Academy of Arts and Sciences, 1999.
- Bremer, M. N., Baker, J. C., and Lehnert, M. D. "A quasar in a compact group of galaxies at  $z = 0.7$ ". *Monthly Notices of the Royal Astronomical Society*, 337:470–476, 2002.
- Bremer, M. N. et al. "XMM-LSS discovery of a  $z = 1.22$  galaxy cluster". *Monthly Notices of the Royal Astronomical Society*, 371:1427–1434, 2006.
- Bresolin, F. and Kennicutt, R. C. "UBVR and  $H\alpha$  photometry of H II regions and OB associations in galaxies: a test for a variable IMF". *The Astronomical Journal*, 113:975–980, 1997.
- Brocklehurst, M. "Calculations of the level populations for the low levels of hydrogenic ions in gaseous nebulae". *Monthly Notices of the Royal Astronomical Society*, 153:471–490, 1971.
- Bunker, A. J. *Searches for distant galaxies*. PhD thesis, University of Oxford, 1996.
- Bunker, A. J., Stanway, E. R., Ellis, R. S., and McMahon, R. G. "The star formation rate of the universe at  $z \sim 6$  from the Hubble Ultra-Deep Field". *Monthly Notices of the Royal Astronomical Society*, 355:374–384, 2004.
- Bunker, A. J., Warren, S. J., Hewett, P. C., and Clements, D. L. "On near-infrared  $H\alpha$  searches for high-redshift galaxies". *Monthly Notices of the Royal Astronomical Society*, 273:513–516, 1995.
- Burke, D. J., Collins, C. A., Sharples, R. M., Romer, A. K., Holden, B. P., and Nichol, R. C. "The Southern SHARC Survey: the  $z = 0.3$ –0.7 cluster X-ray luminosity function 1". *The Astrophysical Journal*, 488:L83, 1997.
- Bushouse, H. A. "Star-formation rates in the nuclei of violently interacting galaxies". *The Astronomical Journal*, 91:255–270, 1986.
- Butcher, H. and Oemler, A. "The evolution of galaxies in clusters. I—ISIT photometry of C1 0024+1654 and 3C 295". *The Astrophysical Journal*, 219:18–30, 1978.
- Caldwell, N., Kennicutt, R., Phillips, A. C., and Schommer, R. A. "A study of star formation in the disks of SA galaxies". *The Astrophysical Journal*, 370:526–540, 1991.
- Caldwell, N., Kennicutt, R., and Schommer, R. "S0's and the lower limit of star-formation rates in disk galaxies". *The Astronomical Journal*, 108:1186–1190, 1994.
- Carroll, S. M., Press, W. H., and Turner, E. L. "The cosmological constant". *Annual Review of Astronomy and Astrophysics*, 30:499–542, 1992.

- Cattaneo, A. "The growth history of supermassive black holes and the origin of the radio-loud-radio-quiet dichotomy". *Monthly Notices of the Royal Astronomical Society*, 333:353–359, 2002.
- Cepa, J. and Beckman, J. E. "Star formation triggering by density waves in the grand design spirals NGC 3992 and NGC 628". *The Astrophysical Journal*, 349:497–502, 1990.
- Cepa, J. et al. "OSIRIS tunable imager and spectrograph". In Iye, M. and Moorwood, A. F., editors, *Optical and IR telescope instrumentation and detectors*, volume 4008 of the *Proceedings of SPIE*, pages 623–631, 2000.
- Charlot, S. and Bruzual, A. G. "Stellar population synthesis revisited". *The Astrophysical Journal*, 367:126–140, 1991.
- Charlot, S. and Fall, S. M. "Attenuation of Lyman-alpha emission by dust in damped Lyman-alpha systems". *The Astrophysical Journal*, 378:471–475, 1991.
- Cianci, S., Bland-Hawthorn, J., and O'Byrne, J. "Designing ultra-narrowband interference filters". In Atad-Ettedgui, E. and Dierickx, P., editors, *Optical fabrication, metrology, and material advancements for telescopes*, volume 5494 of the *Proceedings of SPIE*, pages 520–528, 2004.
- Cole, S., Lacey, C. G., Baugh, C. M., and Frenk, C. S. "Hierarchical galaxy formation". *Monthly Notices of the Royal Astronomical Society*, 319:168–204, 2000.
- Condon, J. J., Cotton, W. D., Greisen, E. W., Yin, Q. F., Perley, R. A., Taylor, G. B., and Broderick, J. J. "The NRAO VLA Sky Survey". *The Astronomical Journal*, 115:1693–1716, 1998.
- Connolly, A. J., Szalay, A. S., Dickinson, M., Subbarao, M. U., and Brunner, R. J. "The evolution of the global star formation history as measured from the Hubble Deep Field". *The Astrophysical Journal*, 486:L11–L14, 1997.
- Cowie, L. L. and Hu, E. M. "High-z Ly  $\alpha$  emitters. I. A blank-field search for objects near redshift  $z = 3.4$  in and around the Hubble Deep Field and the Hawaii Deep Field SSA 22". *The Astronomical Journal*, 115:1319–1328, 1998.
- Cowie, L. L., Hu, E. M., Songaila, A., and Egami, E. "The evolution of the distribution of star formation rates in galaxies". *The Astrophysical Journal*, 481:L9–L13, 1997.
- Dalton, G. B., Efstathiou, G., Maddox, S. J., and Sutherland, W. J. "The APM Galaxy Survey—IV. Redshifts of rich clusters of galaxies". *Monthly Notices of the Royal Astronomical Society*, 269:151–165, 1994.
- Dawson, S. et al. "Spectroscopic properties of the  $z \sim 4.5$  Ly  $\alpha$  emitters". *The Astrophysical Journal*, 617:707–717, 2004.
- Devereux, N. "The spatial distribution of 10 micron luminosity in spiral galaxies". *The Astrophysical Journal*, 323:91–107, 1987.
- Dressler, A. "A catalog of morphological types in 55 rich clusters of galaxies". *The Astrophysical Journal Supplement Series*, 42:565–609, 1980.

- Dressler, A. "The evolution of galaxies in clusters". *Annual Review of Astronomy and Astrophysics*, 22:185–222, 1984.
- Ebeling, H., Edge, A. C., Bohringer, H., Allen, S. W., Crawford, C. S., Fabian, A. C., Voges, W., and Huchra, J. P. "The ROSAT Brightest Cluster Sample—I. The compilation of the sample and the cluster log  $N$ -log  $S$  distribution". *Monthly Notices of the Royal Astronomical Society*, 301:881–914, 1998.
- Ebeling, H., Edge, A. C., and Henry, J. P. "MACS: A quest for the most massive galaxy clusters in the universe". *The Astrophysical Journal*, 553:668–676, 2001.
- Ebeling, H., Voges, W., Bohringer, H., Edge, A. C., Huchra, J. P., and Briel, U. G. "Properties of the X-ray-brightest Abell-type clusters of galaxies (XBACs) from ROSAT All-Sky Survey data—I. The sample". *Monthly Notices of the Royal Astronomical Society*, 281:799–829, 1996.
- Einasto, J. and Einasto, M. "Dark matter in groups and clusters of galaxies". In Valtonen, M. J. and Flynn, C., editors, *Small Galaxy Groups*, number 209 in the A.S.P. Conference Series, pages 360–372, 2000.
- Ellingson, E., Yee, H. K. C., and Green, R. F. "Quasars and active galactic nuclei in rich environments. I—Fields surrounding optically faint quasars". *The Astrophysical Journal Supplement Series*, 76:455–470, 1991a.
- Ellingson, E., Yee, H. K. C., and Green, R. F. "Quasars and active galactic nuclei in rich environments. II—The evolution of radio-loud quasars". *The Astrophysical Journal*, 371:49–59, 1991b.
- Elmegreen, B. G. and Elmegreen, D. M. "Do density waves trigger star formation?". *The Astrophysical Journal*, 311:554–562, 1986.
- Fabry, C. and Buisson, H. "Application of the interference method to the study of nebulae". *The Astrophysical Journal*, 33:406–409, 1911.
- Fabry, C. and Pérot, A. "On a new form of interferometer". *The Astrophysical Journal*, 13:265–272, 1901.
- Felten, J. E., Gould, R. J., Stein, W. A., and Woolf, N. J. "X-rays from the Coma cluster of galaxies". *The Astrophysical Journal*, 146:955–958, 1966.
- Francis, P. J. and Bland-Hawthorn, J. "The mysterious absence of neutral hydrogen within 1 Mpc of a luminous quasar at redshift 2.168". *Monthly Notices of the Royal Astronomical Society*, 353:301–309, 2004.
- Fujita, S. S. et al. "A search for  $\text{Ly}\alpha$  emitters at redshift 3.7". *The Astronomical Journal*, 125:13–31, 2003.
- Gallagher, J. S., Hunter, D. A., and Bushouse, H. "Star-formation rates and [O II] emission in blue galaxies". *The Astronomical Journal*, 97:700–707, 1989.
- Gallego, J., Zamorano, J., Aragon-Salamanca, A., and Rego, M. "The current star formation rate of the local universe". *The Astrophysical Journal*, 455:L1–L4, 1995.

- Gallego, J., Zamorano, J., Aragon-Salamanca, A., and Rego, M. "The current star formation rate of the local universe: Erratum". *The Astrophysical Journal*, 459:L43, 1996.
- Gear, W. K. and Cunningham, C. R. "SCUBA: A camera for the James Clerk Maxwell Telescope". In Emerson, D. T. and Payne, J. M., editors, *Multi-feed systems for radio telescopes*, number 75 in the A.S.P. Conference Series, pages 215–221, 1995.
- Giavalisco, M. "Lyman-break galaxies". *Annual Review of Astronomy and Astrophysics*, 40:579–641, 2002.
- Gladders, M. D., Lopez-Cruz, O., Yee, H. K. C., and Kodama, T. "The slope of the cluster elliptical red sequence: A probe of cluster evolution". *The Astrophysical Journal*, 501:571–577, 1998.
- Gladders, M. D. and Yee, H. K. C. "A new method for galaxy cluster detection. I. The algorithm". *The Astronomical Journal*, 120:2148–2162, 2000.
- Goto, T. et al. "The Cut-and-Enhance Method: Selecting Clusters of Galaxies from the Sloan Digital Sky Survey Commissioning Data". *The Astronomical Journal*, 123:1807–1825, 2002.
- Green, R. F. and Yee, H. K. C. "An imaging survey of fields around quasars. I—A catalog". *The Astrophysical Journal Supplement Series*, 54:495–512, 1984.
- Gunn, J. E. and Gott, J. R. I. "On the infall of matter into clusters of galaxies and some effects on their evolution". *The Astrophysical Journal*, 176:1–19, 1972.
- Haiman, Z. and Spaans, M. "Models for dusty Ly  $\alpha$  emitters at high redshift". *The Astrophysical Journal*, 518:138–144, 1999.
- Hall, P. B. and Green, R. F. "An optical/near-infrared study of radio-loud quasar environments. II. Imaging results". *The Astrophysical Journal*, 507:558–584, 1998.
- Hall, P. B., Green, R. F., and Cohen, M. "An optical/near-infrared study of radio-loud quasar environments. I. Methods and  $z = 1\text{--}2$  observations". *The Astrophysical Journal Supplement Series*, 119:1–23, 1998.
- Hamuy, M., Walker, A., Suntzeff, N., Gigoux, P., Heathcote, S., and Phillips, M. "Southern spectrophotometric standards". *Publications of the Astronomical Society of the Pacific*, 104:533–552, 1992.
- Hawthorn, J. and Kedziora-Chudczer, L. *Taurus User Guide*. Anglo-Australian Observatory, 2002.
- Hicks, T. R., Reay, N. K., and Atherton, P. D. "The application of capacitance micrometry to the control of Fabry-Pérot etalons". *Journal of Physics E: Scientific Instruments*, 17:49–55, 1984.
- Hicks, T. R., Reay, N. K., and Scaddan, R. J. "A servo controlled Fabry-Perot interferometer using capacitance micrometers for error detection". *Journal of Physics E: Scientific Instruments*, 7:27–30, 1974.

- Hippelein, H. et al. "Star forming rates between  $z = 0.25$  and  $z = 1.2$  from the CADIS emission line survey". *Astronomy and Astrophysics*, 402:65–78, 2003.
- Ho, L. C., Filippenko, A. V., and Sargent, W. L. W. "Properties of H II regions in the centers of nearby galaxies". *The Astrophysical Journal*, 487:579–590, 1997a.
- Ho, L. C., Filippenko, A. V., and Sargent, W. L. W. "The influence of bars on nuclear activity". *The Astrophysical Journal*, 487:591–602, 1997b.
- Hogg, D. W. "Distance measures in cosmology". astro-ph/9905116, 2000.
- Holder, G., Haiman, Z., and Mohr, J. J. "Constraints on  $\Omega_m$ ,  $\Omega_\Lambda$ , and  $\sigma_8$  from galaxy cluster redshift distributions". *The Astrophysical Journal*, 560:L111–L114, 2001.
- Horton, A., Parry, I., Bland-Hawthorn, J., Cianci, S., King, D., McMahon, R., and Medlen, S. "DAzLE: The dark ages  $z$  (redshift) lyman- $\alpha$  explorer". In Moorwood, A. F. M. and Iye, M., editors, *Ground-based instrumentation for astronomy*, volume 5492 of the *Proceedings of SPIE*, pages 1022–1032, 2004.
- Hu, E. M., Cowie, L. L., Capak, P., McMahon, R. G., Hayashino, T., and Komiyama, Y. "The luminosity function of Ly  $\alpha$  emitters at redshift  $z \sim 5.7$ ". *The Astronomical Journal*, 127:563–575, 2004.
- Hu, E. M., Cowie, L. L., and McMahon, R. G. "The density of Ly  $\alpha$  emitters at very high redshift". *The Astrophysical Journal*, 502:L99–L103, 1998.
- Hu, E. M. and McMahon, R. G. "Detection of Lyman- $\alpha$  emitting galaxies at redshift  $z = 4.55$ ". *Nature*, 382:231–233, 1996.
- Hubble, E. "The distribution of extra-galactic nebulae". *The Astrophysical Journal*, 79:8–76, 1934.
- Hutchings, J. B., Janson, T., and Neff, S. G. "What is the difference between radio-loud and radio-quiet quasi-stellar objects?". *The Astrophysical Journal*, 342:660–665, 1989.
- Irwin, M., McMahon, R. G., and Hazard, C. "APM optical surveys for high redshift quasars". In Crampton, D., editor, *The Space Distribution of Quasars*, number 21 in the A.S.P. Conference Series, pages 117–126, 1991.
- Irwin, M. J. "Automatic analysis of crowded fields". *Monthly Notices of the Royal Astronomical Society*, 214:575–604, 1985.
- Iwata, I., Ohta, K., Tamura, N., Ando, M., Wada, S., Watanabe, C., Akiyama, M., and Aoki, K. "Lyman break galaxies at  $z \sim 5$ : Luminosity function". *Publications of the Astronomical Society of Japan*, 55:415–432, 2003.
- Jacquinot, P. "The luminosity of spectrometers with prisms, gratings, or Fabry Perot etalons". *Journal of the Optical Society of America*, 44:761–765, 1954.
- Janesick, J. and Elliott, T. "History and advancement of large array scientific CCD imagers". In Howell, S. B., editor, *Astronomical CCD Observing and Reduction Techniques*, number 23 in the A.S.P. Conference Series, pages 1–67, 1992.

- Jones, D. H. *Tunable filter surveys of star-forming galaxies*. PhD thesis, Australian National University, 1999.
- Jones, D. H. and Bland-Hawthorn, J. "Parallelism of a Fabry-Pérot cavity at micron spacings". *Publications of the Astronomical Society of the Pacific*, 110:1059–1066, 1998.
- Jones, D. H., Shopbell, P. L., and Bland-Hawthorn, J. "Detection and measurement from narrow-band tunable filter scans". *Monthly Notices of the Royal Astronomical Society*, 329:759–774, 2002.
- Jones, R. V. and Richards, J. C. S. "The design and some applications of sensitive capacitance micrometers". *Journal of Physics E: Scientific Instruments*, 6:589–600, 1973.
- Joye, W. A. and Mandel, E. "New features of SAOImage DS9". In Payne, H. E., Jedrzejewski, R. I., and Hook, R. N., editors, *Astronomical data analysis software and systems XII*, number 295 in the A.S.P. Conference Series, page 489, 2003.
- Kaiser, N. "On the spatial correlations of Abell clusters". *The Astrophysical Journal*, 284:L9–L12, 1984.
- Kapahi, V., Athreya, R., Subrahmanya, C., Baker, J., Hunstead, R., McCarthy, P., and van Breugel, W. "The Molonglo reference catalog 1 Jy radio source survey. III. Identification of a complete quasar sample". *The Astrophysical Journal Supplement Series*, 118:327–352, 1998.
- Kawasaki, W., Shimasaku, K., Doi, M., and Okamura, S. "An objective and automatic cluster finder: an improvement of the matched-filter method". *Astronomy and Astrophysics Supplement Series*, 130:567–579, 1998.
- Keel, W. C., Kennicutt, R. C., Hummel, E., and van der Hulst, J. M. "The effects of interactions on spiral galaxies. I—Nuclear activity and star formation". *The Astronomical Journal*, 90:708–730, 1985.
- Kellermann, K. I., Sramek, R., Schmidt, M., Shaffer, D. B., and Green, R. "VLA observations of objects in the Palomar Bright Quasar Survey". *The Astronomical Journal*, 98:1195–1207, 1989.
- Kennicutt, R. C. "Star formation in galaxies along the Hubble sequence". *Annual Review of Astronomy and Astrophysics*, 36:189–231, 1998.
- Kennicutt, R. C. "The global Schmidt law in star-forming galaxies". *The Astrophysical Journal*, 498:541–552, 1998.
- Kennicutt, R. C., Tamblyn, P., and Congdon, C. E. "Past and future star formation in disk galaxies". *The Astrophysical Journal*, 435:22–36, 1994.
- Kennicutt, Jr., R. C. "The integrated spectra of nearby galaxies—general properties and emission-line spectra". *The Astrophysical Journal*, 388:310–327, 1992a.
- Kennicutt, Jr., R. C. "A spectrophotometric atlas of galaxies". *The Astrophysical Journal Supplement Series*, 79:255–284, 1992b.

- Kneissl, R., Jones, M. E., Saunders, R., Eke, V. R., Lasenby, A. N., Grainge, K., and Cotter, G. "Surveying the sky with the Arcminute MicroKelvin Imager: expected constraints on galaxy cluster evolution and cosmology". *Monthly Notices of the Royal Astronomical Society*, 328:783–794, 2001.
- Kodaira, K. et al. "The discovery of two Ly  $\alpha$  emitters beyond redshift 6 in the Subaru Deep Field". *Publications of the Astronomical Society of Japan*, 55:L17–L21, 2003.
- Kodama, T., Arimoto, N., Barger, A. J., and Aragón-Salamanca, A. "Evolution of the colour-magnitude relation of early-type galaxies in distant clusters". *Astronomy and Astrophysics*, 334:99–109, 1998.
- Kosowsky, A. "The Atacama Cosmology Telescope". *New Astronomy Review*, 47:939–943, 2003.
- Kudritzki, R.-P. et al. "Discovery of nine Ly  $\alpha$  emitters at redshift  $z \sim 3.1$  using narrowband imaging and VLT spectroscopy". *The Astrophysical Journal*, 536:19–30, 2000.
- Kunth, D., Mas-Hesse, J. M., Terlevich, E., Terlevich, R., Lequeux, J., and Fall, S. M. "HST study of Lyman-alpha emission in star-forming galaxies: the effect of neutral gas flows". *Astronomy and Astrophysics*, 334:11–20, 1998.
- Kurk, J. D. et al. "A search for clusters at high redshift. I. Candidate Ly  $\alpha$  emitters near 1138–262 at  $z = 2.2$ ". *Astronomy and Astrophysics*, 358:L1–L4, 2000.
- Kurk, J. D., Pentericci, L., Röttgering, H. J. A., and Miley, G. K. "A proto-cluster around a radio galaxy at redshift 2.16". *Astrophysics and Space Science Supplement*, 277:543–546, 2001.
- Lacy, M. and Rawlings, S. "Imaging of the field of 4C 41.17 below the Lyman limit". *Monthly Notices of the Royal Astronomical Society*, 280:888–894, 1996.
- Large, M. I., Mills, B. Y., Little, A. G., Crawford, D. F., and Sutton, J. M. "The Molonglo Reference Catalogue of radio sources". *Monthly Notices of the Royal Astronomical Society*, 194:693–704, 1981.
- Le Delliou, M., Lacey, C. G., Baugh, C. M., and Morris, S. L. "The properties of Ly  $\alpha$  emitting galaxies in hierarchical galaxy formation models". *Monthly Notices of the Royal Astronomical Society*, 365:712–726, 2006.
- Lehnert, M. D. and Heckman, T. M. "The nature of starburst galaxies". *The Astrophysical Journal*, 472:546–563, 1996.
- Leitherer, C. et al. "A database for galaxy evolution modeling". *Publications of the Astronomical Society of the Pacific*, 108:996–1017, 1996.
- Lilly, S. J., Le Fevre, O., Hammer, F., and Crampton, D. "The Canada-France Redshift Survey: The luminosity density and star formation history of the universe to  $z \sim 1$ ". *The Astrophysical Journal*, 460:L1–L4, 1996.

- Lilly, S. J., Tresse, L., Hammer, F., Crampton, D., and Le Fèvre, O. "The Canada-France Redshift Survey. VI. Evolution of the galaxy luminosity function to  $z \sim 1$ ". *The Astrophysical Journal*, 455:108–124, 1995.
- Liu, C. T. and Kennicutt, R. C. "Spectrophotometric properties of merging galaxies". *The Astrophysical Journal*, 450:547–558, 1995.
- Loh, M. et al. "The Sunyaev-Zel'dovich Array". *Bulletin of the American Astronomical Society*, 37:1225, 2005.
- Longair, M. S. and Seldner, M. "The clustering of galaxies about extragalactic radio sources". *Monthly Notices of the Royal Astronomical Society*, 189:433–453, 1979.
- Lumsden, S. L., Nichol, R. C., Collins, C. A., and Guzzo, L. "The Edinburgh-Durham southern galaxy catalogue. IV—The cluster catalogue". *Monthly Notices of the Royal Astronomical Society*, 258:1–22, 1992.
- Maccacaro, T. et al. "The Einstein Observatory medium sensitivity survey". *Space Science Reviews*, 30:75–80, 1981.
- Madau, P., Pozzetti, L., and Dickinson, M. "The star formation history of field galaxies". *The Astrophysical Journal*, 498:106–116, 1998.
- Malhotra, S. and Rhoads, J. E. "Luminosity functions of Ly  $\alpha$  emitters at redshifts  $z = 6.5$  and  $z = 5.7$ : Evidence against reionization at  $z \leq 6.5$ ". *The Astrophysical Journal*, 617:L5–L8, 2004.
- Marquardt, D. "An algorithm for least-squares estimation of nonlinear parameters". *Journal of the Society for Industrial and Applied Mathematics*, 11:431–441, 1963.
- Marshall, H. L., Tananbaum, H., Huchra, J. P., Zamorani, G., Braccesi, A., and Zitelli, V. "Optical and X-ray observations of faint quasars in an optically selected sample". *The Astrophysical Journal*, 269:42–48, 1983.
- Matsumoto, Y. *Ruby in a Nutshell*. O'Reilly Media, Inc., 2001.
- McCall, M. L. and Schmidt, F. H. "Supernovae in flocculent and grand design spirals". *The Astrophysical Journal*, 311:548–553, 1986.
- McLure, R. J. and Dunlop, J. S. "The cluster environments of powerful radio-loud and radio-quiet active galactic nuclei". *Monthly Notices of the Royal Astronomical Society*, 321:515–524, 2001.
- Miralda-Escude, J. "Reionization of the intergalactic medium and the damping wing of the Gunn-Peterson trough". *The Astrophysical Journal*, 501:15–22, 1998.
- Moffat, A. F. J. "A theoretical investigation of focal stellar images in the photographic emulsion and application to photographic photometry". *Astronomy and Astrophysics*, 3:455–461, 1969.
- Monet, D. G. et al. "The USNO-B catalog". *The Astronomical Journal*, 125:984–993, 2003.

- Moorwood, A. F. M., van der Werf, P. P., Cuby, J. G., and Oliva, E. “H  $\alpha$  emitting galaxies and the cosmic star formation rate at  $z \simeq 2.2$ ”. *Astronomy and Astrophysics*, 362:9–18, 2000.
- Morgan, W. W. “A preliminary classification of the forms of galaxies according to their stellar population”. *Publications of the Astronomical Society of the Pacific*, 70:364–391, 1958.
- Moss, C. and Whittle, M. “An H  $\alpha$  survey of cluster spirals—Comparison of star formation in clusters and the field”. *The Astrophysical Journal*, 407:L17–L20, 1993.
- Murali, C., Katz, N., Hernquist, L., Weinberg, D., and Davé, R. “The growth of galaxies in cosmological simulations of structure formation”. *The Astrophysical Journal*, 571:1–14, 2002.
- Murdoch, H. S., Crawford, D. F., and Jauncey, D. L. “Maximum-likelihood estimation of the number-flux distribution of radio sources in the presence of noise and confusion”. *The Astrophysical Journal*, 183:1–14, 1973.
- Nagamine, K., Wolfe, A. M., and Hernquist, L. “Detectability of [C II] 158  $\mu\text{m}$  emission from high-redshift galaxies: Predictions for ALMA and SPICA”. *The Astrophysical Journal*, 647:60–73, 2006.
- Nath, B. B. and Roychowdhury, S. “Heating of the intracluster medium by quasar outflows”. *Monthly Notices of the Royal Astronomical Society*, 333:145–155, 2002.
- Neufeld, D. A. and McKee, C. F. “Fermi acceleration of Lyman-alpha photons by shocks”. *The Astrophysical Journal*, 331:L87–L90, 1988.
- Oemler, A. J. “The systematic properties of clusters of galaxies. I. Photometry of 15 clusters”. *The Astrophysical Journal*, 194:1–20, 1974.
- Oemler, A. J., Gunn, J. E., and Oke, J. B. “C 323.1: a QSO in a rich cluster of galaxies”. *The Astrophysical Journal*, 176:L47–L50, 1972.
- Oke, J. B. “Absolute spectral energy distributions for white dwarfs”. *The Astrophysical Journal Supplement Series*, 27:21–35, 1974.
- Oke, J. B. et al. “The Keck Low-Resolution Imaging Spectrometer”. *Publications of the Astronomical Society of the Pacific*, 107:375–385, 1995.
- Oke, J. B. and Gunn, J. E. “Secondary standard stars for absolute spectrophotometry”. *The Astrophysical Journal*, 266:713–717, 1983.
- Olsen, L. F. et al. “ESO imaging survey. II. Searching for distant clusters of galaxies”. *Astronomy and Astrophysics*, 345:681–690, 1999.
- Orr, M. J. L. and Browne, I. W. A. “Relativistic beaming and quasar statistics”. *Monthly Notices of the Royal Astronomical Society*, 200:1067–1080, 1982.
- Ouchi, M. et al. “Subaru Deep Survey. II. Luminosity functions and clustering properties of Ly  $\alpha$  emitters at  $z = 4.86$  in the Subaru Deep Field”. *The Astrophysical Journal*, 582:60–68, 2003.

- Overzier, R. A. et al. "Clustering of star-forming galaxies near a radio galaxy at  $z = 5.2$ ". *The Astrophysical Journal*, 637:58–73, 2006a.
- Overzier, R. A. et al. "Star formation, morphologies and clustering of galaxies in a radio galaxy protocluster at  $z = 4.1$ ". *The Astrophysical Journal*, submitted for publication, 2006b.
- Partridge, R. B. and Peebles, P. J. E. "Are young galaxies visible?". *The Astrophysical Journal*, 147:868–886, 1967.
- Peacock, J. et al. "A measurement of the cosmological mass density from clustering in the 2dF Galaxy Redshift Survey". *Nature*, 410:169–173, 2001.
- Peebles, P. J. E., Daly, R. A., and Juszkiewicz, R. "Masses of rich clusters of galaxies as a test of the biased cold dark matter theory". *The Astrophysical Journal*, 347:563–574, 1989.
- Pen, U.-L. "Analytical fit to the luminosity distance for flat cosmologies with a cosmological constant". *The Astrophysical Journal Supplement Series*, 120:49–50, 1999.
- Pentericci, L. et al. "A search for clusters at high redshift. II. A proto cluster around a radio galaxy at  $z = 2.16$ ". *Astronomy and Astrophysics*, 361:L25–L28, 2000.
- Perlman, E. S., Horner, D. J., Jones, L. R., Scharf, C. A., Ebeling, H., Wegner, G., and Malkan, M. "The WARPS survey. VI. Galaxy cluster and source identifications from phase I". *The Astrophysical Journal Supplement Series*, 140:265–301, 2002.
- Pérot, A. and Fabry, C. "On the application of interference phenomena to the solution of various problems of spectroscopy and metrology". *The Astrophysical Journal*, 9:87–115, 1899.
- Pettini, M., Steidel, C. C., Adelberger, K. L., Dickinson, M., and Giavalisco, M. "The ultraviolet spectrum of MS 1512-CB58: An insight into Lyman-break galaxies". *The Astrophysical Journal*, 528:96–107, 2000.
- Pierre, M. et al. "The XMM-LSS survey. Survey design and first results". *Journal of Cosmology and Astroparticle Physics*, 9:11, 2004.
- Postman, M., Lubin, L. M., Gunn, J. E., Oke, J. B., Hoessel, J. G., Schneider, D. P., and Christensen, J. A. "The Palomar distant clusters survey. I. The cluster catalog". *The Astronomical Journal*, 111:615–641, 1996.
- Press, W. H. and Schechter, P. "Formation of galaxies and clusters of galaxies by self-similar gravitational condensation". *The Astrophysical Journal*, 187:425–438, 1974.
- Rawlings, S. and Jarvis, M. J. "Evidence that powerful radio jets have a profound influence on the evolution of galaxies". *Monthly Notices of the Royal Astronomical Society*, 355:L9–L12, 2004.
- Refregier, A., Valtchanov, I., and Pierre, M. "Cosmology with galaxy clusters in the XMM large-scale structure survey". *Astronomy and Astrophysics*, 390:1–12, 2002.

- Rhoads, J. E. et al. "Spectroscopic confirmation of three redshift  $z \sim 5.7$  Ly  $\alpha$  emitters from the large-area lyman alpha survey". *The Astronomical Journal*, 125:1006–1013, 2003.
- Rhoads, J. E. and Malhotra, S. "Ly  $\alpha$  emitters at redshift  $z = 5.7$ ". *The Astrophysical Journal*, 563:L5–L9, 2001.
- Rhoads, J. E., Malhotra, S., Dey, A., Stern, D., Spinrad, H., and Jannuzi, B. T. "First results from the Large-Area Lyman Alpha survey". *The Astrophysical Journal*, 545:L85–L88, 2000.
- Richard, J., Pello, R., Schaerer, D., Le Borgne, J.-F., and Kneib, J.-P. "Constraining the population of  $6 < z < 10$  star-forming galaxies with deep near-IR images of lensing clusters". *Astronomy and Astrophysics*, accepted for publication, 2006.
- Romer, A. K., Viana, P. T. P., Liddle, A. R., and Mann, R. G. "A serendipitous galaxy cluster survey with XMM: Expected catalog properties and scientific applications". *The Astrophysical Journal*, 547:594–608, 2001.
- Rosati, P. "Results from the ROSAT Deep Cluster Survey". *Astronomische Nachrichten*, 319:79–82, 1998.
- Ruhl, J. et al. "The South Pole Telescope". In Zmuidzinas, J., Holland, W. S., and Withington, S., editors, *Millimeter and submillimeter detectors for astronomy II*, volume 5498 of the *Proceedings of SPIE*, pages 11–29, 2004.
- Ryder, S. D. and Dopita, M. A. "The relationship between past and present star formation in galactic disks from CCD surface photometry". *The Astrophysical Journal*, 430:142–162, 1994.
- Salpeter, E. E. "The luminosity function and stellar evolution". *The Astrophysical Journal*, 121:161–167, 1955.
- Sarazin, C. L. "X-ray emission from clusters of galaxies". *Reviews of Modern Physics*, 58:1–115, 1986.
- Scalo, J. M. "The stellar initial mass function". *Fundamentals of Cosmic Physics*, 11:1–278, 1986.
- Schaller, G., Schaerer, D., Meynet, G., and Maeder, A. "New grids of stellar models from 0.8 to 120 solar masses at  $z = 0.020$  and  $z = 0.001$ ". *Astronomy and Astrophysics Supplement Series*, 96:269–331, 1992.
- Schechter, P. "An analytic expression for the luminosity function for galaxies". *The Astrophysical Journal*, 203:297–306, 1976.
- Schlegel, D. J., Finkbeiner, D. P., and Davis, M. "Maps of dust infrared emission for use in estimation of reddening and cosmic microwave background radiation foregrounds". *The Astrophysical Journal*, 500:525–553, 1998.
- Schmidt, M. "3C 273: A star-like object with large red-shift". *Nature*, 197:1040, 1963.
- Scoville, N. Z., Becklin, E. E., Young, J. S., and Capps, R. W. "A 10 micron survey of star formation in galactic nuclei Virgo spiral galaxies". *The Astrophysical Journal*, 271:512–523, 1983.

- Seldner, M. and Peebles, P. J. E. "Statistical analysis of catalogs of extragalactic objects. X—Clustering of 4C radio sources". *The Astrophysical Journal*, 225:7–20, 1978.
- Sérsic, J. L. and Pastoriza, M. "Properties of galaxies with peculiar nuclei". *Publications of the Astronomical Society of the Pacific*, 79:152–155, 1967.
- Smail, I., Ellis, R. S., Fitchett, M. J., and Edge, A. C. "Gravitational lensing of distant field galaxies by rich clusters—II. Cluster mass distributions". *Monthly Notices of the Royal Astronomical Society*, 273:277–294, 1995.
- Smith, B. J. and Harvey, P. M. "High spatial resolution KAO far-infrared observations of the central regions of infrared-bright galaxies". *The Astrophysical Journal*, 468:139–166, 1996.
- Smith, E. P., Heckman, T. M., Bothun, G. D., Romanishin, W., and Balick, B. "On the nature of QSO host galaxies". *The Astrophysical Journal*, 306:64–89, 1986.
- Standish, Jr., E. M. "Conversion of positions and proper motions from B1950.0 to the IAU system at J2000.0". *Astronomy and Astrophysics*, 115:20–22, 1982.
- Stanway, E. R., Bunker, A. J., McMahon, R. G., Ellis, R. S., Treu, T., and McCarthy, P. J. "Hubble Space Telescope imaging and Keck spectroscopy of  $z \sim 6$  i-band dropout galaxies in the Advanced Camera for Surveys GOODS fields". *The Astrophysical Journal*, 607:704–720, 2004.
- Steidel, C. C., Adelberger, K. L., Giavalisco, M., Dickinson, M., and Pettini, M. "Lyman-break galaxies at  $z \gtrsim 4$  and the evolution of the ultraviolet luminosity density at high redshift". *The Astrophysical Journal*, 519:1–17, 1999.
- Steidel, C. C. and Hamilton, D. "Deep imaging of high redshift QSO fields below the lyman limit. I—The field of q0000-263 and galaxies at  $z = 3.4$ ". *The Astronomical Journal*, 104:941–949, 1992.
- Steidel, C. C. and Hamilton, D. "Deep imaging of high redshift QSO fields below the lyman limit. II—Number counts and colors of field galaxies". *The Astronomical Journal*, 105:2017–2030, 1993.
- Steidel, C. C. and Sargent, W. L. W. "Emission-line and continuum properties of 92 bright QSOs—Luminosity dependence and differences between radio-selected and optically selected samples". *The Astrophysical Journal*, 382:433–465, 1991.
- Stetson, P. B. "DAOPHOT—A computer program for crowded-field stellar photometry". *Publications of the Astronomical Society of the Pacific*, 99:191–222, 1987.
- Stiavelli, M. et al. "Evidence of primordial clustering around the QSO SDSS J1030+0524 at  $z = 6.28$ ". *The Astrophysical Journal*, 622:L1–L4, 2005.
- Stickel, M., Fried, J. W., and Kuehr, H. "Optical spectroscopy of 1 Jy BL Lacertae objects and flat spectrum radio sources". *Astronomy and Astrophysics Supplement Series*, 80:103–114, 1989.

- Stone, R. C. "A comparison of digital centering algorithms". *The Astronomical Journal*, 97:1227–1237, 1989.
- Storrie-Lombardi, L., McMahon, R., Irwin, M., and Hazard, C. "APM  $z >= 4$  QSO survey: Spectra and intervening absorption systems". *The Astrophysical Journal*, 468:121–138, 1996.
- Sunyaev, R. A. and Zel'dovich, Y. B. "Small-scale fluctuations of relic radiation". *Astrophysics and Space Science*, 7:3–19, 1970.
- Tapken, C., Appenzeller, I., Mehlert, D., Noll, S., and Richling, S. "The nature of the Ly  $\alpha$ -emission region of FDF-4691". *Astronomy and Astrophysics*, 416:L1–L4, 2004.
- Thompson, D., Djorgovski, S., and Trauger, J. "A narrow band imaging survey for primeval galaxies". *The Astronomical Journal*, 110:963–981, 1995.
- Thompson, D., Mannucci, F., and Beckwith, S. V. W. "A narrowband imaging survey for high redshift galaxies in the near infrared". *The Astronomical Journal*, 112:1794–1802, 1996.
- Tody, D. "The IRAF data reduction and analysis system". In Crawford, D. L., editor, *Instrumentation in astronomy VI*, volume 627 of the *Proceedings of SPIE*, page 733, 1986.
- Tody, D. "IRAF in the nineties". In Hanisch, R. J., Brissenden, R. J. V., and Barnes, J., editors, *Astronomical data analysis software and systems II*, number 52 in the A.S.P. Conference Series, page 173, 1993.
- Toomre, A. and Toomre, J. "Galactic bridges and tails". *The Astrophysical Journal*, 178:623–666, 1972.
- Tresse, L. and Maddox, S. J. "The H  $\alpha$  luminosity function and star formation rate at  $z \sim 0.2$ ". *The Astrophysical Journal*, 495:691–697, 1998.
- Treyer, M. A., Ellis, R. S., Milliard, B., Donas, J., and Bridges, T. J. "An ultraviolet-selected galaxy redshift survey: new estimates of the local star formation rate". *Monthly Notices of the Royal Astronomical Society*, 300:303–314, 1998.
- Urry, C. M. and Padovani, P. "Unified schemes for radio-loud active galactic nuclei". *Publications of the Astronomical Society of the Pacific*, 107:803–845, 1995.
- Valls-Gabaud, D. "On the Lyman  $\alpha$  emission of starburst galaxies". *The Astrophysical Journal*, 419:7–11, 1993.
- Valtchanov, I. et al. "The XMM-LSS survey. First high redshift galaxy clusters: Relaxed and collapsing systems". *Astronomy and Astrophysics*, 423:75–85, 2004.
- van Breukelen, C., Jarvis, M. J., and Venemans, B. P. "The luminosity function of Ly  $\alpha$  emitters at  $2.3 < z < 4.6$  from integral-field spectroscopy". *Monthly Notices of the Royal Astronomical Society*, 359:895–905, 2005.
- Vanden Berk, D. E. et al. "Composite quasar spectra from the Sloan Digital Sky Survey". *The Astronomical Journal*, 122:549–564, 2001.

- Venemans, B. P. et al. "Discovery of six Ly $\alpha$  emitters near a radio galaxy at  $z \sim 5.2$ ". *Astronomy and Astrophysics*, 424:L17–L20, 2004.
- Venemans, B. P. et al. "Properties of Ly $\alpha$  emitters around the radio galaxy MRC 0316 257". *Astronomy and Astrophysics*, 431:793–812, 2005.
- Venemans, B. P., Kurk, J. D., Miley, G. K., Röttgering, H. J. A., van Breugel, W., Carilli, C. L., De Breuck, C., Ford, H., Heckman, T., McCarthy, P., and Pentericci, L. "The most distant structure of galaxies known: A protocluster at  $z = 4.1$ ". *The Astrophysical Journal*, 569:L11–L14, 2002.
- Warren, S. J., Hewett, P. C., and Osmer, P. S. "A wide-field multicolor survey for high-redshift quasars,  $z \geq 2.2$ . III. The luminosity function". *The Astrophysical Journal*, 421:412–433, 1994.
- Weedman, D. W., Feldman, F. R., Balzano, V. A., Ramsey, L. W., Sramek, R. A., and Wuu, C.-C. "NGC 7714—The prototype star-burst galactic nucleus". *The Astrophysical Journal*, 248:105–112, 1981.
- Werner, M. W. et al. "The Spitzer Space Telescope mission". *The Astrophysical Journal Supplement Series*, 154:1–9, 2004.
- White, S. D. M. and Rees, M. J. "Core condensation in heavy halos—A two-stage theory for galaxy formation and clustering". *Monthly Notices of the Royal Astronomical Society*, 183:341–358, 1978.
- Willis, J. P. et al. "The XMM Large-Scale Structure survey: an initial sample of galaxy groups and clusters to a redshift  $z < 0.6$ ". *Monthly Notices of the Royal Astronomical Society*, 363:675–691, 2005.
- Wilson, A. S. and Colbert, E. J. M. "The difference between radio-loud and radio-quiet active galaxies". *The Astrophysical Journal*, 438:62–71, 1995.
- Wolf, C., Wisotzki, L., Borch, A., Dye, S., Kleinheinrich, M., and Meisenheimer, K. "The evolution of faint AGN between  $z \simeq 1$  and  $z \simeq 5$  from the COMBO-17 survey". *Astronomy and Astrophysics*, 408:499–514, 2003.
- Xu, C. and Sulentic, J. W. "Infrared emission in paired galaxies. II—Luminosity functions and far-infrared properties". *The Astrophysical Journal*, 374:407–430, 1991.
- Yee, H. K. C. and Ellingson, E. "Quasars and active galactic nuclei in rich environments. III—The rapid evolution of active galactic nucleus activity in rich clusters". *The Astrophysical Journal*, 411:43–54, 1993.
- Yee, H. K. C. and Ellingson, E. "Correlations of richness and global properties in galaxy clusters". *The Astrophysical Journal*, 585:215–226, 2003.
- Yee, H. K. C., Ellingson, E., Bechtold, J., Carlberg, R. G., and Cuillandre, J.-C. "A protogalaxy candidate at  $z = 2.7$  discovered by its young stellar population". *The Astronomical Journal*, 111:1783–1794, 1996a.

- Yee, H. K. C., Ellingson, E., and Carlberg, R. G. "The CNOC cluster redshift survey catalogs. I. Observational strategy and data reduction techniques". *The Astrophysical Journal Supplement Series*, 102:269–287, 1996b.
- Yee, H. K. C. and Green, R. F. "An imaging survey of fields around quasars. II—The association of galaxies with quasars". *The Astrophysical Journal*, 280:79–90, 1984.
- Yee, H. K. C. and Green, R. F. "Surveys of fields around quasars. IV—Luminosity of galaxies at  $z \approx 0.6$  and preliminary evidence for the evolution of the environment of radio-loud quasars". *The Astrophysical Journal*, 319:28–43, 1987.
- Yee, H. K. C., Green, R. F., and Stockman, H. S. "Surveys of fields around quasars. III—Intermediate-redshift quasars: Catalog and background galaxy counts". *The Astrophysical Journal Supplement Series*, 62:681–702, 1986.
- York, D. G. et al. "The Sloan Digital Sky Survey: Technical summary". *The Astronomical Journal*, 120:1579–1587, 2000.
- Young, J. S. and Scoville, N. Z. "Molecular gas in galaxies". *Annual Review of Astronomy and Astrophysics*, 29:581–625, 1991.
- Zheng, W. et al. "An overdensity of galaxies near the most distant radio-loud quasar". *The Astrophysical Journal*, 640:574–578, 2006.
- Zwicky, F. "Die rotverschiebung von extragalaktischen nebeln". *Helvetica Physica Acta*, 6:110–127, 1933.
- Zwicky, F. "On the clustering of nebulae". *Publications of the Astronomical Society of the Pacific*, 50:218–220, 1938.
- Zwicky, F., Herzog, E., Wild, P., Karpowicz, M., and Kowal, C. T. *Catalogue of Galaxies and Clusters of Galaxies*. California Institute of Technology, 1968.